

APL SEV 005
(QM-76-120)
JUNE 1977

AD A 045615



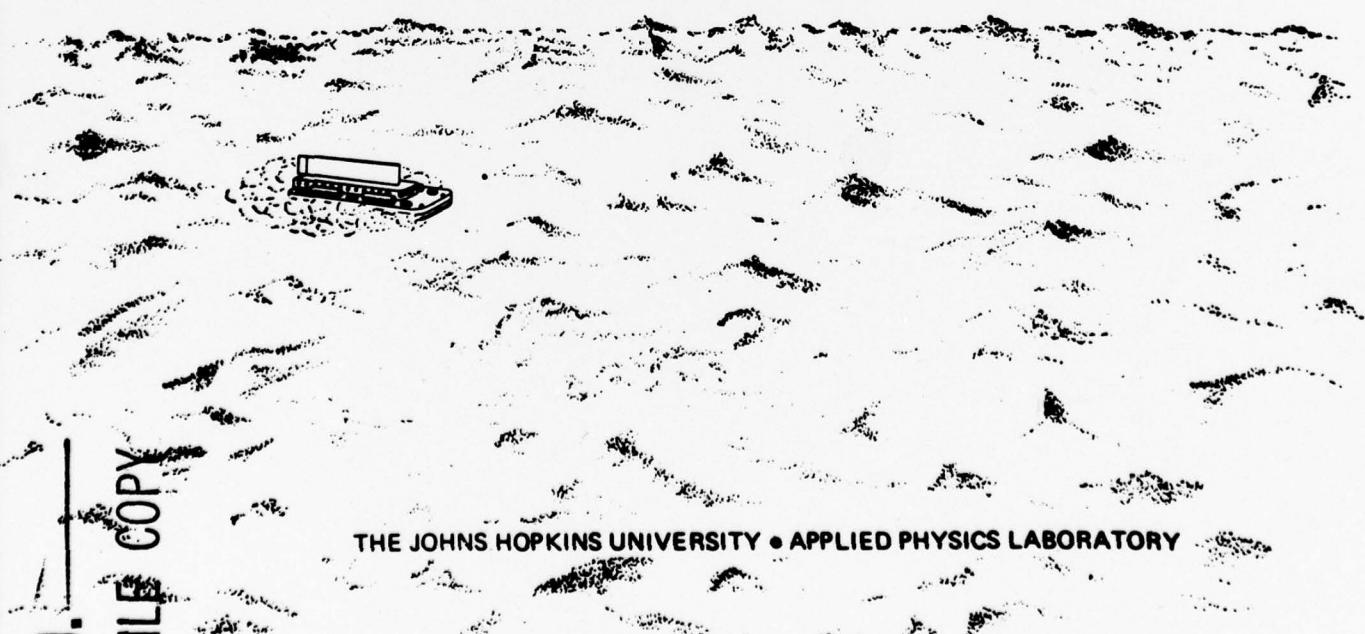
12 2



SEV Program Reports

APL ARCTIC SEV SUBSYSTEM DEVELOPMENT PROGRAM

FINAL SUMMARY REPORT



THE JOHNS HOPKINS UNIVERSITY • APPLIED PHYSICS LABORATORY

AD No. 120C FILE COPY
120C

Approved for public release; distribution unlimited.

Unclassified

SECURITY CLASSIFICATION OF THIS PAGE

**PLEASE FOLD BACK IF NOT NEEDED
FOR BIBLIOGRAPHIC PURPOSES**

REPORT DOCUMENTATION PAGE

ISSN 1062-1024 • 111 • 164-165 • 114-115 • 116-117 • 118-119

Surface Effect Vehicle	Obstacle Measurement
Arctic SEV	94 GHz Radar
Radar Shadowing Concept	Pillbox Antenna
Obstacle Detection and Avoidance	Radome

Aztran

20. ABSTRACT (Continue on reverse side if necessary and identify by block number.)

A study was conducted by APL to define the subsystem requirements in developing a large, high-

Subsystem Requirements in development

Vehicle (SEV). During 1970-1974, APL participated in the Research and Development Phase of the National Glaciation Project.

20. ABSTRACT (Continue on reverse side if necessary and identify by block number.)

20. ABSTRACT (Continue on reverse side if necessary and identify by block number)
A study was conducted by APL to define the navigation, terrain surveillance, and communications subsystem requirements in developing a large, high-speed, long-range Arctic-based Surface Effect Vehicle (SEV). During 1970-1974, APL participated in a program sponsored by ARPA/NSRDC (Advanced Research Projects Agency/Naval Ship Research and Development Center) to develop the technology required to use the SEV's potential as a high performance platform for Arctic operations. APL's task was to provide the obstacle-avoidance, navigation, and communications concepts and the design information for future Arctic SEV applications. The following APL efforts are discussed: development and evaluation of a 94-GHz obstacle-detection system, conceptual design of a complete terrain-avoidance system, tests and analyses in support of the proposed terrain-avoidance and navigation systems, and preliminary communications system design. The results of an APL study of the general characteristics of SEV's and their proposed missions, and a review of obstacle-avoidance techniques previously developed, are also presented.

DD FORM 1 JAN 73 1473

Unclassified

SECURITY CLASSIFICATION OF THIS PAGE

APL SEV 005

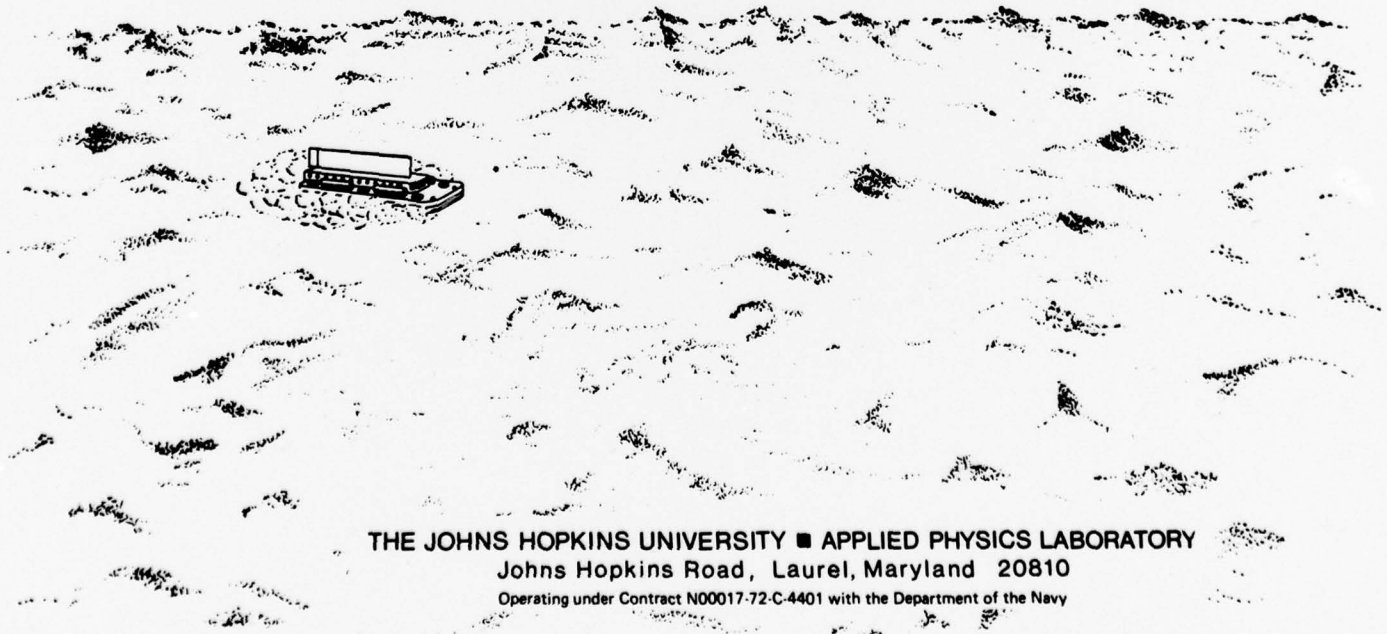
(QM-76-120)

JUNE 1977

SEV Program Reports

**APL ARCTIC SEV SUBSYSTEM
DEVELOPMENT PROGRAM
FINAL SUMMARY REPORT**

SPONSORED BY ARPA UNDER A0 1614



THE JOHNS HOPKINS UNIVERSITY ■ APPLIED PHYSICS LABORATORY
Johns Hopkins Road, Laurel, Maryland 20810
Operating under Contract N00017-72-C-4401 with the Department of the Navy

Approved for public release; distribution unlimited.

THE JOHNS HOPKINS UNIVERSITY
APPLIED PHYSICS LABORATORY
LAUREL MARYLAND

ABSTRACT

APL conducted a study

A study was conducted by APL to define the navigation, terrain surveillance, and communications subsystem requirements in developing a large, high-speed, long-range Arctic-based Surface Effect Vehicle (SEV). During 1970-1974, APL participated in a program sponsored by ARPA/NSRDC (Advanced Research Projects Agency/Naval Ship Research and Development Center) to develop the technology required to use the SEV's potential as a high performance platform for Arctic operations. APL's task was to provide the obstacle-avoidance, navigation, and communications concepts and the design information for future Arctic SEV applications. The following APL efforts are discussed: development and evaluation of a 94-GHz obstacle-detection system, conceptual design of a complete terrain-avoidance system, tests and analyses in support of the proposed terrain-avoidance and navigation systems, and preliminary communications system design. The results of an APL study of the general characteristics of SEV's and their proposed missions, and a review of obstacle-avoidance techniques previously developed, are also presented.

A

ACCESSION FOR	
NTIS	Vide Section <input checked="" type="checkbox"/>
DDC	B.M. Section <input type="checkbox"/>
STANNO. 1010	<input type="checkbox"/>
J.S.I.C.A.P.Y	<input type="checkbox"/>
BY	
DISTRIBUTION/AVAILABILITY CODES	
D	SPECIAL
A	

CONTENTS

List of Illustrations	8
List of Tables	15
1. Introduction	17
Background of Overall SEV Program	17
APL Task and Responsibilities	18
Problem Statement	19
Program Synopsis	19
2. Obstacle Detection and Avoidance	21
System Performance Requirements	22
Vehicle Parameters	22
Terrain Environment	24
Atmospheric Environment	25
Absorption by Uncondensed Atmospheric Gases	26
Attenuation by Suspended Particles: Liquid Water	30
Attenuation by Suspended Particles: Ice and Snow	37
Principle Issues	40
Obstacle Measurement Techniques	40
Radar Shadowing Concept	41
Resolution Requirements	43
Sensor Selection	53
Baseline Design Concept	57
3. Preliminary Experiments	61
CRREL Tests	61
Fog Backscatter Measurements at 95 GHz	62
Experimental Procedure	63
Measurement Results	63
APL Arctic Tests, Pt. Barrow, 1971	69
Test Procedure	70
Fog Attenuation Measurements	74
Preliminary Test Results	76
Conclusions	76

4.	Experimental Obstacle Detection System	79
	Development Approach	79
	System Description	80
	95-GHz Radar Transmitter and Receiver	83
	Radar Controller	88
	Antenna System	91
	Antenna Development	91
	Electrical Design	99
	Mechanical Design	104
	Measured Performance	111
	Radome Characteristics	128
	Antenna Support and Drive Assembly	131
	Construction Approach	131
	Design Constraints and Tradeoffs	132
	Phase I Two-Axis Gimbal	132
	Support Structure for Random and Gimbal	164
	Stabilized Gimbal	167
	Platform Controller	177
	Video Processing and Test Control	179
	Analog/Digital Converter	179
	High-Speed Color TV Display	181
	System Computer	184
	Data-Processing Software	187
	Range Processing	192
	Azimuth Processing	195
	Target Detection	199
	Basic Philosophy	203
	Shadow Processing	205
	Test and Evaluation	216
	Field-Test System Configuration	221
	Field-Test Site	221
	Field-Test Operations	225
	Field-Test Results	230
5.	Navigation System	234
	Navigation Systems	234
	Proposed Navigation System	236
	Aztran Error Analysis	239
	Aztran Performance	240
6.	Communication System	251
	Introduction	251
	Proposed System	251

THE JOHNS HOPKINS UNIVERSITY
APPLIED PHYSICS LABORATORY
LAUREL MARYLAND

7. Conclusions and Recommendations	253
Obstacle Detection and Avoidance	253
Navigation	253
Communications	253
Acknowledgment	255
References	257
Bibliography	261
Appendix A: Vendor Specifications	279
Appendix B: Error-Model Equations	293
Appendix C: An Azimuth Determination System Utilizing the Navy Navigation Satellites	303

ILLUSTRATIONS

1	Basic Vertical Resolution Requirement for Obstacle Detection	23
2	Calculated Total Atmospheric Absorption Coefficient Spectrum for the Centimeter-Millimeter Region at Sea Level	27
3	Atmospheric Transmittance (3.4-mi Path; Temperature, 64°F; Relative Humidity, 57%; Daylight Visual Range, 37.3 mi)	29
4	Typical Values of Atmospheric Extinction Coefficient as a Function of Wavelength	32
5	Theoretical Values of Attenuation by Rain and Fog	35
6	Theoretical Values of Attenuation as a Function of Rate of Precipitation, Using Raindrop Distributions of Laws and Parsons	36
7	Observed and Calculated Attenuations	38
8	Radar Shadowing Concept	42
9	Basic Maneuver Geometry	45
10	Horizontal Beamwidth versus Vehicle Width, Velocity, and Obstacle Width for Radar Shadowing	47
11	Horizontal Beamwidth versus Obstacle Width and Vehicle Velocity for Radar Shadowing	49
12	Avoidance Reaction Time versus Obstacle Width and Horizontal Beamwidth for Shadowing Radar System	50
13	Avoidance Reaction Time versus Obstacle Width and Horizontal Beamwidth for Shadowing Radar System	51
14	Avoidance Reaction Time versus Obstacle Width and Horizontal Beamwidth for Shadowing Radar System	52
15	Vertical Beamwidth versus Antenna Height and Minimum Range for Radar Shadowing	54
16	Horizontal Aperture Requirements for Radar Shadowing	56

17	Preliminary Obstacle Avoidance/Navigation Systems Concept	59
18	Multicolor Obstacle Display Concept	60
19	Normalized Ice Fog N-Unit Measurements at 97 GHz	67
20	Normalized Ice Fog N-Unit Extinction Coefficient Measurements at 97 GHz	68
21	June 1971 Test Site	71
22	Basic Test Configuration, Pt. Barrow Tests	72
23	Reference Targets Layout	75
24	94-GHz Return Data	77
25	SEV Experimental Obstacle Detectors System Functional Block Diagram	81
26	95-GHz Radar Transmitter and Receiver	84
27	Ferrite Switch Attenuation at 94 GHz	86
28	Gain Distribution and Control 300-MHz IF Amplifier	87
29	Logarithmic Video Amplifier Characteristic	89
30	Radar Controller Front Panel	90
31	Antenna First-Mode Vibration Frequencies, When Antenna is Mounted Rigidly Through the Azimuth Drive Adapter Plates	94
32	Simplified Diagram of Parabolic-Cylinder Reflector Fed by Hoghorns	95
33	Geodetic Lens Geometry for Producing Collimated Line Source	96
34	Parabolic Hoghorn for Producing Collimated Line Source in Parallel Plane	97
35	Simplified Diagram of Pillbox Antenna Consisting of Feedhorn and Parabolic Section in Parallel Plate	98
36	Pillbox Configuration	100
37	Illustration of Improved Short-Range Resolution by Focusing	101
38	SEV Antenna Configuration Consisting of Primary Feed, Pillbox, Line-Source Feed, and Parabolic Cylinder	103

THE JOHNS HOPKINS UNIVERSITY
APPLIED PHYSICS LABORATORY
LAUREL, MARYLAND

39	Antenna Assembly	105
40	Antenna Assembly	106
41	Primary Feedhorn Mounting Plate (Interior View)	108
42	Primary Feedhorn Mounting Plate (Exterior View)	109
43	E-Plane Antenna Pattern at 95.0 GHz on 4400-ft Range with Temperature at 70°F . . .	115
44	H-Plane Antenna Pattern at 95.0 GHz on 4400-ft Range with Temperature at 70°F . . .	116
45	Expanded E-Plane Antenna Patten at 95.0 GHz on 4400-ft Range with Temperature at 70°F . .	117
46	Expanded H-Plane Antenna Pattern at 95.0 GHz on 4400-ft Range with Temperature at 70°F . .	118
47	E-Plane Antenna Pattern at 93.5 GHz on 4400-ft Range with Temperature at 0°F . . .	119
48	H-Plane Antenna Pattern at 93.5 GHz on 4400-ft Range with Temperature at 0°F . . .	120
49	Expanded E-Plane Antenna Pattern at 93.5 GHz on 4400-ft Range with Temperature at 0°F . .	121
50	Expanded H-Plane Antenna Pattern at 93.5 GHz on 4400-ft Range with Temperature at 0°F . .	122
51	E-Plane Antenna Pattern at 95.5 GHz on 4400-ft Range with Temperature at -20°F . .	123
52	H-Plane Antenna Pattern at 95.5 GHz on 4400-ft Range with Temperature at -20°F . .	124
53	Expanded E-Plane Antenna Pattern at 95.5 GHz on 4400-ft Range with Temperature at -20°F . .	125
54	Expanded H-Plane Antenna Pattern at 95.5 GHz on 4400-ft Range with Temperature at -20°F . .	126
55	Radome for the 95-GHz Antenna	129
56	Radiation Pattern of the 95-GHz Antenna . .	130
57	Azimuth Drive Bending Load and Torque Flow Path	134
58	Azimuth-Drive Stiffness Test	135
59	Azimuth Bearing Fit-and-Stiffness Test . . .	136
60	Azimuth-Drive Bearing-Seal Arrangement . . .	137
61	Azimuth-Drive-Shaft Shoulder Weld Preparation .	139

62	Azimuth Drive-Assembly Components	140
63	Exploded View of RF Slip Ring Assembly	141
64	RF Slip-Ring Assembly as Modified for Improved Shielding	143
65	Exploded View of Shaft-Encoder Mounting That Provides Torsional Rigidity While Not Imposing Radial or Axial Bearing Loads on Encoder If Drive-Shaft Runout Exists	145
66	Shaft-Encoder Mounting	146
67	Radome Panel Construction	148
68	Radome/Antenna Clearance Diagram	150
69	Vertical Antenna-Mounting Adapter Plate	151
70	Antenna/Azimuth-Drive Resonant Frequency Test	152
71	Antenna/Azimuth-Drive Measurement Resonant Frequencies	153
72	Load Path in Azimuth-Drive Mounting Platform	155
73	Azimuth-Drive Mounting Platform Double-Wall Cylinder with Fully Welded Stiffness	156
74	Azimuth-Drive Mounting Platform Internal-Cell Structure	156
75	Phase II Stabilized Platform Constructed from Phase I Platform	158
76	Azimuth-Drive Block Diagram	161
77	Radome and Gimbal Support Structure with Phase I Gimbal and Antenna	165
78	Radome-Ventilation Blower for Condensation Control	166
79	SEV Antenna on Three-Axis Stabilized Platform	168
80	Conversion from Two-Axis Gimbal to Three-Axis Stable Platform	170
81	Details of Roll-Axis Bearings, Seals, Motor, Pickoff, and Brakes	171
82	Stable Platform Assembly Process	172
83	Outer Gimbal Assembly	173
84	Outer Gimbal Assembly Steps 1 and 2	174

THE JOHNS HOPKINS UNIVERSITY
APPLIED PHYSICS LABORATORY
LAUREL, MARYLAND

85	Outer Gimbal Assembly Steps 3 and 4	175
86	Outer Gimbal Assembly Steps 5 and 6	176
87	Front Panel of the Platform Controller	178
88	Front Panel of the Transient Recorder	180
89	Color Display System Block Diagram	183
90	Display Memory Operation, Pictorial Sketch	185
91	Block Diagram, Single TV Line Memory Organization	186
92	Experimental System Record and Control Software	188
93	Shaft Encoder Azimuth Plot Antenna Scan at 10 Hits/Beamwidth	190
94	Experimental System-Playback Software	191
95	Flow Diagram, Range Processing	196
96	Range Processing	197
97	Flow Diagram, Azimuth Processing	200
98	Azimuth Processing	201
99	Azimuth Processing	202
100	Azimuth Relationship Between Azimuth and Target Processes	204
101	Flow Diagram, Target Processing	206
102	Target Processing	207
103	Shadow Processing Used for High Ground Return, Both Sides of Shadow	209
104	Shadow Processing Used for High Ground Return, One Side of Shadow	210
105	Shadow Processing Used for Low Ground Return, Both Sides of Shadow	212
106	Sliding $M \times N$ Detector with Five Range Bins Shadow Processing	215
107	Shadow Processor Flow Diagram: Determine Average Ground Return and Minimum Shadow Return	217
108	Shadow Processor Flow Diagram: Threshold Ground Return and Shadow Depth	218
109	Shadow Processor Flow Diagram: Determine $M \times N$ Detector Output	219

THE JOHNS HOPKINS UNIVERSITY
APPLIED PHYSICS LABORATORY
LAUREL MARYLAND

110	Shadow Processor Flow Diagram: Check M × N Detector for End Shadow	220
111	Trailer-Mounted Test Setup for Initial SEV Field Tests	222
112	Support and Control Electronics for SEV System	223
113	Interface Electronics and Memory (right) and the Computer Recorder, General Automation Computer, and its Interface (left)	224
114	View Downrange Immediately in Front of Radome .	226
115	Same View as Fig. 114 Except that Grass Has Been Mowed in an Attempt to Reduce Ground Clutter	226
116	Emplacement of the Radome Trailer Mounted on Top of a Steel Frame, with the Electronics Van Parked Beneath	228
117	View Downrange, in Front of the Radome	229
118	SEV Navigation System	237
119	Aztran Concept	238
120	Aztran Errors: Case 1	241
121	Aztran Errors: Case 2	242
122	Aztran Errors: Case 3	243
123	Aztran Errors: Case 4	244
124	Aztran Errors: Case 5	245
125	Aztran Errors versus Pass Elevation for Several Baseline Azimuths at APL	246
126	Aztran Errors: Case 6	248
127	Aztran Errors: Case 7	249
128	Aztran Errors: Case 8	250
A-1	Torque Motor Specification	282
A-2	Thermistor Resistance-Temperature Characteristic	287
A-3	Bulova Servo Products DC Servo Amplifiers Model DCA 1000	291
C-1	Aztran Concept	305
C-2	Coordinates Used in Deriving Equations . . .	307
C-3	Aztran Block Diagram	313

THE JOHNS HOPKINS UNIVERSITY
APPLIED PHYSICS LABORATORY
LAUREL MARYLAND

C-4	Pass Azimuth Errors versus Number of Usable 2-Minute Intervals	314
C-5	Aztran Second-Order Digital Filter	315
C-6	Aztran Equipment	317
C-7	One of Two Aztran Antennas	317

TABLES

1	Number of Ridges per Kilometer, Above a Given Height	25
2	Parameters Affecting Sensor Horizontal Beamwidth for Radar Shadowing	48
3	Measured Particle Sizes, Number per cm ³ , and Laser (63.28 μm) Extinction in Artificial Ice Fog	64
4	Results of Measurements of Millimeter Wave Propagation and Laser Extinction	65
5	Mean Values of the Millimeter Wave Propagation Measurements on Artificial Ice For Normalized for 1 dB/m Extinction of Laser (63.28 μm) Light	69
6	Data Collected During June 1971 Tests	73
7	Characteristics of 94-GHz Fixed Fan-Beam Antenna	93
8	Estimated Losses for 100-Inch Antenna	104
9	Gain, Beamwidth, and Sidelobes at -20°F and at 4400-ft Range	113
10	Gain, Beamwidth, and Sidelobes at 0°F and at 4400-ft Range	113
11	Gain, Beamwidth, and Sidelobes at 70°F and at 4400-ft Range	113
12	Gain, Beamwidth, and Sidelobes at 50°F and at 2-1/8 mi Range	127
13	Gain, Beamwidth, and Sidelobes at 55°F and at 1000-ft Range	127
14	Gain, Beamwidth, and Sidelobes Averaged over Frequency at 1000-ft Range	127
15	Gain, Beamwidth, and Sidelobes Averaged over Temperature and Frequency at 4400-ft Range	127
16	Experimental System Field-Test Parameters	187
17	Range Processing	194
18	Azimuth Processing	198
19	Target Processing	205

THE JOHNS HOPKINS UNIVERSITY
APPLIED PHYSICS LABORATORY
LAUREL MARYLAND

20	Shadow Processing	213
21	Shadow Existence Condition, Five-Bin Sliding M × N Detector	214
22	Field-Test Target Configurations	231
23	Shadow-Processing Results: Obstacle Height Determination	232
A-1	Torque Motor Specifications	281
A-2	Tachometer Data	284
A-3	RA16 Encoder Specifications	286
A-4	Electrical Specifications	290
C-1	Results of Computer Filtered Aztran Passes . . .	318

1. INTRODUCTION

The Arctic environment with its unique obstacles to surface travel, periods of poor or no visibility, and electromagnetic disturbances presents several difficult problems to vehicle piloting, navigation, and communication systems. The development of certain portions of these systems was undertaken by APL/JHU in order to realize an all-weather Arctic Surface Effect Vehicle capable of safe travel over long ranges with reasonable payloads. The required obstacle detection capability and the presentation of such information to the pilot are unique and difficult assignments, but are necessary to permit Arctic Surface Effect Vehicle operation at speeds greater than 40 kt. Detection and recognition of a hazard must take place as far as three miles ahead of the craft in order to allow sufficient time and space for avoidance maneuvers.

BACKGROUND OF OVERALL SEV PROGRAM

Vehicles designed to ride on a cushion of air (commonly referred to as hovercraft or Air Cushion Vehicles (ACV)) have been demonstrated and applied to various missions over the last 10 years. Within the Department of Defense (DoD), such vehicles are commonly referred to as Surface Effect Vehicles (SEV's). The ability of an SEV to travel over unprepared surfaces in otherwise inaccessible areas has led to considerable interest within DoD.

In 1966, DoD conducted a study to define the necessary research and development requirements for a military SEV. As a result of this study and a presidential directive, the Department of Commerce and the Department of the Navy established the Joint Surface Effect Ship Program Office (JSESP) to determine the feasibility of building and operating large ocean vehicles (about 4000 tons) at high speeds (80 kt or greater). For increased air-capture efficiency, the ships considered will have rigid sidewalls that pierce the water surface. Such craft are commonly referred to as Surface Effect Ships (SES's). By 1970, the Maritime Administration decided to defer its interest until after SES technology was further developed. The Navy is continuing toward development of a 2000-ton SES and has conducted their initial test programs of two 100-ton prototype craft in 1972-1973. For Arctic applications SEV's with flexible sidewall designs are of primary interest. Both the Army and the Navy have successfully used small SEV's with flexible skirts (patterned after a British commercial design) in Vietnam. Introduction of the flexible-skirt design has greatly enhanced the ability of the craft to travel over terrain obstacles.

THE JOHNS HOPKINS UNIVERSITY
APPLIED PHYSICS LABORATORY
LAUREL, MARYLAND

Flexible-skirted SEV's are now providing passenger service across the English Channel, routinely.

During 1968 and 1969, based on general recognition of the military potential of the SEV, the Advanced Research Projects Agency (ARPA) conducted studies using members of the military services, industry, Federal Contract Research Centers (FCRC's), and academic institutions to examine the technological status of these machines and their potential missions. In these studies, some 13 mission applications, which represented a typical cross section of candidate missions, were investigated. As a result of these activities, ARPA established that the high-speed SEV represents a potentially attractive concept for which there was sufficient justification to proceed with an advanced technology and vehicle demonstration program. Review of these studies and the continuing need for the capability to operate in Arctic environments indicated that the SEV has outstanding potential for Arctic operations. The availability of an SEV capable of coping with the hostile Arctic environment would open vast areas heretofore inaccessible to other surface vehicles and therefore would offer the military planner a capability not currently available.

In 1970, an ARPA team was formed to develop Arctic SEV technology. The team members are the Naval Ships Research and Development Center (NSRDC), the Aerospace Corporation, the Army's Cold Regions Research and Engineering Laboratory (CRREL), and the Applied Physics Laboratory of The Johns Hopkins University (APL/JHU). NSRDC was responsible for overall technical direction of the SEV program; the Aerospace Corporation conducted parametric vehicle design studies and assisted NSRDC in the technical management function; CRREL was responsible for describing the Arctic environment and terrain as it affects SEV design; and APL/JHU was responsible for developing the pilotage technology (i.e., obstacle avoidance, navigation, and communications system designs) for an Arctic SEV.

In general, the technical objective of the ARPA program was to develop the technology required to exploit the potential offered by the SEV as a high performance military platform for Arctic operations.

APL TASK AND RESPONSIBILITIES

Generally, the APL task responsibilities were to provide the obstacle-avoidance, navigation, and communications concepts and design information for future Arctic SEV applications.

Problem Statement

Piloting a high-speed SEV in the Arctic presents several difficult problems. The limited maneuverability of the craft, its limited ground clearance, and its difficulties on slopes place new demands on the obstacle-avoidance and navigation functions. The large turning radius and long stopping distance require terrain hazard identification considerably in advance of the vehicle, a function that must be provided under all weather conditions, day or night. Obstacle height measurement accuracy within one or two feet must be achieved and, for craft-mounted sensors, the data must be obtained from very low grazing angles.

Navigation is complicated by operations at high latitudes. Magnetic heading references are virtually useless, and inertial systems are difficult to align and require updating for long missions. Azimuth determination is particularly difficult in the Arctic regions. Celestial navigation is limited to clear weather operation with complications resulting from periods of 100% sun-light.

Communications are complicated by propagation anomalies that occur frequently in the Arctic region. Military missions in this region require secure communications unit-to-unit, and unit-to-Continental United States (CONUS).

Program Synopsis

At the onset of the Arctic SEV program, the program was structured to lead to a large-scale test-and-demonstration vehicle for Arctic use on a minimum schedule. On that basis, development efforts on the required pilotage subsystems were planned to proceed in parallel. Within the first three months the program was restructured putting APL's primary first-year emphasis on the terrain-avoidance system and including a limited effort on navigation techniques (Ref. 1). By the beginning of FY 72 the program at APL was further defined to concentrate the effort on development of a 94-GHz obstacle detection system, since that development was identified as a maximum payoff area requiring state-of-the-art development (Refs. 2 and 3). Composite design of a complete terrain-avoidance system would be accomplished with the aid of a unique

Ref. 1. "Contract N00017-62-C-0604; Technical Plan and Cost Estimate for the U.S. Naval Ship Research and Development Center," APL Ltr. AD-4788-39a, 27 July 1970.

Ref. 2. L. L. Warnke, "Program Plan for Development of an Obstacle Detection System - Arctic SEV," APL/JHU S3R-71-349, 13 October 1971.

Ref. 3. T. Thomson and A. C. Schultheis, "NSRDC Arctic SEV Program Plan," APL/JHU S3R-71-368, 4 November 1971.

THE JOHNS HOPKINS UNIVERSITY
APPLIED PHYSICS LABORATORY
LAUREL, MARYLAND

simulation facility (Ref. 4). Final redirection of the program for FY 74 and FY 75 limited the scope of the 94-GHz obstacle-detection system to testing of the shadow concept and deleted the full-scale simulation effort (Ref. 5).

Within the scope of the resulting Arctic SEV program, APL has (1) completed an evaluation of the 94-GHz obstacle-detection system using the shadowing concept, (2) completed conceptual design of a complete terrain-avoidance system, (3) completed a conceptual design of a unique simulation facility, (4) conducted tests and analysis in support of the proposed terrain-avoidance system, (5) conducted tests and analysis in support of a navigation-system concept, and (6) offered some preliminary considerations on the communications systems.

The APL program began in the latter part of FY 70 and the effort within that year was devoted to a study of the general characteristics of SEV's, their proposed missions, a review of obstacle-avoidance techniques previously developed, development of a preliminary concept for obstacle avoidance and navigation, and definition of the required experiments for the first Arctic tests.

The main tasks carried out in FY 71 were to further define a baseline avoidance system concept (discussed in Section 2), and accomplishment of a test series to gather data to support the concept definition (discussed in Section 3). Initial testing of the satellite azimuth-measuring system was also completed (discussed in Section 5).

In FY 72 the primary tasks were related to analysis of test data and initial design of the 94-GHz experimental obstacle-detection system and the simulation facility. The final phases of the program were concerned with development and testing of the 94-GHz experimental obstacle-detection system (discussed in Section 4).

Ref. 4. APL Arctic SEV Program Plan, QM-72-040, APL/JHU SEV-002 (revision of APL Arctic Program Plan, QM-71-033, APL/JHU SEV-001), April 1971.

Ref. 5. L. L. Warnke, "APL Arctic SEV Program - Revised Plan and Schedule for FY 1974 and FY 1975," APL/JHU S3R-73-093, 15 May 1973.

2. OBSTACLE DETECTION AND AVOIDANCE

Pilotage of a large, high-speed SEV in the Arctic presents several difficult problems. The limited maneuverability of the craft, its limited ground clearance, and its difficulties on slopes place new demands on the obstacle-avoidance and navigation functions. The large turning radius and long stopping distance require obstacle hazard identification considerably ahead of the vehicle, and this function must be provided under all weather conditions, day or night. Obstacle height measurement accuracy within a foot or two must be achieved and, for craft-mounted sensors, the data must be obtained from very low grazing angles.

Routine mapping of the Arctic terrain in the classic sense (i.e., development of mapping data over a long period of time) is not possible because of the dynamic nature of the terrain. The detailed terrain structure varies as the ice structure expands and contracts, and the total ice cap is in continual motion. Mapping at a high frequency rate over the total Arctic region by aircraft or satellite systems is not currently assumed practical. Limited use of such data as might be made available (perhaps as provided by vehicles operating for other purposes within the region) may be considered as an aid to the total obstacle-avoidance problem.

Mapping provided by a dedicated fly-ahead vehicle (manned or unmanned) can also provide the required terrain data. Such systems have the advantage of improved look geometry, but have the disadvantage of increased fuel requirements and increased system complexity. This technique might best be employed to solve special problems at limited times rather than the routine obstacle avoidance function.

Craft-mounted sensors can provide the basic routine obstacle-avoidance function, and would probably be required for backup of systems that are not craft-mounted. The range and limitations of such systems must be determined so as to assess properly what mix of systems is optimum for a given SEV mission. That is, the mix of craft-mounted, fly-ahead, and routine mapping systems would be expected to vary with mission objectives. Both the use and sophistication of each technique would depend on the SEV application. For example, if a very sophisticated, routinely applied fly-ahead system was consistent with one set of mission objectives, a very simple craft-mounted system might be envisioned only as a backup with limited operational capability. On the other hand, a sophisticated craft-mounted system might provide the full operational capability most of the time, and a relatively simple fly-ahead system might be used for special problems.

Each of these capabilities was considered to some extent, but the primary effort was concerned with the techniques of craft-mounted sensor systems. The remainder of this discussion will be restricted to the characteristics of craft-mounted obstacle-avoidance systems for Arctic applications.

SYSTEM PERFORMANCE REQUIREMENTS

Development of an obstacle-avoidance system is fundamentally related to the operational doctrine of the specific craft and to the operational environment. Operational doctrine establishes such basic craft parameters as speed, range, maneuverability, and control philosophy, and it also sets bounds on operating times and allowable environmental limitations. The major environmental factors are the character of the terrain and atmospheric conditions in the operational region. In short, the system performance requirements are defined by the mission objectives. The mission establishes the vehicle parameters and the required operating environment and these, in turn, set the requirements for obstacle detection and avoidance.

Vehicle Parameters

Establishment of the basic sensor characteristics for SEV obstacle detection is dependent on three interrelated vehicle parameters: speed, maneuverability, and obstacle clearance capability. Generally speaking, detection requirements are reduced as the speed is lowered, the maneuverability is increased, or the clearance capability is increased. This characteristic is illustrated in Fig. 1, where the vertical resolution requirement of the obstacle detection sensor is shown as a function of these three parameters. For this illustration, the resolution has been computed as half the vehicle clearance capability and the speed and maneuverability are combined in the constant-speed turning-radius parameter. This simple representation of the vertical resolution requirement assumes that the detection range is equal to the turning-radius capability and allows no additional range for control-system reaction time. These aspects will be considered more fully in the later discussion of measurement techniques. Representative design points for two conceptual SEV designs (150-ton and 500-ton) accomplished for the program (Ref. 6) are shown in the figure along with the resolution capability of some typical sensors.

Speed and maneuverability are naturally related to the expenditure of fuel and are thus influenced by the operating range of

Ref. 6. Arctic Surface Effect Vehicle Program Technology Summary and Design Development, NSRDC Report 4595, Naval Ship Research and Development Center, August 1975.

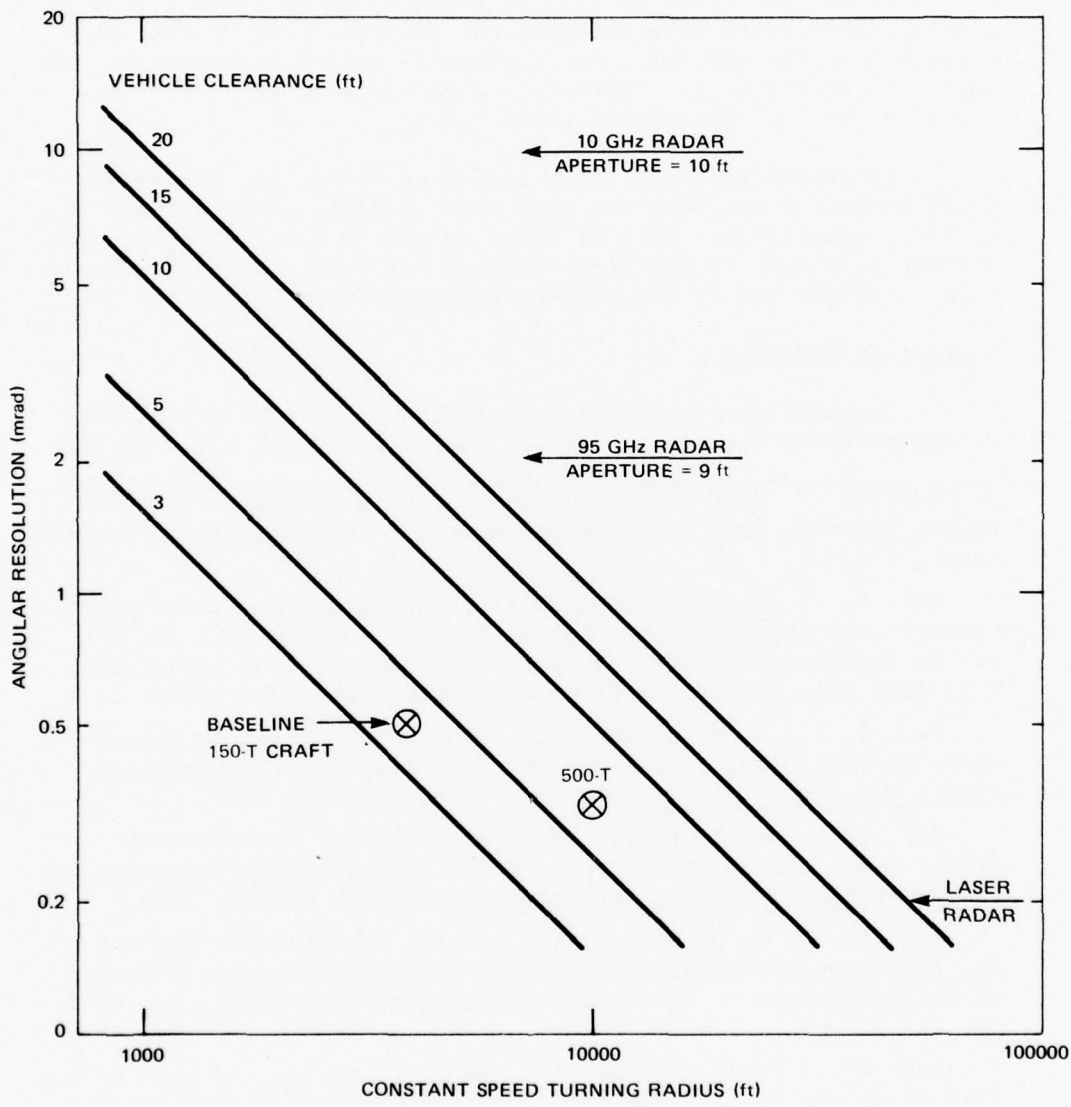


FIG. 1 BASIC VERTICAL RESOLUTION REQUIREMENT FOR OBSTACLE DETECTION

the vehicle. Indeed each of the three parameters that define the obstacle-detection requirement are related to a complex vehicle-design process that is dependent on the vehicle application.

There is one other primary factor relating to the obstacle-detection requirement and that is the response time of the avoidance action. After the sensor has detected an obstacle, there is a delay in relaying this information and then there is a further delay before the control process assesses what action to take and initiates that action. There is a wide range of response times possible for varying control philosophies.

Decreased response time, increased speed, and decreased maneuverability all have the same basic effect on the obstacle detection requirement. Each of these increases the distance at which the obstacle must be detected, whereas the obstacle height resolution is simply set by the vehicle clearance capability.

Terrain Environment

Considerable testing and analysis was carried out by CRREL to characterize the Arctic terrain (Refs. 7 through 13). Through

Ref. 7. "SEV Arctic Environment Data Package," USACRREL Report 16, U.S. Army Cold Regions Research and Engineering Laboratory, 1970.

Ref. 8. P. V. Sellman et al., "Terrain and Coastal Conditions on the Arctic Alaska Coastal Plane," Supplement 1 to "SEV Arctic Environmental Data Package," USACRREL Special Report 165, U.S. Army Cold Regions Research and Engineering Laboratory, 1972.

Ref. 9. W. D. Hibler, III, "Characterization of Cold Regions Terrain Using Airborne Laser Profilometry," Symposium on Remote Sensing in Glaciology, Cambridge, England, 1974.

Ref. 10. W. D. Hibler, III, "Statistical Variations in Arctic Sea Ice Ridging and Deformation Rates," SNAME Symposium on Ice Breaking and Related Technology, Montreal, Canada, 1975.

Ref. 11. W. D. Hibler, III et al., "Statistical Aspects of Sea Ice Ridge Distributions," AIDJEX Bulletin, Vol. 12, Division of Marine Resources, University of Washington, Seattle, WA, 1972, pp. 117-162.

Ref. 12. W. D. Hibler, III and S. F. Ackley, "Height Variation Along Sea Ice Pressure Ridges and the Probability of Finding Holes for Vehicle Crossings," USACRREL Special Report 197, U.S. Army Cold Regions Research and Engineering Laboratory, 1973.

Ref. 13. W. D. Hibler, III and S. F. Ackley, "A Sea Ice Terrain Model and Its Application to Surface Vehicle Trafficability," USACRREL Research Report 314, U.S. Army Cold Regions Research and Engineering Laboratory, 1973.

this effort it was determined that sea ice could be characterized by a single parameter with geographical variations. Table 1 is a statistical summary of the number of ridges per kilometer above a given height, by geographic region. Year-to-year variations of about 1 ft are to be expected. That is, for a year of heavy ridging the height values in the table should be increased by 1 ft. As a result of these studies it was concluded that a minimum obstacle crossing capability of 8 ft should be established to minimize the impact on vehicle mobility. The two designs completed for this program had cushion heights of 9 and 12 ft and these designs were considered in this study to have an obstacle-clearance capability of 7 and 10 ft.

Table 1
Number of Ridges per Kilometer, Above a Given Height

Height (ft)	Region		
	Beaufort Sea	Central Arctic	Offshore
>4	1.0 to 2.0	2.0 to 4.0	4.0 to 7.0
>6	0.2 to 0.5	0.5 to 1.5	1.5 to 4.0
>8	<0.1	0.1 to 0.4	0.4 to 1.0
>10	<0.1	<0.1	0.2 to 0.5

Characterization of the terrain conditions in Alaska is more difficult. In the northern area the terrain is relatively flat and quite well suited to SEV operations. The river systems of interior Alaska offer natural routes for SEV operations. In either of these areas the terrain is stationary and vehicle navigation can be aided by markers and/or beacons. Therefore the obstacle detection systems discussed in this report were designed primarily for Arctic Ocean travel.

Atmospheric Environment

The primary input of the atmospheric environment will be its effect on electromagnetic propagation of the obstacle-detection radars. An electromagnetic signal is attenuated in the atmosphere by two different mechanisms having different frequency dependence

(Refs. 14 through 16). They are, respectively, resonant absorption by the gas molecules of the atmosphere, and attenuation by suspended particles, e.g., dust, condensed water particles of any type, etc. In the Arctic, the particles presumably will be mostly some form of water; liquid or solid.

The effects of the two kinds of attenuation are separate and are additive; they can therefore be discussed separately.

Absorption by Uncondensed Atmospheric Gases

Wavelengths used for obstacle detection must lie in atmospheric "windows" where there is no resonant absorption of energy from the transmitted signal. The well-known radio window is limited at the short wavelength end by absorption caused by resonance peaks in the spectra of oxygen and water vapor. The nitrogen molecule has no resonances in the cm-mm region; CO_2 resonance occurs at a wavelength well below 1 mm, and is therefore not of interest here. Spectrum lines of N_2O , O_3 , and the isotopic forms of water (with deuterium) occur in the region of interest, but may be disregarded because of the low concentration of these molecules in the atmosphere (Refs. 14 and 15). Only the O_2 and H_2O molecule, therefore, need to be considered in the cm-mm region.

The water-vapor molecule has an electric dipole moment, and its spectrum has two marked absorption lines at wavelengths of 1.35 cm and 0.163 cm, respectively; there are several others at wavelengths just under 1 mm. The oxygen molecule is not electrically polar, but has a magnetic moment that reacts with an incident field; its spectrum has several closely-spaced absorption lines near 0.5 cm, and a single line near 0.353 cm, as well as others below 1 mm. All these absorption lines show collision broadening under normal sea-level conditions, so that the atmospheric absorption coefficient does not approach zero anywhere in the cm-mm region. It does, however, become low enough to provide usable transmission windows between the absorption lines.

Figure 2 shows the theoretical attenuation (in dB/km) to be expected in this region, as a function of frequency (with a wavelength scale also). Separate curves are given for oxygen and

Ref. 14. D. E. Kerr (Ed.), Propagation of Short Radio Waves, McGraw-Hill, New York, 1951 (Sections by J. H. Van Vleck and H. Goldstein).

Ref. 15. J. V. Evans and T. Hagfors (Eds.), Radar Astronomy, McGraw-Hill, New York, 1968 (Section by T. F. Rogers).

Ref. 16. H. C. van de Hulst, Light Scattering by Small Particles, John Wiley and Sons, New York, 1957.

THE JOHNS HOPKINS UNIVERSITY
APPLIED PHYSICS LABORATORY
SILVER SPRING MARYLAND

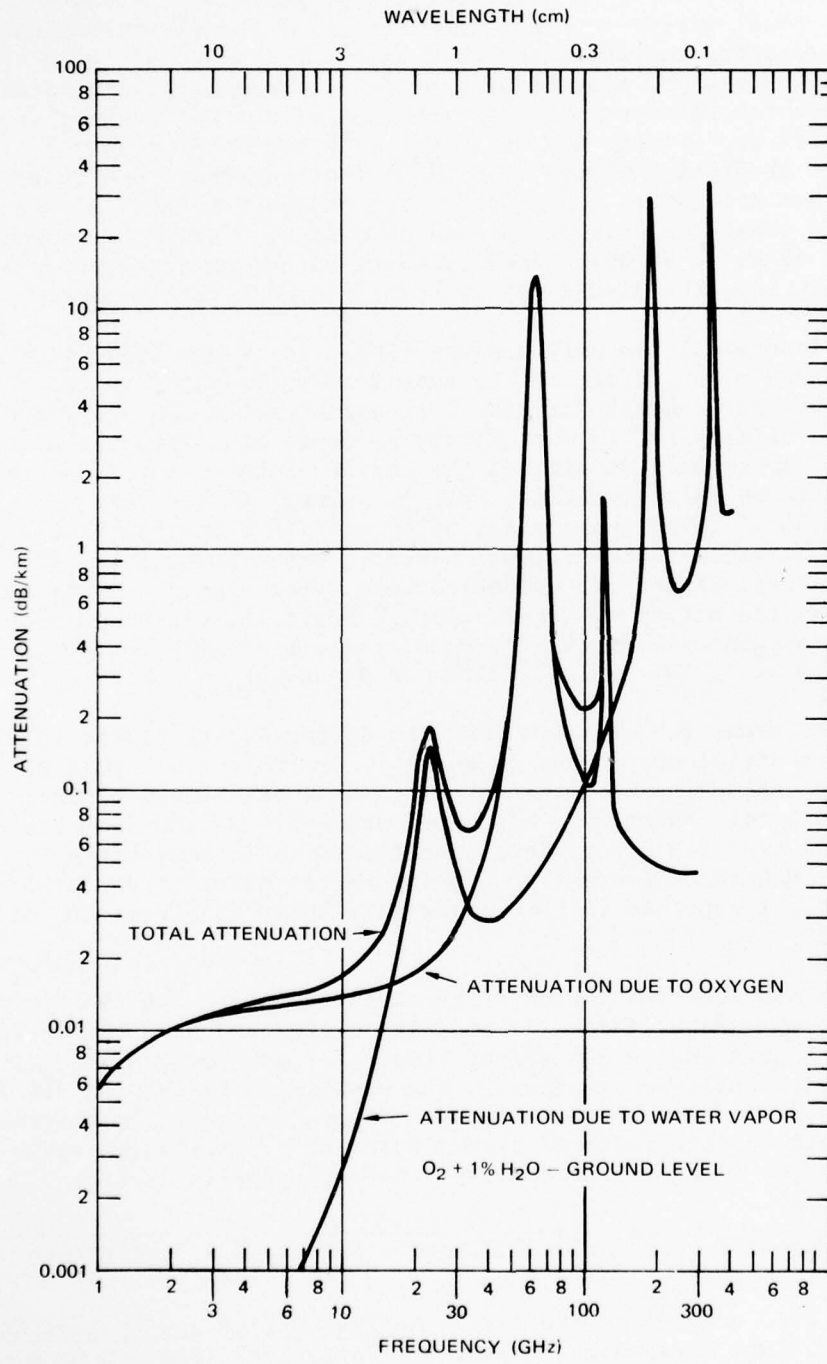


FIG. 2 CALCULATED TOTAL ATMOSPHERIC ABSORPTION COEFFICIENT SPECTRUM FOR THE CENTIMETER-MILLIMETER REGION AT SEA LEVEL (FROM ROGERS, REF. 14)

water vapor. It is assumed for these curves that the clear atmosphere (with no suspended particles) is at sea-level pressure, with the usual oxygen content, and that 1% of the air molecules are water vapor, corresponding to a partial pressure of 10 mb (i.e., a water-vapor content of 7.5 g/m^3). The total calculated absorption for this atmosphere is the sum of the two curves; it is 0.016 dB/dm for a frequency of 10 GHz (the lowest frequency chosen). Absorption minima or windows (but somewhat less transparent than the above) are also present at approximately 35 and 94 GHz. The total (calculated) attenuation is 0.07 dB/km at 35 GHz and 0.22 dB/km at 94 GHz. Both of these values of attenuation are adequately low, the 35-GHz window being the more transparent.

Temperature has only a minor effect on oxygen absorption, but it has a major effect on the amount of water vapor in the air. The water-vapor content for Fig. 2 is a reasonable average for a temperate climate but is more nearly an upper bound for the Arctic region. At Pt. Barrow, Alaska, the surface water-vapor pressure exceeded 10 mb only five times (all in summer) in the year 1967, based on data* taken twice a day at 0^h and 12^h Universal Time. In winter, the water-vapor pressure was more often below 1 mb (i.e., 0.1%, or less, of the air molecules were water vapor). Under such conditions the effect of water vapor is negligible in comparison with the oxygen effect, and the total calculated attenuation is 0.04 dB/km at 35 GHz and 0.12 dB/km at 94 GHz.

Different authors give somewhat different calculated values of these coefficients (Refs. 12 and 14), probably the result of different assumptions for the calculations (with regard to line broadening, for instance). Also, measured values show some discrepancies from the theoretical predictions (sometimes being larger). However, resonant absorption by the gases of the atmosphere is not expected to be a major difficulty at either 10, 35, or 94 GHz.

In the infrared region of the spectrum there are absorption bands of water vapor (Ref. 17) and also of CO₂ and N₂O, but these latter two have negligible effect because of the low concentration. There are transmission windows in the wavelength regions of 3.4 to 4.1 μm , 4.5 to 5 μm , and 8 to 14 μm . Figure 3 shows some observed data on atmospheric infrared transmission as a function of wavelength in μm , taken on a clear day. Note that peaks in Fig. 3

*A data tape from the National Climatic Center, U.S. Department of Commerce, Asheville, NC.

Ref. 17. R. Kingslake (Ed.), Applied Optics and Optical Engineering, Vol. I, Academic Press, New York, 1965 (Section by H. S. Stewart and R. F. Hopfield).

THE JOHNS HOPKINS UNIVERSITY
APPLIED PHYSICS LABORATORY
SILVER SPRING, MARYLAND

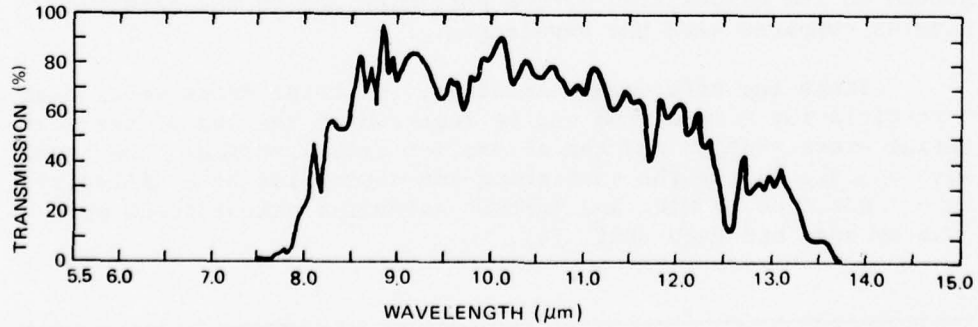
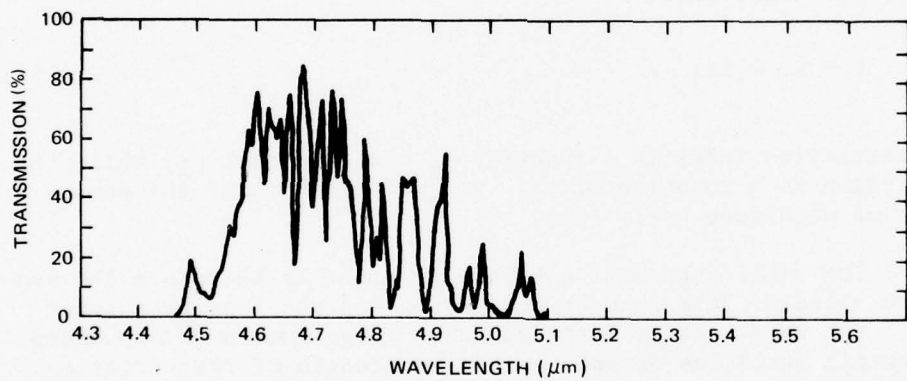
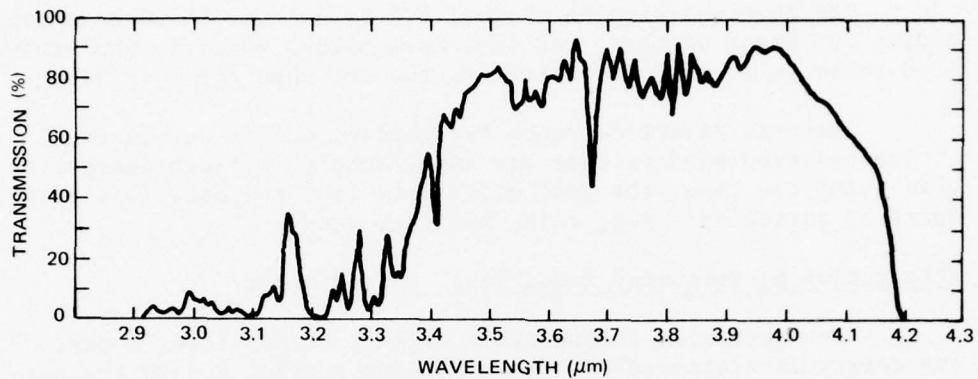


FIG. 3 ATMOSPHERIC TRANSMITTANCE (3.4-MILE PATH, TEMPERATURE 64 °F, RELATIVE HUMIDITY 57 PERCENT, DAYLIGHT VISUAL RANGE 37.3 MILES) (FROM BARNYDT, BROWN, AND DORR, REF. 18)

represent transmission (Ref. 18) while peaks in Fig. 2 represent absorption.

The short-wavelength window, 3.4 to 4.1 μm , would be a good choice for clear weather. As discussed below, however, the window at 8 to 14 μm is much the better of the two when fog is present.

Obstacle detection radar frequencies can be chosen to lie in transmission windows that are satisfactory in clear weather. This being the case, the real difficulty lies in power loss produced by particles: fog, rain, hail, or snow.

Attenuation by Suspended Particles: Liquid Water

When radiation encounters a dielectric particle, a part of the energy is scattered and the remaining portion enters the particle; some of the latter portion will be absorbed and converted into heat. The amount of energy absorbed depends on the magnitude of the imaginary part of ϵ_2 of the complex dielectric constant ϵ of the particle, where

$$\epsilon = \epsilon_1 - i\epsilon_2 . \quad (1)$$

The refractive index is a function of the real part ϵ_1 , while the absorption is a function of ϵ_2 . For water, ϵ_2 is of the same order of magnitude as ϵ_1 (Ref. 14).

The total attenuation by the particle is therefore the sum of two effects: the loss by scattering and the loss by absorption. The total energy loss caused by large number of suspended dielectric particles depends on the wavelength of the radiation, the number, size, and shape of the particles, and the complex dielectric constant of the particle substance. The relative magnitude of the loss by scattering and the loss by particle absorption depend on the composition of the particles and on the particle size as compared with the wavelength.

Since the effects are additive, the total cross section of a particle for attenuation can be regarded as the sum of the scattering cross section and the absorption cross section. The basic work on calculating the scattering and absorption by a dielectric sphere was done by Mie, and further extensive calculations were done by Ryde and Ryde (Ref. 14).

Ref. 18. H. Barhydt, D. P. Brown, and W. B. Dorr, Comparison of Spectral Regions for Thermal Imaging Infrared Sensors, Hughes Aircraft Co., Fullerton, CA.

Attenuation can be calculated rigorously for a large number of spherical particles only if the drop size distribution is known. In the practical case, this distribution is not known. The drop size and number of raindrops per unit volume, for example, are not uniform within a storm region; raindrops may also not be quite spherical, and snowflakes certainly are not. Hence it will be important to obtain observed data on signal propagation in rain and snow.

Considering the theoretical attenuation for small spherical drops having a radius, a (e.g., clouds and fog), the scattering cross section Q_s for a droplet (Ref. 14) is proportional to

$$Q_s \propto \lambda^2 \left(\frac{2\pi a}{\lambda} \right)^6 , \quad (2)$$

where λ is the wavelength of the radiation. Thus for drops of a given size, the scattering varies inversely as the fourth power of the wavelength; this is the well-known Rayleigh scattering. The absorption cross section Q_a for small drops is, however,

$$Q_a \propto \lambda^2 \left(\frac{2\pi a}{\lambda} \right)^3 . \quad (3)$$

For drops that are small in comparison with the wavelength (small a/λ), the scattering cross section Q_s is small in comparison with the absorption cross section Q_a . In this case, the attenuation is caused mostly by absorption, and for a given wavelength, it is proportional to a^3 , or to the volume of the drop. The attenuation produced by a cloud of drops that are small in comparison with the wavelength is thus proportional to the volume of the drops per unit volume of atmosphere, i.e., to the content of condensed water per unit volume.

These conditions hold at a 10.6- μm laser wavelength for haze particles (radius $\approx 0.1 \mu\text{m}$) and perhaps for light fog, but not for clouds where the particle radius is 1 to 10 μm (Ref. 17). A haze is therefore fairly transparent to a 10.6- μm laser beam, but a cloud is not transparent because both scattering and absorption are too great.

Figure 4 shows typical values of the atmospheric extinction coefficient, which includes both scattering and absorption, as a function of wavelength for different atmospheric conditions. These values are consistent with Ref. 17 values, and with Fig. 3. It is immediately obvious that a 10.6- μm laser can be expected to perform better in haze than a wavelength in the 5- μm window. The

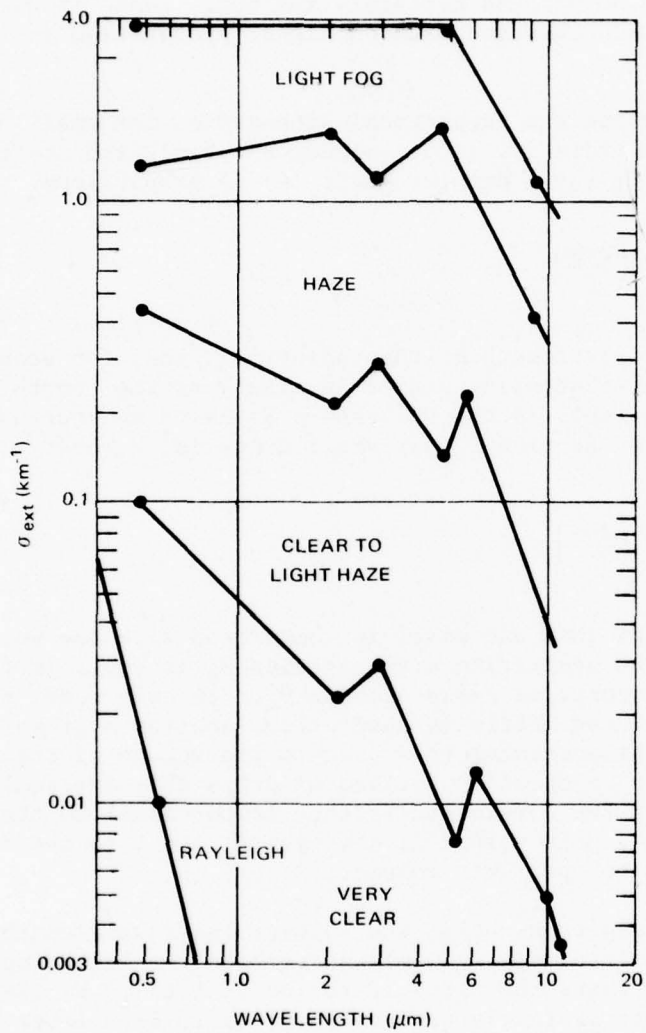


FIG. 4 TYPICAL VALUES OF ATMOSPHERIC EXTINCTION COEFFICIENT AS A FUNCTION OF WAVELENGTH (FROM BARHYDT, BROWN AND DORR, REF. 18)

THE JOHNS HOPKINS UNIVERSITY
APPLIED PHYSICS LABORATORY
LAUREL, MARYLAND

curves of the figure are boundaries for the conditions described as "clear to light haze," "haze," etc. It is of interest to compute the expected signal transmission in these regions.

In the middle of the clear-to-light-haze region the extinction coefficient at 10.6 μm is approximately 0.01 per km. This indicates that 95% of the emitted signal should reach a range of 3 mi (5 km). Some fraction of this would be reflected, and 95% of this fraction would arrive at the detector.

In the middle of the haze region of Fig. 4 the extinction coefficient (at 10.6 μm) is approximately 0.1 km. Only 61% of the signal would therefore reach a range of 3 mi, and 61% of the reflected fraction would arrive at the detector — a considerable degradation. The performance would of course be better at shorter ranges.

A light fog (middle of the region shown, extinction coefficient 0.5 per km) would allow only 8% of the signal to go as far as 3 mi, with a similar loss on the return trip. A laser could still be useful in light fog at shorter ranges: 45% of the signal would reach a range of 1 mi and 45% of the reflected portion would get back to the SEV.

These extinction coefficients are referred to the logarithmic base e and are not to be confused with decibels, which of course pertain to the base 10. If preferred, the extinction coefficients can be converted to decibels by multiplying by $10 \log_{10} e$ (i.e., by 4.343).

In contrast to the laser case, fog and cloud particles are small in comparison with centimeter and millimeter wavelengths; hence, absorption is more important than scattering, and the water-vapor content of the cloud is the important parameter. The same may be true for rain at wavelengths of a few centimeters (if the drops are not too large).

The condensed water content per unit volume is not directly measurable. The precipitation rate, i.e., the volume of water reaching the ground per unit time can, however, be measured. It is often assumed that attenuation during a rain is proportional to the precipitation rate. There is considerable experimental support for this, but the assumption is not well-based theoretically. A given precipitation rate may not always correspond to the same drop-size distribution. Also, the precipitation rate varies from point to point within the same rain shower (Refs. 14 and 19).

Ref. 19. R. K. Crane, "Propagation Phenomena Affecting Satellite Communications Systems Operating in the Centimeter and Millimeter Wavelength Bands," Proc. IEEE, Vol. 59, No. 2, February 1971, pp. 173-188.

Calculated values of attenuation for frequencies above 35 GHz depend heavily on the number of small drops (diameter <2 mm) assumed in the model of drop-size distribution. Any one model is not likely to be valid throughout the region of a shower. Adequately detailed meteorological data are not generally available.

Various methods have been tried in the attempt to measure drop-size distribution: photography of the drops; a blotting paper method (drops caught on a dye-impregnated blotter); a flour method (drops caught in a pan of dry sifted flour); and others. The results obtained so far have not generally been satisfactory.

Figure 5 shows theoretical attenuation coefficients for rain and fog, for the cm-mm region. At 10 GHz, attenuation by rain is 0.3 dB/km for heavy rain (16 mm/h); 0.06 dB/km for moderate rain (4 mm/h); less for lighter rain or fog. The attenuation is markedly greater for higher frequencies: at 35 GHz, 4 dB/km for rain at 16 mm/h; at 94 GHz, 8 dB/km for the same rain, 9 dB/km for heavy fog (2.3 g/m³ of condensed water, optical visibility 100 ft). According to Fig. 5 the attenuation would be greater at 94 GHz than at 35 GHz for all cases shown. The attenuation at 94 GHz would be 1 dB/km for light rain at 1 mm/h or for fog of 0.32 g/m³ of water content (visibility about 400 ft); attenuation at 35 GHz would be about one-fifth as much. These values were calculated on the basis of the raindrop size distribution of Laws and Parsons (Ref. 14). The large increase of the 94-GHz attenuation with respect to the 35-GHz attenuation for light rain or fog comes from the larger proportion of small droplets in the size distribution model for these cases.

The attenuation per drop per cubic meter to be expected from drop radii of 1 or 2 mm is the same for 35 and 94 GHz. For very large drops, however, the theoretical attenuation is a maximum in the 35-GHz region and is less at 94 GHz but by only about 20% for drops of 3.25 mm radius (Ref. 14).

In view of the uncertainty about drop-size distribution in a given rain, it is impossible at present to predict the attenuation over any extended range, with adequate precision.

The theoretical curves for attenuation as a function of precipitation rate are still of some interest, especially in view of the shortage of consistent, observed data. As can be seen, the data of Fig. 5 all correspond to values not very far from the origin of Fig. 6. Rains pertaining to the right half of Fig. 6 are extremely heavy and are rare in most places.

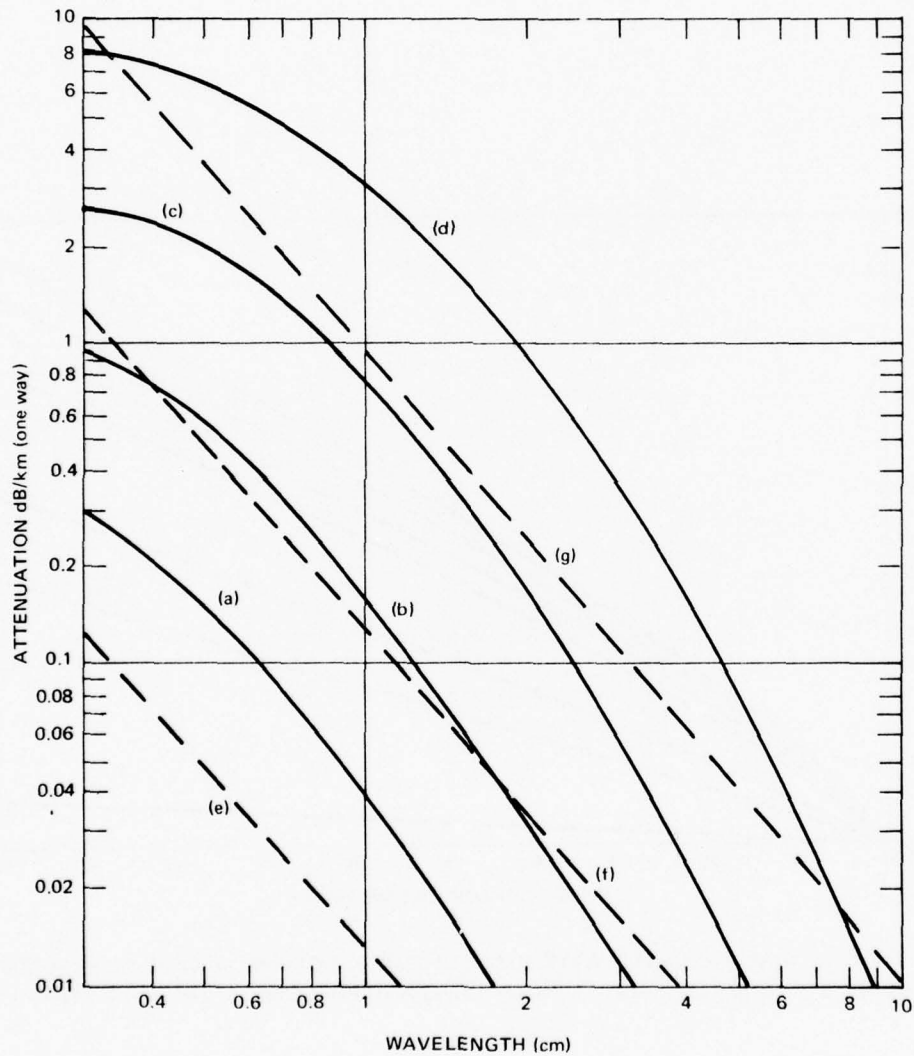


FIG. 5 THEORETICAL VALUES OF ATTENUATION BY RAIN AND FOG. SOLID CURVES SHOW ATTENUATION IN RAIN OF INTENSITY. (a) 0.25 mm/hr (DRIZZLE); (b) 1 mm/hr (LIGHT RAIN); (c) 4 mm/hr (MODERATE RAIN); (d) 16 mm/hr (HEAVY RAIN). DASHED CURVES SHOW ATTENUATION IN FOG OR CLOUD, (e) 0.032 g/m³ (VISIBILITY ABOUT 2000 ft); (f) 0.32 g/m³ (VISIBILITY ABOUT 400 ft); (g) 2.3 g/m³ (VISIBILITY ABOUT 100 ft). (FROM GOLDSTEIN, REF. 14)

THE JOHNS HOPKINS UNIVERSITY
APPLIED PHYSICS LABORATORY
SILVER SPRING MARYLAND

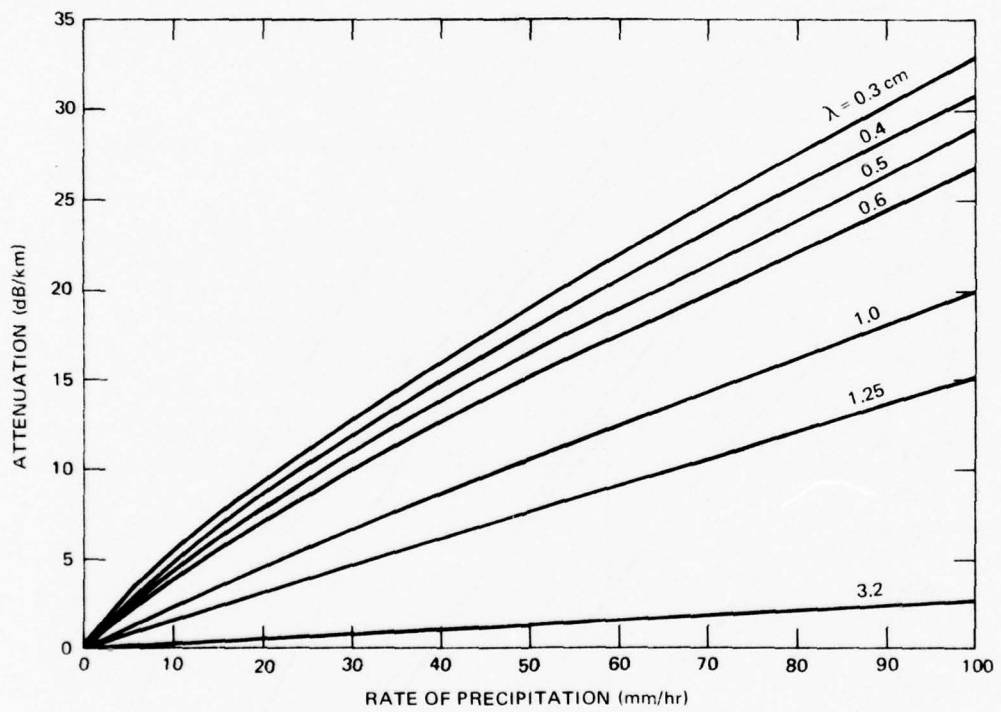


FIG. 6 THEORETICAL VALUES OF ATTENUATION AS A FUNCTION OF RATE OF PRECIPITATION,
USING RAINDROP DISTRIBUTIONS OF LAWS AND PARSONS.(FROM RYDE AND RYDE, REF. 14)

Observed attenuations have generally exceeded the level of theoretical predictions from the rain-rate and drop-size distribution (e.g., Fig. 6). Good agreement between estimated and measured attenuation was, however, reported by Usikov, German, and Vakser for a signal path only 50 m long with two rain gauges 30 m apart, provided that data were used only when the rain rates measured by the two gauges were identical (Refs. 19 and 20). Some of their data observed at millimeter wavelengths (but not 3.2 mm) are shown in Fig. 7. The observations cover a wide range of rain rates. The results are in good agreement with the theoretical values of Fig. 6. This agreement between theory and observations taken over a short path with closely-spaced rain gauges indicates that the Mie theoretical treatment is correct, and that observed discrepancies from it are due not to a lack in the theory but rather to inadequacy of meteorological data in most studies.

Measured attenuations during very heavy rains were used by Gray* to estimate the probability of occurrence of severe attenuation. He estimates from data on a 100-GHz signal that shower attenuation exceeded 26 dB/km during 0.01% of the time (i.e., during less than 1 h) in New Jersey in 1970. Some statistical information about occurrence of heavy rain rate in Washington, DC is presented in Ref. 21 and is reasonably consistent with D. A. Gray's conclusions. Very heavy rains are probably rarer in the Arctic than along the U.S. eastern seaboard; however, there is a scarcity of data.

Attenuation by Suspended Particles: Ice and Snow

Less is known about attenuation by solid particles than by liquid particles. Theoretical studies have been made (Refs. 14, 16, 22, and 23), but are more difficult for solids because the particles are usually not spherical.

*D. A. Gray (Bell Laboratories), private communication.

Ref. 20. O. Ya. Usikov, V. L. German, and I. Kh. Vakser, "Investigation of Absorption and Scattering of Millimeter Waves under Conditions of Precipitation," Ukr. Phys. J., Vol. 6, No. 5, trans. by Aztec School of Languages, 1961, pp. 618-641.

Ref. 21. G. E. Weibel and H. O. Dressel, "Propagation Studies in Millimeter-Wave Link Systems," Proc. IEEE, Vol. 55, No. 4, April 1967, pp. 497-513.

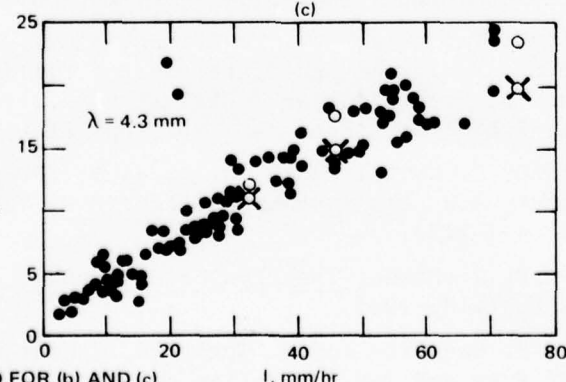
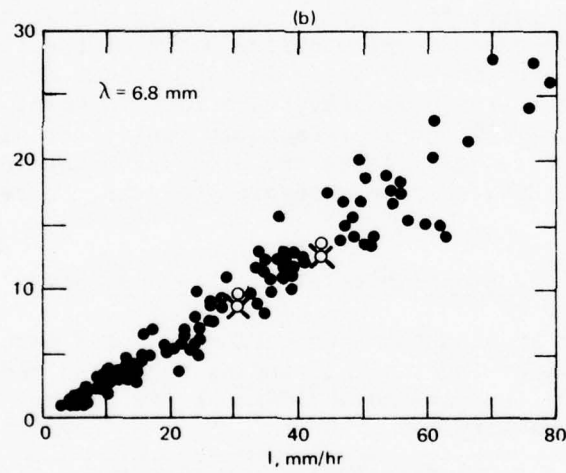
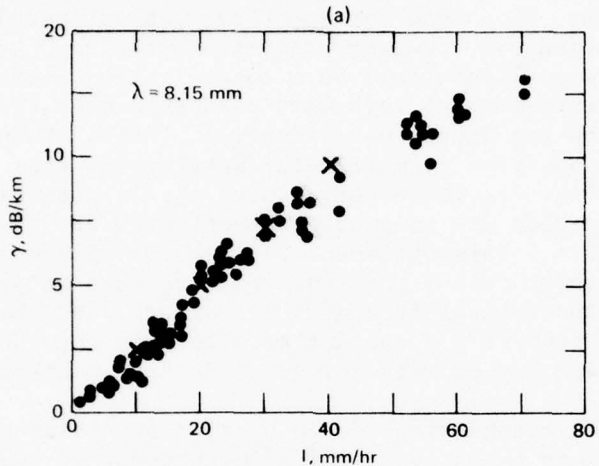
Ref. 22. B. J. Mason, The Physics of Clouds, Clarendon Press, Oxford, England, 1971.

Ref. 23. P. Hoekstra and D. Spanogle, "Radar Cross Section Measurements of Snow and Ice for Design of SEV Pilotage System," CRREL Report under ARPA Order 1615, U.S. Army Cold Regions Research Laboratory, June 1971.

THE JOHNS HOPKINS UNIVERSITY
APPLIED PHYSICS LABORATORY
SILVER SPRING MARYLAND

LEGEND FOR (a)

- OBSERVED ATTENUATION
- ✖ CALCULATED USING AVERAGE DROP SIZE DISTRIBUTION
OF TEN OBSERVED RAIN SAMPLES



LEGEND FOR (b) AND (c)

- OBSERVED ATTENUATION
- OBSERVED, WITH SIMULTANEOUS RAIN SAMPLE COLLECTION (DROP SIZE)
- ✖ CALCULATED, USING OBSERVED DROP SIZE DISTRIBUTION (SIMULTANEOUS)

FIG. 7 OBSERVED AND CALCULATED ATTENUATIONS (FROM USIKOV, GERMAN, AND VAKSER, REF. 20)

Water in clouds or fog can be supercooled; liquid droplets occur commonly down to temperatures of -20°C and may be found down to -35°C ; however, below -40°C the droplets freeze. Thus a fog at a temperature of -20°C or -30°C may consist of particles of either water or ice, or a mixture.

Snow crystals may occur as hexagonal plates, prisms, dendritic stars, and all variations and combinations of these; the type of crystal may be related to the temperature at which it is formed.

Hail occurs in various forms: snow pellets, rounded or conical; ice pellets, spherical, spheroidal, conical or irregular; larger hailstones (balls or pieces of ice), which may have any shape from spheroidal to discoidal or irregular, may have lobed or spiked surfaces, and may contain air bubbles or liquid water.

Absorption of energy by ice clouds (dry) is much less than absorption by water clouds of the same water content because the imaginary part of the complex index of refraction is much smaller for ice than for water. Attenuation by ice is temperature-dependent and is markedly less at -40°C than at 0°C .

The whole question of attenuation by suspended water particles that may be partly or wholly solid and may exist in a great variety of sizes and shapes is so complicated that any short, summarizing statement must be somewhat qualitative; however, it may be said that the absorption of energy by solid water is likely to be small. What is probably more important here is the backscatter, which may mask the return from the desired target.

Recent tests were made at the Cold Regions Research and Engineering Laboratory (CRREL) of the U.S. Army, to measure the radar returns from snow-covered surfaces and ice objects, at 10, 35, and 95 GHz (Refs. 23 and 24). Data on these returns were obtained only during good weather. When snow was falling, the volume clutter from the target range seriously degraded the possibility of target detection at both 10 and 35 GHz. This would also be important at higher frequencies, but no 95-GHz data on falling snow are reported. It was found possible to reduce the weather clutter by going from horizontal to linear cross-polarization of the signal, but this also decreased the return from desired objects. The study of weather clutter was not an objective of the

Ref. 24. "SEV Reasibility Study, RAT SCAT Radar Backscatter and Cross Section Measurements of Snow and Ice," report AFSWC-TR-71-19 prepared for RAT SCAT (Radar Target Scatter Division), Air Force Special Weapons Center (Holloman Air Force Base, NM) by General Dynamics, Convair Aerospace Division (Fort Worth, TX), May 1971.

test program and was not pursued further. This subject should be further investigated.

In summary, selection of radar frequencies for obstacle detection is limited to three basic choices by atmospheric effects: 10 GHz, 35 GHz, and 95 GHz. A frequency of 10 GHz is relatively insensitive to atmospheric conditions and represents the best choice from this viewpoint. Both 35 GHz and 95 GHz will suffer limitations in moderate to heavy rain with the attenuation at 95 GHz being about five times more than that at 35 GHz. Heavy fog will also result in a significant attenuation at 95 GHz. At laser wavelengths the best choice appears to be 10.6 μm , but a radar at this wavelength will still be limited to relatively clear weather conditions.

Principle Issues

Basically all the major technology required to develop a capable craft-mounted obstacle-detection and avoidance system for an Arctic SEV is available. However, the all-weather high-resolution capability required for a high-speed SEV with limited maneuverability may be difficult to achieve for some missions. Laser radar systems cannot achieve an all-weather capability. Radar systems at frequencies of 10 GHz and below can achieve the all-weather capability, but their resolution capability is seriously limited. Millimeter-wave radars provide a compromise capability, yielding better weather performance than lasers and higher resolution capability than the lower-frequency radars. Lacking a general solution to the sensor problem for a high-speed Arctic SEV, the baseline design concept was based on a multisensor approach.

The experimental obstacle-detection system developed in this program has done much to define millimeter-wave detection capabilities and has contributed to millimeter-wave radar-component development. However, the avoidance aspect of the multisensor baseline design concept requires additional development work. Optimum integration of the sensors and the detection and avoidance processing procedures is an important area for development. An Arctic demonstration vehicle and a capable system simulation are the basic tools required for a systematic attack on the composite design of an obstacle detection and avoidance system for various Arctic SEV applications.

OBSTACLE MEASUREMENT TECHNIQUES

Two measurement techniques were considered for the craft-mounted detection system: direct measurement and shadow measurement. The direct measurement is based on using a radar with an

angular resolving capability (i.e., antenna beamwidth) equal to the angle subtended by the minimum required height resolution at the maximum range. The actual antenna beamwidth can be somewhat larger if the signal returns are sufficiently strong to allow an effective beamwidth reduction through processing techniques. The shadow measurement is based on a procedure that determines obstacle height by detecting the length of the shadow cast by the obstacle.

Direct measurement at radar frequencies will require large-aperture antennas for the resolutions required by a high-speed SEV. At 10 GHz the aperture size can approach 100 m. At the maximum reasonable frequency of 95 GHz an aperture of about 10 m may be required. However, a laser radar operating at 10.6 μm can achieve the required angular resolution with an optical aperture of about 25 cm. The required aperture for direct measurement is straightforwardly calculated from the height resolution and the maximum range, where these values are determined from the vehicle characteristics.

Radar Shadowing Concept

The radar shadowing concept is illustrated in Fig. 8. The top view, looking down on the obstacle, shows the obstacle going completely across the radar beam. The elevation view shows the radar antenna at a height, h_a , with the obstacle of height, h_o , at a range of R_o . The obstacle essentially blocks a portion of the beam and prevents it from illuminating the ground immediately behind. Thus a "shadow" is created as indicated by the cross-hatched areas. The ground surface again becomes visible to the radar at a range, R_s , behind the obstacle. The corresponding radar return video would be as shown, with the obstacle return being somewhat larger than the surrounding ground return. The return in the shadowed region drops essentially to the receiver noise level, and at the end of the shadow, the level increases because of ground return. Assuming a known antenna height, h_a , and by measuring the two ranges, R_o and R_s , one can determine the obstacle height, h_o , using similar triangles, as

$$h_o = \frac{R_s h_a}{R_s + R_o} .$$

A problem arises when the obstacle width is less than the transmitted beam; and only partial blockage occurs. Returns from the illuminated areas adjacent to the shadowed region tend to obscure the shadow itself. For this reason, the horizontal beamwidth of the radar sensor should be made as narrow as possible. For low grazing angles, where R_o is much greater than h_a , the shadow

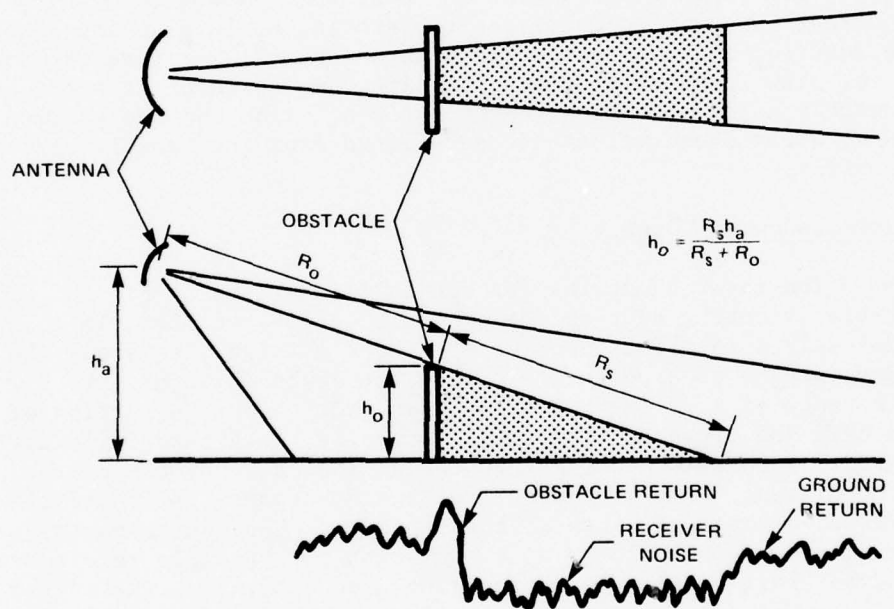


FIG. 8 RADAR SHADOWING CONCEPT

THE JOHNS HOPKINS UNIVERSITY
APPLIED PHYSICS LABORATORY
LAUREL, MARYLAND

length R_s is very sensitive to small changes in obstacle height, h_o . Consequently we can integrate and average the returns in the shadow region over relatively long ranges, and thus enhance the ability to detect the end of the shadow.

Resolution Requirements

Radar shadowing requires a sensor beamwidth that is very narrow in the horizontal direction and somewhat broader in the vertical plane. The requirement on the horizontal beamwidth is controlled by the desired operating speed and maneuverability of the vehicle, and is also affected by pilot reaction time. The vertical beamwidth requirement is related to the antenna height above ground and the total required detection range, minimum to maximum.

The basic problem on the horizontal resolution is that of being able to determine the height of an obstacle at sufficient range to execute an avoidance maneuver. If the vehicle is traveling directly toward the obstacle, the maneuver must be such that there is a reasonable clearance between the side of the vehicle and the edge of the obstacle. The worst situation exists when there is a continuous wall across the path of the vehicle. For this case, the vehicle must either come to a full stop or execute a complete 90° turn. However, this condition is somewhat easier to detect because of the extreme width of the obstacle.

A more detailed examination of the problem requires some knowledge of the maneuvering capability of the vehicle. In the following analysis, it is assumed that it would be undesirable for the vehicle to slow down or appreciably change speed. Excessive maneuvers consume fuel and can affect the overall operational performance of the vehicle in terms of range and payload. It is also assumed that the avoidance maneuver consists of a constant-speed turn, with the acceleration being applied always perpendicular to the line of travel. This path results in a circular arc where the radius, r , is defined by

$$r = \frac{v_o^2}{a} . \quad (4)$$

The angular velocity of the radius vector is also related to the vehicle velocity, v_o , and acceleration, a , by

$$\omega = \frac{a}{v_o} (\text{rad/s}) . \quad (5)$$

THE JOHNS HOPKINS UNIVERSITY
APPLIED PHYSICS LABORATORY
LAUREL, MARYLAND

As the vehicle traces the arc, it must move a sufficient distance, d_e , transverse to the original line of travel to clear the obstacle. At the time the maneuver is started, the distance to the obstacle is denoted by d_n . The geometry of this situation is illustrated in Fig. 9. Using the Eqs. (4) and (5) and this geometry, d_n and d_e can be expressed in terms of V_o and a as:

$$d_n = \frac{V_o^2}{a} \sin \frac{at}{V_o} \quad (6)$$

and

$$d_e = \frac{V_o^2}{a} \left(1 - \cos \frac{at}{V_o}\right), \quad (7)$$

where t is time, measured from the start of the maneuver.

At a minimum, d_e must equal one-half the sum of the vehicle width (W_v) and obstacle width (W_o).

$$d_e(\min) = \frac{W_v + W_o}{2}. \quad (8)$$

Substituting Eq. (7) into Eq. (8) and solving for t establishes the time required for a safe maneuver to be executed.

$$t = \frac{V_o}{a} \cos^{-1} \left[1 - \frac{a(W_o + W_v)}{2V_o^2} \right]. \quad (9)$$

Inserting this value of t into Eq. (6) and solving for d_n determines the absolute minimum range at which the obstacle height must be detected.

A more reasonable detection range must account for some pilot reaction time, T_p . This time would include such things as the pilot's interpretation of the displayed situation, his decision as to which direction to turn, and any preparation of the vehicle required to start the maneuver. While this parameter is somewhat difficult to evaluate analytically, its effect can be included and at least categorized.

THE JOHNS HOPKINS UNIVERSITY
APPLIED PHYSICS LABORATORY
LAUREL, MARYLAND

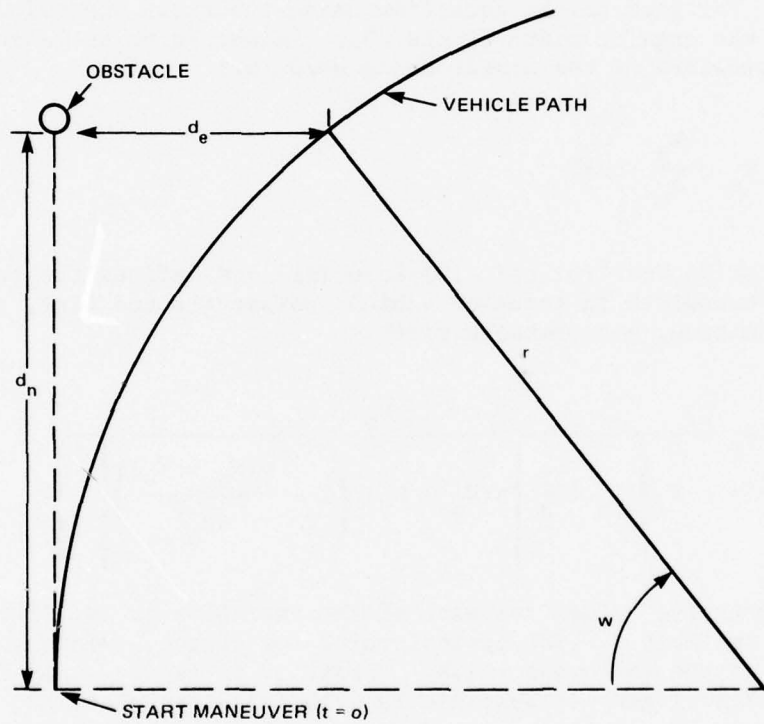


FIG. 9 BASIC MANEUVER GEOMETRY

THE JOHNS HOPKINS UNIVERSITY
APPLIED PHYSICS LABORATORY
LAUREL, MARYLAND

The total obstacle detection range (R_o) is then defined by:

$$R_o = T_p \cdot V_o + \frac{V_o^2}{a} \sin \frac{at}{V_o} . \quad (10)$$

Substituting Eq. (9) into Eq. (10) relates R_o to only the vehicle parameters, pilot reaction time, and the width of the obstacle.

There is an additional relationship between R_o and obstacle width. For good height detection using the radar shadowing technique, the angular width of the obstacle should be no less than the beam-width of the sensor being used, or:

$$\theta_s = \frac{W_o}{R_o} \text{ (rad)} . \quad (11)$$

Substituting Eqs. (9) and (10) into (11) now defines the required sensor beamwidth in terms of vehicle parameters and size, pilot reaction time, and obstacle width:

$$\theta_s = \frac{W_o}{V_o \left\{ T_p + \frac{1}{a} \left[a(W_o + W_v) \left(1 - \frac{a(W_o + W_v)}{4V_o^2} \right) \right]^{\frac{1}{2}} \right\}} . \quad (12)$$

Representative values for each of the variables in Eq. (12) are listed in Table 2. The typical value for obstacle width was selected on the following basis. First, it is assumed that the basic shape of a single ice obstacle is such that its height and width are approximately the same. Second, a clearance height of 10 to 15 ft is considered typical for the size of vehicles considered. Finally, a small single hazardous obstacle represents the worst case from a detection and height determining standpoint, as will be seen from subsequent analysis of Eq. (12).

The sensor beamwidth, θ_s , is seen to vary almost directly with obstacle width and inversely with vehicle velocity. Pilot reaction time, acceleration, and vehicle width have somewhat of a second-order effect. The variation of θ_s with respect to W_v is examined first.

Figure 10 is a plot of θ_s versus W_v for various values of V_o , a , and W_o . T_p is held constant at its typical value of 10 s.

THE JOHNS HOPKINS UNIVERSITY
APPLIED PHYSICS LABORATORY
LAUREL, MARYLAND

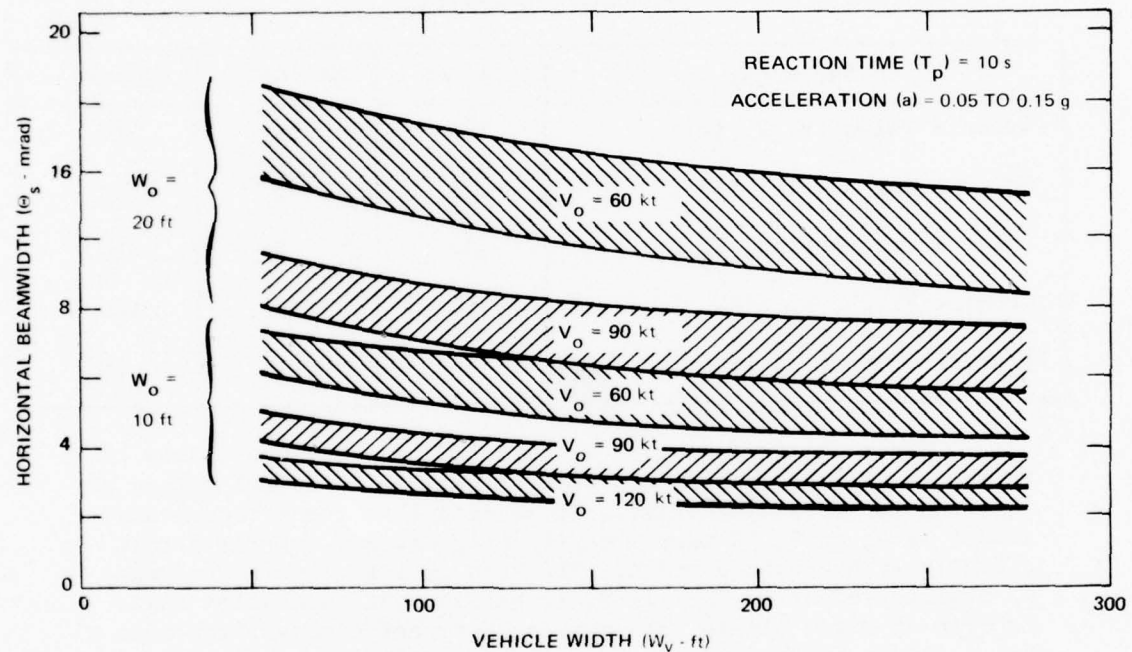


FIG. 10 HORIZONTAL BEAMWIDTH VS. VEHICLE WIDTH, VELOCITY, AND OBSTACLE WIDTH FOR RADAR SHADOWING

The shaded areas cover the full range of acceleration from 0.05 to 0.15 g's for each of the indicated conditions. As predicted, the vehicle width has little effect. Generally speaking, as W_v is varied over its entire range, the required resolution changes by a factor of less than 1.5 when the other variables are held constant. It is also seen that changes in acceleration have little effect under these conditions.

Table 2
Parameters Affecting Sensor Horizontal Beamwidth
for Radar Shadowing

Parameter	Maximum	Minimum	Typical
Vehicle Velocity, V_o (kt)	120	60	90
Maneuvering Acceleration, a (g's)	0.15	0.05	0.10
Pilot Reaction Time, T_p (s)	25	0	10
Vehicle Width, W_v (ft)	350	50	100
Obstacle Width, W_o (ft)		5	10

Figure 11 is a plot of θ_s versus W_o for various values of V_o and a . T_p and W_v are held constant at their typical values of 10 s and 100 ft respectively. It is seen that the second-order affect of W_o on θ_s is nearly negligible, since θ_s varies almost directly with obstacle width. The same is also true for changes in vehicle velocity, V_o . If V_o is halved, the resolution angle doubles in size. Again, changes in maneuvering capability have a small effect on the resolution. Given a typical obstacle width of 10 ft, the resolution varies from 3 to 6 mrad, depending on the desired velocity.

The typical pilot reaction time, T_p , was selected on an arbitrary basis only. As stated previously, this parameter is not easily defined and can be influenced considerably by the design of the vehicle maneuvering and control systems. Solving Eq. (12) for T_p allows T_p to be evaluated in terms of the remaining parameters. Figures 12, 13, and 14 are plots of required reaction time versus obstacle width for velocities of 90, 60, and 120 kt, respectively, for various sensor beamwidths. The vehicle width is again fixed at 100 ft. The curves can be interpreted from at least two points of view. Referring to Fig. 12, for an obstacle width of 10 ft and a sensor beamwidth of 4 mrad, allowable pilot reaction time varies

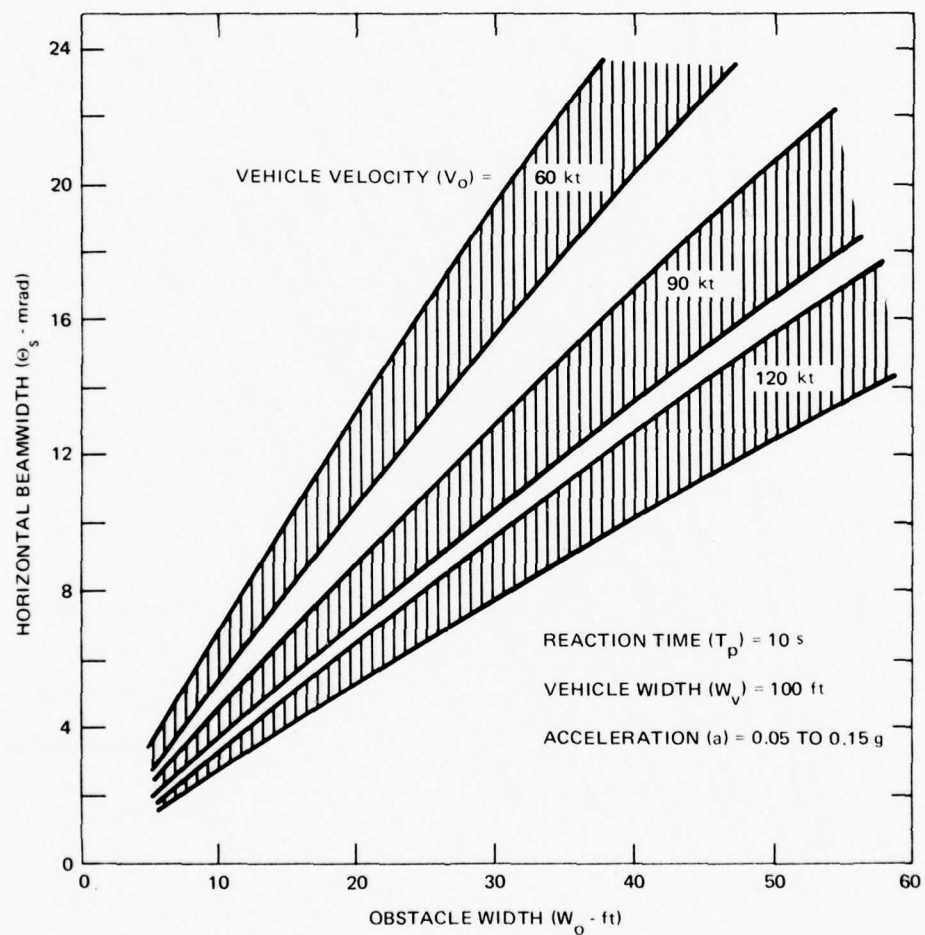


FIG. 11 HORIZONTAL BEAMWIDTH VS. OBSTACLE WIDTH AND VEHICLE VELOCITY FOR RADAR SHADOWING

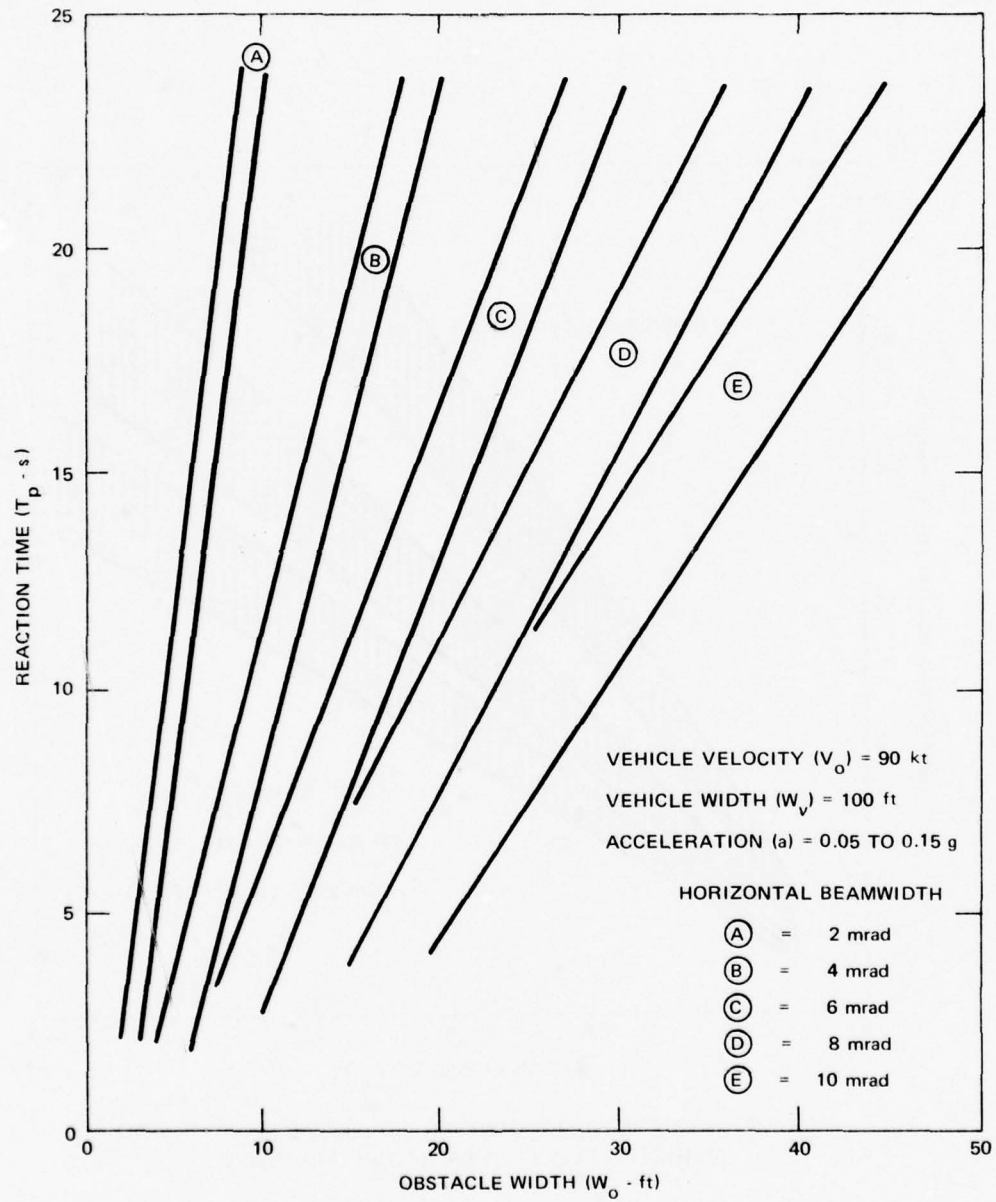


FIG. 12 AVOIDANCE REACTION TIME VS. OBSTACLE WIDTH AND HORIZONTAL BEAMWIDTH FOR SHADOWING RADAR SYSTEM

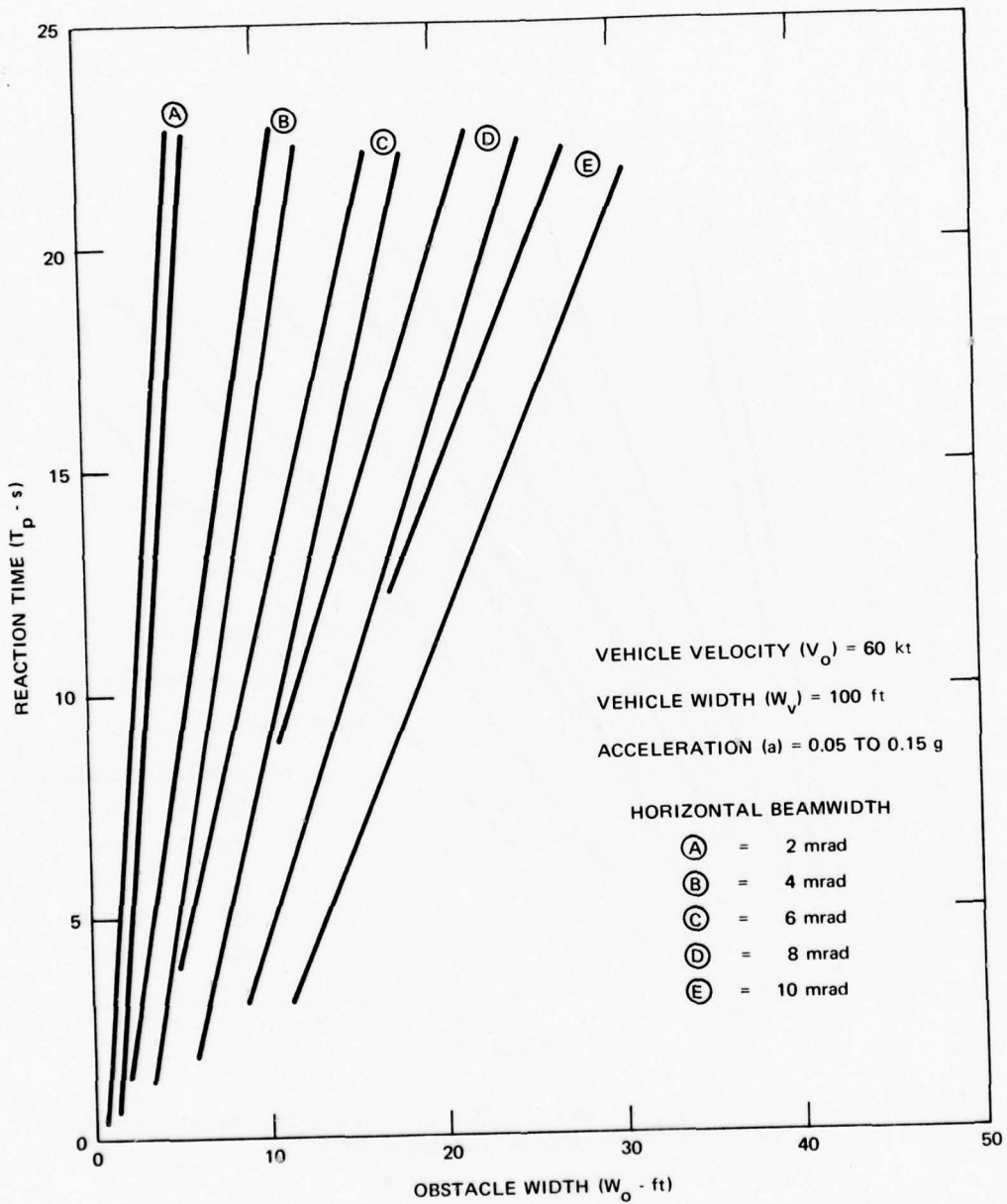


FIG. 13 AVOIDANCE REACTION TIME VS. OBSTACLE WIDTH AND HORIZONTAL BEAMWIDTH FOR SHADOWING RADAR SYSTEM

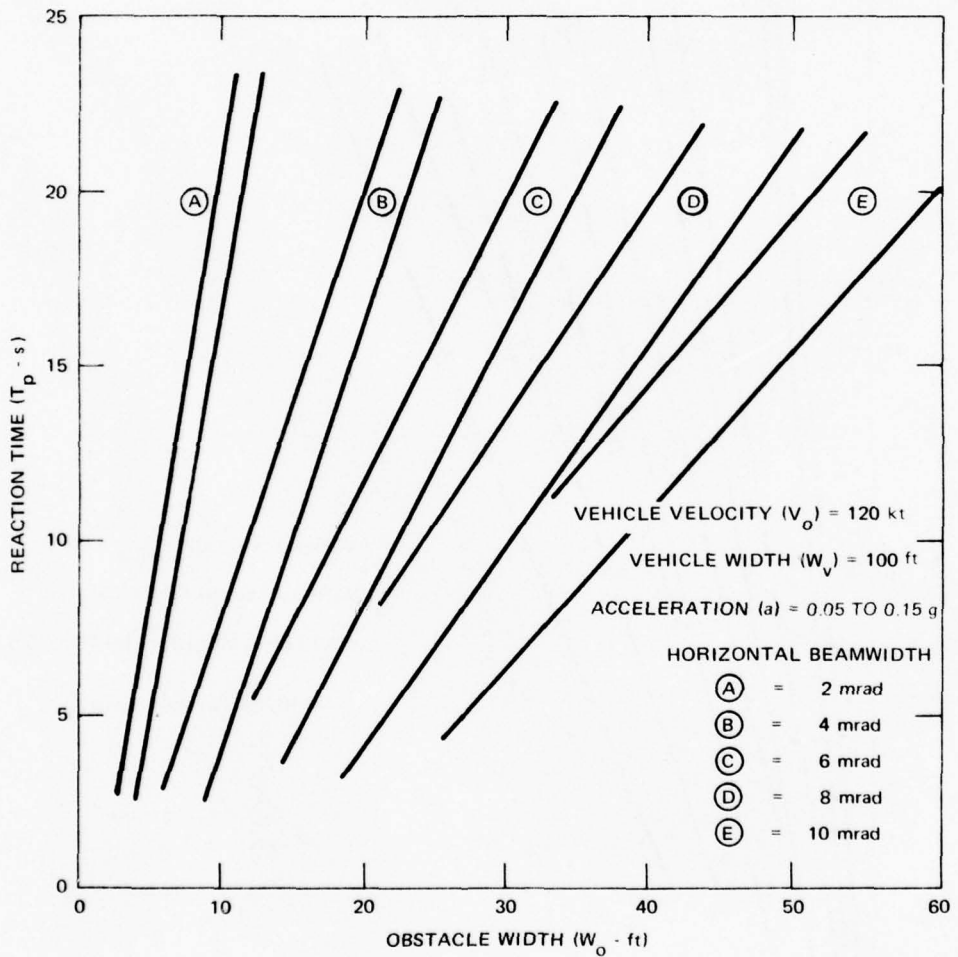


FIG. 14 AVOIDANCE REACTION TIME VS. OBSTACLE WIDTH AND HORIZONTAL BEAMWIDTH FOR SHADOWING RADAR SYSTEM

from 8 to 12 s depending on the acceleration. A 6-mrad sensor under the same conditions allows only 3 to 6 s of reaction time.

The second approach is to select some minimum allowable T_p and determine that θ_s satisfies it for a given set of conditions. A horizontal line is drawn through the selected T_p , along with a vertical line through the desired minimum obstacle width, W_o . The sensor curve that lies to the left and above the point of intersection of these two lines will satisfy the requirements. This is also illustrated in Fig. 12. For a T_p of 5 s and a W_o of 10 ft, a 4-mrad sensor is required. If the minimum width is increased to 20 ft, a 10-mrad sensor can be used. The typical values of T_p and W_o (10 s and 10 ft, respectively) result in a point that falls in the middle of the 4-mrad sensor range.

The vertical beamwidth is established by the two angles, α and β , defined by the angle between the maximum range line-of-sight and the horizontal and the minimum range line-of-sight and the horizontal (deflection angles from the antenna, Fig. 8). The larger angle, β , is a function of the antenna height, h_a , and the desired minimum range for obstacle detection, R_{\min} , is

$$\beta = \tan^{-1} \left(\frac{h_a}{R_{\min}} \right) . \quad (13)$$

The smaller angle, α , is related to the antenna height and the obstacle range at which a given height obstacle must be detected. Typically α will be small enough that it can be neglected. For this condition the vertical beamwidth is established simply by the minimum range requirement, Eq. (13)

Figure 15 is a plot of required sensor vertical beamwidths as a function of antenna height for some typical values of R_{\min} . It should be noted that these curves represent minimum values in that no allowance has been made for a varying pitch angle on the vehicle itself. Since the antenna is hard mounted to the vehicle, additional vertical coverage in the antenna pattern should be provided.

In summary, Eqs. (12) and (13) relate the required horizontal and vertical beamwidths to basic vehicle design parameters. Typical values for horizontal beamwidth vary from 1 to 10 mrad and typical values for the vertical beamwidth vary from 1 to 8° .

Sensor Selection

As noted in the previous discussion of atmospheric effects, radar obstacle detection is restricted to specific atmospheric

THE JOHNS HOPKINS UNIVERSITY
APPLIED PHYSICS LABORATORY
LAUREL, MARYLAND

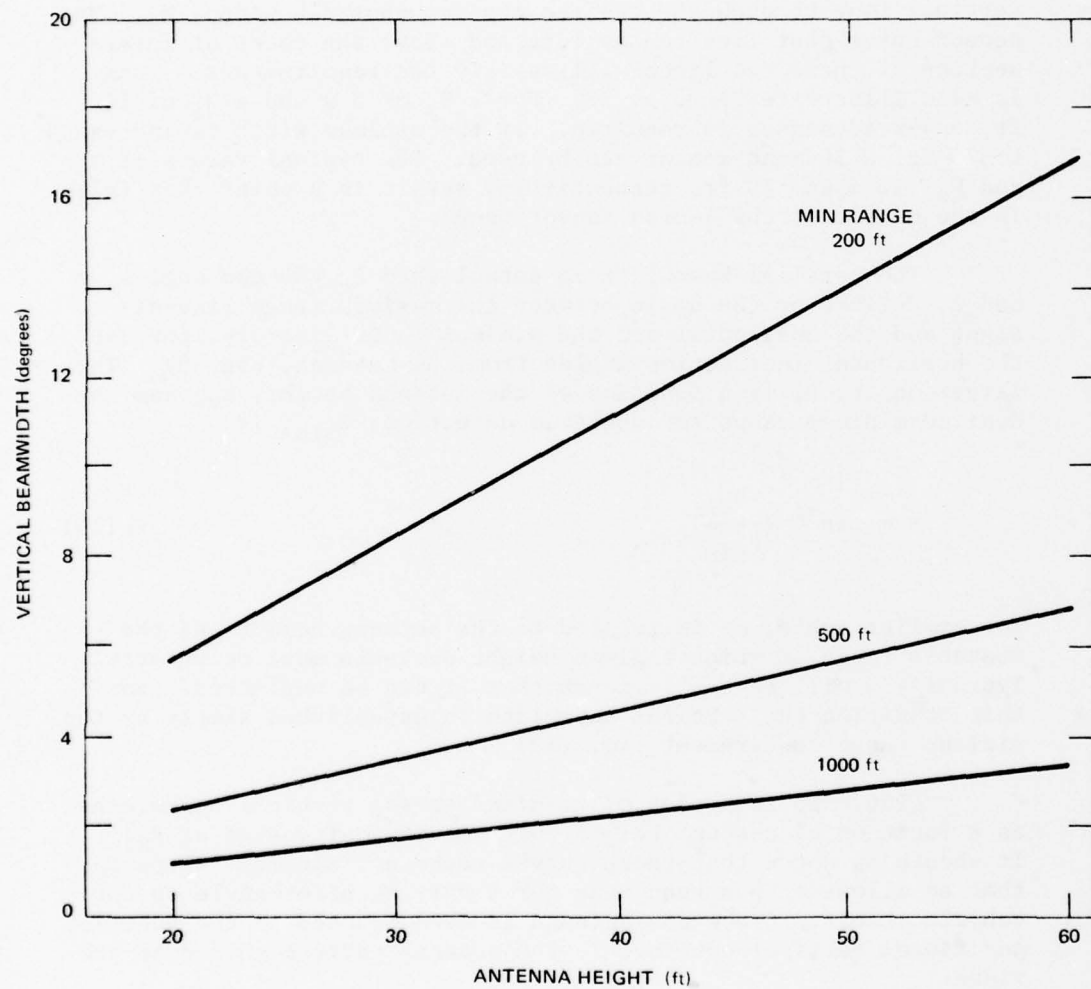


FIG. 15 VERTICAL BEAMWIDTH VS. ANTENNA HEIGHT AND
MINIMUM RANGE FOR RADAR SHADOWING

THE JOHNS HOPKINS UNIVERSITY
APPLIED PHYSICS LABORATORY
LAUREL, MARYLAND

transmission windows at frequencies above 10 GHz. An additional constraint is imposed by the availability of devices and practical size limitations. Device technology at 10 GHz is well advanced and there is no apparent lack of device capability at this frequency. However, application of a direct measurement technique at this frequency would require an aperture size that would be impractical for general high-speed SEV applications. Use of the shadow technique at 10 GHz is more practical, but still requires a relatively large aperture in one direction.

For direct measurement the vertical beamwidth requirement for a high-speed SEV is approximately 1/3 mrad. The horizontal beamwidth can be increased somewhat to the 1- to 2-mrad region. At 10 GHz these angular resolutions require an aperture of approximately 20 by 90 m (20 m in the horizontal direction, 90 m vertically). In the shadow approach the horizontal beamwidth is retained in the 1- to 2-mrad range, but the vertical beamwidth expands to several degrees. Therefore, for the shadow system the large dimension of a 10-GHz antenna would be approximately 20 m in the horizontal direction. Figure 16 shows the horizontal aperture requirements for a 10-GHz radar used in the shadow mode as a function of velocity and minimum obstacle detection width for the three design cases shown in Figs. 12 through 14.

The frequency choices of 35 GHz and 95 GHz are also available for the obstacle detection system. Although device technology is more advanced at 35 GHz than 95 GHz, both appear to be sufficiently advanced to support development of a practical obstacle-detection system. Atmospheric transmission at 35 GHz is generally better than at 95 GHz, but for the typical Arctic environment this factor does not appear to have much statistical significance. The benefit of smaller aperture size favors the use of 95 GHz.

Direct measurement techniques are more nearly practical at 95 GHz, but a vertical aperture size of approximately 10 m will still present a significant design challenge for a high-speed SEV. Aperture requirements at 95 GHz for the shadow measurement technique are more readily realized. Figure 16 shows the 95 GHz horizontal aperture requirements for the same cases shown for 10 GHz.

When laser radar techniques are considered, the direct measurement approach is not limited by aperture size. The required resolutions are readily achieved at optical wavelengths. All the possible atmospheric windows available for a laser radar will be restricted by some weather conditions; there is no "all-weather" option. The best wavelength choice considering atmospheric limitations and device availability is at 10.6 μ m.

THE JOHNS HOPKINS UNIVERSITY
APPLIED PHYSICS LABORATORY
LAUREL MARYLAND

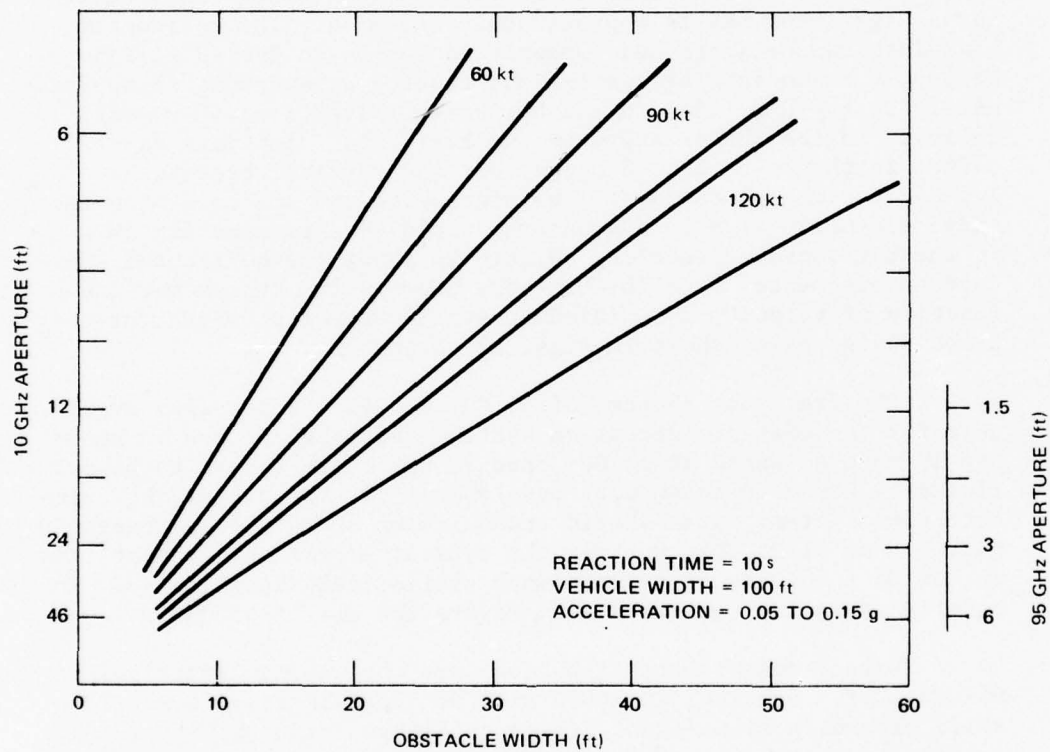


FIG. 16 HORIZONTAL APERTURE REQUIREMENTS FOR RADAR SHADOWING

Baseline Design Concept

None of the obstacle detection capabilities considered in this study were capable of meeting all the requirements for a high-speed SEV. Therefore the basic design concept considered a mix of detection capabilities allowing the broadest range of operating capability.

For clear-weather operation, a 10.6- μm laser radar can be designed to meet the most demanding detection requirements, using direct measurement techniques. However, the high-resolution system will require high-speed processing techniques to cover very large regions. Therefore this system will be restricted to operate only in a relatively small region around the flight-path vector. The laser system output will be a forward-looking three-dimensional image. Each segment of terrain will be defined in azimuth, elevation, and range. Angular position data will be relative to the vehicle's inertial platform. A full contour of the forward terrain sector can be determined, but it will be restricted by look-geometry. For example, an impassable crevasse behind a passable ridge will not be detectable until the crevasse becomes visible to the laser looking over the ridge.

A carbon dioxide laser operating at 10.6 μm would be used for the transmitter. A receiver optic with an aperture of approximately 10 in., with a mercury-cadmium-telluride array would be used for detection. The detector array requires cooling to 77°K.

A 95-GHz radar will also provide detection in the forward sector using shadow processing techniques. This system will provide backup to the laser system in clear weather, and will become the prime sensor when weather limits use of the laser system. When both the 95-GHz and laser systems are operating, the 95-GHz sensor can be used to provide a wider sector scan at a reduced resolution. This dual-mode approach will provide a wider range of observation for selection of avoidance maneuvers when an obstacle is detected. The 95-GHz radar can also be provided with a direct measurement processing technique as a means for determining terrain slope and to provide the full resolution requirement at reduced ranges.

The 10-GHz radar will provide the general search capability and will provide a reduced-capability all-weather forward-looking terrain-sensing function. In this forward sector, shadowing techniques will be applied to determine differential terrain heights. When only this system is operating, the terrain slope is assumed to be that which is experienced by the SEV in its current position as measured relative to the vehicle's inertial platform. Aside from the terrain data processing function, this radar is a relatively standard design.

Figure 17 illustrates the basic characteristics of the obstacle detection system for a high-speed SEV. The navigation concept is also shown and will be discussed later in this report. The scanning apertures will be positioned as high as possible on the craft to allow the most favorable practical viewing geometry.

In the preliminary design concept, a multicolor obstacle display device was included. Three colors are used to clearly separate regions of definite hazards, potential hazards, and no hazards. The display concept is illustrated in Fig. 18.

The display is normally centered on the vehicle velocity or true heading vector, but would include a manual override capability for viewing any sector around the craft. While the main purpose of the display is to show the relative positions of obstacles, additional information concerning the present speed and maneuvering capability of the vehicle is made available to the pilot. These data consist of a projected vehicle stopping position along the heading vector, and two long dashed lines indicating the maximum maneuvering limit of the vehicle. Range markers would also be available to superimpose on the display. Navigational aids include a numerical display of the present true heading and an arrow indicating the desired heading, which is based on the present geographic position of the vehicle and its ultimate destination. Numerical displays of the present ground speed and wind velocity would be provided with a pictorial situation indication of the wind direction and drift angle of the vehicle. The display format is strongly influenced by the maneuvering controls available to the pilot, and options may be added as these controls become better defined.

The display is driven by a central computer that processes data from the three sensing systems. Processing modes vary, depending upon the status of the sensing systems and the weather conditions. Status lights will be provided to indicate the present condition of the sensing systems and the processing mode.

THE JOHNS HOPKINS UNIVERSITY
APPLIED PHYSICS LABORATORY
LAUREL, MARYLAND

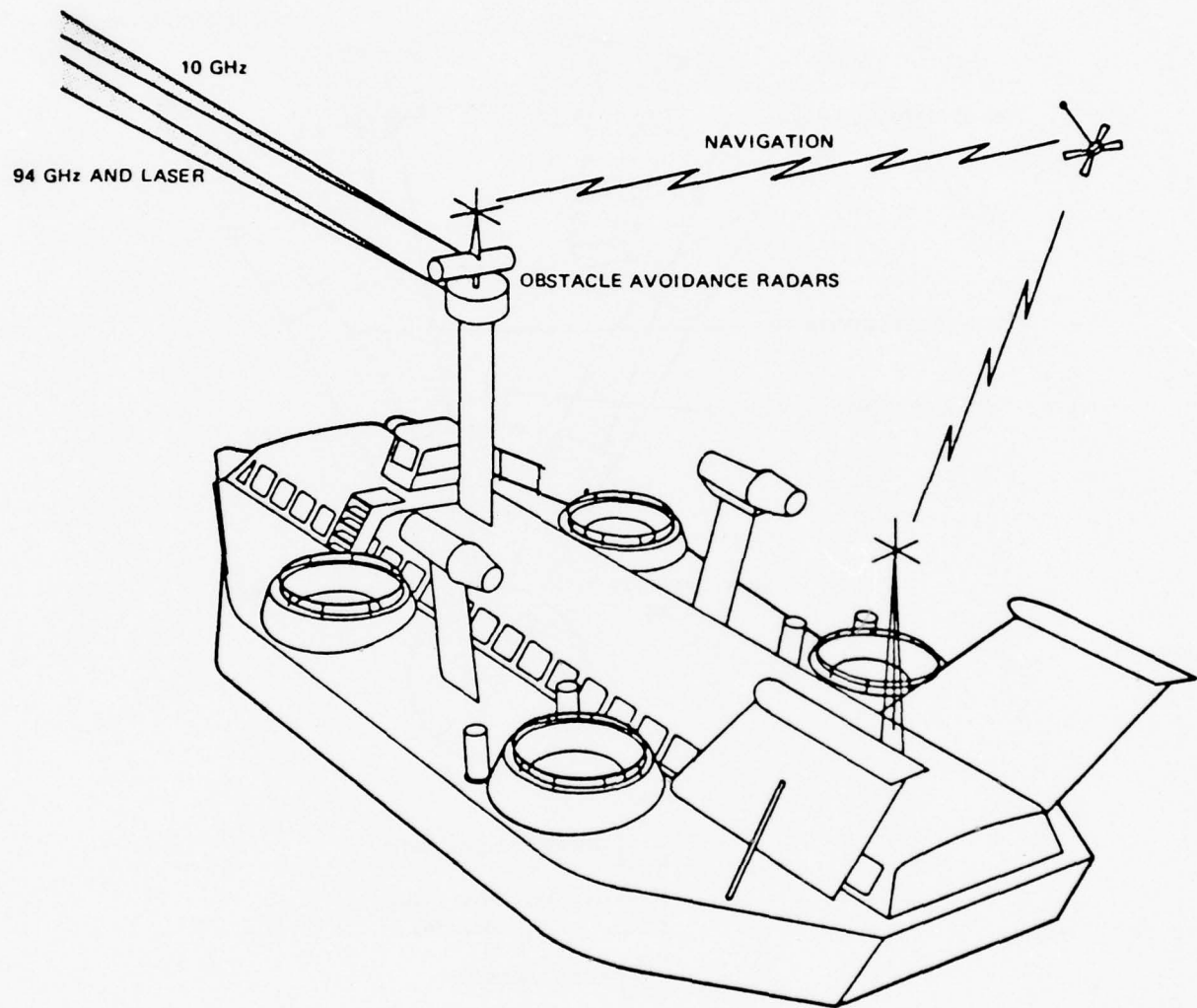


FIG. 17 PRELIMINARY OBSTACLE AVOIDANCE/NAVIGATION SYSTEMS CONCEPT

THE JOHNS HOPKINS UNIVERSITY
APPLIED PHYSICS LABORATORY
LAUREL, MARYLAND

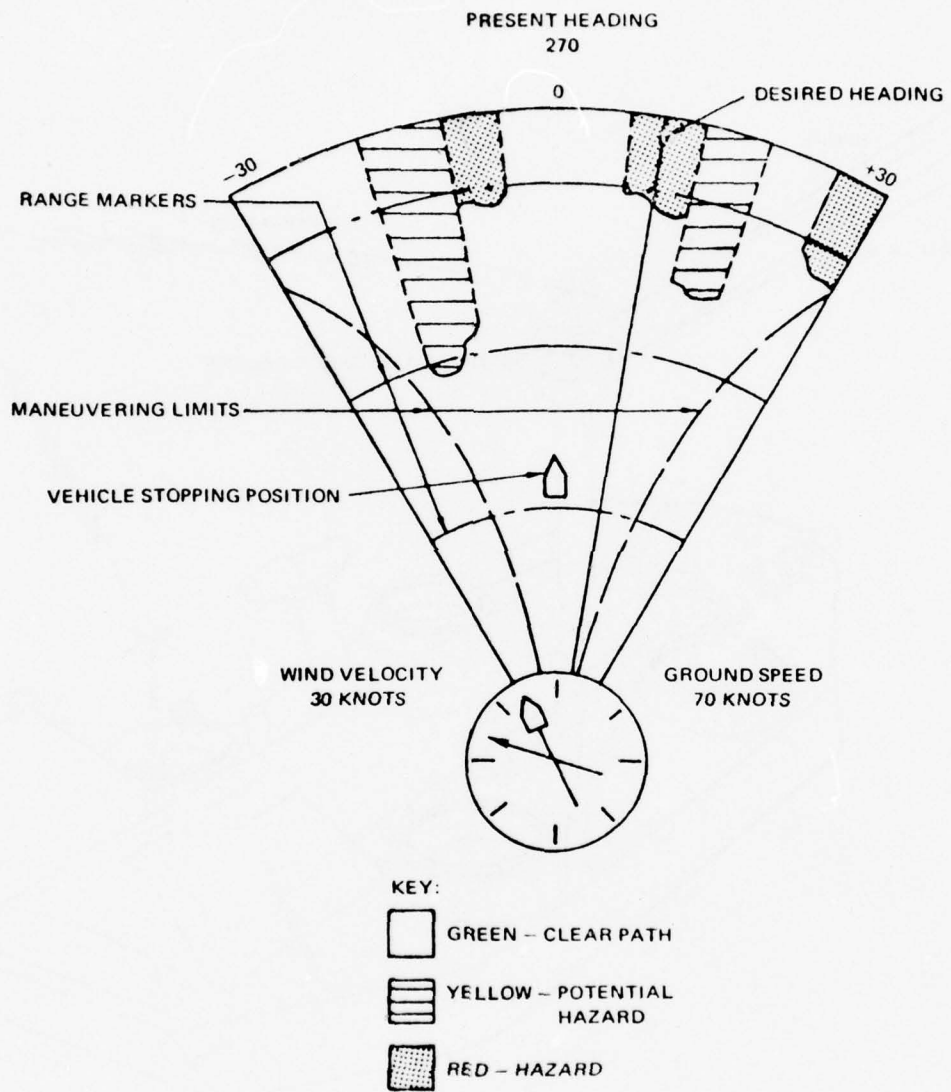


FIG. 18 MULTICOLOR OBSTACLE DISPLAY CONCEPT

3. PRELIMINARY EXPERIMENTS

Early in the Arctic SEV program, it was found that no data existed on the radar reflection characteristics of ice and snow at low grazing angles, particularly at 95 GHz. Data were also lacking on the propagation characteristics of 95 GHz under fog conditions similar to those that often prevail in the Arctic region. As a result, several test programs were indicated to develop an Arctic terrain and weather-radar data base. Radar cross-section measurements of ice and snow at low grazing angles and at frequencies of 10, 35, and 95 GHz were made by the Cold Regions Research and Engineering Laboratory (CRREL) of the U.S. Army in conjunction with the Radar Target Scatter (Rat Scat) division of the Air Force Special Weapons Center. Tests were also conducted by the University of Texas to measure the dielectric constant of low temperature fogs at a frequency of 95 GHz. In order to determine the characteristics of radar returns from typical terrain on the Arctic ice pack, APL conducted field tests at Pt. Barrow, AK. Both 95- and 10-GHz radar returns from the ice pack were recorded for further analysis. The results of these tests indicated that the 95-GHz radar had considerable promise for meeting the requirements of an Arctic SEV obstacle detection system.

CRREL TESTS

Since the installation requirements of the on-board SEV radar indicated a system that must scan the surface at low grazing angles (1° and lower), and since an Arctic operation was planned, experiments were conducted to obtain data on the following environmental parameters:

1. Terrain clutter from snow and ice surfaces at low grazing angles at various frequencies, and
2. The radar cross section of ice and snow objects.

Radar backscatter and cross-section measurements of snow surfaces and ice objects were performed on a frozen, snow-covered lake at Lyme, New Hampshire from 10 January to 15 March by Rat Scat (Ref. 25) at the request of CRREL. Calibrated backscatter (clutter)

Ref. 25. "SEV Feasibility Study - RAT SCAT Radar Backscatter and Cross Section Measurements of Snow and Ice," AFSWC-TR-71-19, Radar Target Scatter Division (RAT SCAT)/Air Force Special Weapons Center, May 1971.

THE JOHNS HOPKINS UNIVERSITY
APPLIED PHYSICS LABORATORY
LAUREL, MARYLAND

measurements of smooth snow with man-made perturbations at grazing angles of 0.38° , 0.65° , and 1.0° and frequencies of 10 and 35 GHz were made. Backscatter characteristics for several ice obstacles on the snow cover as well as the calibrated radar cross section of pure-ice and sea-ice blocks and a pure-ice sphere were determined at horizontal, vertical, and linear polarizations.

CRREL concluded (Ref. 26) that the radar terrain clutter measurements at the grazing angles for both rough and smooth snow vary from -50 to -70 dB and are not strongly dependent upon frequency. Based upon tests made using a 10-GHz (X-band), a 35-GHz (K-band or Ka-band), and a 95-GHz (V-band) radar, it was found that the X-band radar and the Ka-band radar tended to give returns as good as those of the V-band radar when they were used to detect obstacles on ice. The CRREL report (Ref. 26) discusses the Rat Scat data plots and reviews the literature on the dielectric properties of snow, fresh-water ice, and sea ice.

FOG BACKSCATTER MEASUREMENTS AT 95 GHz

A research contract was let to the Electrical Engineering Research Laboratory/The University of Texas (UT) at Austin, to measure the complex refraction index, the phase constant, and the radio wave signal loss of millimeter-wave radiation associated with ice fogs formed over the temperature range from -30° to -48°C . The measurements were made using an environmental chamber that had a volume of 70 ft^3 and in which temperatures could be controlled down to -50°C . A high-Q Fabry-Perot cavity was designed and constructed to make the electromagnetic measurements. The resonant center frequency of the cavity was about 97 GHz and the Q of the cavity was about 10^5 . The following briefly summarizes the UT work (Refs. 27, 28, and 29).

Ref. 26. P. Hockstra and D. Spanogle, "Radar Cross Section Measurements of Snow and Ice for Design of SEV Pilotage Systems," CRREL Report under ARPA order 1615, U.S. Army Cold Regions Research and Engineering Laboratory, June 1971.

Ref. 27. J. Perry, "Summary of Measurements on Millimeter Wave Propagation through Ice Fog," U.S. Army Cold Regions Research and Engineering Laboratory, June 1973.

Ref. 28. J. W. Perry and A. W. Straiton, "Dielectric Constant of Ice at 35.3 and 94.5 GHz," J. Appl. Phys., Vol. 43, No. 2, February 1972, pp. 731-733.

Ref. 29. J. W. Perry, Ph.D. Thesis, University of Texas, 1971.

Experimental Procedure

In addition to propagation measurements at 97 GHz, the following physical measurements were made on the ice fog:

1. Measurements of the particle size distribution and densities of the fog were made using a four-stage cascade impactor to collect fog samples. Two glass slides coated with magnesium oxide are employed so that the ice-fog particles form craters on impact with the film of magnesium oxide. The size of the impact craters is related to the size of the particles. This technique has the advantage that photographing and counting can be done in a comfortable environment, while the particles are collected at the ambient temperature of the ice fog. It suffers, like all other impactors, from errors in an individual's technique, and has additional error caused by relatively unknown collection efficiency.
2. Measurements were also made of the attenuation of a helium-neon laser ($63.28 \mu\text{m}$) through the ice fog, simultaneously with the millimeter wave propagation studies.

Measurement Results

A total of 69 different electromagnetic measurements of the complex permittivity of a fog were made covering the temperature range from -30° to -48°C . Measured particle size distribution and the laser extinctions measured for some ice fogs in the chamber are shown in Table 3. As a comparison, typical concentrations reported (Ref. 30) on ice fog in Fairbanks, AK have ranged from 200 particles per cm^3 , to almost 1000 particles per cm^3 . The artificial fogs are, therefore, representative of the lowest concentrations found in man-impacted areas. Also Ohtake (Ref. 30) found the mean diameter of the particles making up the ice fog to change the temperature and to be about $7 \mu\text{m}$ at -40°C and about $20 \mu\text{m}$ at -36°C . The results of Table 3 are in general agreement with the relative size distribution found in ice fog by Ohtake and the shift to larger particle diameter if the temperature is raised.

The laser extinction is a parameter that can be measured with ease and accuracy and the data on millimeter-wave propagation have, therefore, been normalized to 1 dB/m laser extinction. The reason for this type of normalization was the finding that an ice fog could be characterized by its laser extinction. This characterization probably works, because an ice fog, unlike a water fog,

Ref. 30. T. Ohtake, "Unusual Crystal in Ice Fog," J. Atmos. Sci., Vol. 27, No. 3, 1970, pp. 509-511.

Table 3
 Measured Particle Sizes, Number per cm³, and Laser (63.28 μm)
 Extinction in Artificial Ice Fog

Experiment Number	Temperature (°C)	Particle Size (μm)				Number per cm ³	Laser Extinction (dB/m)
		5-12	12-19	19-26	>26		
1	-47	121	13	4	1	139	1.33
2	-47	155	4	1	0	160	1.16
3	-47	164	8	1	0	173	1.20
10	-43	167	12	0	0	179	1.42
11	-43	162	6	0	0	168	1.50
8	-39	151	13	0	0	164	1.46
9	-39	174	2	0	0	176	1.42
4	-35	86	17	1	1	105	1.37
5	-35	117	48	1	1	167	1.14
6	-35	85	10	5	1	101	1.04
7	-35	113	38	2	1	154	1.24
14	-30	253	32	32	0	317	1.50

has a relatively narrow particle size distribution, which depends mainly on the fog temperature.

The measured data on the millimeter-wave propagation, the laser extinction, and the normalized data are listed in Table 4. The number, N, is defined as

$$N = (n - 1) \times 10^6 ,$$

where n is the refractive index of the fog.

The results of all the measurements are plotted in Figs. 19 and 20. In Table 5 the mean values of milliwave propagation are given.

The results in Table 5 and Fig. 20 show that the critical parameter in determining the millimeter-wave attenuation by ice fog is the ambient temperature rather than the particle size distribution. Since the temperature from -30°C to -35°C is rather critical to ice-fog formation, it is reasonable to suppose that

THE JOHNS HOPKINS UNIVERSITY
 APPLIED PHYSICS LABORATORY
 LAUREL, MARYLAND

Table 4

Results of Measurements of Millimeter Wave Propagation
 and Laser Extinction

(The last two columns represent the data normalized for 1 dB/m
 laser extinction.)

Temperature (°C)	N	Laser Extinction (dB/m)	X (cm ⁻¹)	X/(dB/m)	N-Units (dB/m)
-38	3.44	1.59	6.95×10^{-7}	4.37×10^{-7}	2.16
-39.5	3.42	1.31	15.2×10^{-7}	11.60×10^{-7}	2.61
-38	2.50	1.22	18.1×10^{-7}	14.80×10^{-7}	2.05
-38	4.43	1.64	5.22×10^{-7}	3.18×10^{-7}	2.70
-38	2.76	1.77	8.55×10^{-7}	4.84×10^{-7}	1.56
-38.5	3.73	1.40	12.8×10^{-7}	9.15×10^{-7}	2.66
-38.5	3.58	1.51	12.9×10^{-7}	8.55×10^{-7}	2.37
-33	6.05	2.25	3.64×10^{-6}	1.62×10^{-6}	2.69
-35	4.12	2.07	5.44×10^{-6}	2.62×10^{-6}	1.99
-34	6.65	2.88	5.32×10^{-6}	1.85×10^{-6}	2.31
-35	3.98	2.31	6.36×10^{-6}	2.75×10^{-6}	1.72
-35	6.27	2.88	6.75×10^{-6}	2.34×10^{-6}	2.18
-34	3.74	1.86	3.06×10^{-6}	1.65×10^{-6}	2.01
-35	6.54	2.55	4.55×10^{-6}	1.78×10^{-6}	2.56
-34.5	6.29	2.92	3.03×10^{-6}	1.04×10^{-6}	2.15
-34	4.57	2.38	4.07×10^{-6}	1.71×10^{-6}	1.92
-34	5.50	3.33	6.35×10^{-6}	1.91×10^{-6}	1.65
-35	2.34	1.10	3.42×10^{-6}	3.11×10^{-6}	2.12
-34	2.67	1.92	3.25×10^{-6}	1.69×10^{-6}	1.39
-34	3.05	2.56	6.90×10^{-6}	2.70×10^{-6}	1.19
-35	2.86	2.16	4.15×10^{-6}	1.92×10^{-6}	1.32
-34	2.13	1.06	4.16×10^{-6}	3.92×10^{-6}	2.01
-34.5	6.57	2.50	7.0×10^{-6}	2.80×10^{-6}	2.63
-35	2.79	1.90	3.98×10^{-6}	2.10×10^{-6}	1.47
-27.5	2.82	1.57	3.92×10^{-6}	2.5×10^{-6}	1.8
-29	5.76	2.07	7.95×10^{-6}	3.84×10^{-6}	2.78
-30	2.72	2.31	10.1×10^{-6}	4.37×10^{-6}	1.18
-30	1.89	2.44	12.6×10^{-6}	5.16×10^{-6}	0.775
-29.5	1.60	1.94	9.6×10^{-6}	4.95×10^{-6}	0.825
-29	1.46	1.94	10.4×10^{-6}	5.35×10^{-6}	0.754
-29	1.74	1.96	5.08×10^{-6}	2.59×10^{-6}	0.890
-29	2.39	1.96	5.95×10^{-6}	3.04×10^{-6}	1.22
-29	1.76	1.96	9.25×10^{-6}	4.72×10^{-6}	0.9
-30	2.92	1.66	4.58×10^{-6}	2.76×10^{-6}	1.76
-30	2.20	1.48	4.22×10^{-6}	2.85×10^{-6}	1.49

THE JOHNS HOPKINS UNIVERSITY
 APPLIED PHYSICS LABORATORY
 LAUREL, MARYLAND

Table 4 (cont'd)

Temperature (°C)	N	Laser Extinction (dB/m)	X (cm ⁻¹)	X/(dB/m)	N-Units (dB/m)
-46	2.36	1.46	5.50×10^{-7}	3.76×10^{-7}	1.62
-46	2.46	1.35	10.40×10^{-7}	7.70×10^{-7}	1.82
-45.5	2.37	1.46	6.25×10^{-7}	4.28×10^{-7}	1.63
-46	2.44	1.42	9.55×10^{-7}	6.71×10^{-7}	1.72
-46	2.41	1.46	8.70×10^{-7}	5.95×10^{-7}	1.65
-46.5	2.71	1.90	4.80×10^{-7}	2.53×10^{-7}	1.43
-47	1.28	1.28	5.50×10^{-7}	4.30×10^{-7}	1.90
-46.5	2.68	1.80	6.40×10^{-7}	3.56×10^{-7}	1.49
-46.5	2.32	1.17	7.25×10^{-7}	6.20×10^{-7}	1.98
-42.5	2.59	1.57	9.57×10^{-7}	6.10×10^{-7}	1.65
-43	2.70	1.55	10.40×10^{-7}	6.70×10^{-7}	1.74
-42.5	3.52	1.55	10.30×10^{-7}	6.65×10^{-7}	2.27
-43	3.08	1.19	9.00×10^{-7}	7.55×10^{-7}	2.59
-43	2.10	1.13	9.15×10^{-7}	8.10×10^{-7}	1.86
-42.5	2.89	1.40	4.9×10^{-7}	3.52×10^{-7}	2.06
-42.5	3.35	1.61	7.25×10^{-7}	4.50×10^{-7}	2.08
-43	3.33	1.57	13.60×10^{-7}	8.65×10^{-7}	2.12
-44	3.08	1.44	5.95×10^{-7}	4.14×10^{-7}	2.14
-42	2.96	1.51	14.50×10^{-7}	9.60×10^{-7}	1.96
-42	6.05	2.53	10.90×10^{-7}	4.31×10^{-7}	2.39
-42	3.42	1.48	7.84×10^{-7}	5.30×10^{-7}	2.31
-43	2.70	1.72	8.00×10^{-7}	4.65×10^{-7}	1.57
-43.5	5.55	3.00	18.90×10^{-7}	6.30×10^{-7}	1.85
-43	2.42	1.25	7.25×10^{-7}	5.80×10^{-7}	1.94
-39	7.94	2.76	25.4×10^{-7}	9.2×10^{-7}	2.87
-39	7.96	2.92	9.0×10^{-7}	3.08×10^{-7}	2.73
-39	8.51	3.03	13.1×10^{-7}	4.32×10^{-7}	2.81
-38	4.05	2.13	6.95×10^{-7}	3.26×10^{-7}	1.90
-38	4.37	2.02	8.70×10^{-7}	4.31×10^{-7}	2.16
-38	3.43	1.61	26.8×10^{-7}	16.60×10^{-7}	2.13
-37	3.39	1.35	14.50×10^{-7}	10.72×10^{-7}	2.51
-38	2.79	1.28	22.8×10^{-7}	17.80×10^{-7}	2.18
-38	3.13	1.24	4.50×10^{-7}	3.6×10^{-7}	2.52
-37	2.84	1.28	8.85×10^{-7}	6.91×10^{-7}	2.22

THE JOHNS HOPKINS UNIVERSITY
APPLIED PHYSICS LABORATORY
LAUREL, MARYLAND

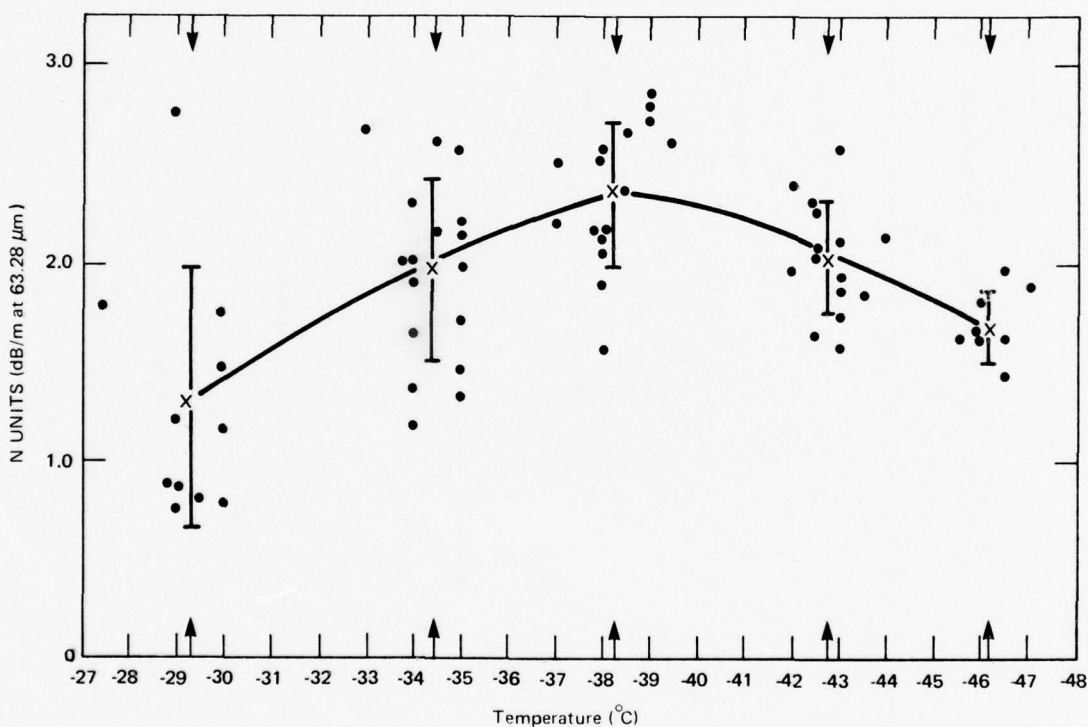


FIG. 19 NORMALIZED ICE FOG N-UNIT MEASUREMENTS AT 97 GHz

THE JOHNS HOPKINS UNIVERSITY
APPLIED PHYSICS LABORATORY
LAUREL, MARYLAND

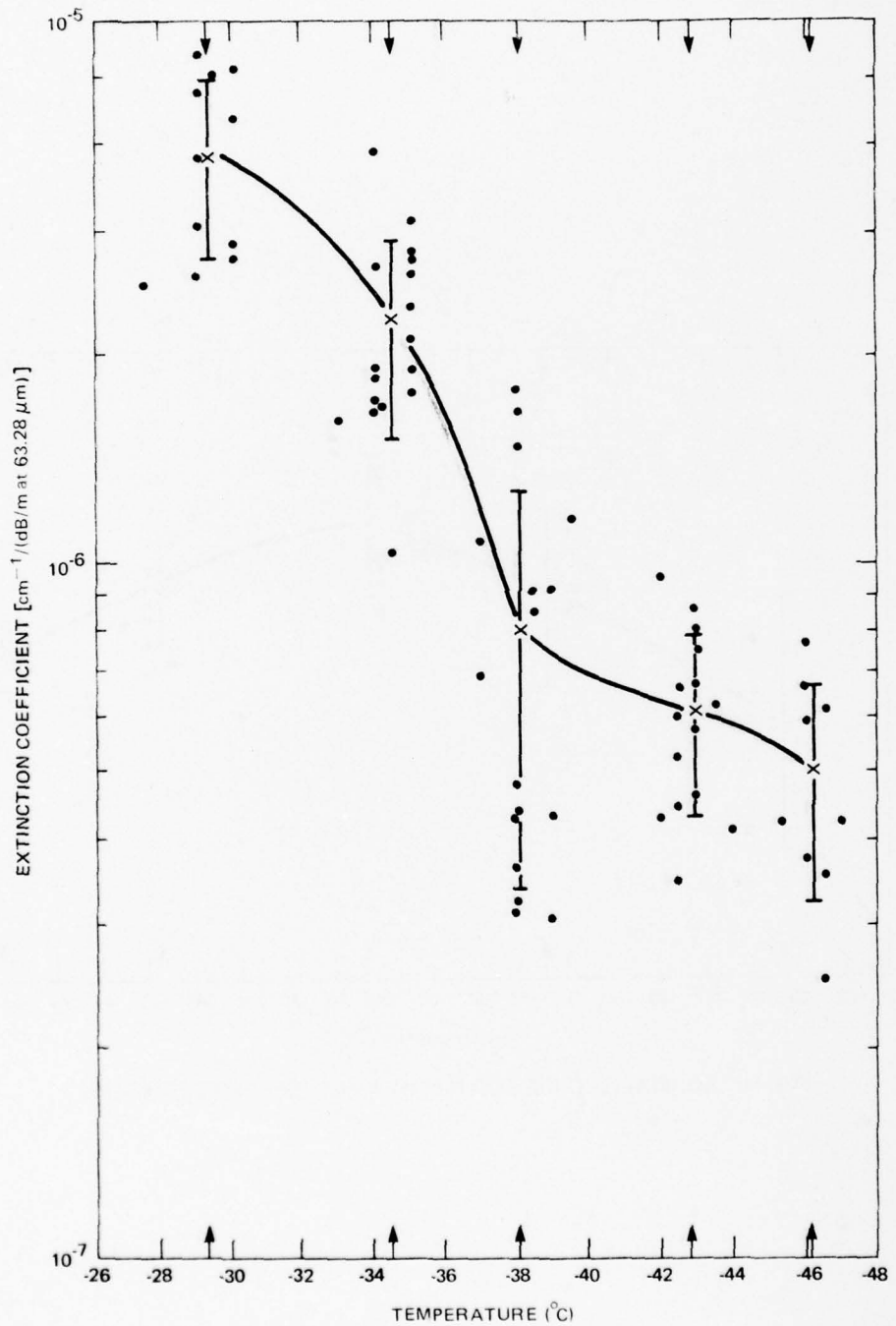


FIG. 20 NORMALIZED ICE FOG N-UNIT EXTINCTION COEFFICIENT MEASUREMENTS AT 97 GHz

THE JOHNS HOPKINS UNIVERSITY
 APPLIED PHYSICS LABORATORY
 LAUREL, MARYLAND

Table 5

Mean Values of the Millimeter Wave Propagation
 Measurements in Artificial Ice Fog Normalized for 1 dB/m
 Extinction of Laser ($63.28 \mu\text{m}$) Light

Temperature (°C)	N-Units	Mean Extinction Coefficient (cm^{-1})	Differential Phase Shift, (rad/km)	Attenuation (dB/km)
-29.3	1.31 ± 0.64	$3.83 \pm 1.1 \times 10^{-6}$	2.7	1.7 ± 0.7
-34.4	1.96 ± 0.46	$2.21 \pm 0.7 \times 10^{-6}$	3.9	1.0 ± 0.3
-38.3	2.36 ± 0.36	$8.08 \pm 4.68 \times 10^{-6}$	4.8	0.4 ± 0.2
-42.8	2.04 ± 0.28	$6.12 \pm 1.79 \times 10^{-6}$	4.2	0.3 ± 0.1
-46.2	1.69 ± 0.18	$5.0 \pm 1.71 \times 10^{-6}$	3.4	0.2 ± 0.1

some percentage of the ice fog is liquid. Liquid water could be present either as films on the ice particles, or as a small percentage of liquid droplets. The laser extinction is relatively independent of temperature because of the similarities in the complex refractive index of ice and water.

APL ARCTIC TESTS, PT. BARROW, 1971

Tests were conducted by APL in the Arctic during two time periods in 1971: 17 to 22 May and 22 June to 4 July (Ref. 31). During the May (1971) tests, 10-GHz radar data were collected; in addition, 94-GHz radar data were collected during the second test period. Since bad weather during the May tests precluded the use of aerial photography to gather the necessary ground truth data, the following discussion concerns mainly the second series of tests. The specific test objectives were as follows:

1. Collect data for radar shadowing analysis at 10 and 94 GHz,
2. Collect data for direct terrain mapping at 94 GHz and at $1.06 \mu\text{m}$,

THE JOHNS HOPKINS UNIVERSITY
APPLIED PHYSICS LABORATORY
LAUREL, MARYLAND

3. Collect data from the 10-GHz, 94-GHz, and 1.06- μm sensors for later use in a hybrid simulation,
4. Collect ground truth data for correlation with the sensor data, and
5. Collect data on propagation limits to the extent possible over the test span.

The initial objectives of the follow-on data processing and evaluation efforts were as follows:

1. Convert the data to digital format and archive it for continuing use,
2. Extract fundamental statistical measures,
3. Evaluate the major data characteristics and limitations, and
4. Establish the basic data processing facility.

Test Procedure

All operations were conducted from a fixed site on shore (Fig. 21), with analog video data being recorded as the three sensors were used to scan the ice field from the fixed site. Terrain scans for the laser and 94-GHz radar were accomplished manually. A precision rotary table provided the azimuth scan, and a tilt mechanism on the table provided the elevation scan. To collect 10-GHz data, a scan controller was added to the SK-5 radar to allow slow-scan operation and scan reversal. All data were recorded on a high-speed 15-MHz recorder and two backup recorders. The basic test configuration is shown in Fig. 22.

For the 94-GHz radar, a scan consisted of an elevation sweep through 3° at a fixed azimuth, then a half-beamwidth azimuth step followed by a return elevation sweep. Timing was arranged to provide two elevation sweeps during the 50-s recording interval per track on the Newell recorder. Approximately seven hours of running time were required to complete the 94-GHz radar sector scan. Table 6 summarizes the data collected during the June tests.

Laser scanning was restricted by the low (1 pps) pulse rate. For each track of recorded data, the mount was positioned at 0° elevation and at a fixed azimuth, then the elevation was decreased in half-beamwidth steps between pulses on every other pulse. This procedure provided approximately 25 elevation settings per tape run

THE JOHNS HOPKINS UNIVERSITY
APPLIED PHYSICS LABORATORY
LAUREL, MARYLAND

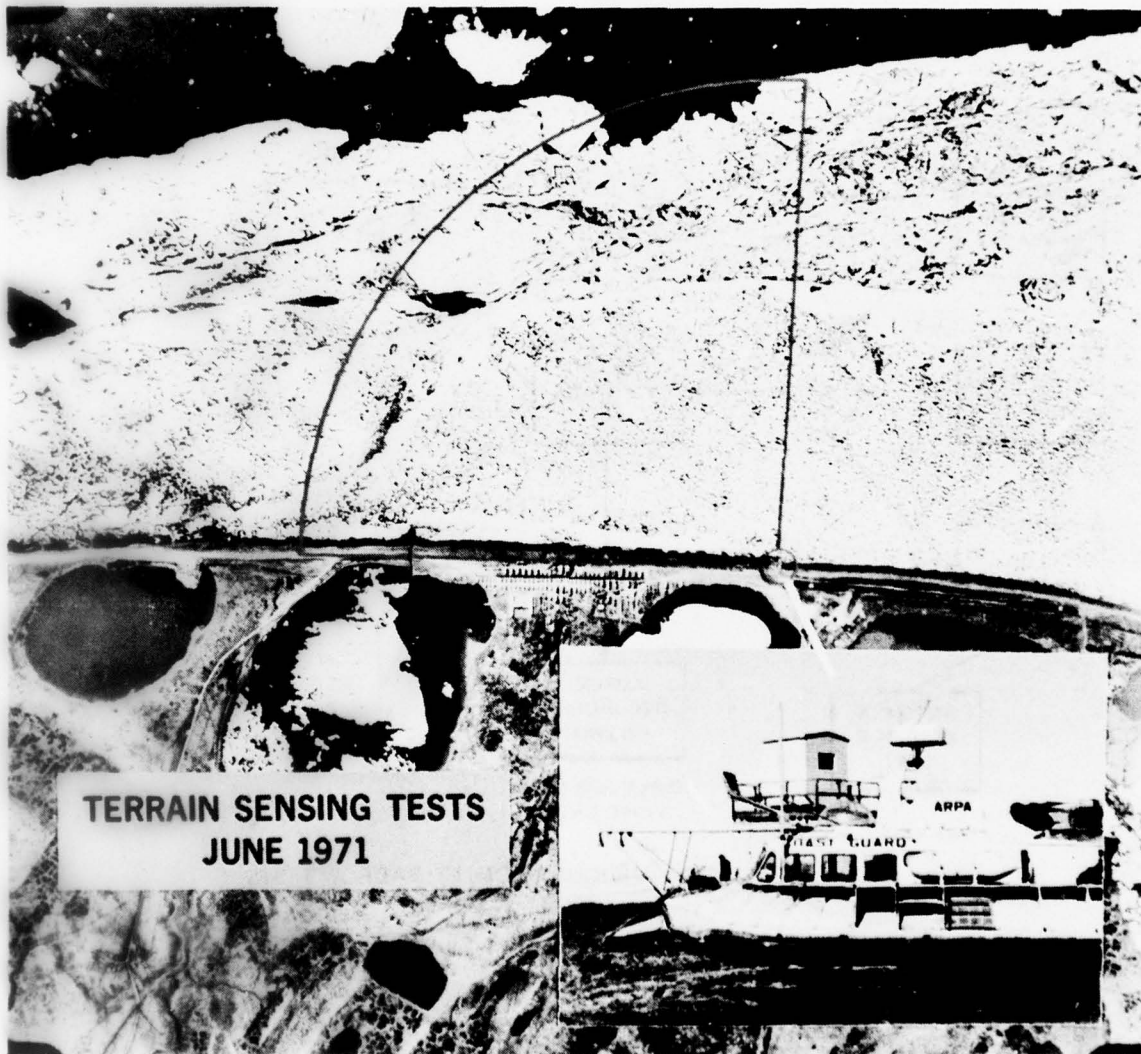


FIG. 21 JUNE 1971 TEST SITE

THE JOHNS HOPKINS UNIVERSITY
APPLIED PHYSICS LABORATORY
LAUREL, MARYLAND

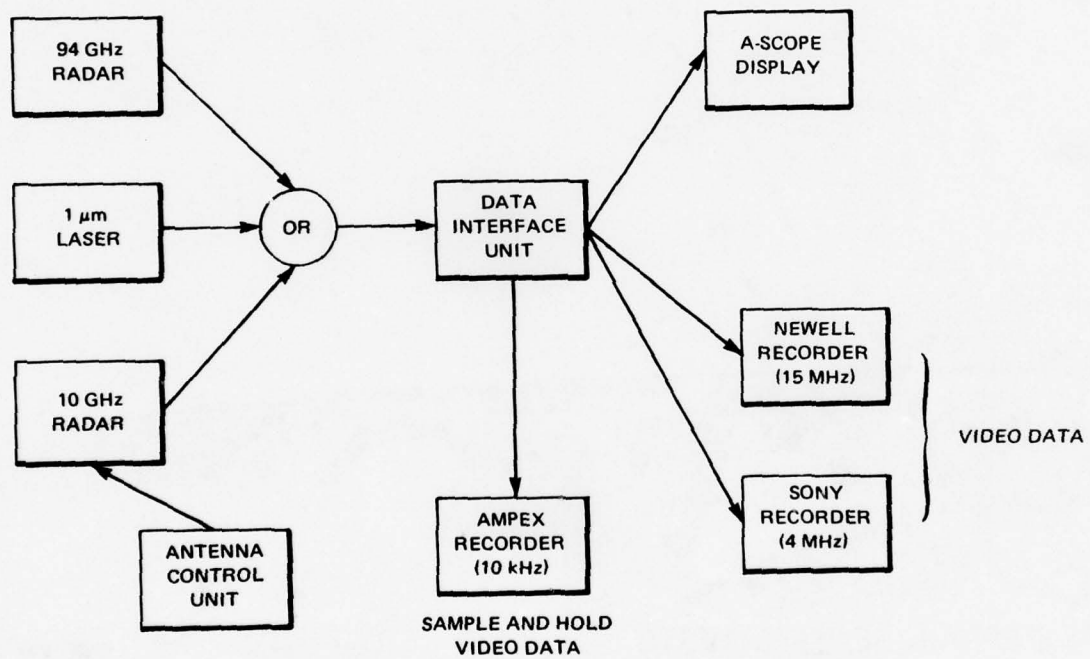


FIG. 22 BASIC TEST CONFIGURATION, PT. BARROW TESTS

THE JOHNS HOPKINS UNIVERSITY
APPLIED PHYSICS LABORATORY
LAUREL, MARYLAND

Table 6
Data Collected During June 1971 Tests

Magnetic Tape Data	
10-GHz radar	Fifty-three 120° azimuth sweeps at various gain and STC settings
94-GHz radar	Three hundred forty-six 3° elevation sweeps covering 84° of the test area (manual scan)
1.06-μm laser	Twenty-eight 1° elevation sweeps covering 1° of the test area (manual scan)
Television	Three 90° azimuth sweeps at 0°, -1°, and -2° elevation angles
Still Photographs	
Aerial photography	One hundred thirty-two frames, three full mapping runs of test sector on different days
Obstacles	Eight frames of specific obstacles as seen through the laser telescope with corresponding 94-GHz radar and laser data
	Sixteen frames of the test sector as viewed from the instrumentation site at different times
Scope pictures	Sixty-six frames of A-scope displays of 10-GHz and 94-GHz radar and laser returns
Documentation	Seventy-six frames of general documentation
Time Sequence Photography	
	Four hundred eighty frames of segment of test sector, every 15 minutes for five days (fixed camera mount)
Motion Pictures	
Obstacles	Panorama of test sector taken from the 94-GHz radar/laser/TV mount
Documentation	Six hundred feet of general documentation

or approximately 1° of elevation scan. Azimuth was then changed by a one-half beamwidth step and the procedure was repeated. A 1° azimuth scan by this procedure required about one hour of running time.

Television data were recorded while the mount was slowly swept in azimuth over the test sector. Three sweeps were made with the mount elevation set at 0° , -1° , and -2° . A single azimuth scan was also conducted with a motion picture camera positioned on the mount.

Fog Attenuation Measurements

To obtain laser attenuation measurements in fog, the mount was positioned using the laser telescope to illuminate both flat reference reflectors (Fig. 23). The forward reflector was a rectangle approximately one-half beamwidth wide and three beamwidths long. The far reflector was a square larger than the laser beamwidth. Reflector alignment was adjusted so that, when the laser was sighted on the forward reflector, the far reflector completely encompassed the laser beam. Two returns could thus be measured for a single laser pulse at two different ranges. This procedure was used to overcome any pulse-to-pulse power variations of the laser. Differential amplitude was measured in clear weather and again in fog to determine the attenuation; however, data gathered by this procedure proved to be inconsistent. Most probably the effective beamwidth also varied with the atmospheric conditions to a degree that masked the attenuation measurement.

Fog attenuation measurements with the 94-GHz radar were attempted by measuring the differential return from two reference spheres. In this case, the targets were not aligned for single-pulse returns as with the laser. Instead, average returns were measured for many pulses on each sphere. This measurement proved unsuccessful because the range of variability in clear weather measurements was greater than the small attenuations that were experienced in the relatively light fogs during the test.

Fog-particle measurements were made by CRREL during the attenuation tests. These data provided measurements of particle size distributions and particle density.

Laser and 94-GHz radar data were also recorded against specific ice obstacles. Ranges were recorded for both the laser and 94-GHz radar, and amplitude of the returns were recorded for the 94-GHz radar with the aid of a precision attenuator. With the attenuator set to zero, the noise level was measured on the video

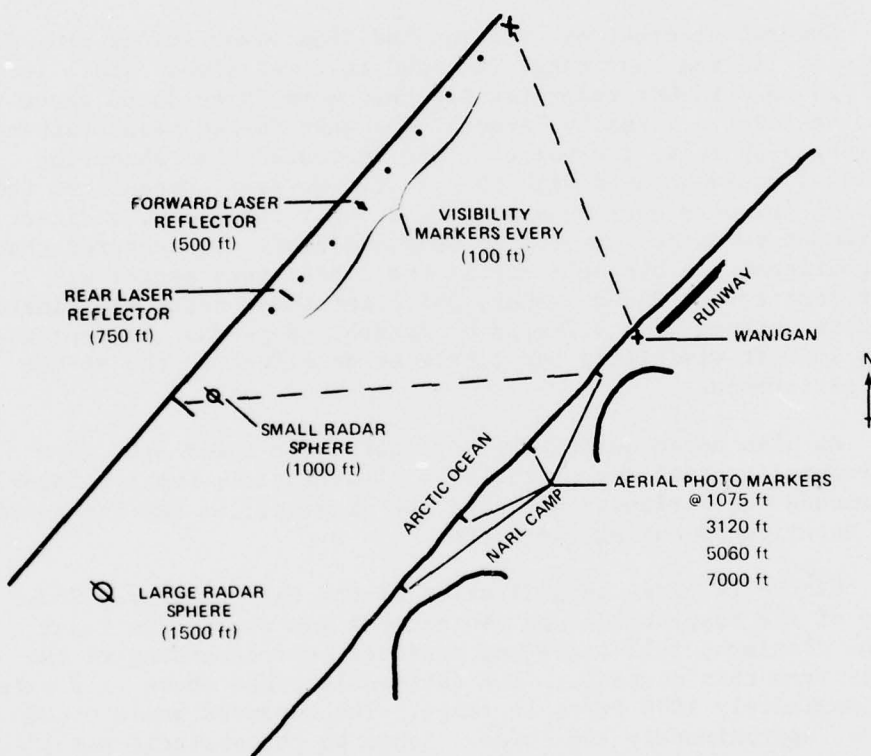


FIG. 23 REFERENCE TARGETS LAYOUT

detector; the attenuation was increased until the measured pulse height was equal to the previously measured noise amplitude. The signal-to-noise ratio was then read directly on the attenuator. A photograph was then taken of the obstacle through the laser telescope. The elevation was moved for the photograph to allow a clearer picture to be made of the obstacle by minimizing the effect of the overlaying reticle pattern. Azimuth to the obstacle was also recorded to allow later correlation with the aerial photography. This measurement was made for five obstacles dispersed through the test sector and also for each reference sphere.

Preliminary Test Results

Several conclusions were reached from observations made in the field. In the near range (to 6000 ft), relatively small ice obstacles gave 94-GHz radar returns that were 25 to 35 dB above the noise level. Visually "smooth" ice gave 94-GHz radar returns averaging 5 dB above the noise. This indicated that shadowing techniques could be used with the radar. However, because of the potential for very narrow beamwidths at this frequency, a direct measurement technique could also be considered. It appeared that no significant ice obstacle within the 1.5-mi test sector was transparent to the 94-GHz radar, which for these tests was limited to a 2-ft antenna with a 7-mrad beamwidth. Fogs down to approximately 1000 ft visibility had little or no effect on the 94-GHz radar performance.

As also noted during the May tests, the laser also gave good returns against any obstacle of significance, but the laser performance was seriously degraded, as expected, in the fog conditions experienced during the tests.

Figure 24 gives an indication of the data quality. Shown is one of the laser telescope photographs and the 94-GHz radar A-scope displays, full-scale and expanded, corresponding to the returns from this obstacle. The full-scale range shown is 2 μ s/cm or approximately 1000 ft/cm in range. The expanded scale is 200 ns/cm or approximately 100 ft/cm. Range to the obstacle was 1340 m, and the signal amplitude was 30 dB above the noise. Obstacle size can be determined from the telescope reticle (1 mrad per minor division) as approximately 4.7 m high and 7 m wide at the base. Also note the small return from the ice hump about 150 ft closer. In the obstacle picture this is the rise just below center; it was about 3 ft high.

Conclusions

The following conclusions and recommendations resulted from the Arctic field tests:

THE JOHNS HOPKINS UNIVERSITY
APPLIED PHYSICS LABORATORY
LAUREL, MARYLAND

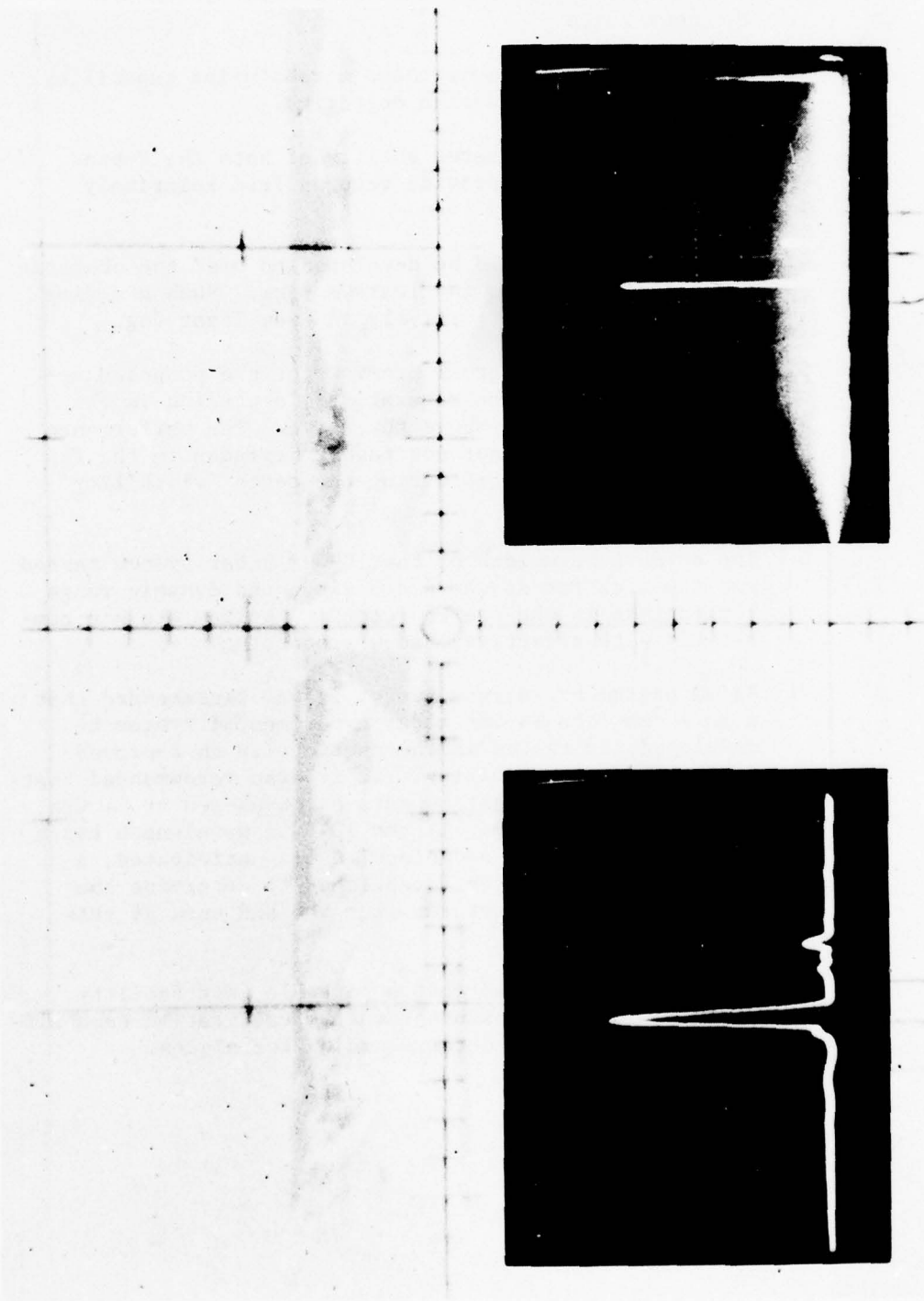


FIG. 24 94-GHz RETURN DATA

THE JOHNS HOPKINS UNIVERSITY
APPLIED PHYSICS LABORATORY
LAUREL, MARYLAND

1. X-band data appear suitable for shadow processing in the near range.
2. The laser system demonstrated a resolution capability appropriate to the design objective.
3. There was a demonstrated ability of both the X-band radar and laser to provide returns from relatively small obstacles.
4. A 1.06- μm radar could be developed to meet the obstacle detection objectives in clear weather. Such a device would not operate effectively in even light fog.
5. A 94-GHz radar has great promise for the proposed application in that the returns from obstacles in the test area were well above the noise. The performance of this sensor was not noticeably degraded in the fog conditions experienced during the tests (visibility down to 1000 ft).
6. The azimuth beamwidth of the 10-GHz radar system tested was too wide for shadow processing, and dynamic range limitations in the analog recording system are not compatible with effective shadow processing.
7. Based on the Pt. Barrow tests, it was recommended that a more complete 94-GHz radar experimental system be developed and tested in the Arctic with an improved data-recording capability. It is also recommended that more detailed propagation data be developed at 94 GHz, 1.06 μm , and 10.6 μm . If the 10.6 μm wavelength has a significant weather advantage, as is anticipated, a test program should be established to determine the character of radar returns from ice and snow at this wavelength.
8. It was also concluded that a portable test facility would be useful to assure complete calibration capabilities and economical data-recording techniques.

THE JOHNS HOPKINS UNIVERSITY
APPLIED PHYSICS LABORATORY
LAUREL, MARYLAND

4. EXPERIMENTAL OBSTACLE DETECTION SYSTEM

The final phase of the APL Arctic SEV program was the development of an experimental obstacle detection system. The system was designed to allow experimentation with processing procedures for radar shadow measurement techniques using a 95-GHz radar. The system was also designed to operate on a test vehicle after a high-speed processor is added. Development of the operating high-speed processor would be deferred until the experimental processor work was completed.

DEVELOPMENT APPROACH

The primary reason for development of the experimental system was to provide a test bed for evaluating the radar shadowing concept as the shadowing related to obstacle height determination for an Arctic SEV. During system design, considerable emphasis was given to three major areas.

The first major area involved selection of a sensor. A 95-GHz radar implementation was selected based both on previous analysis and on results from the preliminary field tests conducted at Pt. Barrow. This frequency provides the best tradeoffs in terms of resolution, antenna size, and all-weather capability. Having made this decision, the next question was development of a suitable antenna; here angular resolution and physical size were the two considerations. The radar shadow concept requires a narrow horizontal beamwidth. However, narrow beamwidths imply large physical sizes. Based on the assumption that this sensor was being considered for an SEV in the 100- to 1000-ton class, an antenna size of about 10 ft seemed reasonable. Such an antenna at 95 GHz results in a beamwidth of about 2 mrad. This antenna had to be developed.

Azimuth scan requirements were based on the assumption that this sensor could be used on an actual test vehicle. An azimuth sector scan of 60° was deemed necessary for adequate coverage of the terrain. It was also felt that a one-second update time on the 60° sector should be sufficient from a pilot's display standpoint. These two characteristics establish the torque and drive requirements on the azimuth-scan implementation.

The second major design area was development of a suitable pilot's display. Here again, the basic philosophy was to assume

use of this display on an actual test vehicle. The display-format concept was a limited angle PPI display with color-coded terrain-height data. Processing of each radar return results in a raw line of terrain data for the display. Therefore, the hardware and display device must be capable of handling these color-coded vectors at the pulse repetition frequency (PRF) of the radar. A maximum vector processing time of 500 μ s was set as a design goal. To provide flexibility for different display formats, no hardware restrictions were placed on the position, orientation, or length of the vectors. A standard color television monitor was selected for the actual display device in order to provide flicker-free viewing.

The third major area of concern was data processing and system control. While processing of the radar returns to determine shadow lengths and obstacle heights is probably the most important part of the system, it is also the least known part. It was felt that many processing techniques would require investigation and evaluation. Therefore, the implementation of this data processing should have considerable flexibility for alteration. Consequently, the decision was made to digitize the raw analog radar returns at video, with all subsequent processing being accomplished in computer software. Also, the raw digitized video would be recorded on computer compatible magnetic tape for ease in post-test playback and analysis.

These data processing and recording restrictions prevent the system, as a whole, from operating in any real-time environment. Real time, as implied here, is the capability to analyze and process every radar pulse transmitted. In other words, the process must be capable of operating at the PRF of the radar. This would naturally be a requirement for any test vehicle configuration. However, this would require the development of a special-purpose high-speed processor. Such an approach was not considered cost effective, since the processing is not well defined. Definition of the processing techniques would be accomplished much easier with the flexibility of computer software. Once an optimized process had been developed it could be implemented in a form to satisfy the real-time speed requirement, and inserted in the system in place of the computer. The remaining parts of the system were designed to operate in the real-time environment.

SYSTEM DESCRIPTION

A simplified functional block diagram of the experimental system is shown in Fig. 25. The radar itself operates at 95 GHz

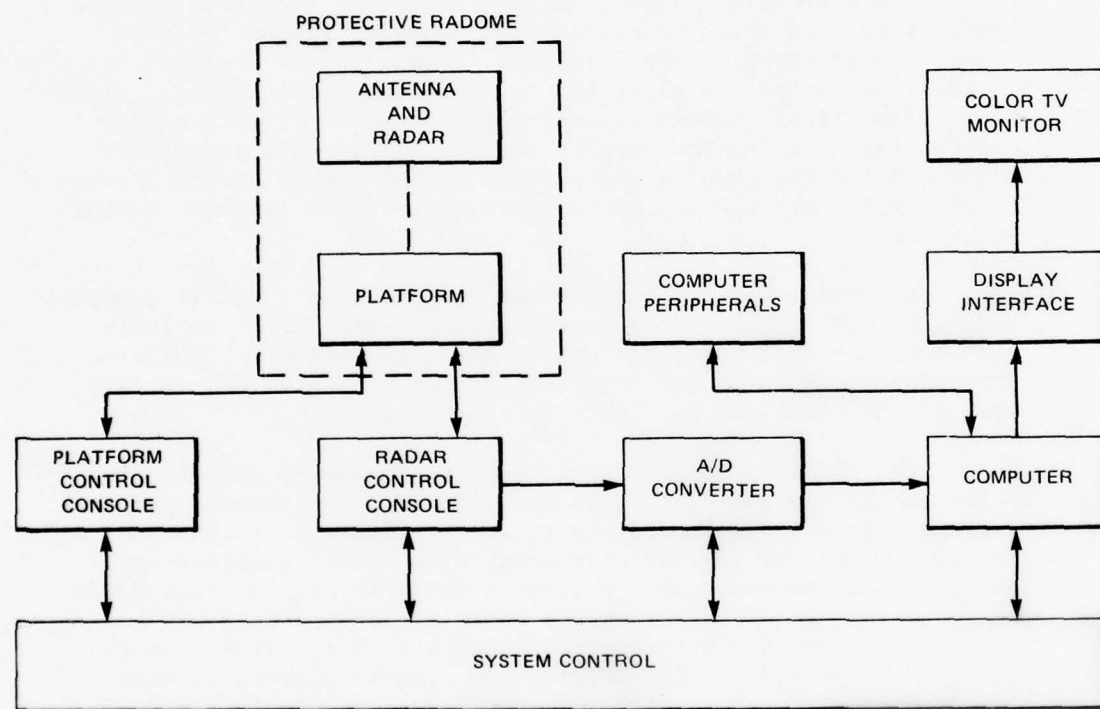


FIG. 25 SEV EXPERIMENTAL OBSTACLE DETECTION SYSTEM
FUNCTIONAL BLOCK DIAGRAM

THE JOHNS HOPKINS UNIVERSITY
APPLIED PHYSICS LABORATORY
LAUREL, MARYLAND

and uses a pulsed-magnetron transmitter. The radar receiver is comprised of a single heterodyne mixer, local oscillator, IF amplifier and square-law envelope detector. Receiver protection from the high-power transmit pulse is provided by a four-port circulator and a waveguide ferrite switch. All of these components are mounted in a specially designed RF enclosure that is attached directly to the antenna structure.

The fixed fan-beam antenna provides beamwidths of 0.1° by 1.5° in the horizontal and vertical planes, respectively. Its dimensions are approximately 8 ft by 3 ft, and it stands about 3 ft high. The total antenna and RF enclosure assembly is mounted on a fixed-elevation variable-azimuth pedestal. The pedestal, in turn, is mounted inside a cylindrical support housing 10 ft in diameter and approximately 3 ft deep. Provision is included for manually adjusting the elevation angle on the total pedestal assembly. A spherical, metal, space-frame radome, 13 ft in diameter and truncated to fit the support housing, provides a protective enclosure for the antenna and pedestal. The remaining components of the system are mounted in standard relay racks external to this enclosure.

The radar control console was developed at APL. It provides manual control of the radar transmitter and receiver. Suitable visual monitors of the radar status are also included. While no provision is included for computer control of the radar, certain monitor functions are available to the computer.

The platform control console, also developed at APL, provides monitoring and control of the antenna azimuth-drive pedestal. A visual digital display of the relative azimuth of the antenna is provided, which is the direct readout of a 16-bit absolute-angle shaft encoder attached to the azimuth drive shaft. Several modes of operation are available in the console. The antenna can be manually commanded via front panel switch to a specific azimuth angle on the encoder. The antenna can also be scanned at some constant angular rate, which is manually adjustable from a front-panel control. Bidirectional data interfaces between the console and the computer are provided, such that antenna azimuth-position monitoring and control functions can be implemented in computer software. All servo-loop electronics are packaged within the console.

Analog returns from the radar receiver are transformed into digital format in the high-speed analog-to-digital (A/D) converter. It is a general-purpose commercially-available unit with capability to digitize analog signals to 8-bit accuracy over sampling intervals as low as 10 ns. Internal storage of 2048 digitized samples is provided. Front-panel controls allow manual adjustment

THE JOHNS HOPKINS UNIVERSITY
APPLIED PHYSICS LABORATORY
LAUREL, MARYLAND

of sampling time interval, full-scale sensitivity, and triggering levels. Interfacing hardware is included to provide complete computer software control of the unit.

The data display device consists of a commercial, studio-quality, color TV monitor. It has a standard 525-line raster capable of about 500 resolution elements per line. The interface that drives the monitor was developed at APL, specifically for the SEV pilot-display application. Via a digital memory, it provides full refresh capability for the three primary TV colors (red, blue, and green) covering 512 picture elements on each of the 480 lines in the raster. It is designed to display data in vector form where there may be several color transitions along each vector. There is no hardware limitation on the origin, length, or orientation of the vector consistent with the number of resolution elements in the TV raster. Operation of the interface is entirely under computer software control.

All data processing and system control functions are accomplished in a commercial general-purpose minicomputer. It is a basic 16-bit machine with an 8192-word core memory. Typical instruction execution time is 1 μ s. The peripheral equipment includes a teleprinter, line printer, card reader, and one magnetic tape recorder. Primary data recording for the entire system is accomplished via the magnetic tape unit.

Two major computer programs have been developed to test and evaluate the radar shadowing technique. The first one is a data recording and control program, which provides precision azimuth positioning of the antenna, sets the A/D converter operation, and controls transfer of the digitized video to the computer and subsequently to storage on magnetic tape. It also has options for printing the raw data samples and processing the data for display on the color TV monitor. The second program is used for reading the raw data tapes and contains the radar shadowing data processing software. It is written in such a manner that various methods for obstacle and shadow detection can be evaluated. Options are provided to display data at various levels of data processing.

95-GHz RADAR TRANSMITTER AND RECEIVER

Figure 26 is a block diagram of the 95-GHz radar transmitter and receiver. In general most of the components are commercially available, but where required, special circuits were designed and built at APL.

The heart of the transmitter is a Model DX-287 magnetron manufactured by the Amperex Corporation. The vendor specified

THE JOHNS HOPKINS UNIVERSITY
APPLIED PHYSICS LABORATORY
LAUREL, MARYLAND

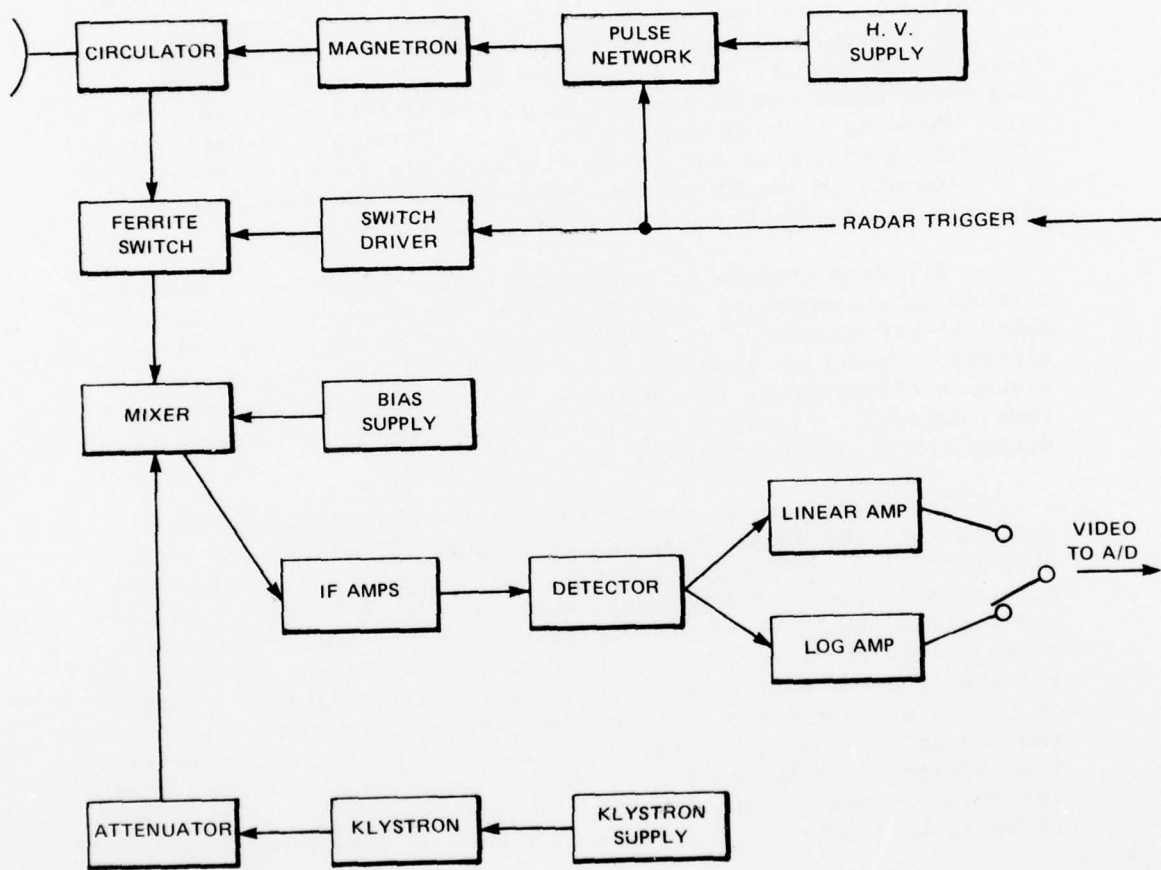


FIG. 26 95-GHz RADAR TRANSMITTER AND RECEIVER

THE JOHNS HOPKINS UNIVERSITY
APPLIED PHYSICS LABORATORY
LAUREL, MARYLAND

maximum peak output power as 10 kW. However, laboratory tests on the unit and subsequent operation in the radar itself indicate a more realistic power output in the 2 to 4 kW range. To avoid overheating, the duty factor on the magnetron firing pulse must not exceed 2×10^{-4} .

High voltage pulses for the magnetron are generated in a pulse forming network (PFN) that couples to an LC delay line via a conventional transformer. This unit is designed specifically for use with the DX-287 magnetron, and is manufactured by the Capitron Division of AMP Incorporated. Multiple taps are provided on the delay line for selecting pulse widths of 85, 100, or 200 ns. The delay line is charged through blocking diodes and a charging choke from a variable high-voltage power supply. Discharge of the delay line is accomplished through a hydrogen thyratron tube. The magnetron pulse is approximately 8 to 10 kV at 25 to 30 A. The RF output from the magnetron is via WR-10 waveguide.

Receiver protection from the high-power transmit pulse is provided by two ferrite devices. A high-power four-port circulator provides about 20 dB of isolation to the receiver with an insertion loss of 1 dB to the antenna. This unit is a model W160 built by TRG (Technical Research Group (of Alpha Insulation Inc.)). An additional attenuation of 50 dB is provided by a ferrite switch. A coil surrounding the ferrite material provides the magnetic field that changes the states of the switch. The attenuation is maximum when the coil current is zero. A current of about 150 mA reduces the attenuation to near its minimum of 1 dB. Figure 27 is a plot of attenuation versus coil current. The unit is a TRG Model W120. A special current-driver amplifier to minimize the switch turn-on time was designed and built at APL. The attenuation is reduced to less than 4 dB in approximately 1 μ s, thus limiting the usefulness of the radar at ranges less than 500 ft.

The local oscillator function for the radar is provided by a Model 90V10A reflex klystron manufactured by OKI Electronics. The klystron is mechanically tunable over an 85 to 95 GHz range. For any mechanical setting, the reflection voltage can be varied to change the frequency by about 150 MHz. Maximum power output of the tube is approximately 50 mW at the upper frequency limit.

For temperature stability, the tube is submerged in oil and mounted inside a relatively large oil bath. Use of the bath proved to be very effective in eliminating frequency drifts after a 20-minute warm-up. Initial drifts were reduced still further by utilizing a 200- Ω , 65-W resistor to heat the oil prior to turning on the klystron. The DC voltages, filament power, and tube protective functions are provided in a universal, laboratory-type

THE JOHNS HOPKINS UNIVERSITY
APPLIED PHYSICS LABORATORY
LAUREL, MARYLAND

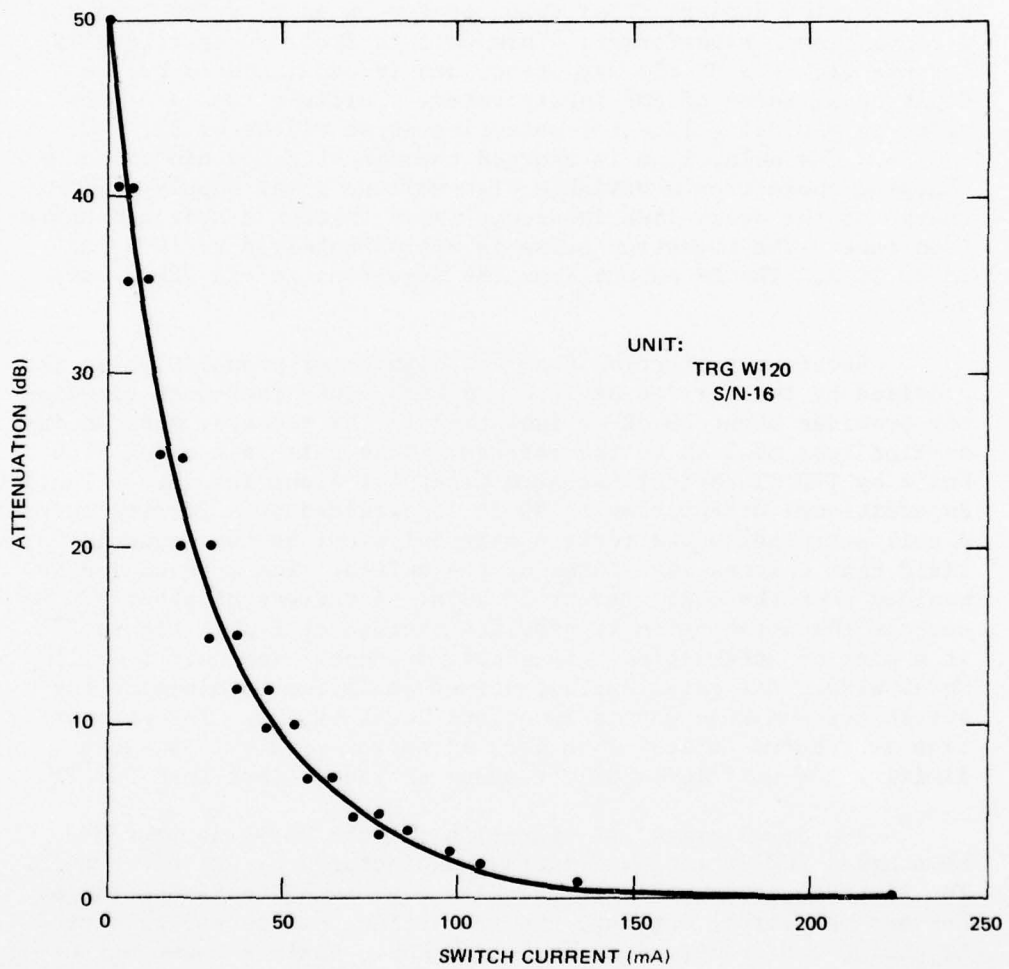


FIG. 27 FERRITE SWITCH ATTENUATION AT 94 GHz

THE JOHNS HOPKINS UNIVERSITY
APPLIED PHYSICS LABORATORY
LAUREL, MARYLAND

klystron power supply. This unit used is a PRD Electronics Model 819-A power supply.

The radar return and the local oscillator output are mixed by a single-conversion balanced mixer. The mixer is a TRG Model W968. The balanced arrangement, in conjunction with the high IF frequency (300 MHz), minimizes the degradation by noise sidebands in the local oscillator signal.

A 3-dB short-slot, hybrid side-wall coupler is used to mix the two signals. The mixer crystals are a pair of gallium arsenide Schottky-barrier diodes set in replaceable wafer mounts. The conversion loss of the mixer is reduced by applying a DC bias current to the crystals. Approximately 1.5 mA is required through each diode, a value found empirically to give a near minimum on the mixer noise figure without causing any degradation in diode operation.

To facilitate reasonable cancellation of the local oscillator induced noise, the signals from the two diodes must be added 180° out of phase. A transformer is used to accomplish this addition and provides the proper impedance matching to the input stages of the IF amplifier. The single-sideband transducer loss of the mixer is specified at 10.5 dB by TRG.

Based on the mixer considerations stated above, the IF frequency was set at 300 MHz. The necessary gain is achieved using wideband "unit amplifiers" manufactured by Avantek, Inc. Two tubular bandpass filters are used to set the center frequency to 300 MHz. Figure 28 indicates the types of modules used in the IF and the associated gain distribution. The positioning of the filters and their bandwidths is also shown. Two of the modules provide up to 80 dB of manual gain control.

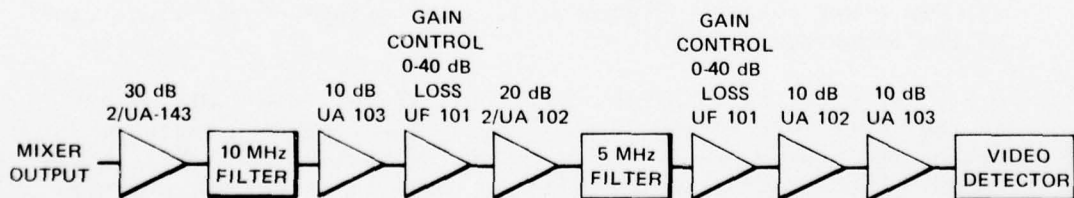


FIG. 28 GAIN DISTRIBUTION AND CONTROL 300-MHz IF AMPLIFIER

The detector used is very nearly square law, with an output voltage proportional to input power. Measured values show the detector output is approximately equal to the input raised to the 1.8 power. This detection process has the unfortunate characteristic of nearly doubling the apparent dynamic range. A change of 40 dB in received power results in a 72 dB change at the detector output. A video amplifier having a gain of 23 dB is built into the detector module.

Since the radar shadowing technique required processing of returns that can vary over a wide range in amplitude, a separate logarithmic video amplifier (manufactured by American Astrionics, Inc.) is provided to drive the high-speed analog-to-digital converter. Bandwidth of the amplifier is extended to 20 MHz on the upper end. AC coupling within the amplifier limits the low-frequency response to approximately 1 kHz. Figure 29 is a plot of the amplifier output voltage versus input voltage (in dB).

A resolution of one part in 256 is provided by the 8-bit A/D converter. Typically, the gain controls of the IF amplifier were set such that a one-bit change at the converter output was representative of 0.2-dB change in power at the receiver input. This setting also provides sufficient gain to have receiver noise only at the output of the logarithmic amplifier. Adequate resolution for virtually all video processing is available while maintaining a full 40-dB dynamic range at the receiver input. This eliminates the need for any form of dynamic gain control circuits.

RADAR CONTROLLER

The Radar Controller provides most of the necessary manual controls to initialize and control the operation of the 95-GHz radar transmitter and receiver components. All controls for the transmitter are located on the Radar Controller chassis itself. Operation of the klystron local oscillator is accomplished through its own power supply. Figure 30 is a photograph of the front panel of the Radar Controller.

AC power is supplied to the unit through the POWER switch in the lower left corner of the panel. The remaining switches across the bottom provide AC power to the various components indicated. The klystron switch supplies power to the klystron power supply (not shown) and controls the power to the heater resistor mounted in the klystron oil bath. When the main power switch is ON and the klystron switch is OFF, power is applied to the heater resistor and the HEATER lamp will be on. This is the first step in the turn-on sequence to bring the oil bath and the klystron up to temperature. After several minutes, the klystron switch may be

THE JOHNS HOPKINS UNIVERSITY
APPLIED PHYSICS LABORATORY
LAUREL, MARYLAND

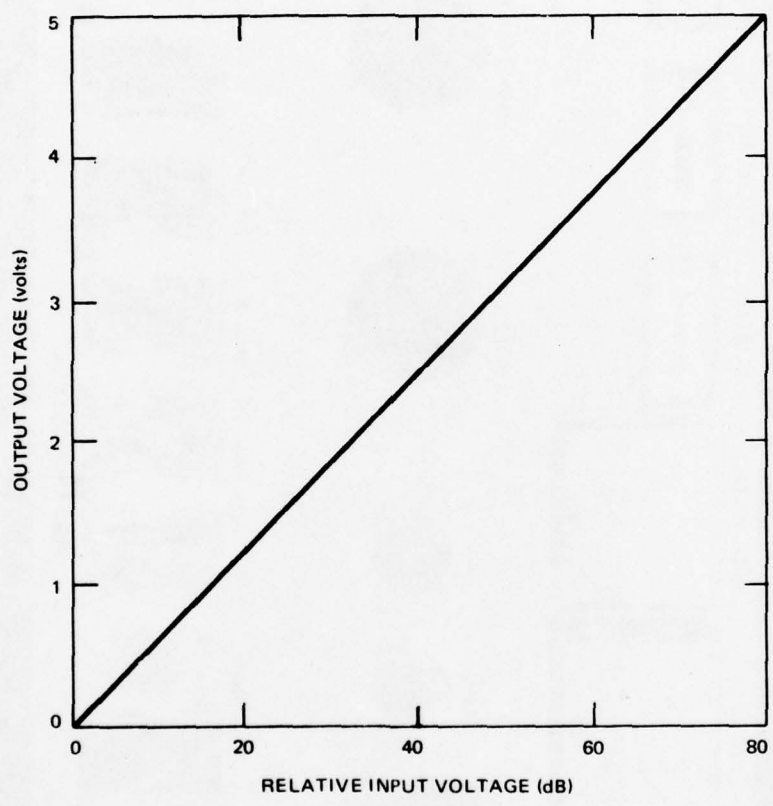


FIG. 29 LOGARITHMIC VIDEO AMPLIFIER CHARACTERISTIC

THE JOHNS HOPKINS UNIVERSITY
APPLIED PHYSICS LABORATORY
LAUREL, MARYLAND

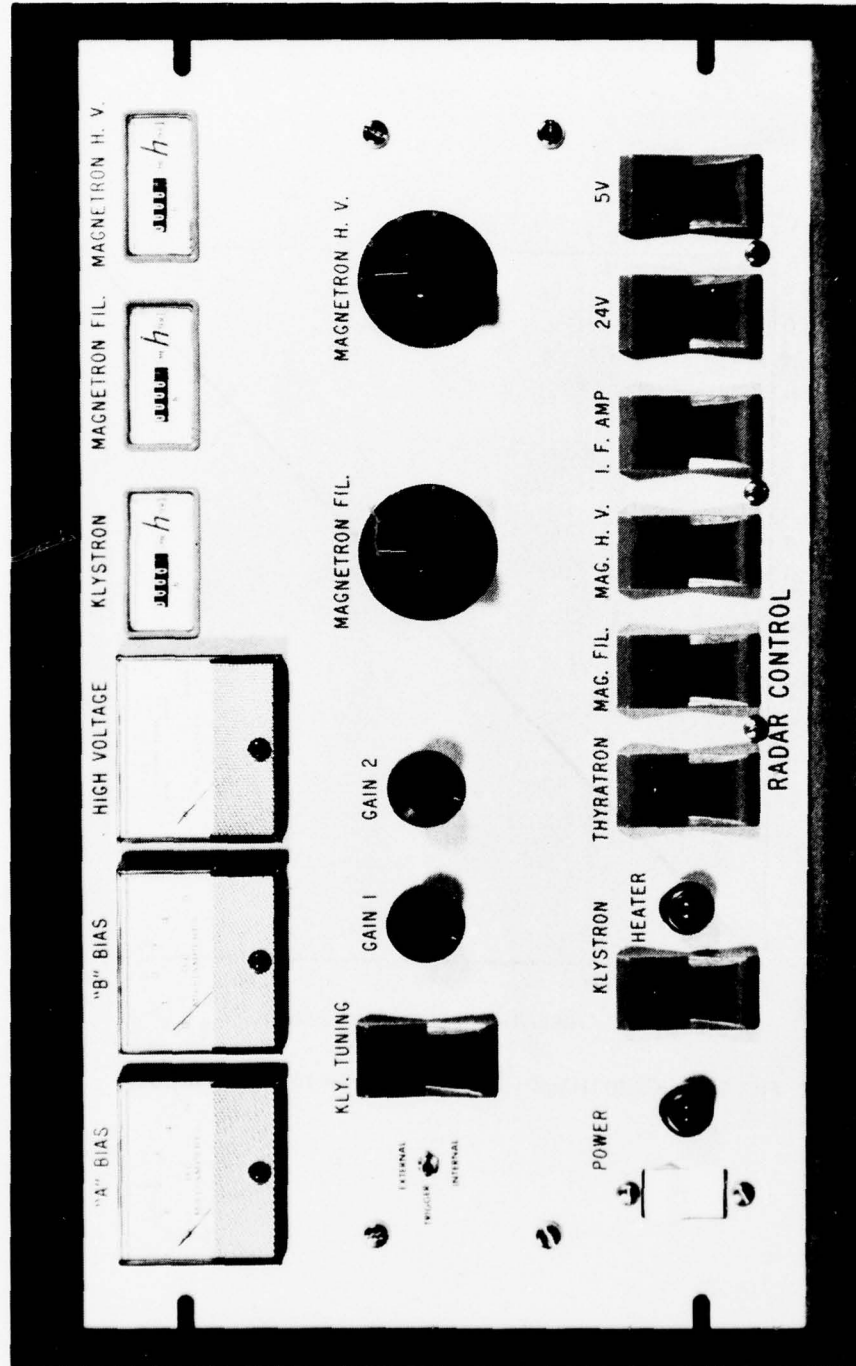


FIG. 30 RADAR CONTROLLER FRONT PANEL

THE JOHNS HOPKINS UNIVERSITY
APPLIED PHYSICS LABORATORY
LAUREL, MARYLAND

turned on and power applied to the klystron filament. When the klystron switch is turned on, power is removed from the heater resistor.

Actuation of the THYRATRON switch supplies AC power to the thyratron filaments and to a small blower that supplies cooling air to the magnetron. The MAGNETRON FIL. and MAGNETRON H.V. (high voltage) switches control the power to their respective variable transformers mounted in the center right portion of the panel, used to vary the magnetron voltages. The IF switch, in addition to supplying power to the receiver, turns on the bias supply for the mixer diodes. The "A" BIAS and "B" BIAS current monitors in the upper left corner of the panel monitor the mixer bias current. The 24 V switch is used to supply power to the radar trigger-pulse amplifiers, and the 5 V switch is used to supply power to the digital control logic.

Three running-time meters indicate the total operating time of the klystron, magnetron filament, and the magnetron high voltage.

ANTENNA SYSTEM

The SEV radar system required a large, 95-GHz, fan-beam antenna that would both maintain its performance and be pointed precisely while mounted on a high-speed SEV designed for travel in the Arctic environment. Such requirements dictated a 95-GHz radome that would protect the antenna and the azimuth drive from the environment but would have negligible effect on the antenna gain, beam pointing direction, and sidelobe levels.

A survey was made of current industrial antenna and radome technology. Responses varied from claims that neither the antenna nor the radome could be built, to offers to build a 95-GHz scanning phased array. After due consideration, an attempt contract was let to the Engineering Experiment Station of Georgia Institute of Technology (EES) and a radome contract to ESSCO, Inc. of Concord, MA. The results of the efforts of these two organizations are described in the paragraphs that follow.

Antenna Development

Factors that were considered in arriving at the final antenna design were specifications and performance and configuration.

Specifications and Performance Summary. The performance specifications imposed on the antenna were as follows:

THE JOHNS HOPKINS UNIVERSITY
APPLIED PHYSICS LABORATORY
LAUREL, MARYLAND

Frequency	94 GHz
Beamwidth	0.11° by 1.5°
Gain	50 dB
Maximum sidelobe level	-20 dB
Polarization	Linear
RF power	8 kW peak
Temperature extremes	-20°F to 80°F
Maximum wind loading	20 mph

The environmental specifications reflected the temperature inside the radome and the wind extremes for antenna range testing.

As the azimuth drive design matured, a 10-Hz minimum fundamental resonant frequency of vibration was imposed as an additional specification.

The SEV antenna design realized by EES met every particular of the specification. The characteristics of the completed design are shown in Table 7 and Fig. 31.

Configuration. Several candidate antennas were considered as being potentially capable of meeting the performance requirements. These included:

1. The parabolic-cylinder reflector fed by a hoghorn (Fig. 32).
2. The parabolic-cylinder reflector fed by a geodesic lens (Fig. 33).
3. The parabolic-cylinder reflector fed by a parabolic hoghorn (Fig. 34).
4. The parabolic-cylinder reflector fed by a parabolic pillbox (Fig. 35).

The parabolic pillbox feed geometry was selected because (a) the reflector shape could be more easily maintained, (b) the primary feed could be easily aligned, and (c) the focal point and reflector shape tend to be self compensating with temperature when the same metal is used throughout the structure.

Table 7
 Characteristics of 94-GHz Fixed Fan-Beam Antenna

RF	
Frequency	93.5 to 96.0 GHz
VSWR	1.3:1 (maximum)
Power handling	2.0 kW peak (unpressurized) 8.0 kW peak (pressurized)
Antenna Beam and Sidelobe Characteristics*	
H plane -3 dB beamwidth	0.11°
E plane -3 dB beamwidth	1.47°
H plane highest sidelobe†	-26.4 dB
E plane highest sidelobe†	-20.5 dB
Sizes	
Aperture	100 in. in H plane 5.8 in. in E plane
Overall	102 in. wide × 44 in. deep × 31 in. high (without transmitter box)
Weight (without transmitter box)	
Horizontal mounting	441 lb
Vertical mounting	425 lb
Mechanical Resonances‡	
Horizontal mounting:	
Parallel	18 Hz
Transverse	22 Hz
Torsional	29 Hz
Vertical mounting:	
Parallel	22 Hz
Transverse	14 Hz
Torsional	>50 Hz

*Averaged over the frequency range 93.5 to 96.0 GHz and over the temperature limits -20 to +70°F at 4400-ft range.

†Below mainbeam peak signal.

‡Parallel: in the direction of the parallel plates.

Transverse: normal to the parallel plates.

THE JOHNS HOPKINS UNIVERSITY
APPLIED PHYSICS LABORATORY
LAUREL, MARYLAND

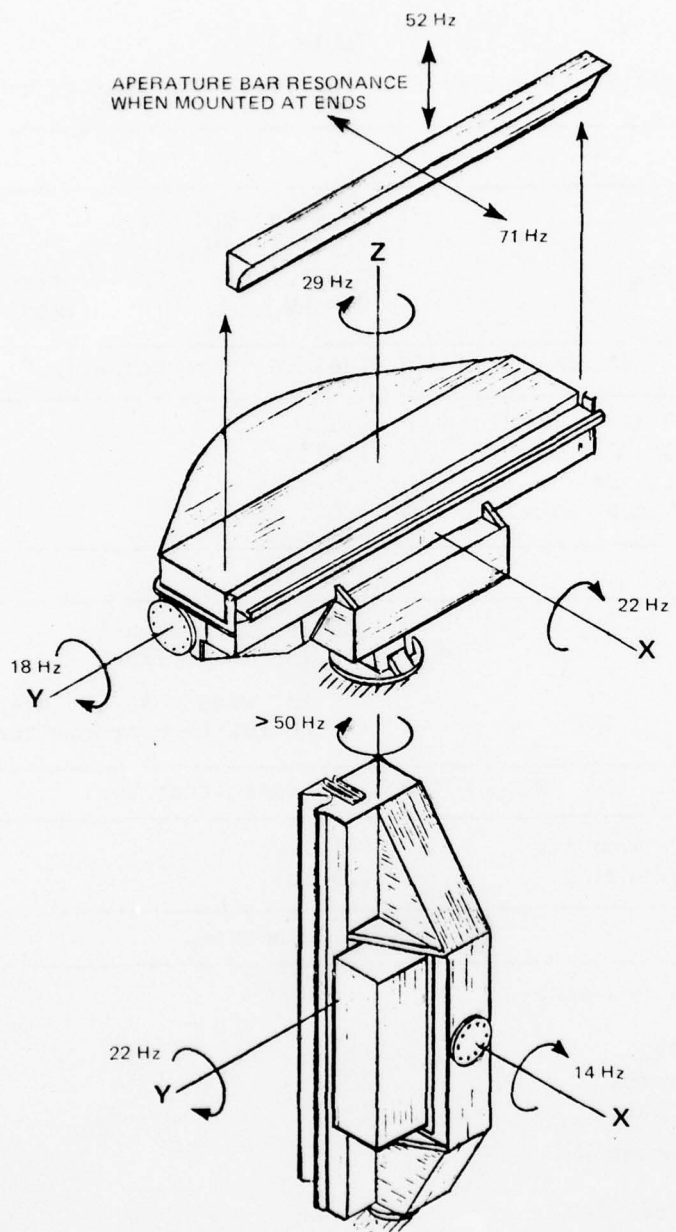


FIG. 31 ANTENNA FIRST-MODE VIBRATION FREQUENCIES WHEN ANTENNA IS MOUNTED RIGIDLY THROUGH THE AZIMUTH DRIVE ADAPTER PLATES

THE JOHNS HOPKINS UNIVERSITY
APPLIED PHYSICS LABORATORY
LAUREL, MARYLAND

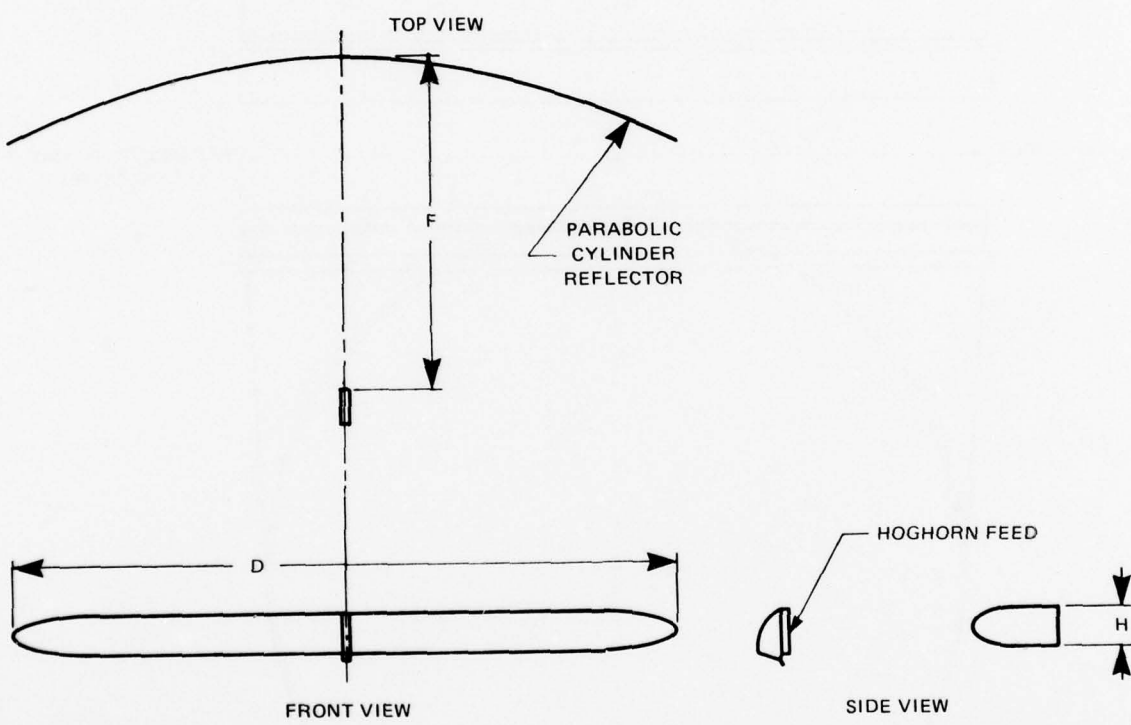


FIG. 32 SIMPLIFIED DIAGRAM OF PARABOLIC-CYLINDER REFLECTOR
FED BY HOGHORN

THE JOHNS HOPKINS UNIVERSITY
APPLIED PHYSICS LABORATORY
LAUREL, MARYLAND

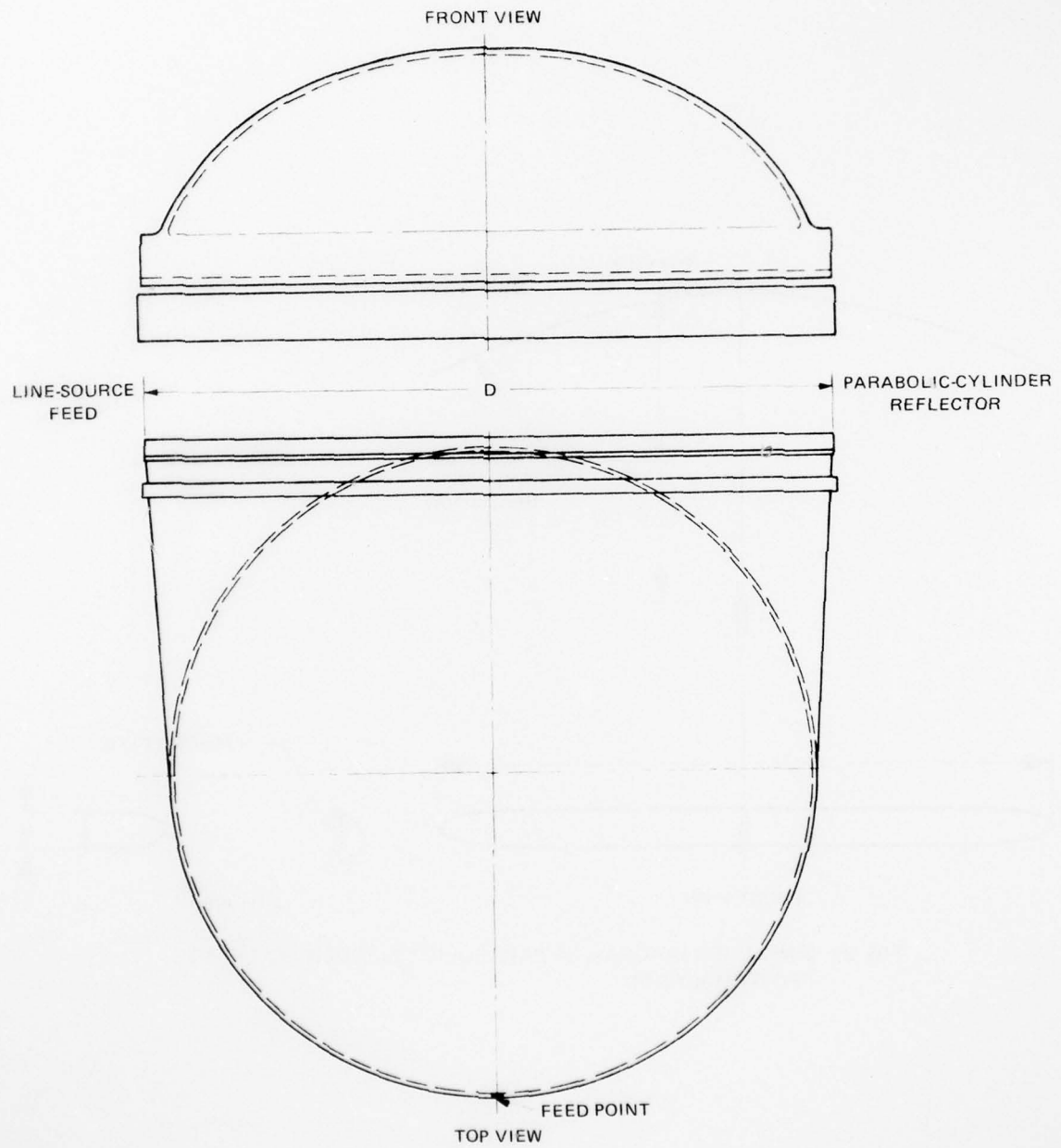


FIG. 33 GEODESIC LENS GEOMETRY FOR PRODUCING COLLIMATED LINE SOURCE

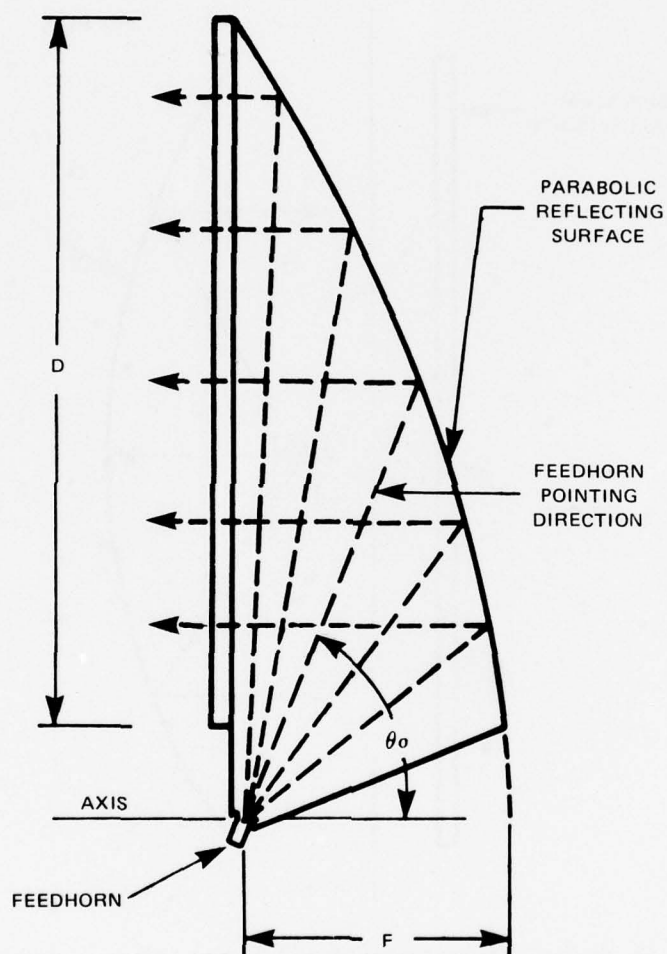


FIG. 34 PARABOLIC HORN FOR PRODUCING COLLIMATED LINE SOURCE IN PARALLEL PLATE

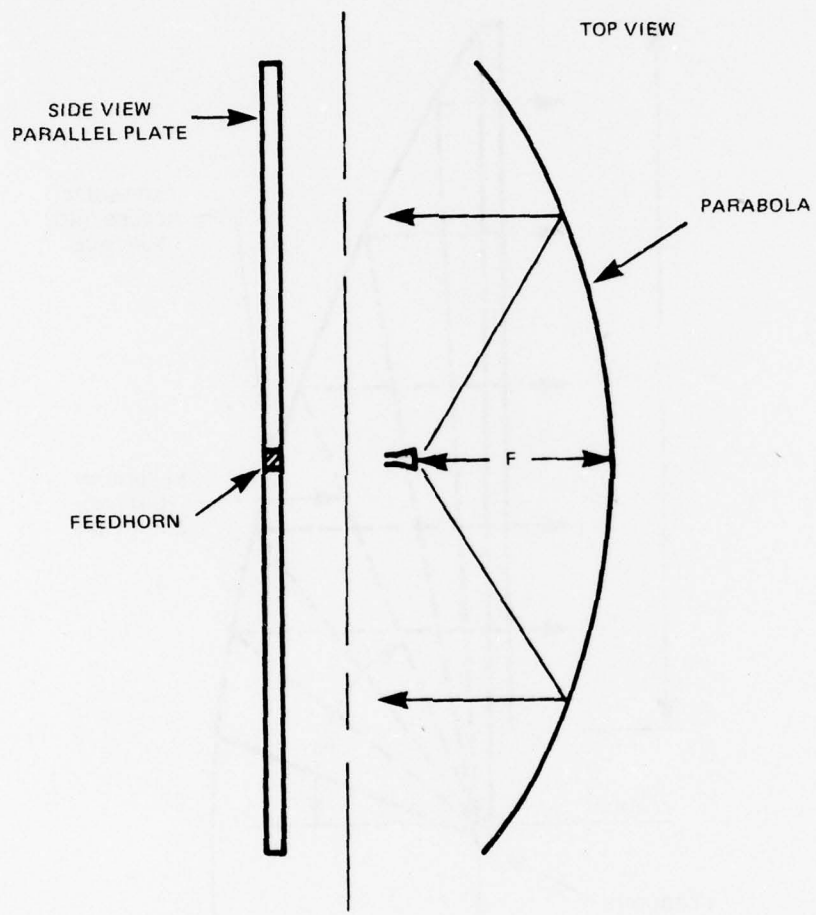


FIG. 35 SIMPLIFIED DIAGRAM OF PILLBOX ANTENNA CONSISTING OF FEEDHORN AND PARABOLIC SECTION IN PARALLEL PLATE

In the pillbox configuration (Fig. 36), the primary feed-horn radiates into a parallel-plate region. The parallel plates are terminated by a parabolic reflector that collimates the feed-horn radiation into a plane wave traveling back toward the front of the antenna. The plane wave is radiated by the line-source feedhorn, illuminating the parabolic cylinder reflector and producing the required fan beam.

Electrical Design

Near-Field Focusing. Conventional antennas (focused at infinity) cannot resolve targets separated by much less than one antenna diameter. This resolution limit occurs when the target is in the Fresnel region (i.e., near-field) of the antenna. In the Fresnel region, energy travels outward in a tube roughly the size of the aperture. In contrast, energy in the Fraunhafer (i.e., far-field) region diverges in its typical far-field angular radiation pattern. For good resolution at long ranges in the Fraunhafer region, a conventional antenna must be large to obtain a narrow beamwidth; however, at short ranges a larger aperture produces worse resolution. Thus the size of a conventional antenna must be compromised if operation in the Fresnel region is anticipated. For the 94-GHz SEV antenna, the Fresnel region extends from about 40 to about 13 000 ft; hence, operation in the Fresnel region is expected to be common.

One possible solution to the dilemma of aperture size involves focusing the antenna at a point in the Fresnel region (rather than focusing at infinity). To accomplish this the aperture phase distribution is changed from its usual constant value to a quadratic variation. The technique produces the conventional far-field pattern at the secondary focal point. As illustrated in Fig. 37, the focused aperture produces a narrow beam at the secondary focal plane as well as over a considerable region radially around the focal plane. Hence, short-range resolution of the antenna is improved.

To determine what improvement is obtained by this focusing technique, a computer program was written that superimposes a quadratic phase distribution on a typical aperture-amplitude taper. The resulting aperture illumination approximates the illumination obtained by moving the primary feed off the focal point (but remaining on the axis) of a parabolic reflector. Pattern variation was evaluated versus range for various focal distances. Calculations indicated that a narrow beam with deep nulls is formed at the focal plane. At ranges shorter or longer than the focal range the nulls tend to fill in and the main beam broadens. In addition, shoulders appear on the main beam above the -20 dB level. However, the well-formed sidelobes are less than -20 dB, as is desired. From the

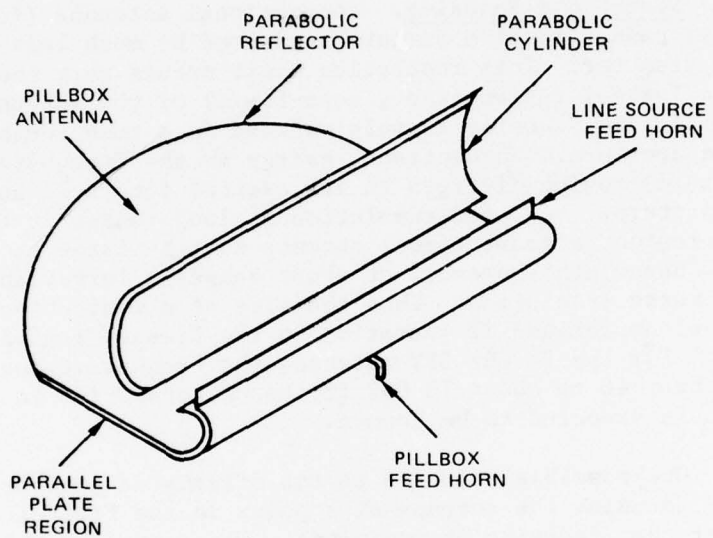


FIG. 36 PILLBOX CONFIGURATION

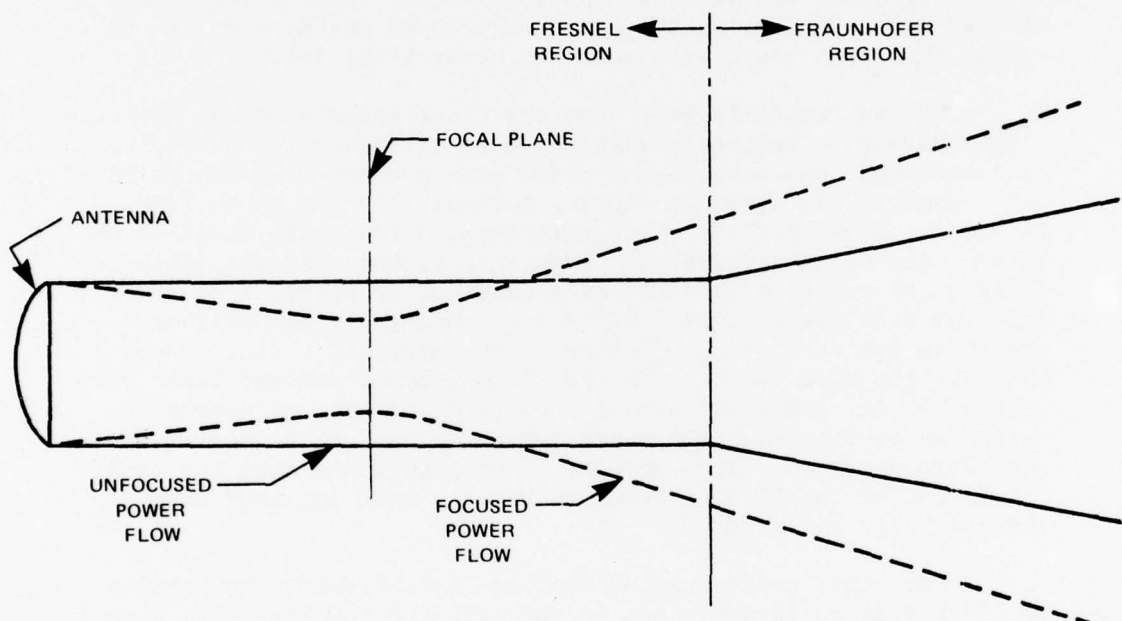


FIG. 37 ILLUSTRATION OF IMPROVED SHORT-RANGE RESOLUTION BY FOCUSING

computed patterns it appears that focusing anywhere between 3000 and 6000 ft gives a reasonable compromise between a narrow beamwidth both near and far from the antenna. Focusing at 4400 ft was used for the 94-GHz SEV antenna, since such a range was available at EES. This focusing was accomplished by simply displacing the feed approximately 0.03 in. from the focal point, away from the reflector, along the reflector axis.

Plate Spacing, Losses, and Gain. The spacing of the parallel plates changes a number of times through the system. The separation distance in the plate regions flares from waveguide height (0.050 in.) at the feed point to 0.252 in. (2 wavelengths) for the entire pillbox region. A spacing of 0.050 in. is used in the circular bend. The loss decreases considerably with the increased spacing; however, the spacing must be reduced below cut-off for all modes except the dominant mode in the bend region to ensure that mode conversion does not occur (Fig. 38).

It was initially felt that the plate spacing in the vicinity of the parabolic reflector might have to be reduced to 0.050 in. to ensure that no higher-order modes were generated by the reflector. However, it would be simpler mechanically not to do this. To resolve this conflict of requirements, a 1/4-scale model of the antenna was built and tested. This antenna had the same field-to-depth (F/D) ratio as the full-size antenna, an aperture of 25 in., and used wide spacing, viz. 0.252 in., throughout the pillbox region to the parabolic reflector. The parabolic reflector was built by the same fabrication technique planned for and later used on the 100-in. aperture antenna. Pattern and gain measurements were made on the 1/4-scale model versus frequency; no moding problems were observed. As a result, it was concluded that the parallel plates of the 100-in. aperture antenna need not neck down at the parabolic reflector.

Once this configuration has been established, the details of electrical performance can be investigated and tradeoffs discussed. The aperture area required is determined by the required gain, which depends on the losses involved. A tabulation of nominal losses for the above configuration is shown in Table 8.

Thus the aperture size corresponding to 54.5 dB (50 dB + losses of 4.5 dB) is the minimum area that will produce the desired antenna gain of 50 dB. As a safety factor, it was recommended that the aperture gain be increased to at least 56 dB. For example, the dimensions 5.8 in. by 100 in. produce beamwidths of 1.52° by 0.088° , respectively, and a corresponding aperture gain of 56.5 dB; therefore it was decided that an antenna having the prescribed configuration and these aperture dimensions was optimum for producing a fixed fan beam at 94 GHz.

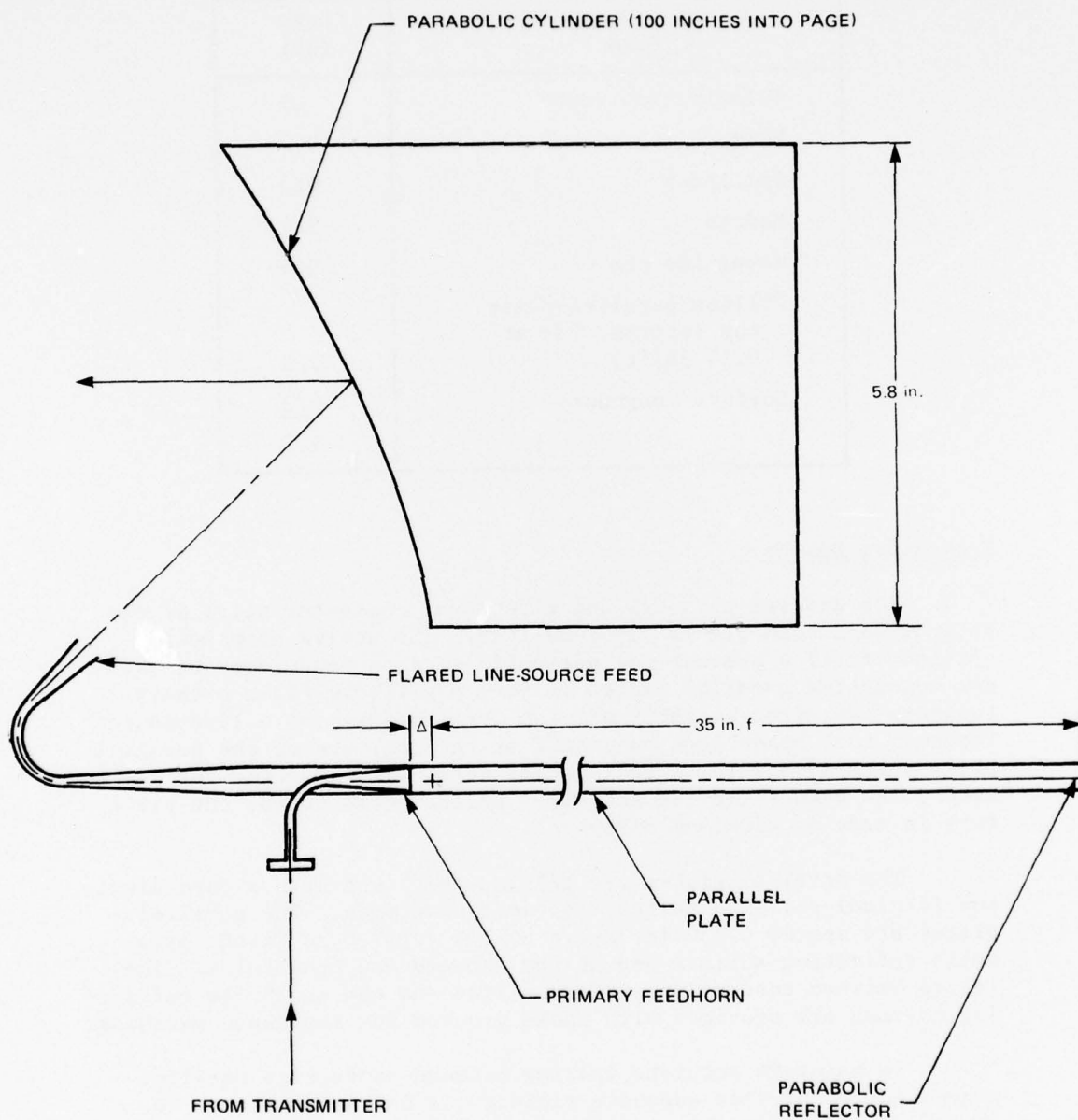


FIG. 38 SEV ANTENNA CONFIGURATION CONSISTING OF PRIMARY FEED,
PILLBOX, LINE-SOURCE FEED, AND PARABOLIC CYLINDER

Table 8
Estimated Losses for 100-Inch Antenna

Item	Loss (dB)
Illumination taper	2.0
VSWR	0.2
Spillover	0.2
Radome	0.4
Waveguide run	0.5
Pillbox parallel-plate run (approx. 7 ft at 0.13 dB/ft)	0.9
Surface roughness	<u>0.3</u>
	4.5

Mechanical Design

The general physical and electrical characteristics of the antenna have been previously described. The active components consist of (1) a symmetrical parabolic section sandwiched between two conductive parallel plates to form a pillbox; (2) a primary feedhorn installed slightly off the focal point; (3) a line-source feedhorn that bends back on itself at the aperture of the parallel-plate section; and (4) a cylindrical parabolic reflector for collimating the beam (Figs. 39 and 40). Except where noted, the structure is made of aluminum alloy.

The parallel plates are 1/3 in. thick and have a pure aluminum (Alclad) polished surface on the active side. The parallel plates are spaced 0.250 in. apart by bar separators at the parabolic reflecting surface and at the extreme end boundaries. The joints between conducting surface plates and the parabolic reflecting surface are provided with choke grooves for impedance matching.

To maintain accurate spacing between conducting parallel plates and to provide adequate rigidity, a backup structure is attached to, and is made a part of, each conducting plate. The structure is a stressed-skin box with the exterior skin of 0.040-in. material separated from the conducting plate by 7-in. longitudinal ribs. Cross stiffeners are used to provide additional skin support and to space the longitudinal members.

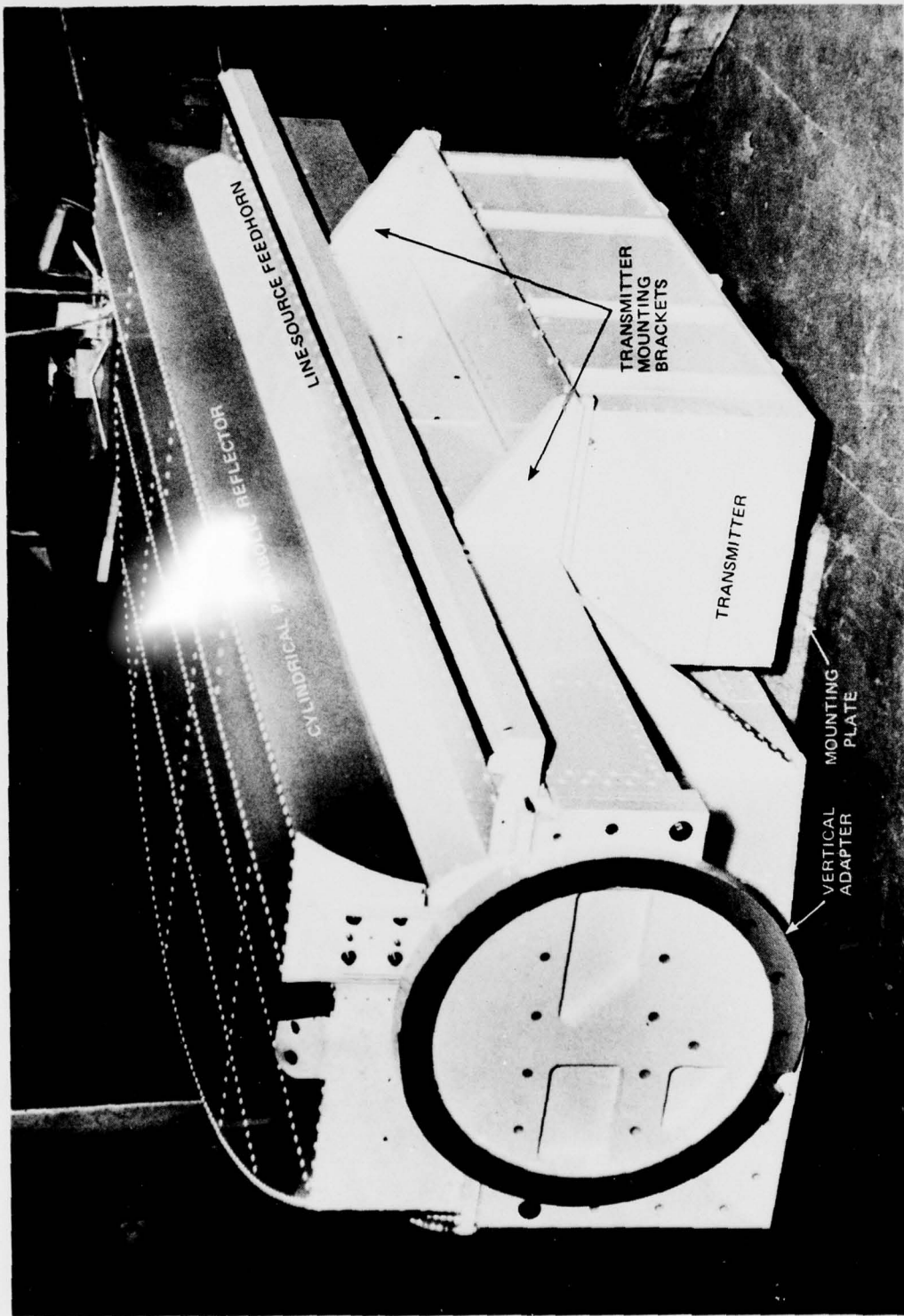


FIG. 39 ANTENNA ASSEMBLY, VERTICAL MOUNTING ADAPTER

THE JOHNS HOPKINS UNIVERSITY
APPLIED PHYSICS LABORATORY
LAUREL, MARYLAND

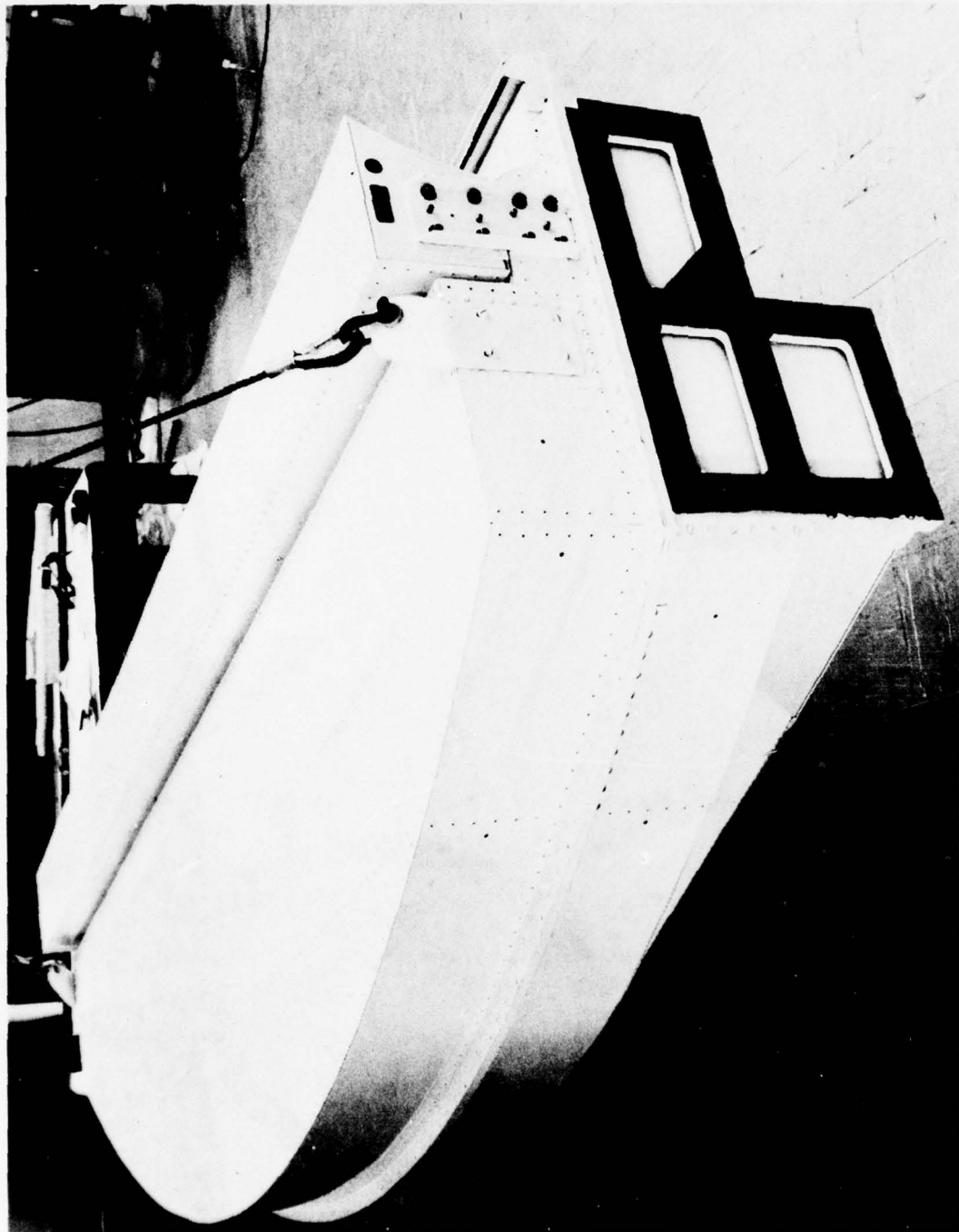


FIG. 40 ANTENNA ASSEMBLY, SIDE VIEW

Blind rivet fasteners are used extensively, but the parallel conducting plates were fastened to the backup structure by flat-head screws countersunk to the screw slot depth. The exposed heads of the screws were then machined flush with the active conducting surface. Locking sealant is used on the threads of all screws.

The primary feedhorn was made by electroplating copper onto a shaped mandrel, which was removed afterward. A diaphragm of polyester film (Mylar) 0.005 in. thick is installed in the flared section of the feedhorn across the microwave path. The film is retained by clamp screw pressure. The feedhorn is installed in a slot in the lower conducting surface and fits snugly between upper and lower conducting plates. The feedhorn is mounted to and supported by an aluminum disk fitted into the bottom of the lower conducting surface plate at the focal point of the antenna (Figs. 41 and 42). When the feedhorn is mounted initial adjustment of the feedhorn toward and away from the parabolic reflecting surface of the pillbox antenna can be made. The adjustment should not be changed from the final test-range setting. The disk containing the feedhorn was also adjusted for axial alignment and should not be moved.

The line-source feedhorn is machined from two solid bars of aluminum tooling plate. The space between conducting plates narrows to 0.050 in. in the horn as the space approaches the bend radius. The spacing continues at 0.050 in. around the bend radius and then flares in the straight portion of the horn to the horn aperture. There is also a small spacer fastened at the center at this point as well as throughout the length. The feedhorn assembly is bolted to the pillbox structure through integral flanges on the feedhorn. Accuracy of position is assured by dowels fitted through the flanges into the mating aperture surfaces on the pillbox structure. A polyester (Mylar) radome 0.005 in. thick is attached to the output lips of the horn and is retained by aluminum fastening strips held down by screws.

The feedhorn was machined on a horizontal milling machine fitted with a hydraulic tracer. Templates were made on a numerically-controlled milling machine. Final surface finishing was done by hand.

The cylindrical parabolic reflector is a built-up structure comprising a solid-metal reflector surface and a box-like stiffening member permanently attached to the rear of the reflector. The reflector is supported on the conducting surface assembly to the rear of the feedhorn by channel brackets, one at each end. After alignment of the cylindrical reflector with a template, the mounting brackets were doweled to prevent misalignment.

THE JOHNS HOPKINS UNIVERSITY
APPLIED PHYSICS LABORATORY
LAUREL, MARYLAND

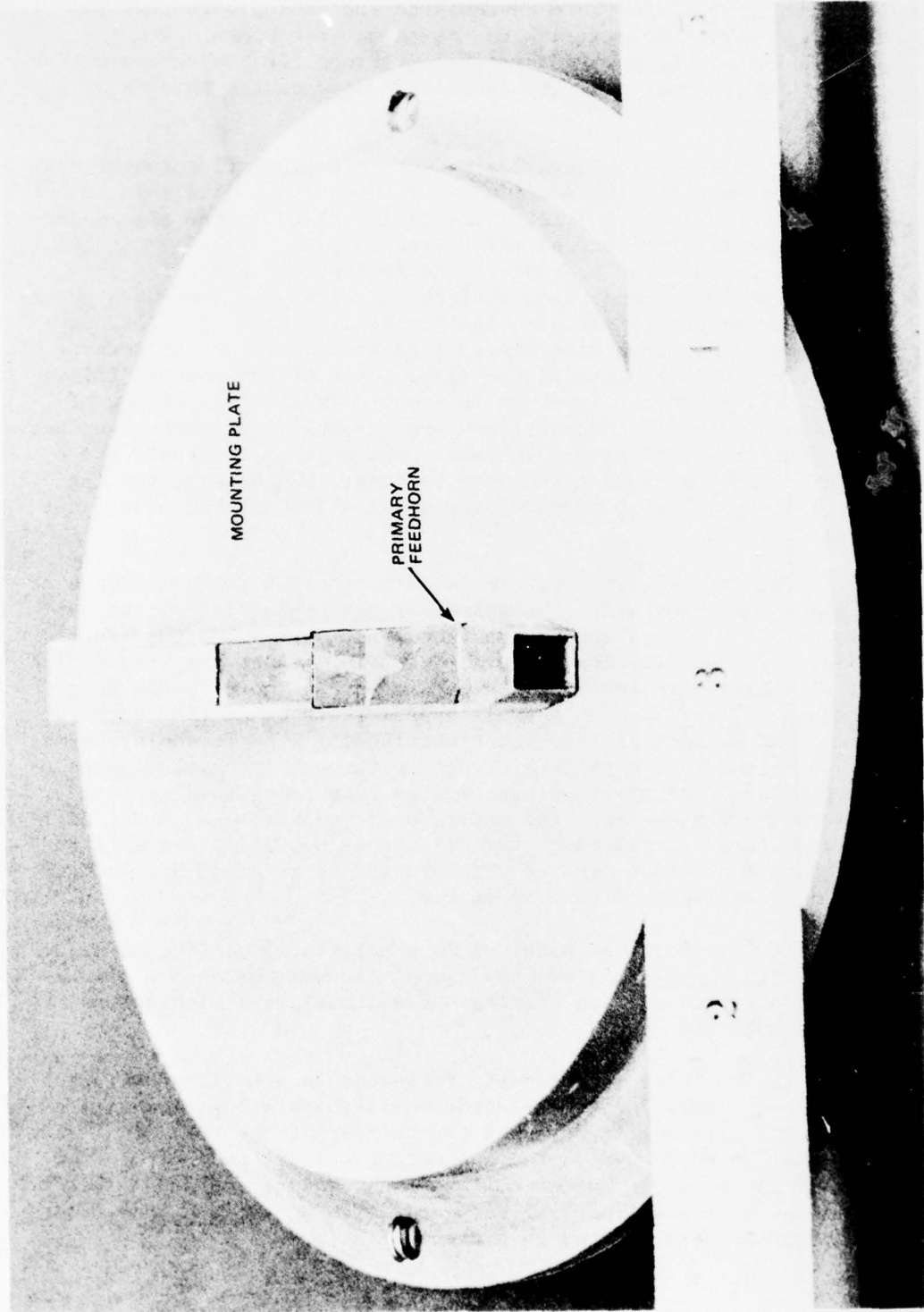


FIG. 41 PRIMARY FEEDHORN MOUNTING PLATE (INTERIOR VIEW)

THE JOHNS HOPKINS UNIVERSITY
APPLIED PHYSICS LABORATORY
LAUREL, MARYLAND

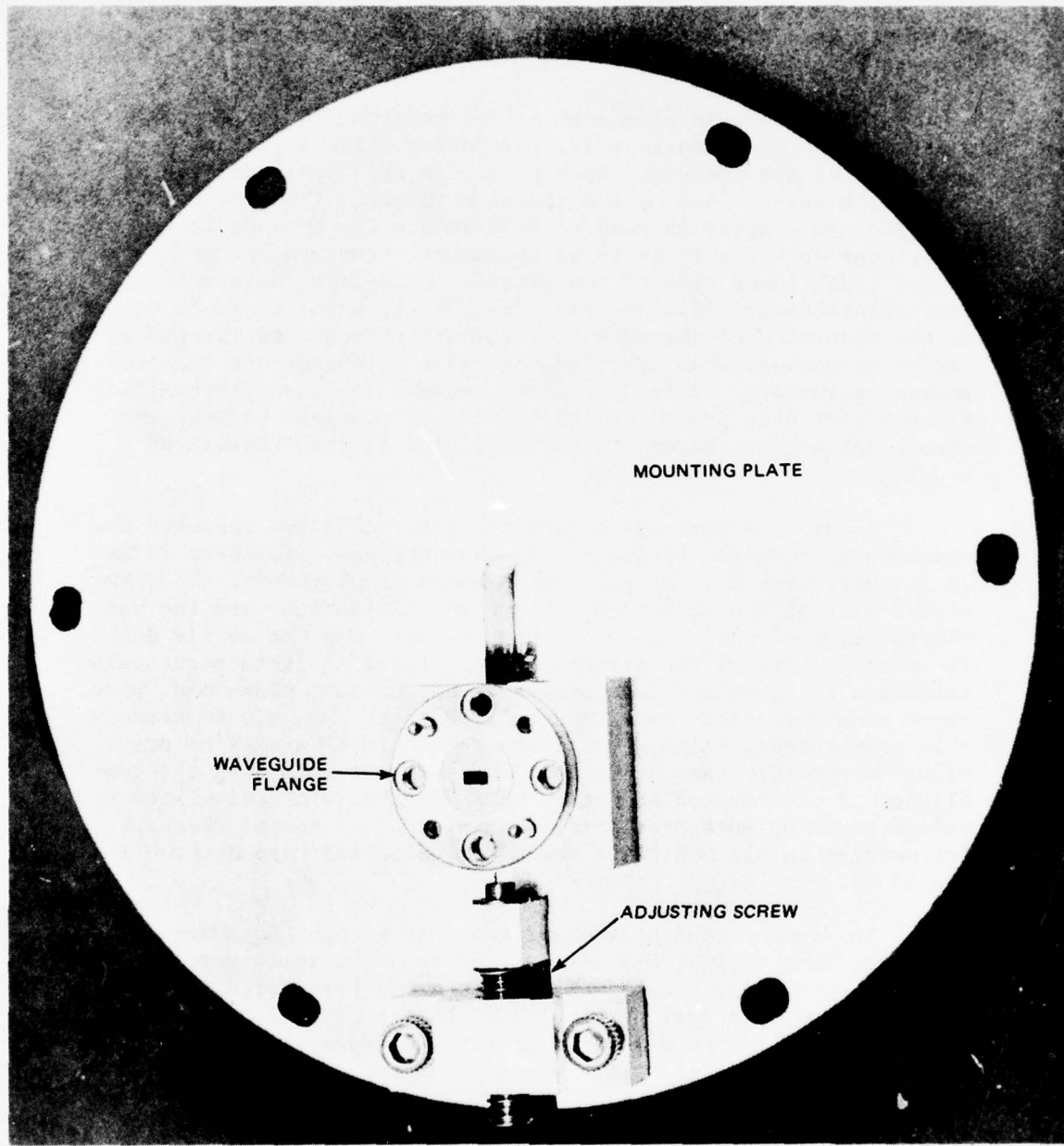


FIG. 42 PRIMARY FEEDHORN MOUNTING PLATE (EXTERIOR VIEW)

A strongback is attached to the lower conducting-surface back-up structure to provide transverse rigidity to the antenna and to facilitate mounting in the horizontal position. A mounting plate is incorporated at the midpoint of the strongback. Doubler plates at this point distribute the weight loading to the antenna structure.

The antenna is also adapted for mounting in the vertical position. To accommodate this, a mounting plate is fitted to the lower end of the antenna. Doubler plates are also used here to distribute weight loading and reaction forces. For each mounting position, an adapter is used to accommodate the antenna to the positioner on which it is to be operated. Brackets are mounted on the front lower side of the antenna to support the transmitter (not furnished by EES); see Fig. 39. The transmitter is fastened to the underside of the antenna structure through end flanges and may be supported, when upbolted, on rails extending out from the antenna structure. Removable shims between rails and transmitter flanges have been provided. An opening is provided through the strongback to give access to the rear side of the transmitter housing.

To avoid interference with the position servo response the fundamental resonant frequency of vibration was kept above 10 Hz in all attitudes and for all common modes of vibration. In view of the size of the structure, the weight limitation, and the mass distribution of the antenna components, this was not easily done. The complex form of the structure made it difficult to accurately calculate the resonant frequencies so approximate means and "worst-case" simplifications were used to reduce the analysis to reasonable proportions. Also, experience gained in this area on previous antenna programs contributed to judgment regarding the compliance of the riveted structure when compared with calculated values based on more nearly rigid joints. Fundamental resonant frequencies in all positions and modes as tested were between 14 and 29 Hz.

To prevent condensation of moisture within the antenna during cooling cycles, dry air was fed into the space between the parallel conducting plates. Since the pressure exerted by the air is distributed over the full area of the plates, a pressure of 1 psi would impose a separating force of approximately 3200 lb on the parallel plates. This exceeds design values, but since the antenna is not pressure tight, it is expected that no damage will result if the leak-down rate matches or exceeds the possible air input rate. However, at low temperatures, there is the risk that ice from trapped moisture may seal leakage escape paths and thus allow pressure to build up to damaging levels.

For the reasons presented above, air pressure must be limited to 0.75 in. of water pressure. This may be done by supplying the air from a blower having a limiting head pressure of this value. The system may also be protected by the use of a pressure-limiting valve, but this is not considered to be so reliable as a blower that is self-limiting by virtue of inherent performance characteristics.

The antenna is designed to be operable under 1-g acceleration loading. Deflections of the antenna have been evaluated, again on "worst-case" conditions, and calculated maximum deflections have been found to be within operating range limitations.

The contract specifications set the operating temperature range at -20°F to +80°F. Calculations indicate that a differential of 20°F between the temperature of the interior conducting surface and that of the exterior skin would produce distortions sufficient to affect performance adversely. The outside of the antenna was painted white to reduce the heating by sunlight, and to minimize the likelihood that resulting distortions would have a significant effect on performance.

It is unlikely that normal in-service temperature changes would cause physical damage to the structure. During range tests, rapid changes of temperature over the operating range did not produce any permanent distortion. No attempt was made to measure transient distortion.

Measured Performance

The procedures used to measure the RF performance characteristics of the 100-in.-aperture pillbox antenna are discussed in the following paragraphs.

The initial setup measured the primary feedhorn VSWR outside the parallel plates. The primary feedhorn was then installed in the pillbox and the VSWR measurements were repeated. The measurements versus frequency were as recorded below.

Frequency (GHz)	Feedhorn VSWR	Complete Antenna VSWR
94.1	1.28:1	1.20:1
94.5	1.26:1	1.30:1
96.0	1.20:1	1.28:1

THE JOHNS HOPKINS UNIVERSITY
APPLIED PHYSICS LABORATORY
LAUREL, MARYLAND

High-power tests on the antenna were performed by APL personnel. The results of these tests were satisfactory, although the 8-kW peak power output was not achieved. Maximum peak-power output obtained from the magnetron was 2.0 kW at 96.3 GHz.

The amplitude of the radiation patterns were measured for the primary feedhorn. The horn was designed for an H-plane illumination taper of 16 dB below peak at the edges of the 100-in. reflector. Measured data indicate that the fabricated horn has an edge illumination taper of approximately 22 dB; however, it was decided that this amount of taper would not seriously detract from overall antenna performance. The effect of this taper would be to increase the H-plane -3 dB beamwidth of the 100-in. aperture from 0.090° to 0.094° , and to reduce the sidelobe level from -25 dB to -30 dB. A very slight reduction in gain, on the order of 0.1 to 0.2 dB, will also be produced with this higher illumination taper.

The 100-in. pillbox antenna was next installed on the azimuth drive located atop a building at EES. Provision was made for pumping dry air into the antenna whenever it was outside in the antenna range environment. Equipment was first prepared for operating the transmitter at a 4400-ft range separation. Initially, the antenna was mounted horizontally to permit measurement of 360° H-plane (azimuth) patterns. Preliminary 360° H-plane and limited E-plane patterns were measured. The 4400-ft range was chosen for the initial measurements so that the H-plane pattern could be focused at this range. This focusing was done by moving the primary feedhorn in small increments and measuring the effect on beamwidth, gain, and sidelobe performance.

At an established focused position of the primary feedhorn (on the 4400 ft range), a series of data was taken as a function of temperature (0°F , -20°F , and $+70^\circ\text{F}$) and frequency. No major degradation of performance was evident over the frequency band and temperature range. Complete 360° H-plane patterns were measured during these temperature tests. It is evident from these data that the H-plane radiation pattern past $+4^\circ$ of the mainbeam area is below 40 dB.

The antenna was repositioned to the vertical on the turntable so complete 360° E-plane patterns could be plotted. Only minimal H-plane pattern data could be plotted in this orientation, since it was possible for the torque rating of the azimuth drive elevation axis to be exceeded if wind loading was present, thus opportunities for taking these data were limited.

A summary of the results showing the sidelobe level, beamwidth, and gain versus frequency is given in Tables 9, 10, and 11.

THE JOHNS HOPKINS UNIVERSITY
 APPLIED PHYSICS LABORATORY
 LAUREL, MARYLAND

Table 9
 Gain, Beamwidth, and Sidelobes at -20°F and at 4400-ft Range

Frequency (GHz)	Gain (dBi)	Beamwidth (deg)		Sidelobe Level (dB)	
		H Plane	E Plane	H Plane	E Plane
93.5	50.5*	0.11	1.45	-26.0	-20.2
94.0	49.3*	0.11	1.46	-28.8	-20.0
94.5	50.0*	0.11	1.46	-25.8	-19.8
95.0	49.8*	0.11	1.46	-27.5	-20.5
95.5	49.6*	0.12	1.50	-26.5	-21.2
96.0	n.m.	0.12	1.49	-24.0	-20.0

Table 10
 Gain, Beamwidth, and Sidelobes at 0°F and at 4400-ft Range

Frequency (GHz)	Gain (dBi)	Beamwidth (deg)		Sidelobe Level (dB)	
		H Plane	E Plane	H Plane	E Plane
93.5	53.2	0.11	1.46	-24.0	-20.2
94.0	51.9	0.12	1.51	-27.0	-20.5
94.5	49.7*	0.11	1.47	-26.2	-20.5
95.0	47.5*	0.11	1.48	-24.8	-20.2
95.5	49.5*	0.10	1.45	-26.5	-21.0
96.0	n.m.	0.12	1.47	-26.0	-22.0

Table 11
 Gain, Beamwidth, and Sidelobes at +70°F and at 4400-ft Range

Frequency (GHz)	Gain (dBi)	Beamwidth (deg)		Sidelobe Level (dB)	
		H Plane	E Plane	H Plane	E Plane
93.5	53.3	0.11	1.45	-27.3	-20.2
94.0	52.9	0.11	1.51	-28.0	-21.0
94.5	51.0	0.11	1.46	-27.8	-20.5
95.0	49.6	0.11	1.52	-27.5	-22.0
95.5	49.9	0.11	1.45	-25.0	-20.8
96.0	n.m.	0.11	1.44	-26.5	-20.0

*These patterns were measured with a heavy layer of frost on both the line source radome and the parabolic cylinder reflector.

NOTE: n.m. = not measured

Figures 43 through 54 are typical radiation patterns for the E- and H-planes. These pattern data include expanded mainbeam patterns and complete 360° patterns. The data presented depict the antenna's performance over the frequency band and environment limits.

The transmitter setup was moved from the 4400-ft range to a site that provided a range of 2-1/8 mi. This separation between transmit and receive antennas satisfied the far-field criterion of $2D^2/\lambda$. The pillbox was initially mounted horizontally to measure the H-plane azimuth pattern. Data were measured at ambient temperature (approximately 50°F). The environment box was then completely removed, and the antenna structure exposed to bright sunlight for long time intervals. No signs of mechanical or electrical variation caused by sunlight were observed. Measurements were made at the 2-1/8 mi range for only one frequency, because of a tight schedule and the associated problems of achieving enough receiver sensitivity to record data. At the measurement frequency of 95.0 GHz, the H-plane azimuth, full-360° and expanded-mainbeam patterns, and antenna gain were recorded. The antenna was re-mounted vertically, and E-plane azimuth, 360°, and expanded-mainbeam patterns were recorded. Minimal H-plane (mainbeam) patterns were also re-recorded. The results are summarized in Table 12.

The transmitter was next relocated at the 1000-ft range. The measurements made at this range were the same as those on the 2-1/8 mi range. A summary of measured data is given in Table 13.

The data taken at the 4400-ft range were averaged over the frequencies at which measurements were made; results are given in Table 14. Finally, the 4400-ft range data were averaged over both frequency and temperature; results are given in Table 15. The average sidelobe level for this complete set of measurement data was determined to be -26.4 dB in the H-plane and -20.5 dB in the E-plane.

A nominal -3 dB beamwidth of 0.11° in the H-plane and 1.47° in the E-plane were measured over the frequency band and temperature excursions. The average gain was measured to be 51.6 dB above isotropic.

The pillbox antenna was focused at a finite distance (4400 ft) by displacing the primary feed a small distance (about 0.030 in.) from the focal point and away from the parabolic reflector. The initial calculations indicated that a 0.09° beamwidth should be obtainable from the 100 in. aperture with a 16 dB edge illumination. However, pattern measurement on the final antenna showed a

THE JOHNS HOPKINS UNIVERSITY
 APPLIED PHYSICS LABORATORY
 LAUREL, MARYLAND

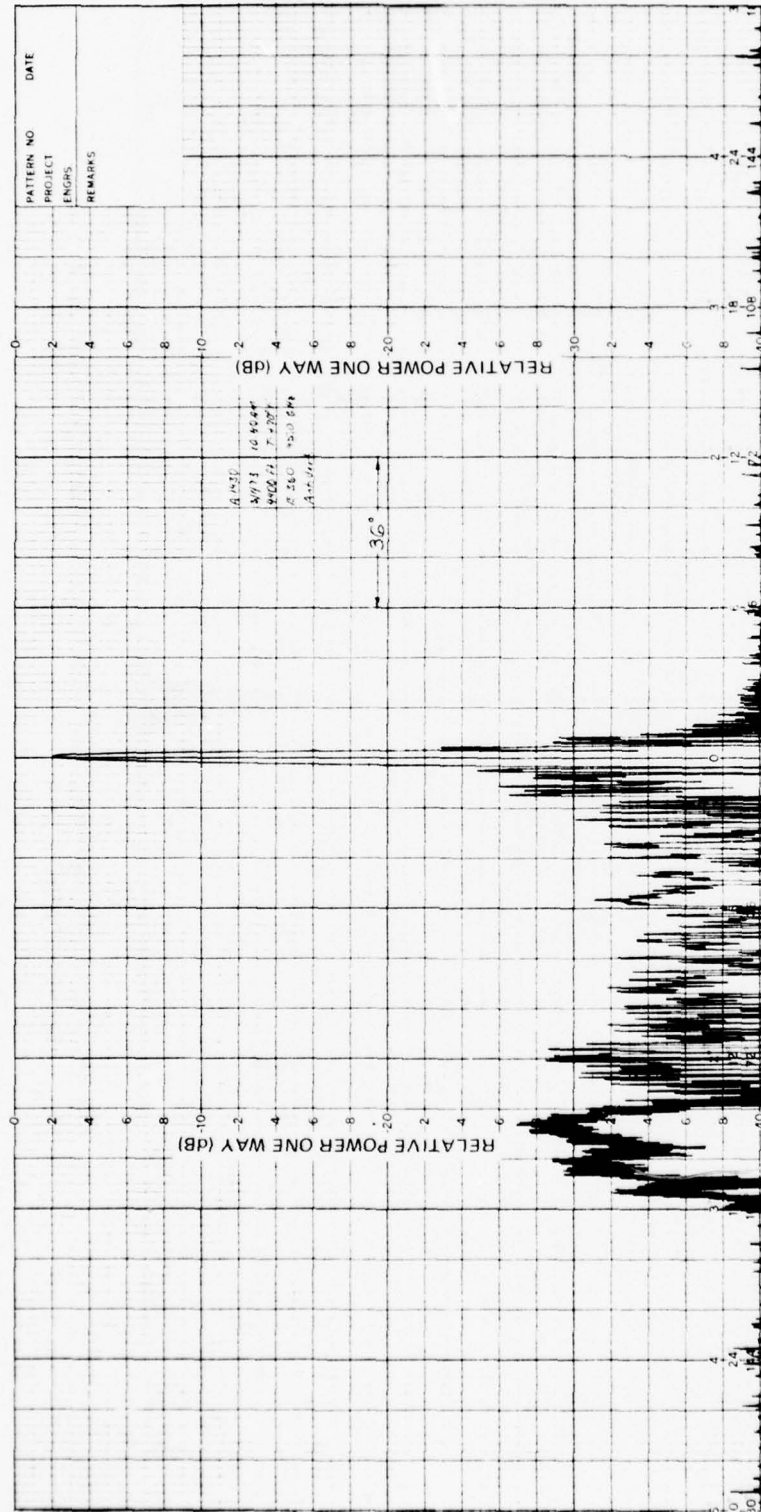


FIG. 43 E-PLANE ANTENNA PATTERN AT 95.0 GHz ON 4400 FOOT RANGE WITH TEMPERATURE AT 70°F

THE JOHNS HOPKINS UNIVERSITY
APPLIED PHYSICS LABORATORY
LAUREL MARYLAND

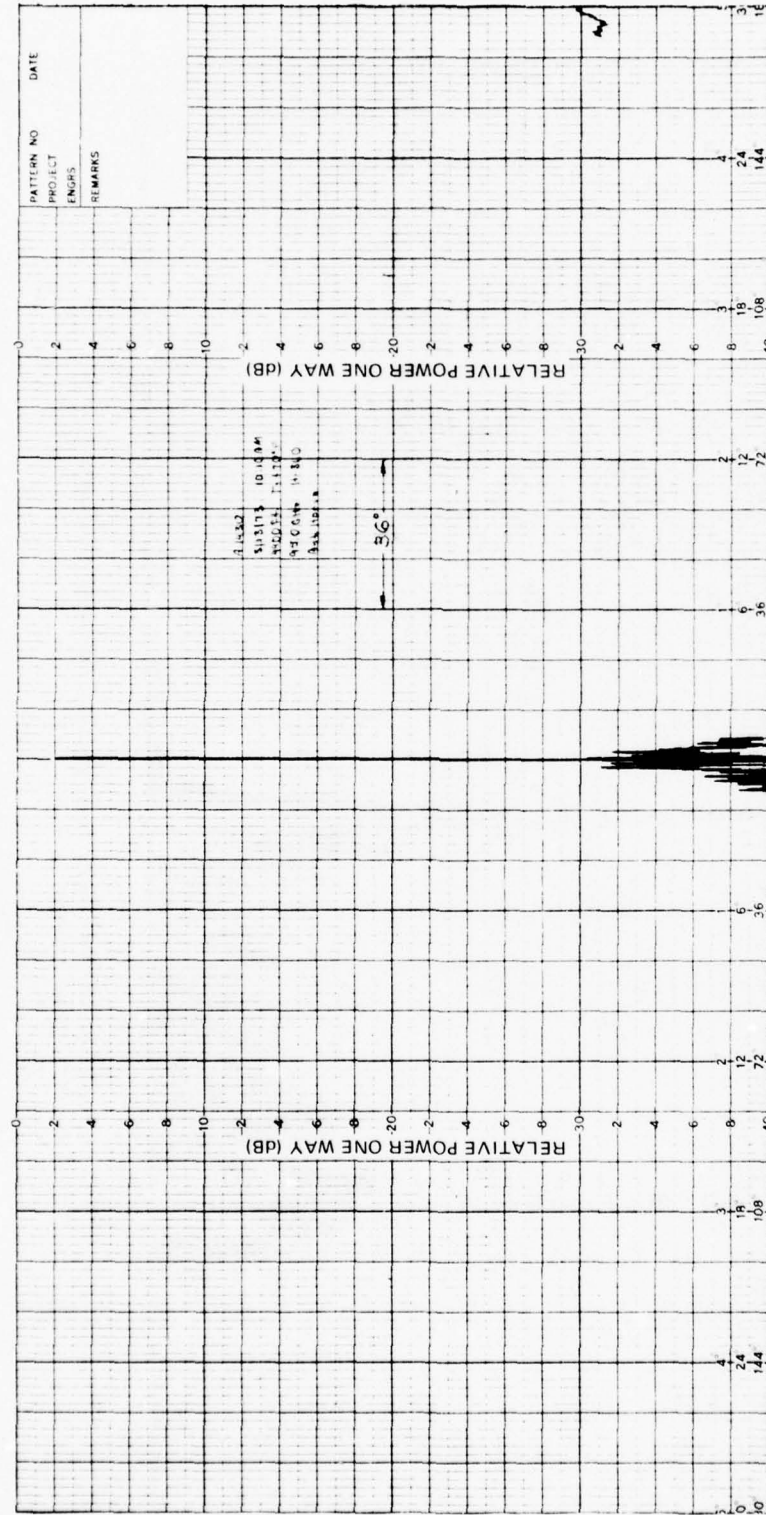


FIG. 44 H-PLANE ANTENNA PATTERN AT 95.0 GHz ON 4400 FOOT RANGE WITH
TEMPERATURE AT 70° F

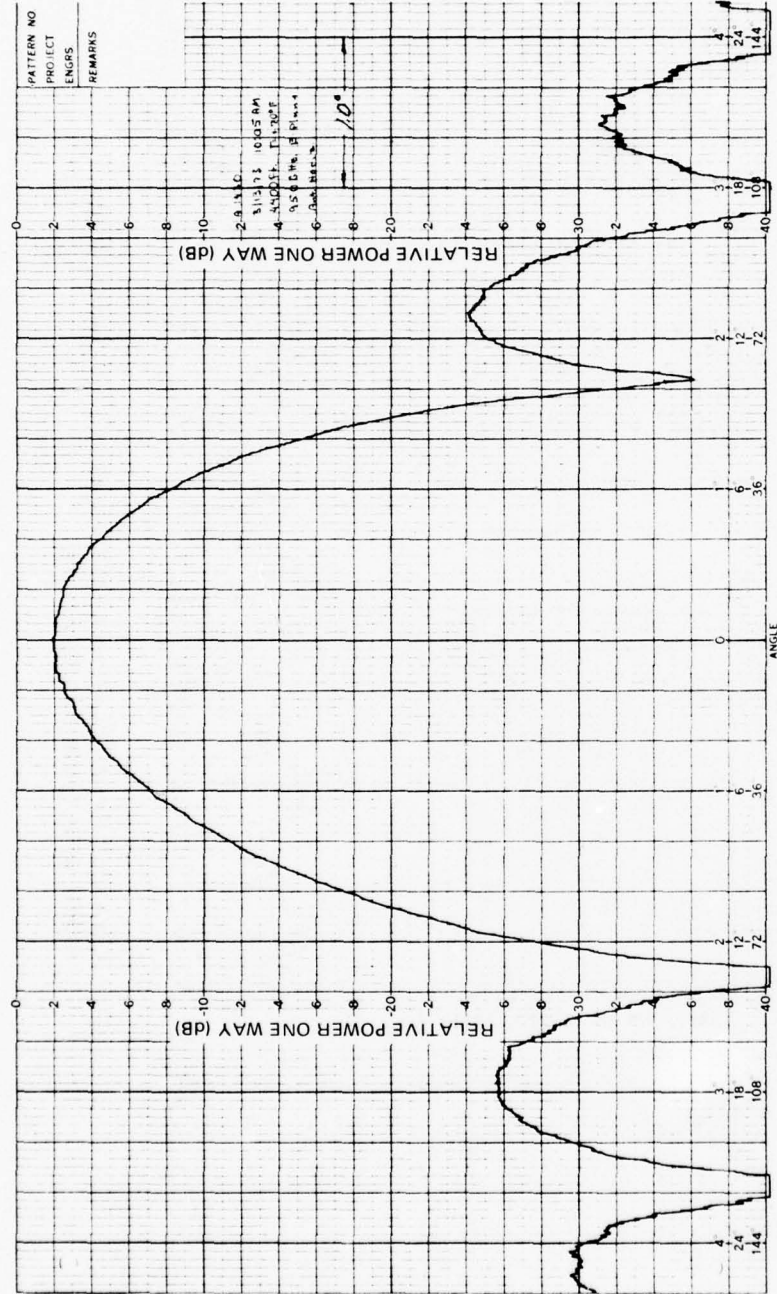


FIG. 45 EXPANDED E-PLANE ANTENNA PATTERN AT 95.0 GHz ON 4400 FOOT RANGE WITH TEMPERATURE AT 70°F

THE JOHNS HOPKINS UNIVERSITY
APPLIED PHYSICS LABORATORY
LAUREL, MARYLAND

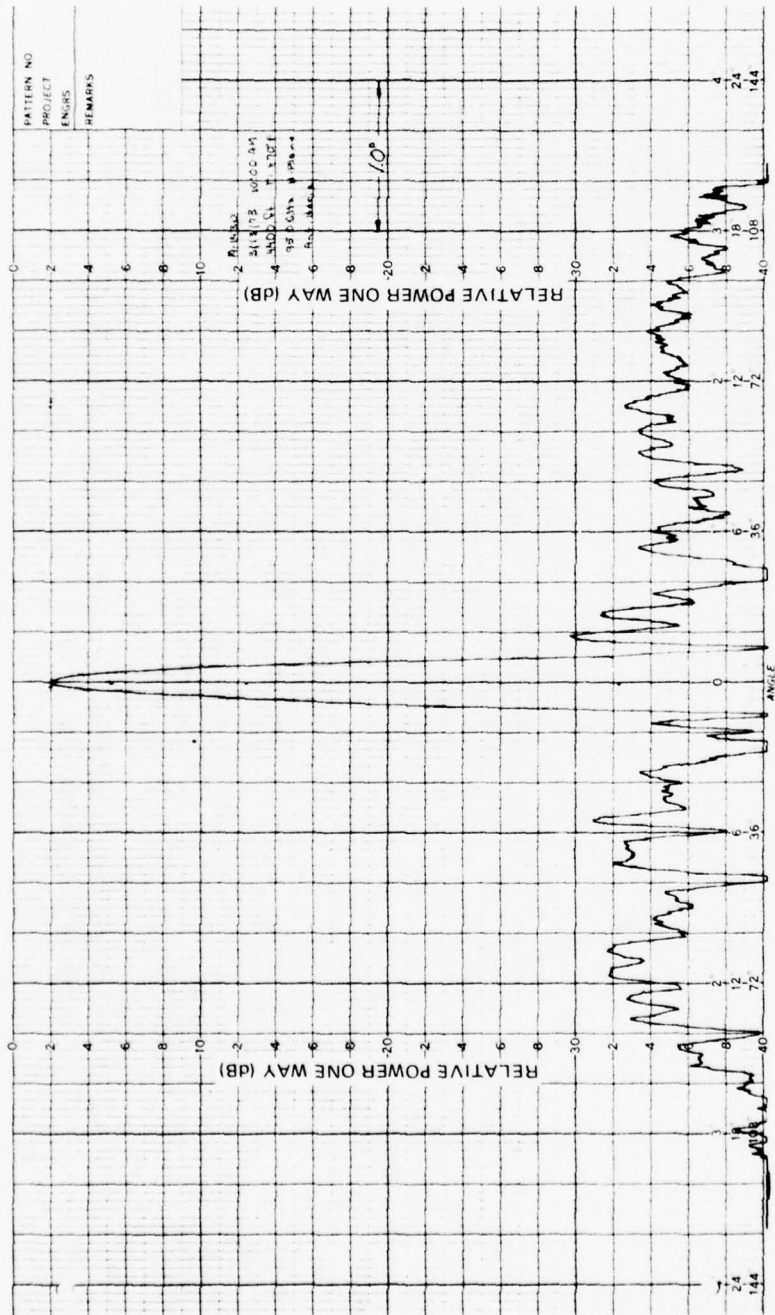


FIG. 46 EXPANDED H-PLANE ANTENNA PATTERN AT 95.0 GHz ON 4400 FOOT RANGE WITH TEMPERATURE AT 70°F

THE JOHNS HOPKINS UNIVERSITY
APPLIED PHYSICS LABORATORY
LAUREL, MARYLAND

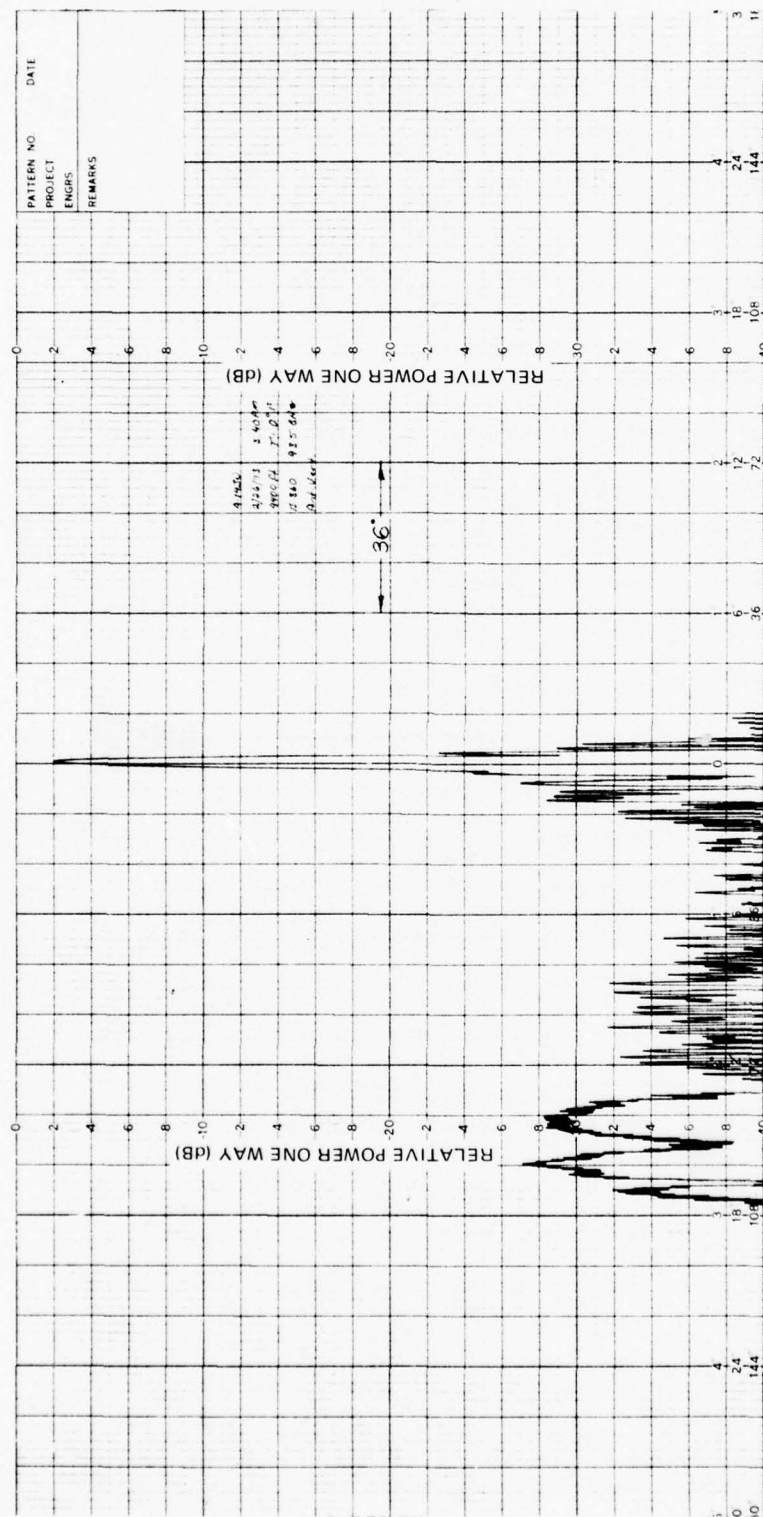


FIG. 47 E-PLANE ANTENNA PATTERN AT 93.5 GHZ ON 4400 FOOT RANGE WITH TEMPERATURE AT 0° F

THE JOHNS HOPKINS UNIVERSITY
APPLIED PHYSICS LABORATORY
LAUREL, MARYLAND

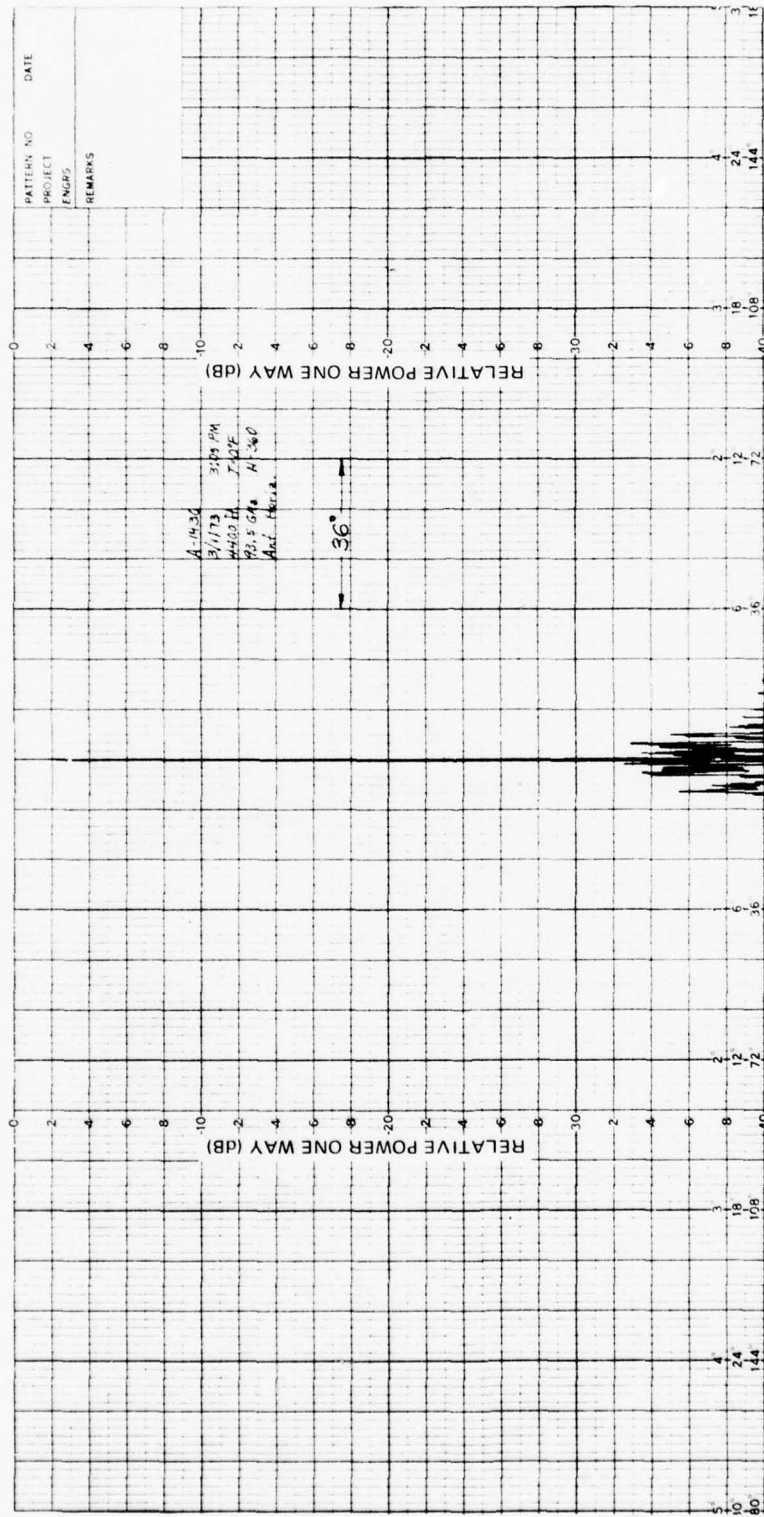


FIG. 48 H-PLANE ANTENNA PATTERN AT 93.5 GHz on 4400 FOOT RANGE WITH TEMPERATURE AT 0°F

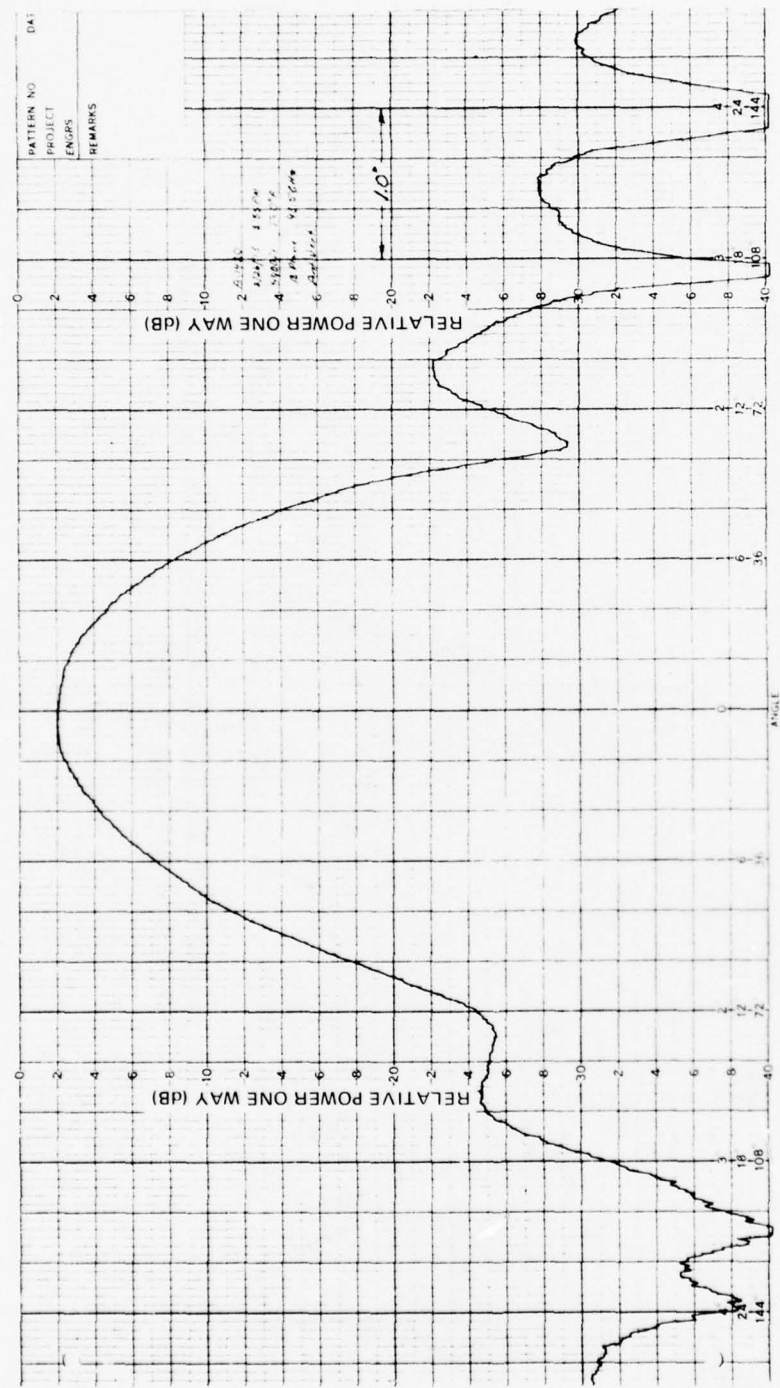


FIG. 49 EXPANDED E-PLANE ANTENNA PATTERN AT 93.5 GHz ON 4400 FOOT RANGE WITH TEMPERATURE AT 0°F

THE JOHNS HOPKINS UNIVERSITY
APPLIED PHYSICS LABORATORY
LAUREL, MARYLAND

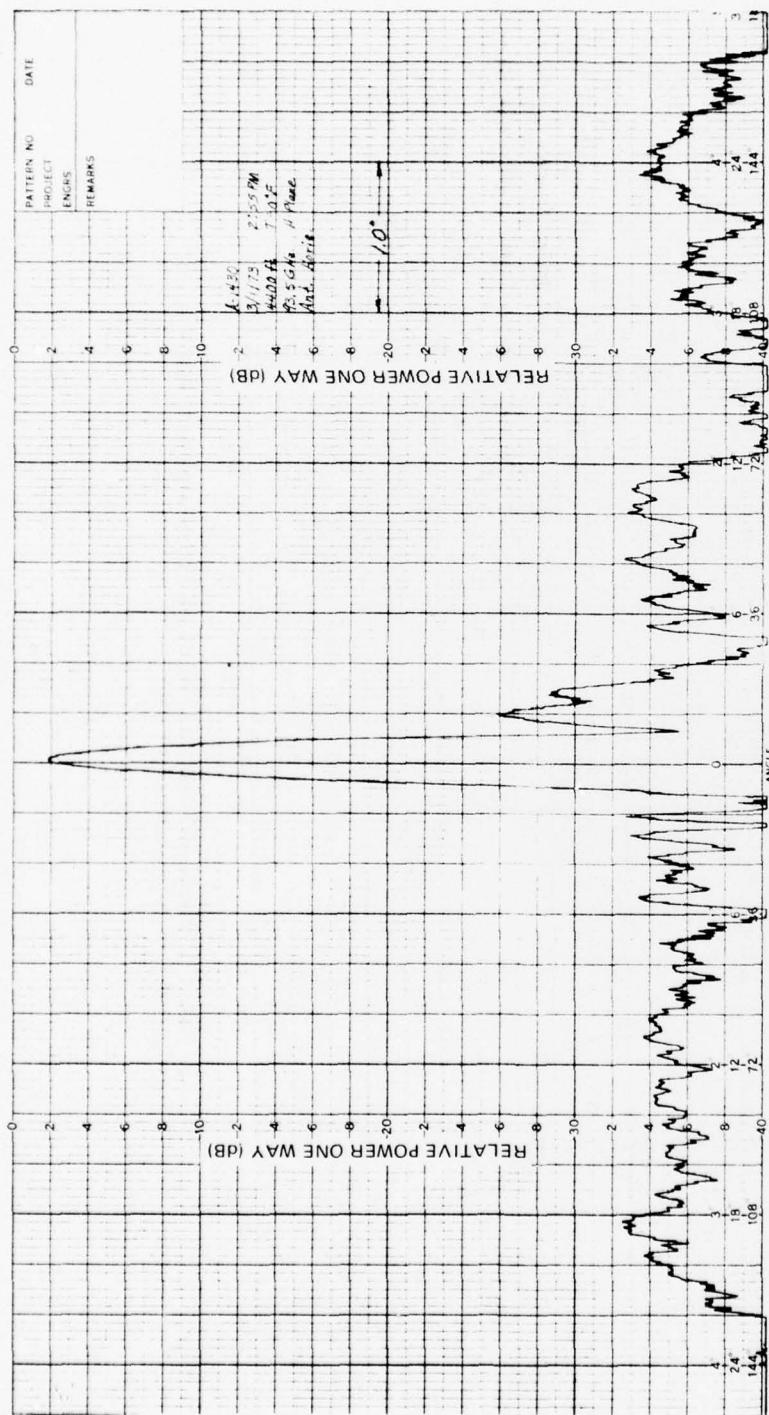


FIG. 50 EXPANDED H-PLANE ANTENNA PATTERN AT 93.5 GHz ON 4400 FOOT RANGE WITH TEMPERATURE AT 0° F

THE JOHNS HOPKINS UNIVERSITY
APPLIED PHYSICS LABORATORY
LAUREL, MARYLAND

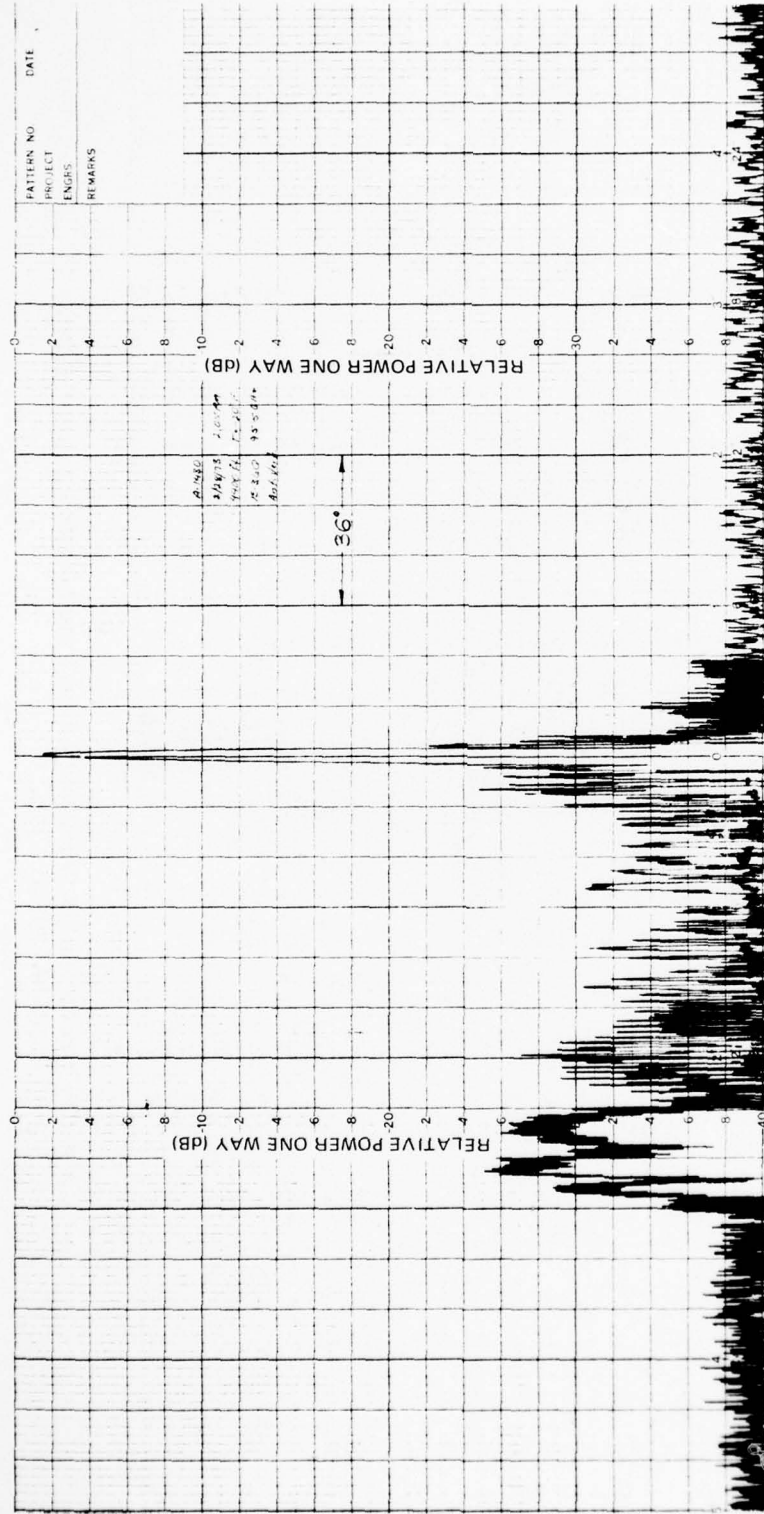


FIG. 51 E-PLANE ANTENNA PATTERN AT 95.5 GHz ON 4400 FOOT RANGE WITH
TEMPERATURE AT -20°F

THE JOHNS HOPKINS UNIVERSITY
 APPLIED PHYSICS LABORATORY
 LAUREL, MARYLAND

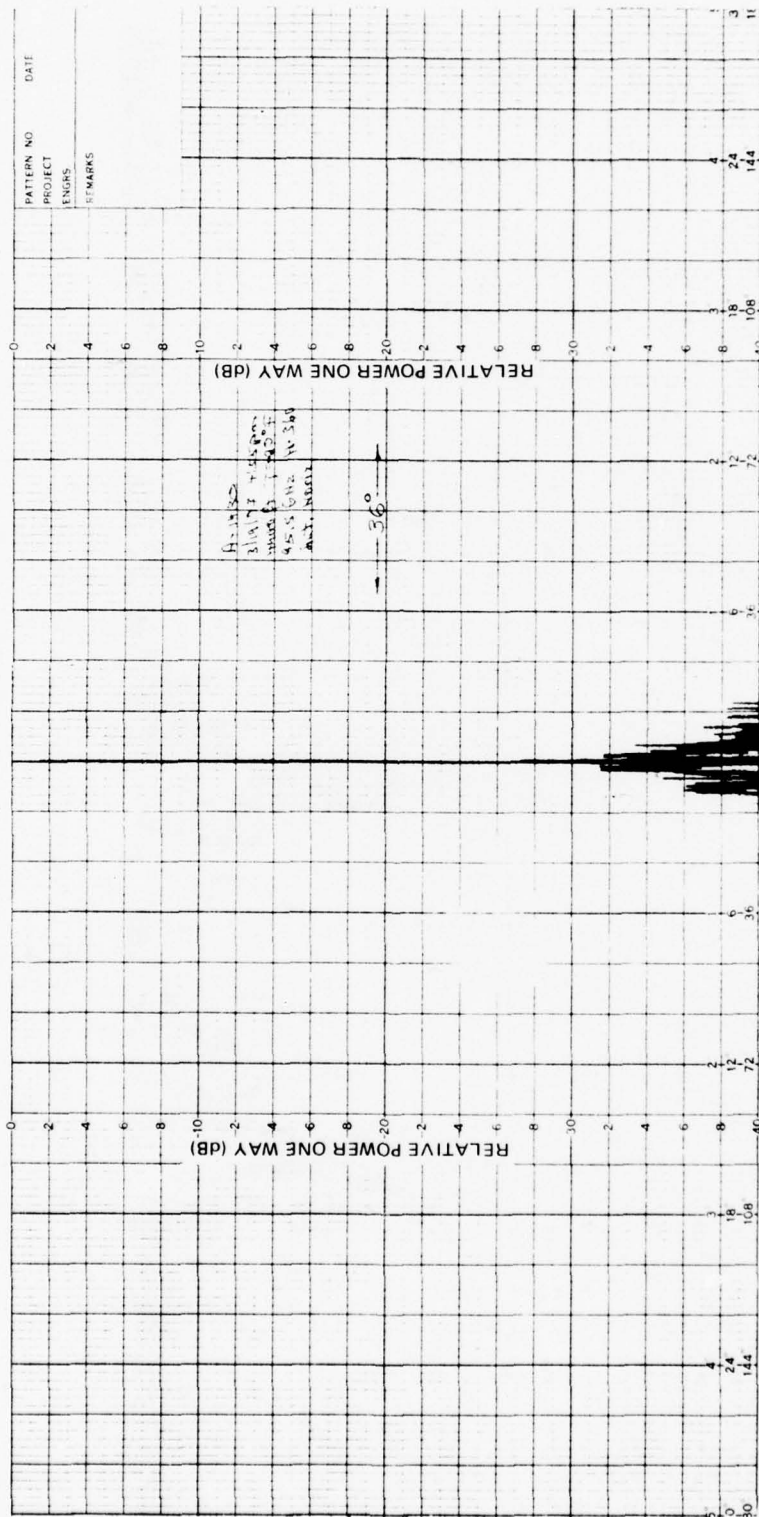


FIG. 52 H-PLANE ANTENNA PATTERN AT 95.5 GHz ON 4400 FOOT RANGE WITH TEMPERATURE AT -20°F

THE JOHNS HOPKINS UNIVERSITY
APPLIED PHYSICS LABORATORY
LAUREL, MARYLAND

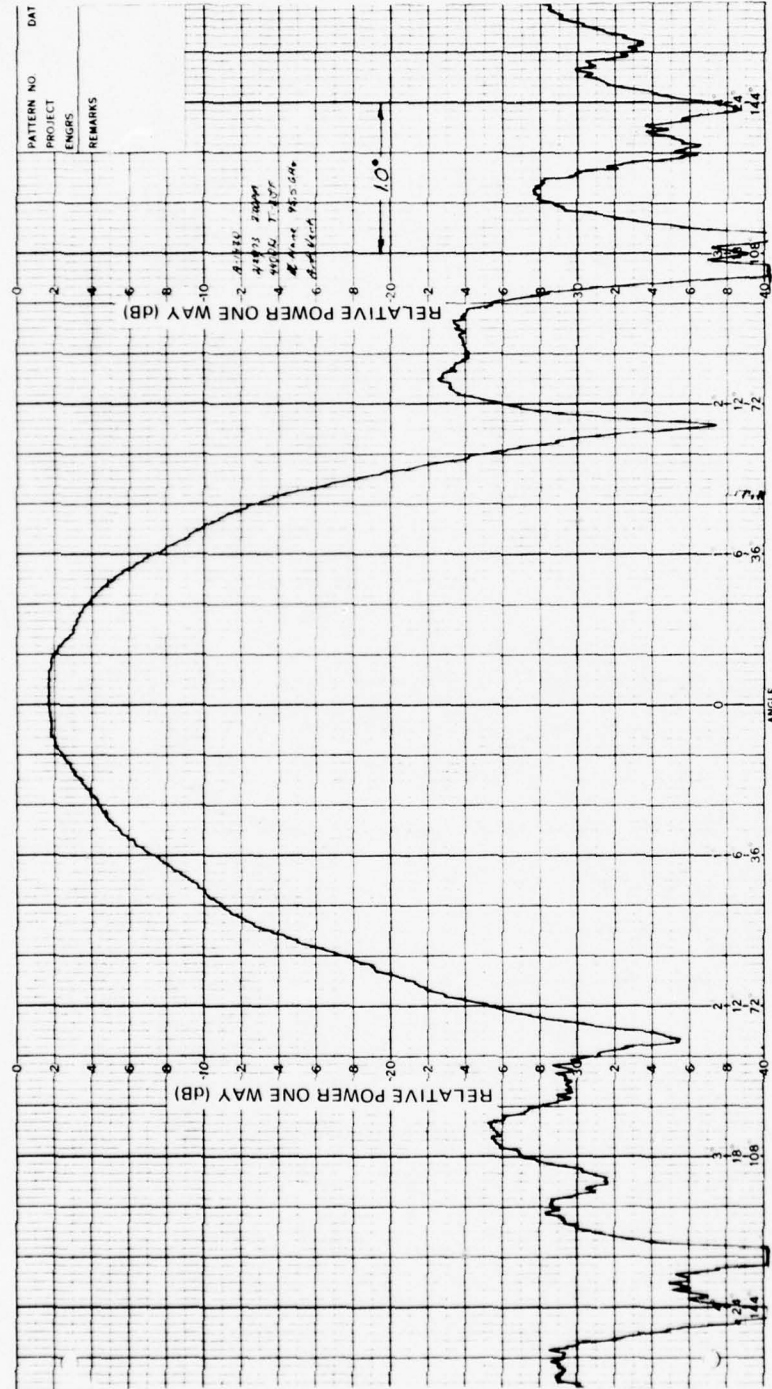


FIG. 53 EXPANDED E-PLANE ANTENNA PATTERN AT 95.5 GHz ON 4400 FOOT RANGE WITH TEMPERATURE AT -20°F

THE JOHNS HOPKINS UNIVERSITY
APPLIED PHYSICS LABORATORY
LAUREL, MARYLAND

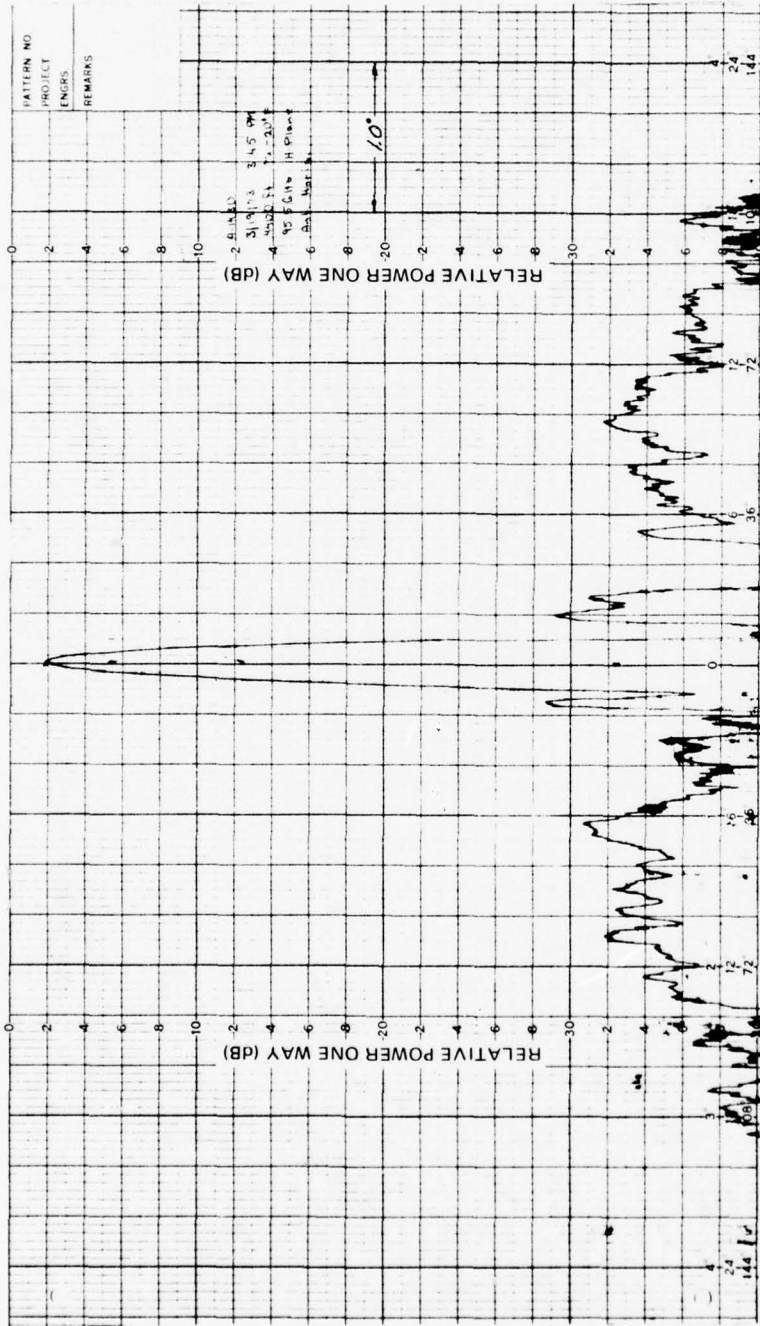


FIG. 54 EXPANDED H-PLANE ANTENNA PATTERN AT 95.5 GHz ON 4400 FOOT RANGE WITH TEMPERATURE AT -20°F

Table 12

Gain, Beamwidth, and Sidelobes at 50°F and at 2-1/8 mi Range

Frequency (GHz)	Gain (dBi)	Beamwidth (deg)		Sidelobe Level (dB)	
		H Plane	E Plane	H Plane	E Plane
95.0	48.9	0.11	1.49	-28.2	-22.0

Table 13

Gain, Beamwidth, and Sidelobes at 55°F and at 1000-ft Range

Frequency (GHz)	Gain (dBi)	Beamwidth (deg)		Sidelobe Level (dB)	
		H Plane	E Plane	H Plane	E Plane
95.0	47.6	0.15	1.45	-27.0	-21.0

Table 14

Gain, Beamwidth, and Sidelobes Averaged over Frequency at
4400-ft Range

Temperature (°F)	Measured Gain (dBi)	Corrected Gain* (dBi)	Beamwidth (deg)		Sidelobe Level (dB)	
			H Plane	E Plane	H Plane	E Plane
-20	49.8	51.8	0.11	1.47	-26.2	-20.3
0	50.4	51.6	0.11	1.47	-26.1	-20.7
+70	51.3	51.3	0.11	1.47	-27.0	-20.7

*Gains measured with heavy frost on both the line-source radome and on the parabolic-cylinder reflector have had 2 dB added to them.

Table 15

Gain, Beamwidth, and Sidelobes Averaged over Temperature and Frequency at 4400-ft Range

Measured Gain (dBi)	Corrected Gain (dBi)	Beamwidth (deg)		Sidelobe Level (dB)	
		H Plane	E Plane	H Plane	E Plane
50.5	51.6	0.11	1.47	-26.4	-20.5

beamwidth of 0.11° . The reason for the beam broadening became apparent when the aperture of the antenna was probed. Instead of 16 dB, the antenna had a 30-dB edge taper. Measurements on the primary feed showed that its H-plane aperture was too large, since it produced better than a 25 dB edge illumination (-22 dB feedhorn taper, plus -3 dB path loss). The exact level of the feed radiation toward the edge of the parabolic reflector was uncertain because of multipath errors in the measurement setup. Thus the increased feed taper combined with the shorting plates at the edges of the reflector produced a greater taper than was anticipated.

Computer pattern calculations were made, assuming a 30-dB edge illumination to compare with experimental results. The predicted half-power beamwidth was 0.16° at 1000 ft, 0.11° at 4400 ft, and 0.11° at 2-1/8 mi, all in good agreement with the measured values. Since aperture blockage effects were not included in the predicted sidelobe levels, the measured values were somewhat higher than predicted.

It was deemed unnecessary to build another primary feedhorn having a smaller edge taper, since the beamwidth of the 100 in. aperture was adequate for the radar system.

Radome Characteristics

The 95-GHz antenna is protected from the hostile Arctic environment by a 13.4-ft diameter radome developed by ESSCO, Inc. The radome is a metal space-frame design, i.e., it consists of webbs of pseudorandomly placed metal members holding triangular shaped dielectric membranes (Fig. 55). The membrane material is Esscolam V, a strong dielectric with a dielectric constant of 2.8 and a loss tangent of 0.012 (at 95 GHz). The material thickness is $\lambda/2$ at 95 GHz. The membrane surface is coated with Tedlar to prevent water adherence. The metal members have a 0.35 in. \times 1.15 in. rectangular cross section with the long dimension toward the antenna. The longest member is 33.6 in. in length. The radome is designed to operate in 150-mph wind and over a temperature range of -65°F to +140°F. It will withstand an ice and snow load of 75 psf. A blower system prevents the formation of ice on the radome surface by circulating air within the radome.

Extensive tests were conducted on the antenna/radome combination. It was determined that the radome insertion loss was less than 1 dB as had been theoretically predicted. No boresight shift was detected, indicating that it was certainly less than 0.1 beamwidths, i.e., $< 0.01^\circ$. Changes in levels of 20 dB sidelobes were less than 1 dB; of 25 dB sidelobes less than 3 dB; and of 30 dB sidelobes, 5 dB (Fig. 56). Extensive stress and thermal analyses indicated conservative mechanical design.

THE JOHNS HOPKINS UNIVERSITY
APPLIED PHYSICS LABORATORY
LAUREL, MARYLAND

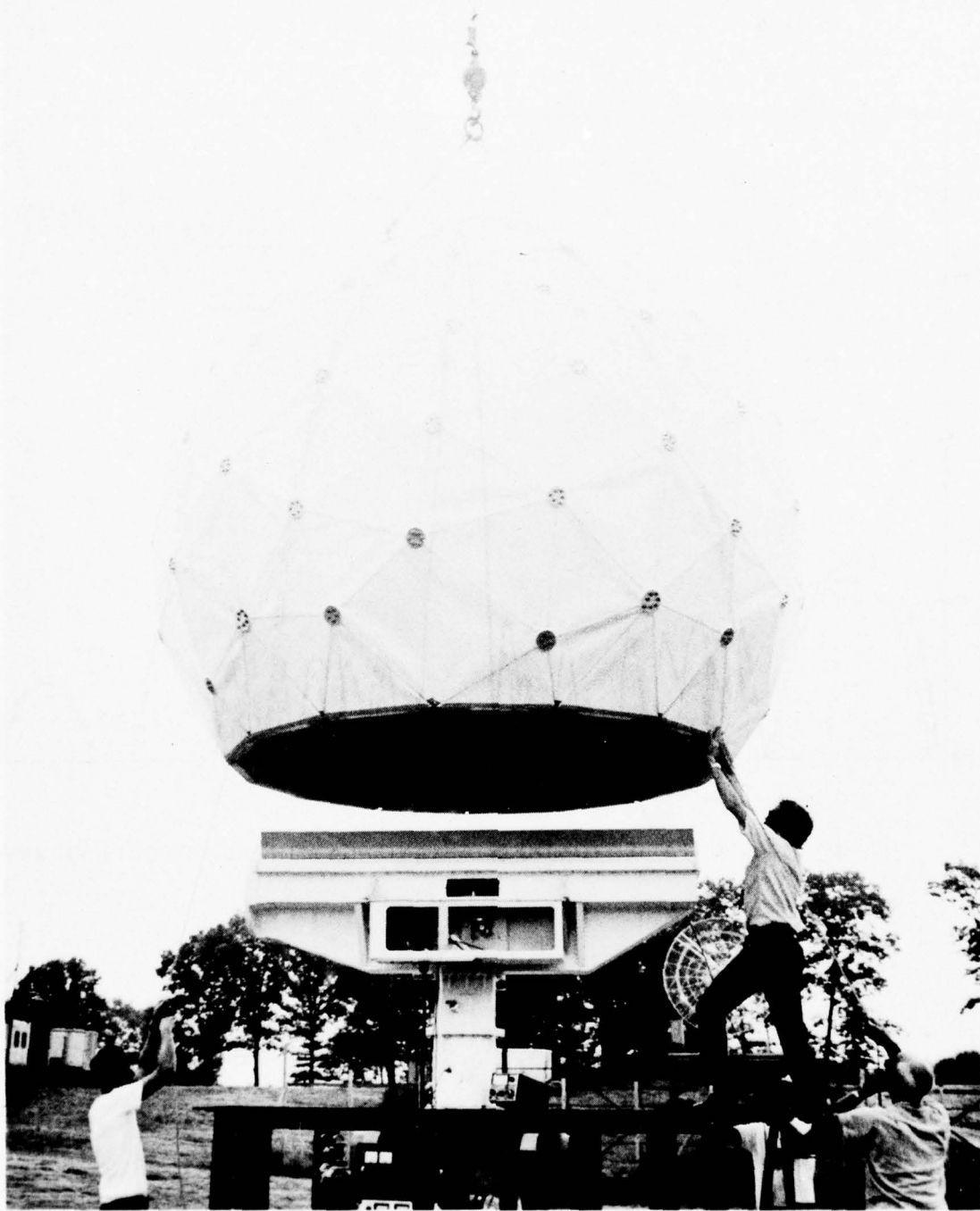


FIG. 55 RADOME FOR THE 95-GHz ANTENNA

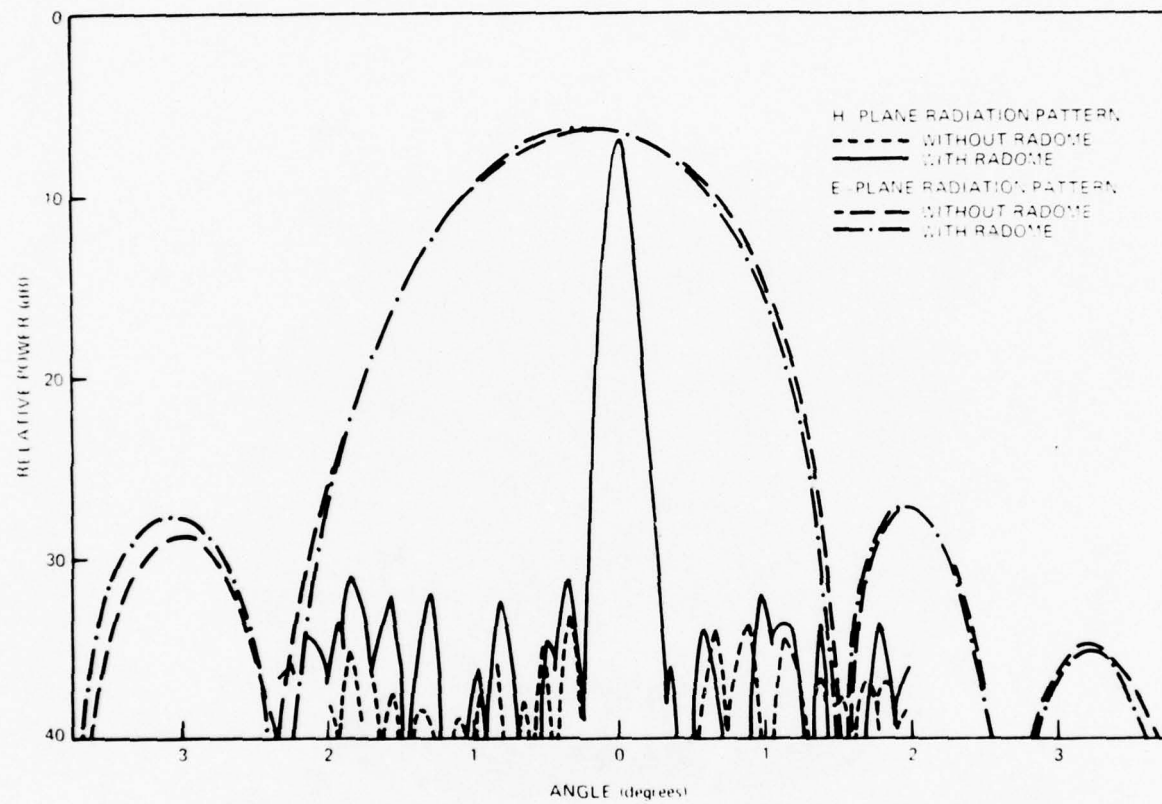


FIG. 56 RADIATION PATTERN OF THE 95-GHz ANTENNA WITH AND WITHOUT RADOME

ANTENNA SUPPORT AND DRIVE ASSEMBLY

Two methods for measuring the height of an obstacle utilizing a 95-GHz radar antenna with a fan beam of $0.1^\circ \times 1.0^\circ$ at the 3-dB points were considered. One method required mounting the antenna to produce a beam 0.1° wide $\times 1.0^\circ$ high; the other method required remounting the antenna to produce a beam 1° wide $\times 0.1^\circ$ high. In both cases, the positional accuracy of the beam centerline in elevation had a total error budget of ± 145 urad due to the large turning radius of the SEV. In turn, the turning radius of the SEV required knowledge of the terrain obstacles at a range of 5 km where the uncertainty of the triangulated height measurement of the obstacle could not exceed a half skirt height. In order to navigate, a knowledge of the terrain full circle was required. Thus the innermost axis of rotation was in train, which required a design that used slip rings and in which the transmitter electronics were part of the innermost gimbaled mass.

To meet the high accuracy requirements, the stable platform employed an inertial reference unit (IRU). The total stroke of the two outer gimbals, roll and pitch, was required to be a 20° -cone half-angle with soft stops to protect the electronic equipment. In addition, each gimbal was mass balanced about its gimbal axes. The two outer gimbals were the most complex because the antenna projected itself in one orientation about 10 ft above the axis of rotation. The accuracy requirement also dictated a servo loop bandwidth of high values, in turn requiring a first mechanical resonance of about 18 Hz including the counterweight.

Construction Approach

The complexity of the gimbal design necessitated that as much design time as possible be allocated to the gimbal. Accordingly, a parallel design effort was started on the following:

1. Radome,
2. Antenna,
3. Inertial reference unit, and
4. Stable platform gimbal system.

The stable platform gimbal order required was train/roll/pitch where the innermost axis is mentioned first. The train axis is referred to in this report as azimuth. The final plan was to construct a two-axis gimbal first with azimuth/elevation for Phase I experiments, and to convert to a three-axis stable platform with azimuth/roll/pitch for the Phase II experiments.

The three identical torque motors and associated power amplifiers were long-lead items and were ordered early in the program. Since they were identical, identical mechanical designs could be used for both roll and pitch, thus reducing design and fabrication time.

The housing for the radome and gimbal support was designed and fabricated to accommodate both Phase I and Phase II and to be adaptable for either Arctic or land tests.

Design Constraints and Tradeoffs

The error budget for absolute angular position of the innermost gimbal, namely the rotating antenna, greatly influenced the following design areas:

1. Transverse stiffness of main azimuth bearing,
2. Bearing selections,
3. Antenna interface flange, and
4. Mass balance required about its axis of rotation of each rotating element.

Transportability of the assembled experiment was a factor in determining the size of the radome and housing. The antenna size and the required gimbal stroke (20° -cone half-angle) with soft bumpers determined the size of the inner profile. These factors influenced the following:

1. Gimbal center relative to radome spherical center;
2. Moment arm available for counterweights;
3. Radome radius;
4. Antenna clearance to radome internal structure;
5. Physical space for limit stops;
6. Physical space for counterweights; and
7. Physical space for man entry, egress, and service.

Phase I Two-Axis Gimbal

The Phase I gimbal required a full-circle azimuth drive capable of erecting the azimuth axis parallel to local gravity,

using a precision level. It was also desired that the gimbal be capable of nodding $\pm 1^\circ$ in elevation, with a microradian angular position pickoff.

Azimuth Drive Bearing and Antenna Coupling Stiffness. The azimuth drive was allocated 70 μrad of the available 290 μrad in the error budget. This allocation required that the shaft coupling between the torque motor and the antenna be short, large in diameter, and webbed between alternate bolts.

Since it has been found that there is less bearing trouble where factory preloaded duplex bearings are used, a lightly pre-loaded low-friction duplex bearing was designed to be at the heart of the relatively stiff cone-shaped load path (Fig. 57). The 70- μrad deflection was allocated to the assembly, which required a flange-to-flange transverse stiffness of $7 \times 10^6 \text{ ft-lb/rad}$. The bearing chosen was a Kaydon model KG 160 BHOL, which is a back-to-back duplex ball bearing. In order to achieve stiffness and low friction, the mating parts were produced with a class-3 fit.

The transverse spring rate of the azimuth drive shaft and of the bearing assembly was measured by applying graduated torque loads to the antenna mounting flange and recording the angular deflection of the antenna and mounting flanges. The test assembly is shown in Fig. 58. A spring rate of $6.56 \times 10^6 \text{ ft-lb/rad}$ was measured (Fig. 59). The test employed the optical-lever principle to magnify the small angular deflections. A focusable laser was employed with a beamsplitter to yield two optical-levers each 66 ft long. The differential motion of the two optical levers represented the deflection of the shaft and bearing.

Azimuth Drive Bearing Seals. SEV Arctic operations impress the need for low-viscosity lubricants and seals against wind-driven snow and dirt. The bearings specified were of the low-friction, grease-plated, nonseal type. The azimuth drive was designed to have a closed environment on one side of the bearing, thus a seal was required on only one side. Prior experience has indicated that the Teflon-leaf seal is low friction and quite satisfactory. The bearing was protected by an overhanging disk and, on both sides, by a close-running clearance shield (Fig. 60).

Azimuth Drive Shaft Weldment. A major design goal was to achieve the highest possible first torsional resonance; this leads to compactness and lighter weight. The first, or lowest, torsional resonant mode determines the maximum servo bandwidth that can be achieved without special notch filtering.

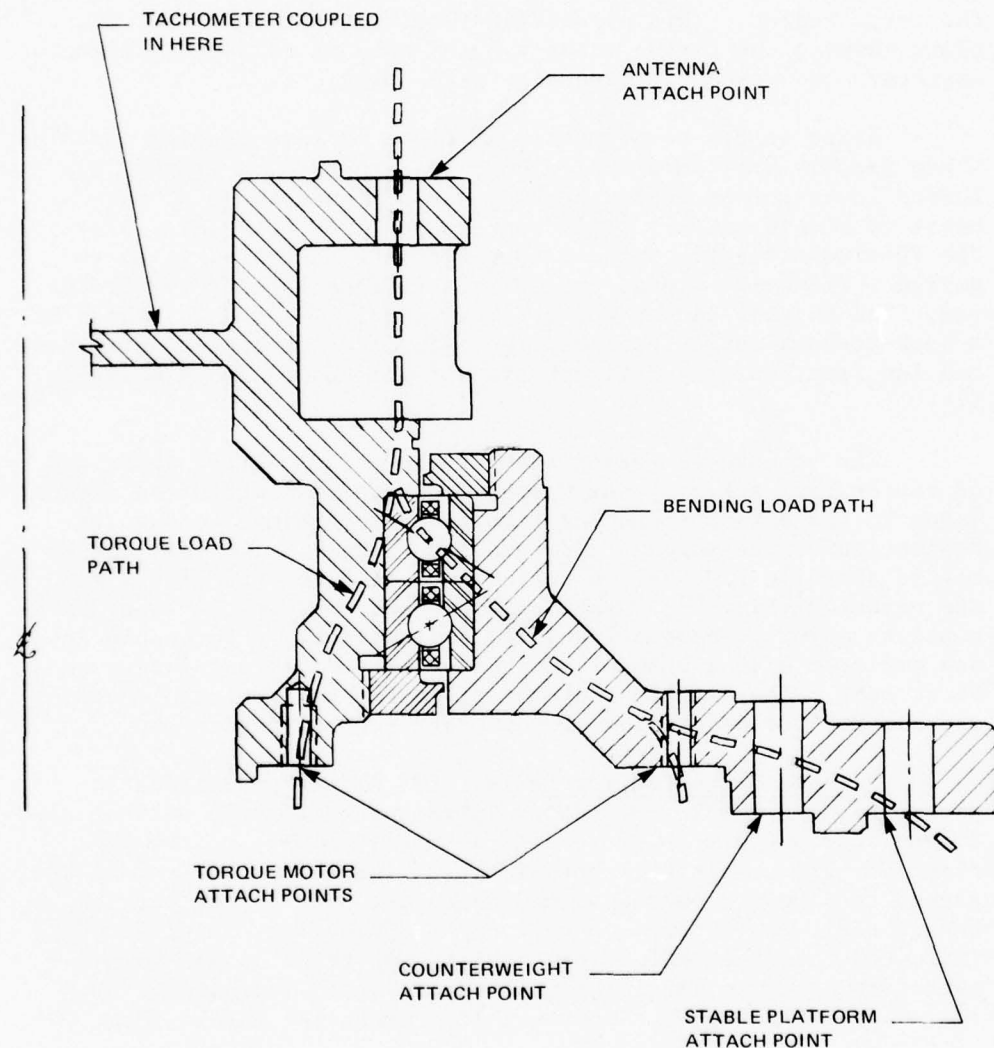


FIG. 57 AZIMUTH DRIVE BENDING LOAD AND TORQUE FLOW PATH

THE JOHNS HOPKINS UNIVERSITY
APPLIED PHYSICS LABORATORY
LAUREL, MARYLAND

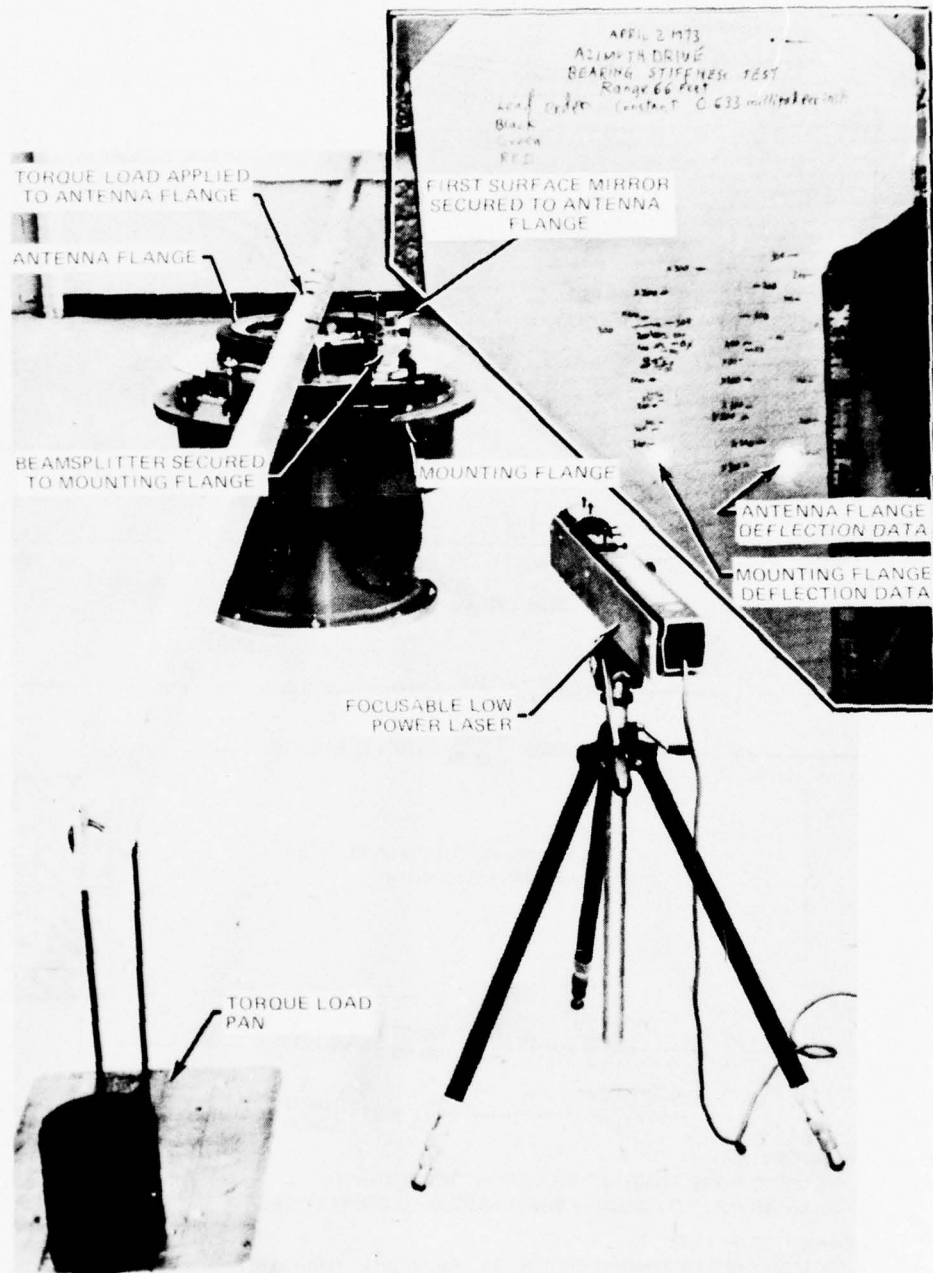
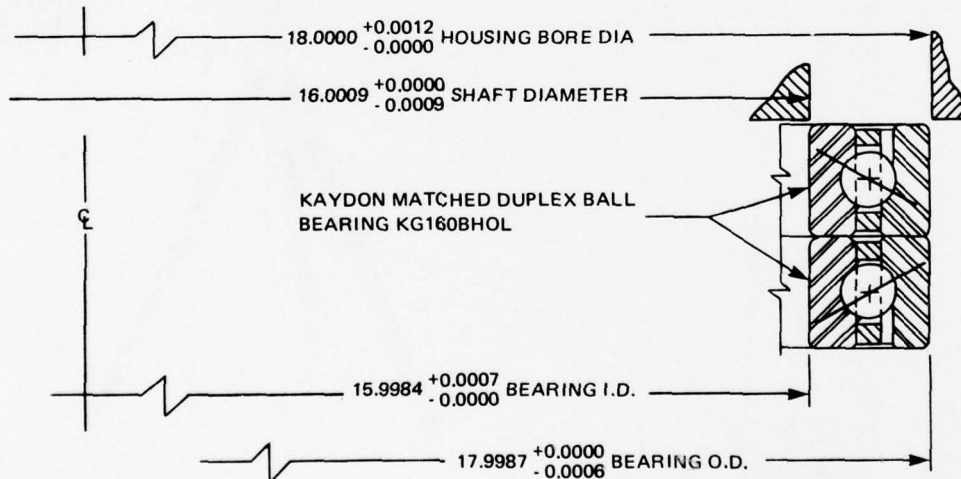
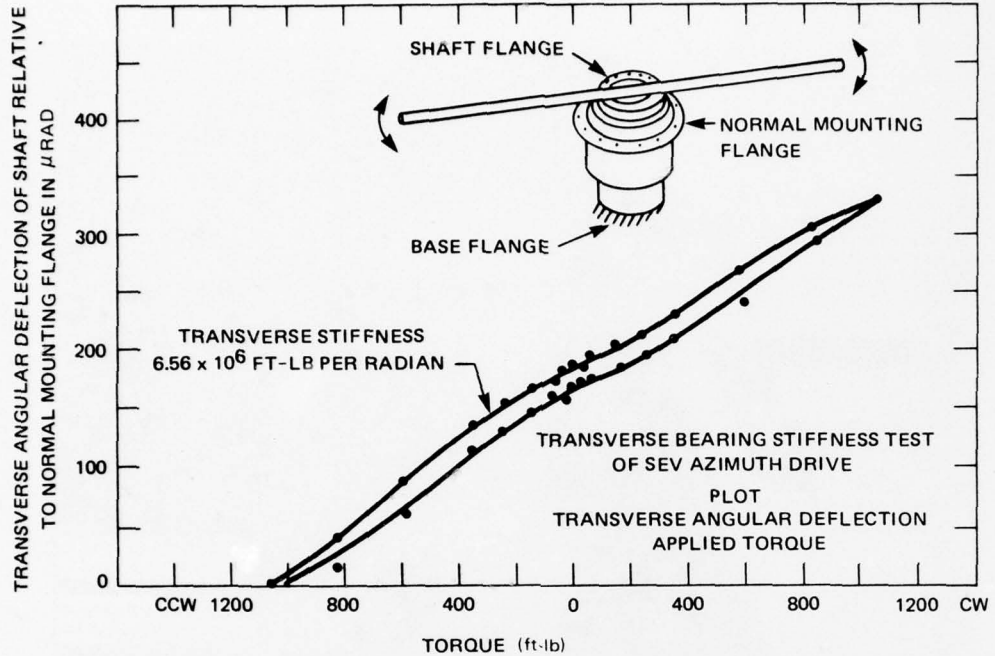


FIG. 58 AZIMUTH-DRIVE STIFFNESS TEST



RESULTANT FIT:

BEARING BORE TO SHAFT + 0.0009 TO 0.0025 TIGHT
BEARING O.D. TO HCUSING BORE = 0.0010 TO 0.0031 LOOSE

BEARING STIFFNESS:

DESIGN CENTER TRANSVERSE STIFFNESS 7.0×10^6 ft-lb/rad
MEASURED TRANSVERSE STIFFNESS 6.56×10^6 ft-lb/rad

FIG. 59 AZIMUTH BEARING FIT-AND-STIFFNESS TEST

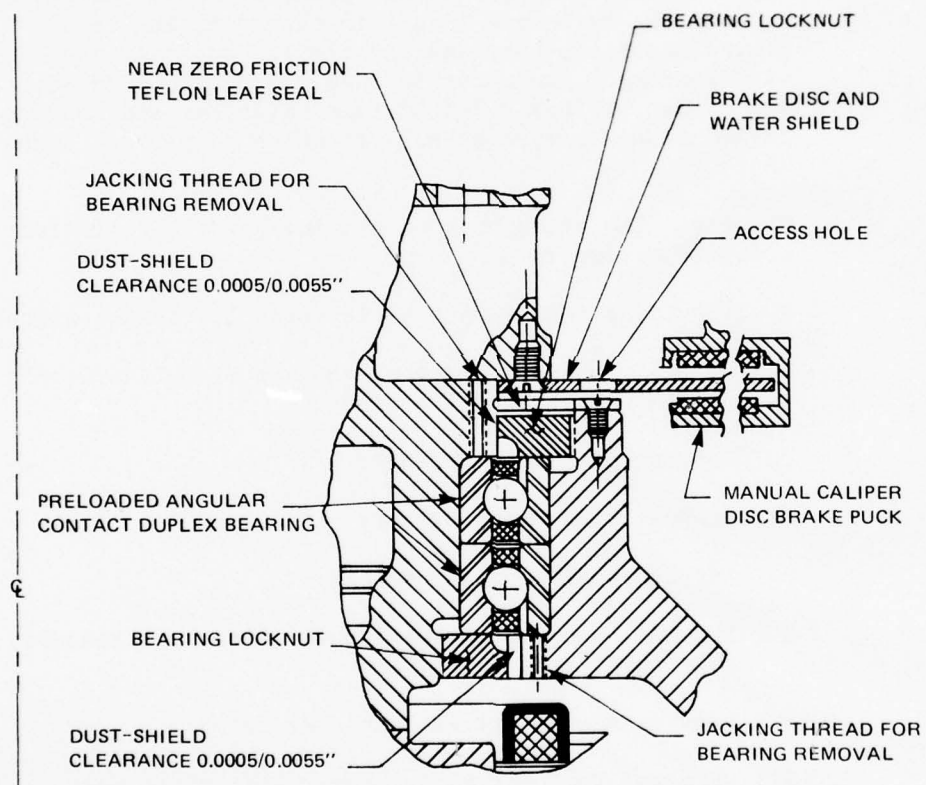


FIG. 60 AZIMUTH-DRIVE BEARING SEAL ARRANGEMENT

High stiffness can best be maintained in solid structures; however, machining from a solid billet was not practical. To maintain the stiffness required and avoid welding warpage, close fitting premachined pilots were used in a three-piece weldment (Fig. 61). This design enabled most of the machine work to be accomplished on relatively light parts. The design also allowed critical lathe machining to be done from one side.

Azimuth Drive Assembly. The azimuth drive assembly components are shown in Fig. 62.

1. Torque Motor: The torque motor, a Magnadyne, Inc. 300 ft-lb permanent magnet motor (Appendix A) was selected to meet the estimated torque in the event the radome proved unsatisfactory and the gimbal had to withstand wind loading. The motor is face mounted on both stator and rotor. It has a 2-ft outside diameter and has a 13-in.-diameter through-hole in which to package components.
2. Housing: The azimuth drive housing has the following design functions:
 - a. Provide a total dust shield for all internal parts;
 - b. Be stiff enough to support 850 lb of counterweight at a high resonant frequency;
 - c. Support slip ring brushes;
 - d. Support tachometer stator;
 - e. Support shaft encoder stator;
 - f. Provide access holes with dust covers for assembly of all internal parts; and
 - g. Provide an electrical connector panel.
3. Slip Rings: The control and power slip rings were located inside the torque motor. Since assembly is nearly inaccessible, a key design feature allowed the brush-block holders to maintain uniform brush pressure on all slip rings and to position the brushes without lateral rubbing. This was achieved by utilizing circular pilots and axial slide grooves for positioning the brush rigging (Fig. 63).

THE JOHNS HOPKINS UNIVERSITY
APPLIED PHYSICS LABORATORY
LAUREL, MARYLAND

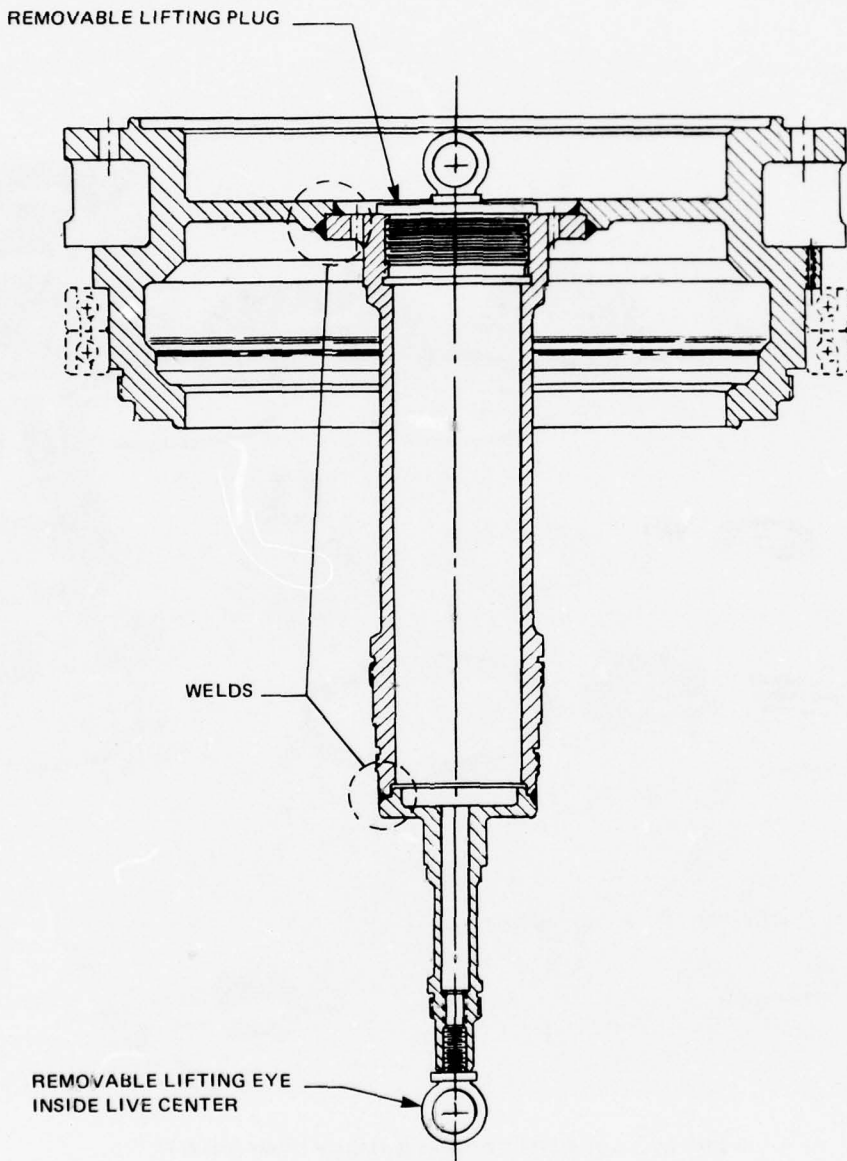


FIG. 61 AZIMUTH DRIVE-SHAFT-SHOULDER WELD PREPARATION

THE JOHNS HOPKINS UNIVERSITY
APPLIED PHYSICS LABORATORY
LAUREL, MARYLAND

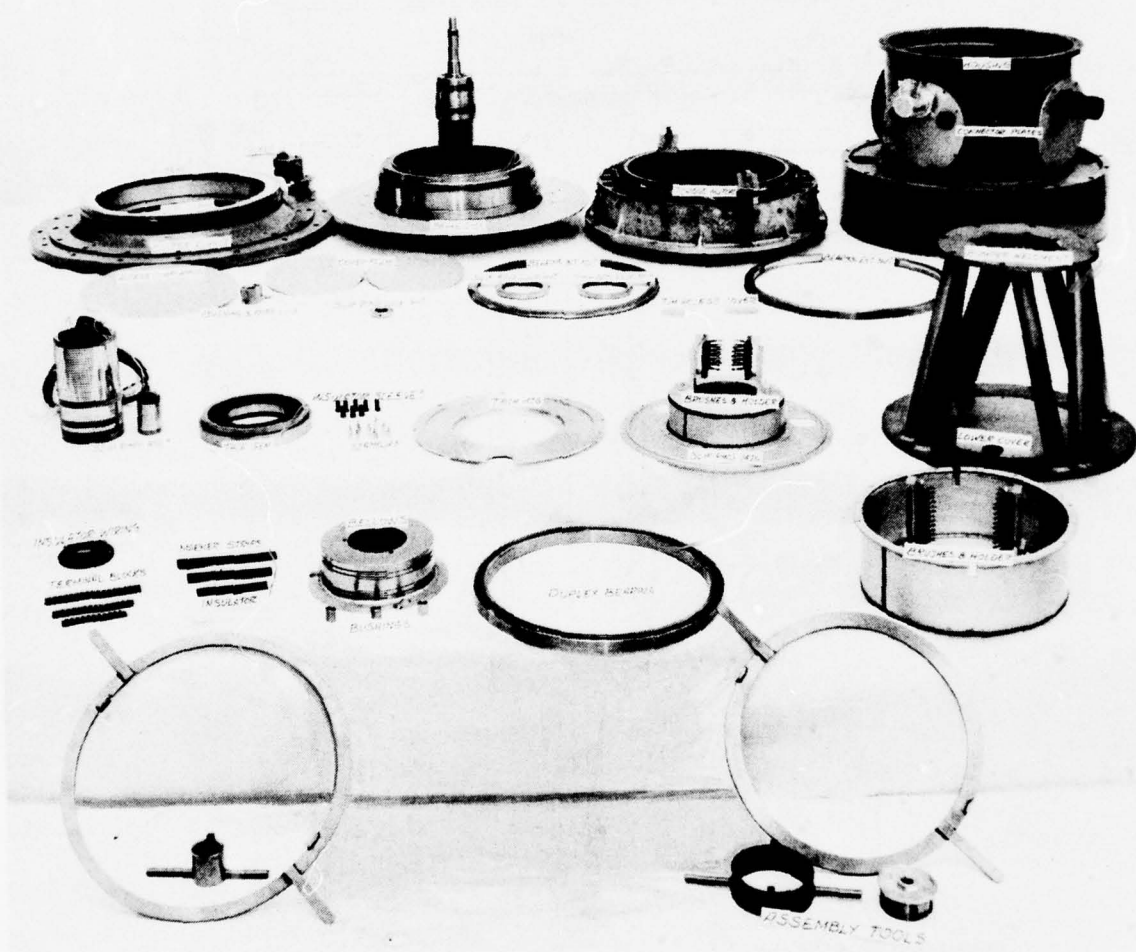


FIG. 62 AZIMUTH DRIVE-ASSEMBLY COMPONENTS

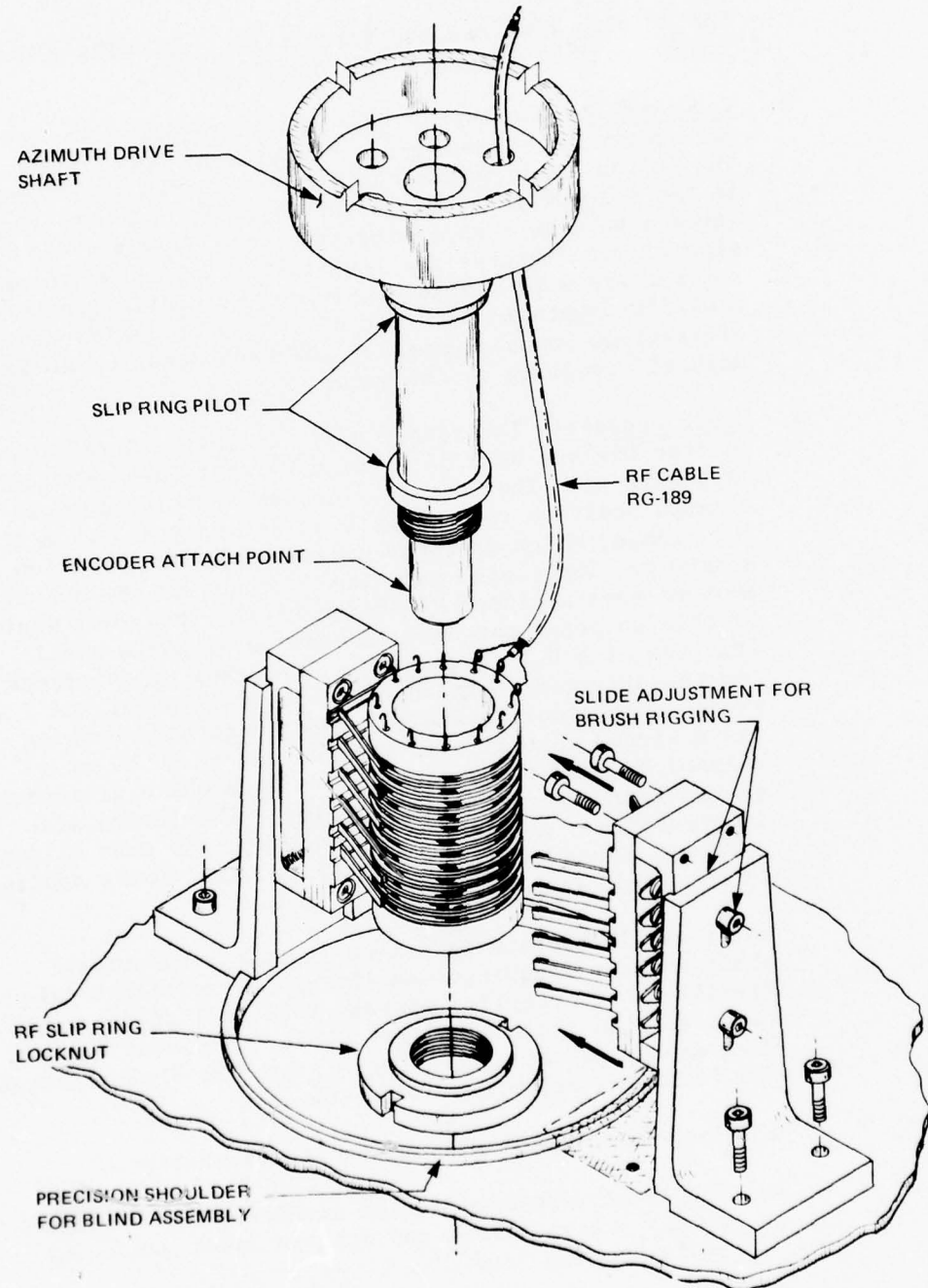


FIG. 63 EXPLODED VIEW OF RF SLIP RING ASSEMBLY

The power slip ring was modified by the manufacturer to protect against high-voltage arcing. Two groups of high voltage rings at 3000 volts were isolated by skipping several rings.

The RF slip ring was modified at APL, allowing a design improvement in the RF shielding (Fig. 64).

4. Tachometer: Tachometer feedback is required in precision servo loops such as in the present application. The Inland Motor Corporation Model TG 5723 was chosen; it has a low wire-breakage rate with No. 40 wire that gives a voltage sensitivity of 11.6 V/(rad/s). The significant features are low ripple (0.2% peak to peak) and magnets with a stable temperature coefficient of 0.01%/°C (Appendix A). One of the major design considerations was placement of the tachometer to avoid magnetic coupling to the motor.
5. Shaft Encoder: The rotary shaft encoder selected was an Itec Digisec RA16/55(S) with 2¹⁶ bits per revolution (Appendix A). The unit provided absolute whole-word azimuth position readout with an accuracy of 0.5 m at 5-km range, which is commensurate with the elevation accuracy. The choice was also dictated by the requirement to have a closed digital-position loop that would be able to point the antenna beam to within a small fraction of a 0.1° beamwidth. The level of tolerance for the selected shaft encoder was 10 lb axial and 7 lb radial. In order to achieve this, a special housing was designed that allowed the two shafts to be misaligned by many thousandths of an inch while achieving extremely rigid torsional coupling. The design also incorporated a unique two-way housing lock that allowed complete assembly with no radial or axial loads applied to the shaft encoder.

The flexible housing is unique in that conventional shaft encoder mountings usually employ a bellows-like flexible shaft coupling whereas this application employs a rigid shaft coupling. This inside-out design, when employing the unique two-way housing lock, allowed the following major improvements:

- a. The shaft length was substantially shorter;
- b. The large-diameter flexing members allowed longer spring elements that can achieve lower axial and radial spring rates;

THE JOHNS HOPKINS UNIVERSITY
APPLIED PHYSICS LABORATORY
LAUREL, MARYLAND

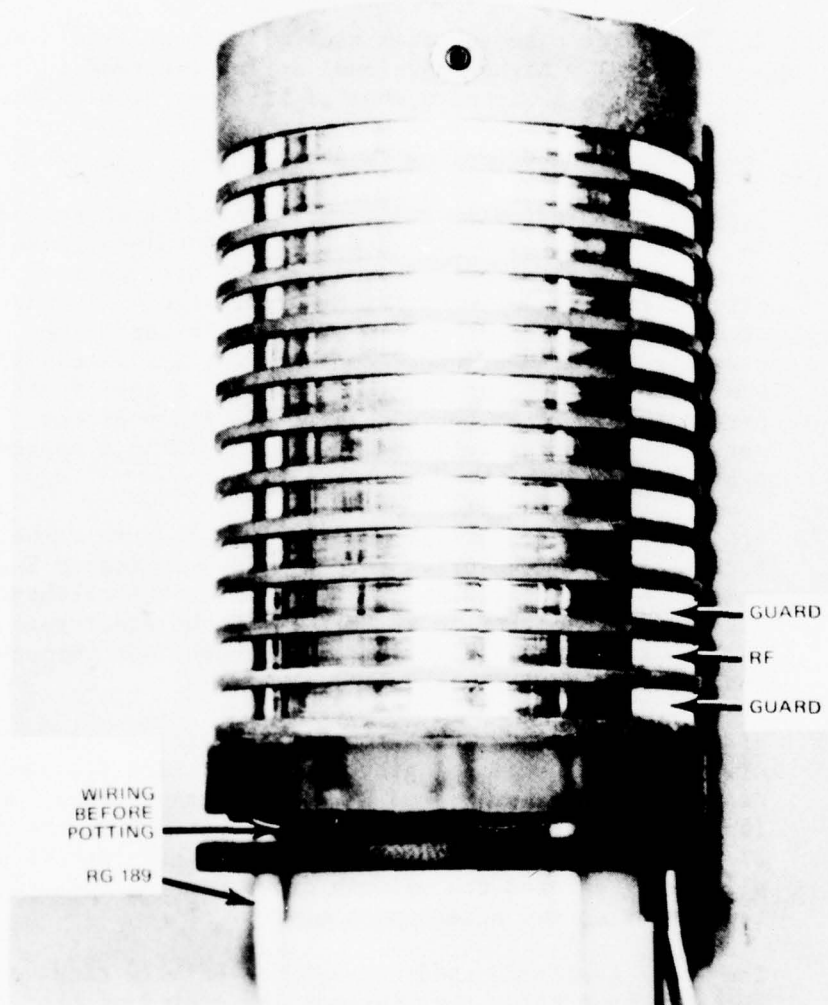


FIG. 64 RF SLIP-RING ASSEMBLY AS MODIFIED FOR IMPROVED SHIELDING

- c. The lower axial and radial spring rates allowed greater tolerance for shaft runout;
- d. Greater shaft runout tolerance equated to lower cost;
- e. Greater shaft runout tolerance extended the accuracy of digital systems to a greater number of bits per revolution; and
- f. The large-diameter flexible cylinder allowed a substantially higher torsional spring constant in consort with a higher number of bits per revolution.

The design of the housing is shown in Figs. 65 and 66.

- 6. Brakes: The test plan called for a nodding experiment in which azimuth was positioned and maintained locked in position. It was also essential to provide restraint for equipment during transportation. In the azimuth drive a disk brake proved doubly useful because it provided a shield against dust and liquid for the main bearings and locking as well. A set of caliper brakes designed for use on recreation vehicles served the purpose well and functioned with no appreciable backlash.
- 7. Armature Temperature: To monitor the armature temperature of the azimuth drive torque motor, a Victory Engineering Corp. Model 32A-13 #9 thermistor was calibrated and installed on the inner surface of the armature. The leads were secured by RTV and brought out through the upper slip ring assembly.
- 8. Wiring Provisions: The azimuth drive wiring was divided into functional groups, namely, high voltage, digital signal, power, and RF. These groups were kept isolated by cable runs and separate connectors. To implement portability and maintain dust-tight integrity, all wiring entered the azimuth drive housing through connectors on two access-port covers.

The leads that traversed through the RF slip ring were shielded by passing them through the center of the steel shaft and terminating them in BNC connectors atop the shaft. The other wires from the slip ring assembly were passed through special antichafing dielectric grommets to terminal boards in the recess atop the antenna flange.

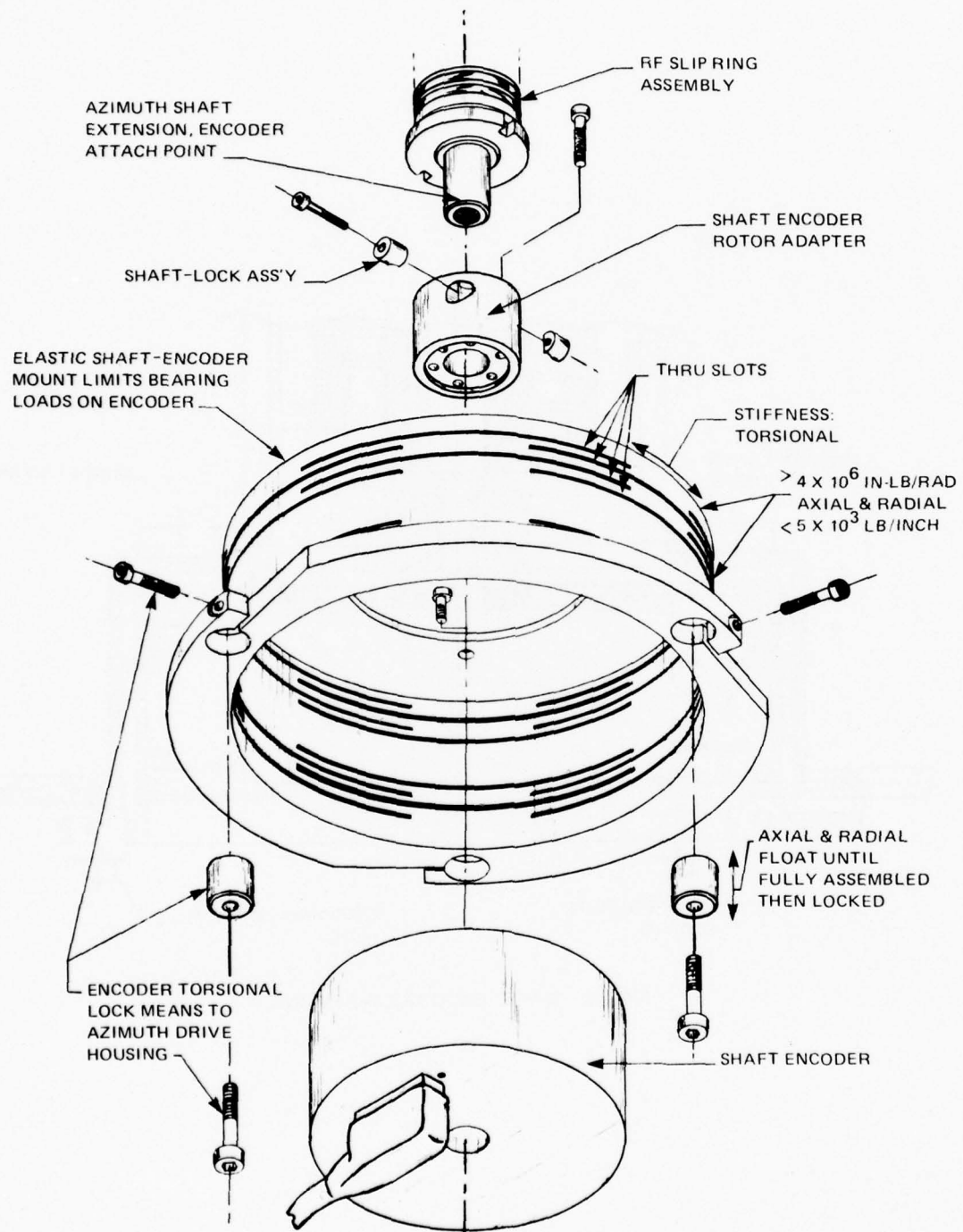


FIG. 65 EXPLODED VIEW OF SHAFT-ENCODER MOUNTING THAT PROVIDES
TORSIONAL RIGIDITY WHILE NOT IMPOSING RADIAL OR AXIAL BEARING
LOADS ON ENCODER IF DRIVE-SHAFT RUNOUT EXISTS

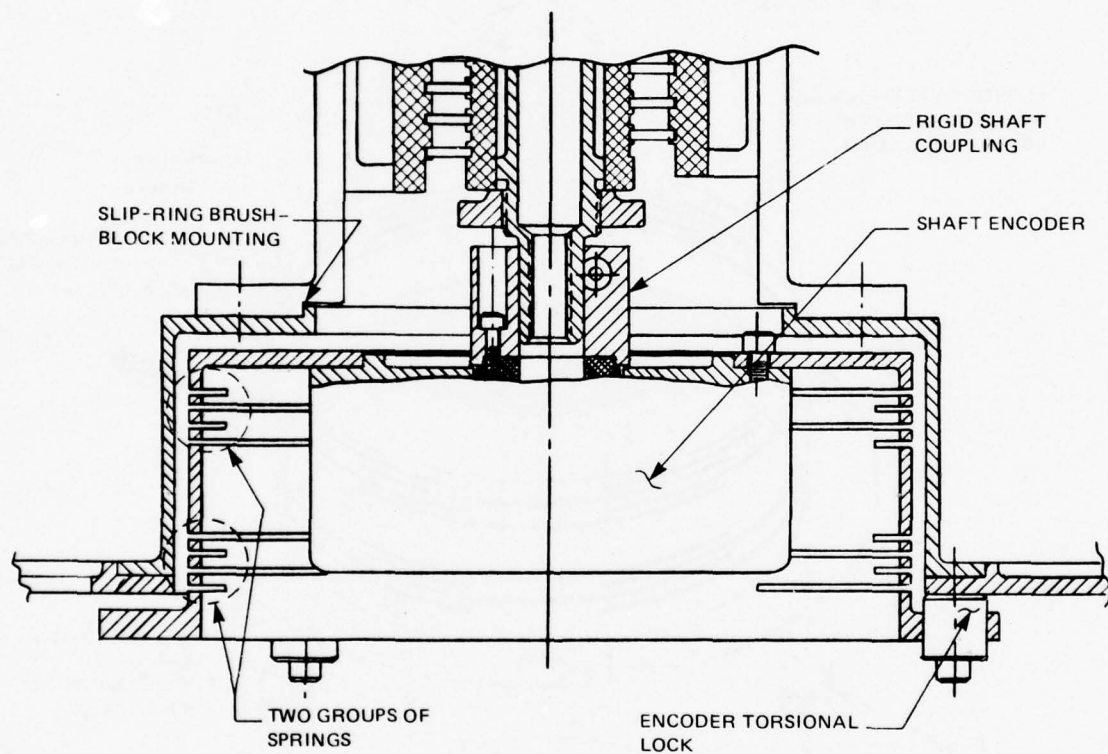


FIG. 66 SHAFT-ENCODER MOUNTING

THE JOHNS HOPKINS UNIVERSITY
APPLIED PHYSICS LABORATORY
LAUREL, MARYLAND

9. Friction: Friction measurements as taken at various times during construction, were as follows:

Bearing assembled:

Running - 8.4 in.-lb
Starting - 21.0 in.-lb (max)

Bearing plus torque motor:

Starting - 42.0 in.-lb

Bearing, torque motor, slip ring, tachometer:

Starting - 52 in.-lb

Azimuth drive fully assembled, average of 16 readings, horizontal axis:

Starting - 58 in.-lb CW
Starting - 64 in.-lb CCW
Running - 52 in.-lb both ways

Azimuth drive fully assembled without antenna, vertical axis:

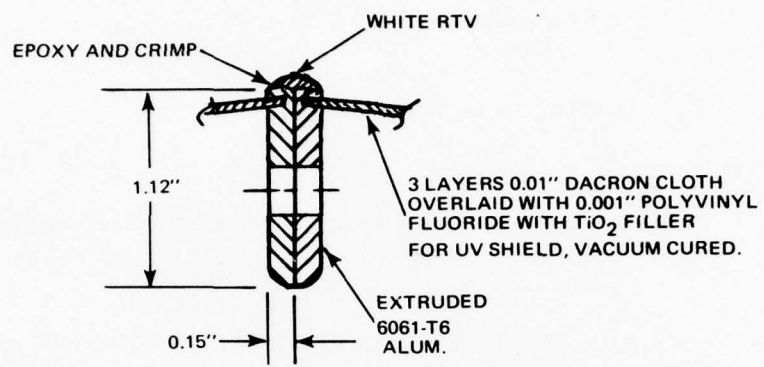
Starting - 57 in.-lb

Azimuth drive with horizontal antenna, vertical axis:

Starting - 72 in.-lb (max)
50 in.-lb (min)
Running - 54 in.-lb

Antenna Mechanical Interface. The antenna interface was designed so the long dimension could be mounted either horizontally or vertically (i.e., the narrow beamwidth could be positioned vertically or horizontally). In either case the antenna required a 2-in. clearance from the radome inner structure with ± 20 -degree roll and pitch excursions during azimuth scanning. The webs of the radome triangular panels were of different lengths (Fig. 67) and this, in addition to radome flexing under wind loads, result in clearance variation.

The radome clearance control diagram is shown in Fig. 67. The weight (587 lb) of the antenna assembly at a lever arm of about 5 ft above the gimbal center created considerable unbalance, which



SECTION THRU TYPICAL WEBS

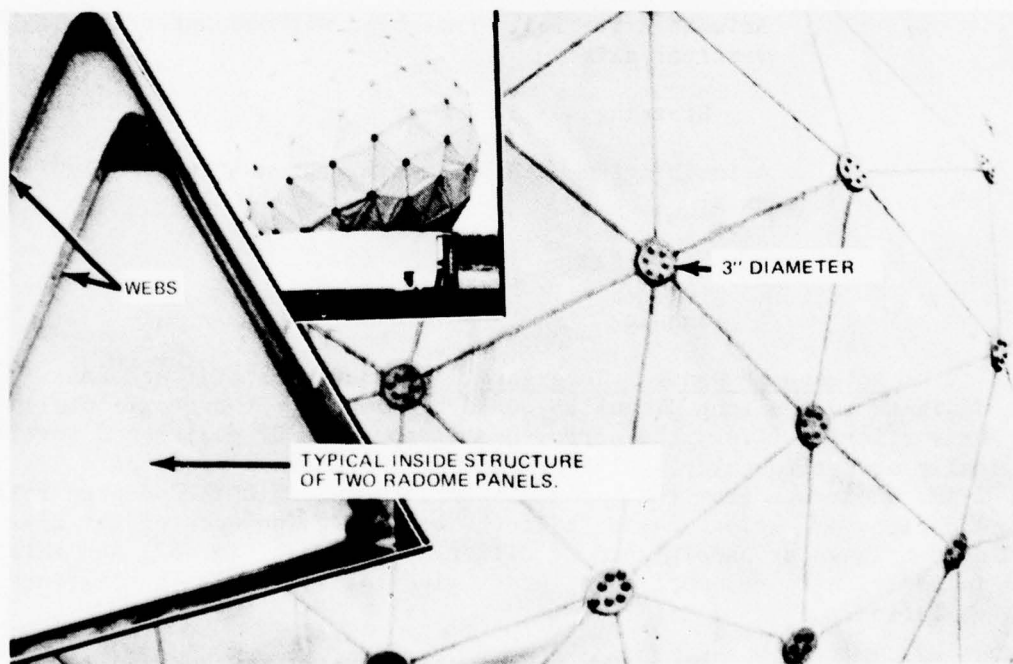


FIG. 67 RADOME PANEL CONSTRUCTION

was counteracted by placing the gimbal center as high as possible relative to the azimuth drive mounting platform. The remaining moment was balanced by using more than 800 lb of lead counterweight. This amount of counterweight placed a severe restraint on the available space beneath the gimbal.

Due to the fragile nature of the 95-GHz magnetron and plumbing, soft 1-g bumpers were used as shown in Fig. 68. Also shown is an automobile tire, the inflation of which is controlled to regulate the impact load of running into the gimbal stops.

The vertical antenna configuration required that an irregular L-shape be adapted to the circular drive flange (Fig. 69). The thickness of the adapter was critical to the antenna/radome clearance; the thicker the adapter, the more limited the gimbal angle. For each pound added, about a half-pound of counterweight was required; the adapter weighed 45 lb. The adapter had to have great transverse stiffness in order to assure the required high resonant frequency.

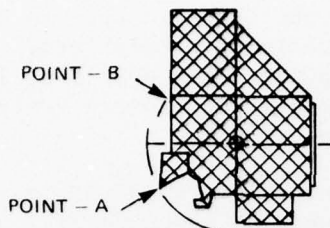
The adapter for the horizontal antenna configuration was required to adjust the height of the radar aperture to pass between the corners of the radome space frame as well as to adjust for 6.3 in. of center-of-gravity shift. The stiffness was maintained by constructing the adapter as a parallelepipedon skewed on one side and heavily buttressed. The adapter weighed 61 lb.

Antenna/Azimuth Drive Transverse Resonance Test. A basic goal in the SEV platform design was a high mechanical resonance, that goal being a 4-Hz servo bandwidth to maintain the desired platform accuracy.

The first mode bending frequency of the antenna when mounted on the azimuth drive was measured by the apparatus shown in Fig. 70. A shaker, providing 25 lbf and acting through a tubular stinger necked at both ends, drove the antenna. An orthogonal pair of accelerometers was used as the pickoff. The fundamental frequency was determined by observing Lissajous patterns of input versus pickoff on an oscilloscope. The antenna consists of a system of distributed springs and masses; however, these are in series with the antenna adapter and the azimuth drive transverse stiffness of the bearing. The resultant frequencies were 10.1 and 11.5 Hz (Fig. 71). Total weight of the antenna, electronic package, and adapter under test was 587 lb.

Azimuth Drive Mounting Platform. The main requirement for the azimuth drive housing was stiff support of the azimuth drive for two different gimbal designs: first, a two-axis gimbal with

THE JOHNS HOPKINS UNIVERSITY
APPLIED PHYSICS LABORATORY
LAUREL, MARYLAND



**ANTENNA
PLAN VIEW**

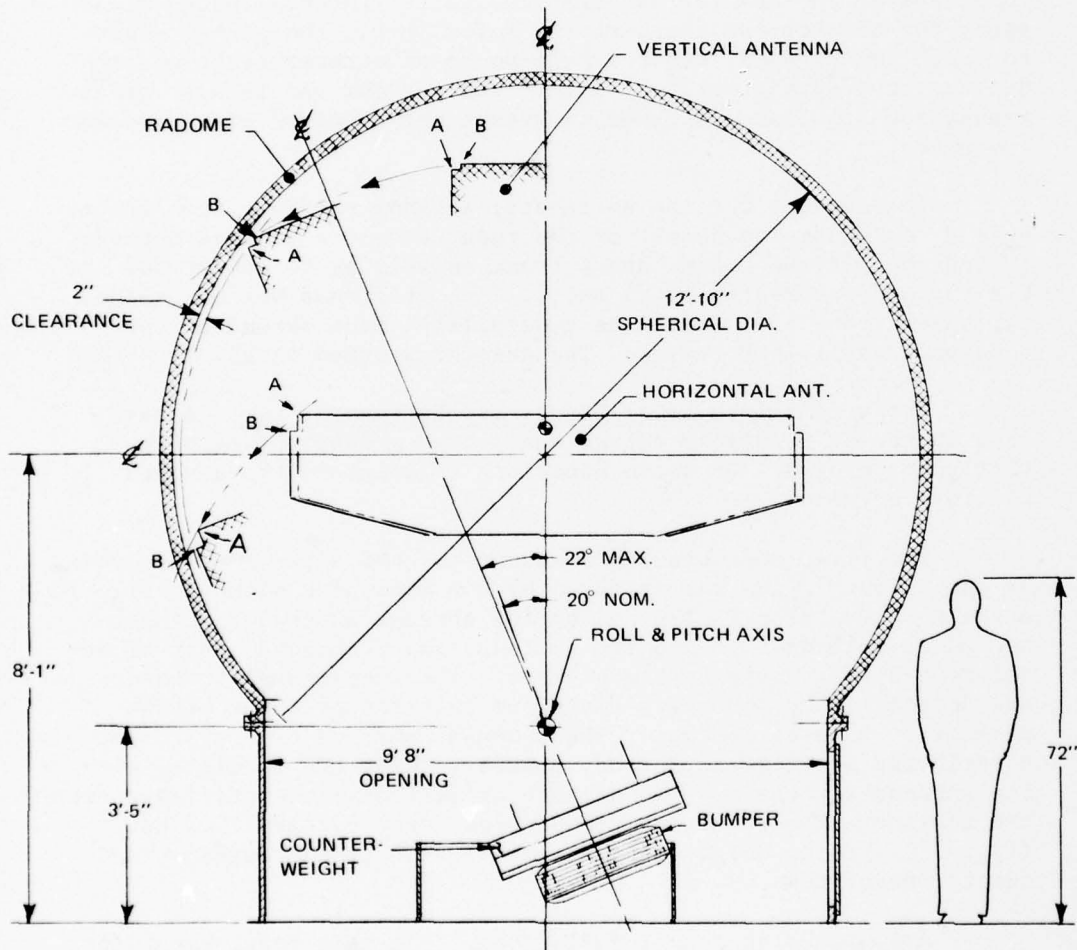


FIG. 68 RADOME/ANTENNA CLEARANCE DIAGRAM

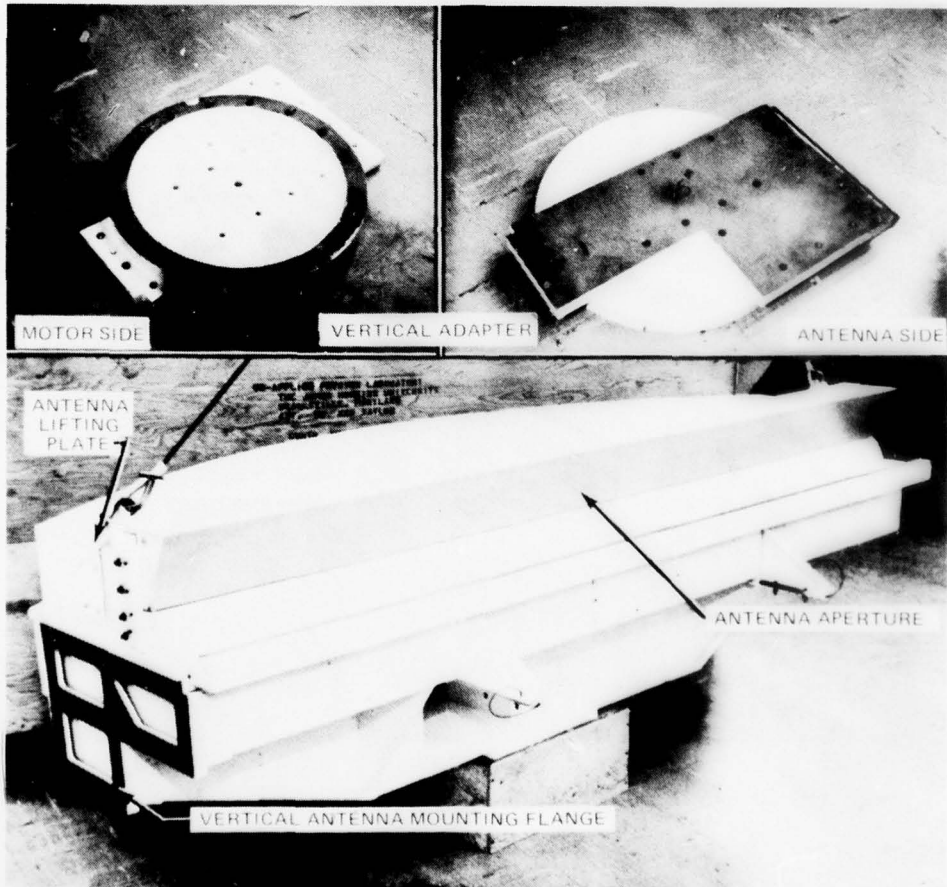
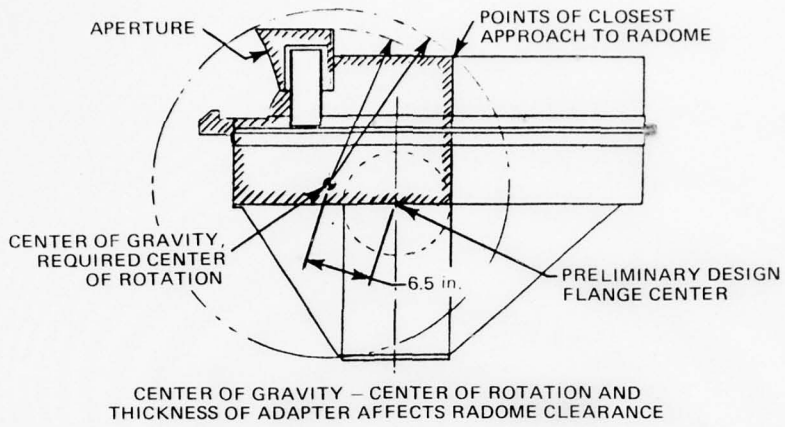


FIG. 69 VERTICAL ANTENNA-MOUNTING ADAPTER PLATE

THE JOHNS HOPKINS UNIVERSITY
APPLIED PHYSICS LABORATORY
LAUREL, MARYLAND



FIG. 70 ANTENNA/AZIMUTH DRIVE RESONANT FREQUENCY TEST

THE JOHNS HOPKINS UNIVERSITY
APPLIED PHYSICS LABORATORY
LAUREL, MARYLAND

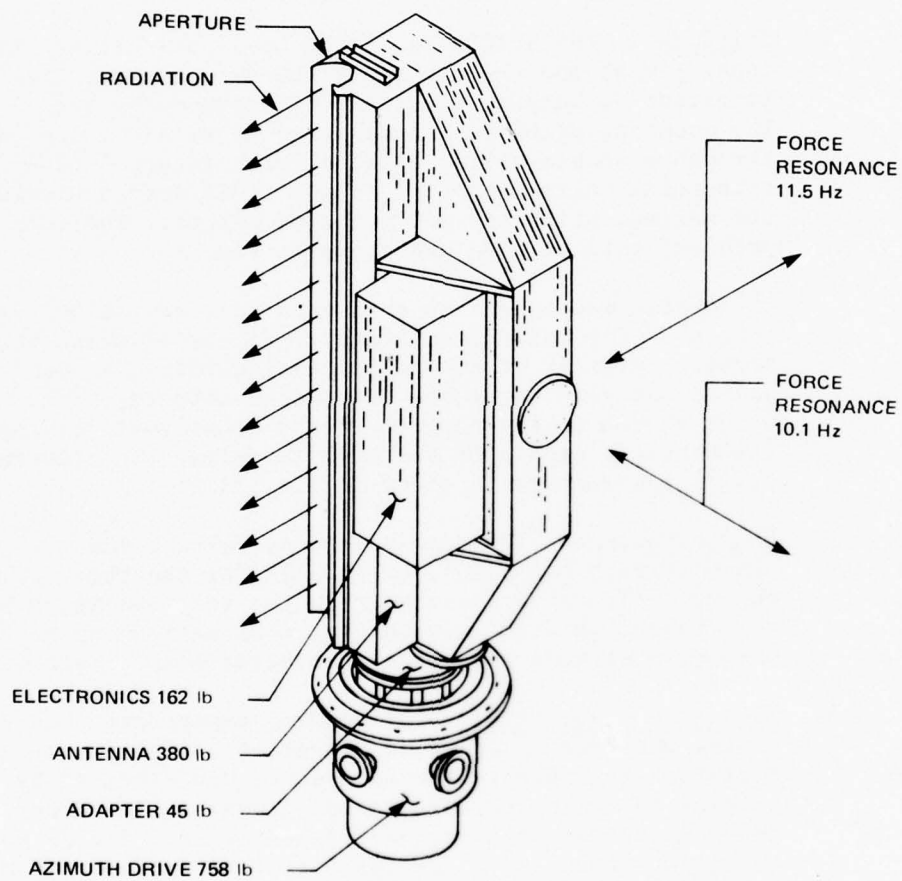


FIG. 71 ANTENNA/AZIMUTH DRIVE MEASURED RESONANT FREQUENCIES

the order azimuth/elevation, where the elevation stroke was $\pm 5^\circ$; and second, a three-axis inertially stabilized gimbal with the order azimuth/roll/pitch, with $\pm 20^\circ$ amplitude in both roll and pitch. The secondary requirements were to provide (a) as much counterbalancing effect by useful structural members as possible; (b) an elevation-drive capability; (c) a rigid elevation-lock capability; (d) an elevation-position pickoff with microradian accuracy; (e) the volumetric space and mounting pads for an inertial reference unit; (f) attachment means so that the azimuth drive mounting platform could become the middle ring of a three-axis gimbal; and (g) precision level mounting pads.

1. Stiffness: The stiffness of the load path between the inner gimbal and the outermost foundation was extremely important to keeping the resonant frequencies high. The mounting platform was designed to transmit the load through a double-walled cylinder with internal closed triangular cells with five sides. This design provided the maximum stiffness per pound of weight. The load path and welding plan are shown in Fig. 72.

The design was unique in that each cell was welded almost shut for maximum stiffness. Figure 73 shows the housing cylinder after the internal welding was completed; it also shows the internal stiffening ring, which shared in the support of the counterweights and the stator elements of the azimuth drive. The internal cylinder structure is shown in Fig. 74.

2. Counterbalance: The need to counterbalance the top-heavy antenna was great, especially for the three-gimbal design. Figure 72 indicates how the roll and pitch axes were raised as high as possible, thus making the required structure provide as much counterbalance as possible.
3. Elevation Power Drive: The nodding experiment required a slow but precise drive in elevation as well as a microradian pickoff. The slow speed was dictated by the complex real-time data-reduction process. The power drive consisted of a Dayton flange-mounted, 3/4 HP motor equipped with solid-state speed control driving a USM Corp. harmonic drive having 80:1 single-pass reduction with near zero backlash. The output was equipped with a ball-bearing scotch-yoke eccentric drive, also fabricated with near-zero backlash. The elevation axis was thus driven 3.82° peak-to-peak at a maximum sinusoidal rate of 1.37 Hz.

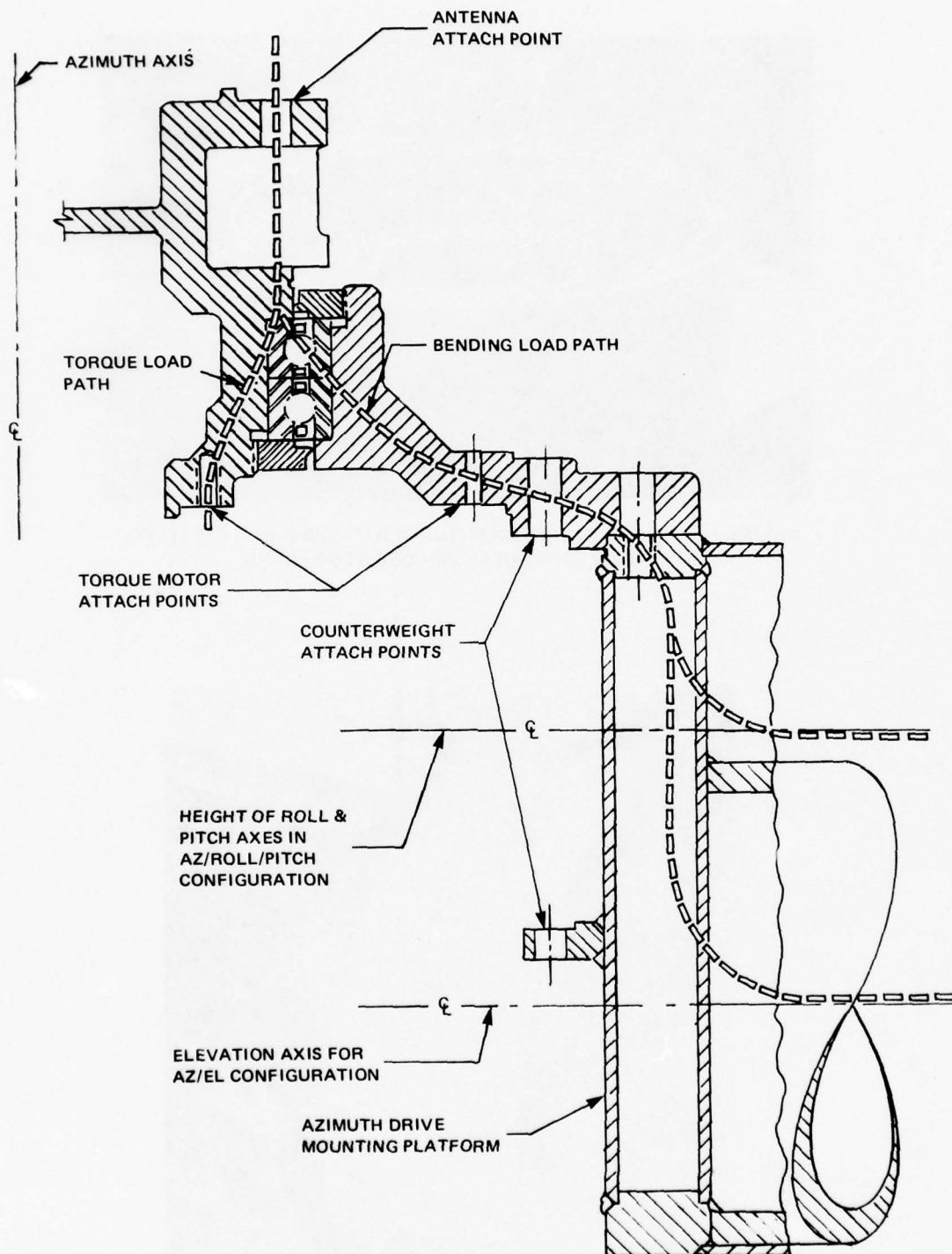


FIG. 72 LOAD PATH IN AZIMUTH DRIVE MOUNTING PLATFORM

THE JOHNS HOPKINS UNIVERSITY
APPLIED PHYSICS LABORATORY
LAUREL, MARYLAND

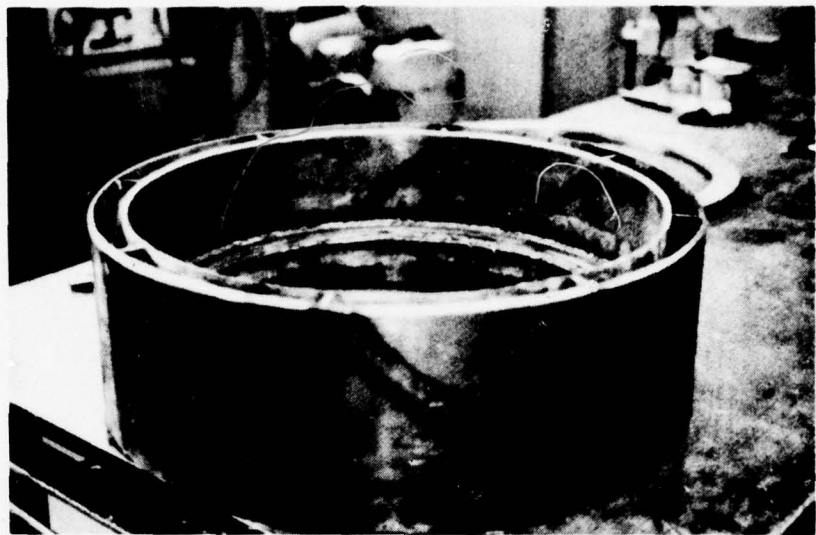


FIG. 73 AZIMUTH-DRIVE MOUNTING PLATFORM DOUBLE-WALLED CYLINDER WITH FULLY WELDED STIFFENERS

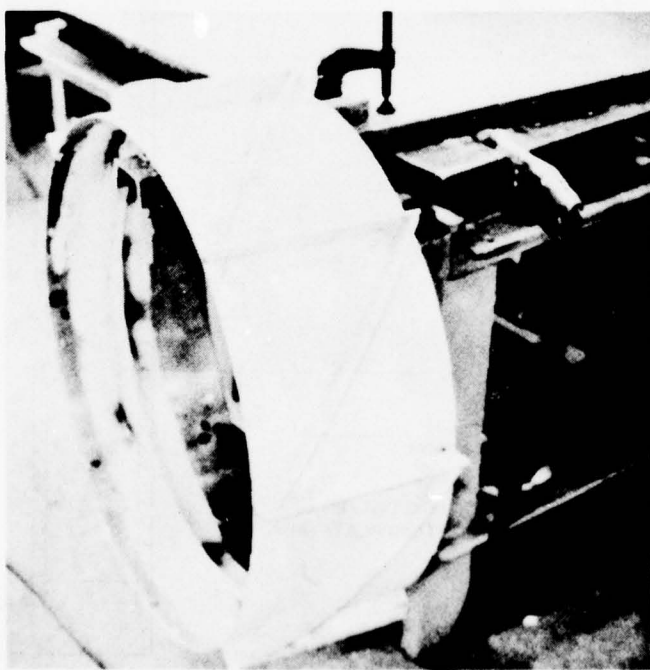


FIG. 74 AZIMUTH-DRIVE MOUNTING PLATFORM INTERNAL-CELL STRUCTURE

4. Elevation Pickoff: The elevation axis position pickoff was implemented using a sector gear and an ant backlash gear having a gear-pass ratio of 5:1. This mechanism drove a Precision Instrument Corp. Model 505 carbon-film potentiometer. The resolution of the combined system was 7.5 μ rad.
5. Elevation Bearings and Seals: The elevation axis was journaled by two pairs of lightly-preloaded ball bearings back-to-back (Kaydon Model KF080DHOL) in order to obtain low friction and zero play. One pair was locked in place and the other pair was floated axially to accommodate thermal expansion.

The bearings were the same ones selected for use in the three-axis design. The seals used were Aeroquip Omni-seal Model AR10104-448A1H Teflon and had the garter spring removed to reduce friction.
6. Elevation Lock: Elevation limit stops were used to lock the elevation gimbal during shipment. Jack screws, threaded into a gusset of the gimbal support housing, are turned out against the inner surface of the stops and locked in place by check nuts.
7. Conversion Plans for Space-Stabilized Operation: All design aspects of the Phase II program three-gimbal operation were planned into the Phase I equipment. Figure 75 shows the cutting down of the azimuth drive mounting platform to form the space-stabilized platform; the cutting plane was preplanned with one of the cellular construction bulkheads falling just inside the cutting plane. Thus, no precision machine work was necessary to adapt to the three-axis gimbal concept.
8. Inertial Reference Unit: During the Phase II three-gimbal operation, an inertial reference unit (IRU) was to be mounted on the azimuth drive mounting platform. The IRU was to be servo-driven and thus space-stabilized with the azimuth axis vertical. The IRU (Fig. 75) was designed for aircraft service as a distance measuring unit, and, as such, had a quick disconnect mechanical interface. An interface tray was designed that could align the IRU with the gimbal axes. The packaging of the IRU was severely hampered by the bounds placed on available space by the swept volume of the rotating antenna.

THE JOHNS HOPKINS UNIVERSITY
APPLIED PHYSICS LABORATORY
LAUREL MARYLAND

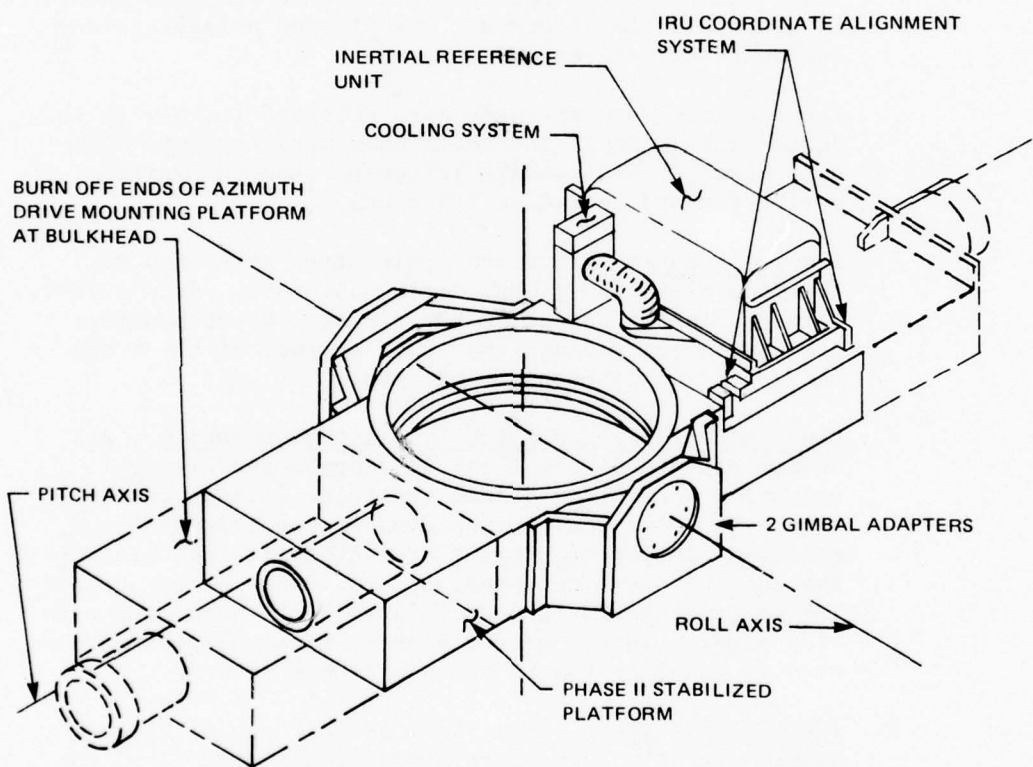


FIG. 75 PHASE II STABILIZED PLATFORM CONSTRUCTED FROM PHASE I PLATFORM

THE JOHNS HOPKINS UNIVERSITY
APPLIED PHYSICS LABORATORY
LAUREL MARYLAND

Azimuth Drive Performance. The azimuth drive was interfaced with a complex, digital, real-time computer to accomplish obstacle detection and terrain avoidance. There were two main forms of feedback, analog-velocity, and digital-absolute shaft encoder. The following forms of control were implemented:

1. Angular-velocity-analog rate control:

Manual command
Computer command

2. Digital position:

Manual command
Computer command

3. Digital-position, clock-controlled rate ramp:

Computer command.

The final adjustment of the azimuth drive electronics for a horizontally mounted antenna resulted in the following characteristics:

Bandwidth: 4 Hz (frequency where open loop gain ≈ 1)

Resonant peak: 3 Hz

Damping (ζ): 0.5

Velocity limit in velocity mode: 2.04 rad/s

Velocity limit in position mode: 0.25 rad/s

Static position error: ± 1 bit $\pm 96 \mu\text{rad}$

First mechanical resonance: 38 Hz

Strongest mechanical resonance: 94 Hz

Maximum acceleration: 4.3 rad/s^2 .

The mechanical resonance and maximum acceleration were fixed by mechanical and motor constraints. All other quantities were readily adjustable within the platform control chassis.

THE JOHNS HOPKINS UNIVERSITY
APPLIED PHYSICS LABORATORY
LAUREL MARYLAND

TERMS:

ζ	damping factor	dimensionless
θ_c	input shaft angle command	rad
θ_e	position lag error	rad
θ_o	output shaft angle	rad
$\dot{\theta}$	shaft angular velocity	rad/s
f_n	undamped natural frequency	Hz
ω_n	undamped natural frequency	rad/s
ω	frequency	rad/s
K_v	velocity error constant	s^{-1}
S	Laplacian variable	s^{-1}

1. Velocity Mode: In the velocity mode, the tachometer output is forced to equal the speed command, which is simply an adjustable voltage level. Cogging, which is inversely proportional to speed, was noticeable in the slow speeds. Since a more precise velocity scan is available in the position mode, no attempt was made to fine-tune the velocity mode by increasing the loop gain. This mode was intended as a simple means for obtaining approximate scan rates.

Loop gains have been apportioned so that velocities up to 2 rad/s could be commanded. However, at this speed the motor back EMF is 52 volts and any attempt to decelerate from this speed would exceed the internal power dissipation of the power amplifier. Velocity commands during tests were limited to 1 rad/s.

2. Position Mode: In the position mode, the velocity or rate loop becomes an inner loop furnishing the required damping. Actually, a different amplifier is switched into this inner loop so that loop gain can be set independently of the gain used in the velocity mode (Fig. 76).

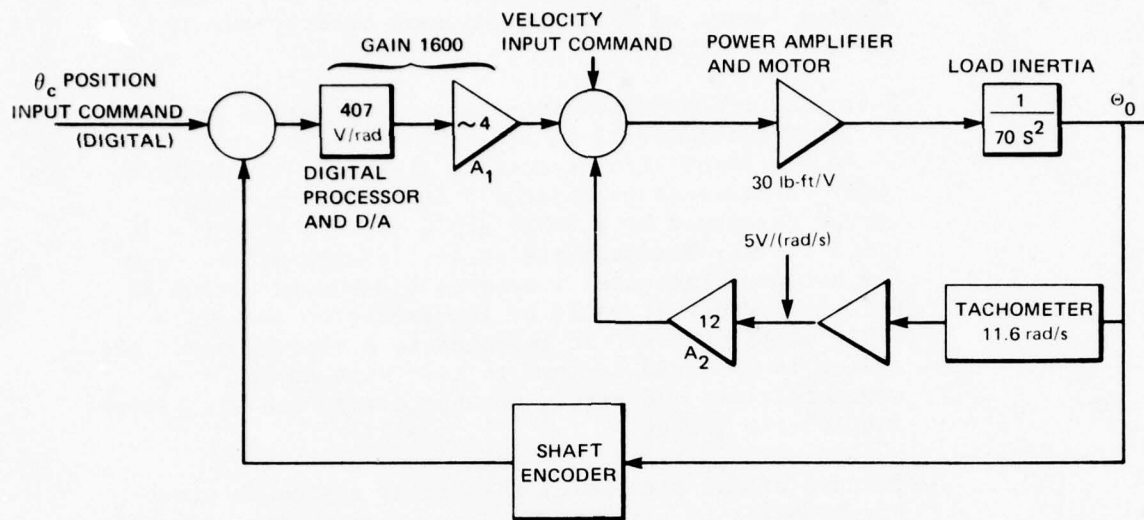


FIG. 76 AZIMUTH DRIVE BLOCK DIAGRAM

Insofar as the linear region is concerned, the identical characteristics may be obtained by apportioning gain differently among A₁, A₂, and the power amplifier (see Fig. 76). Selection must be based upon nonlinear questions such as saturation and velocity limiting. To maintain stability, it was deemed desirable to confine saturation principally to the outer loop so that damping due to the inner loop always remains effective. This is particularly desirable if an integrator were to be inserted in the outer loop to improve the low-frequency gain. (For the immediate application, the use of an integrator has been unnecessary.) With the power amplifier and motor capable of 300 lb-ft, saturation is obtained at a power amplifier input of 10 V. Since the maximum output of A₁ is less than 15 V, the power amplifier is allowed only slight saturation. The transfer function of 30 lb-ft/V is the product of 20 lb-ft/A for the motor, 2.5 A/V for the main portion of the power amplifier, and a 0.6 V gain in the preamplifier section of the power amplifier.

This system contains the characteristic equation $s^2 + 26s + 680 = 0$, which, when compared to the standard form $s^2 + 2\zeta\omega_n s + \omega_n^2$ yields a natural frequency of $\omega_n = 26$ or

$f_n = 4.15$ Hz and a damping factor of $\zeta = 0.5$. For a damping factor of 0.5, the resonant peak occurs at $0.7 f_n = 2.9$ Hz.

Selection of the outer loop gain was governed primarily by the requirement of no more than a 2-bit error. Since one least significant bit of the 16-bit shaft encoder corresponds to about 1×10^{-4} rad, the motor torque developed by a 1-bit error is $10^{-4} \times 1600 \times 30 = 4.8$ lb-ft. Measurements on the azimuth drive, with the antenna, indicated a maximum break-away torque of 6 ft-lb. Hence it would be impossible to sustain a 2-bit static error. In response to a step command, the system is observed to come to rest with any of four possibilities: no error, one-bit error, one-bit jitter, and two-bit jitter.

Because of the high gain, the linear region is necessarily small in response to a step. From Fig. 76, this linear region is 10/1600 radian, or approximately 6 mrad (0.36°). For input steps larger than 10 mrad, A_1 saturates at just under 15 V and the motor accelerates until A_2 matches the A_1 saturated output. (Care was taken in the circuit design to ensure that A_2 can always overcome A_1 .) At this time, the motor torque is reduced to a value just enough to overcome the running friction (4.5 ft-lb) and a constant speed is obtained of $\dot{\theta} = 14/60 = 0.25$ rad/s. When close proximity to the command position is obtained, a high reverse torque is generated to stop the antenna with one overshoot. This can be observed on the power supply current meter for the power amplifier or on the amplifier current warning lamp.

Note that if it is desired to scan at a speed exceeding 0.25 rad/s in this mode, the bandwidth must be increased. Increasing bandwidth should not be fundamentally difficult since the lowest mechanical resonant frequency is so high (38 Hz). However, some additional circuit precautions will have to be undertaken since a 500-Hz and a 1-kHz oscillation were observed to appear as the loop gain was increased. The source appeared to be the power amplifier. While these oscillations do not prohibit proper servo response, they do cause undesired heating in the power amplifier and motor. For the present bandwidth, it was easy to introduce additional filtering into the power amplifier.

3. Sector Scan: A number of methods are available for producing a limited sector scan. The simple velocity mode

can be used where the input command is a square wave whose amplitude determines the scan rate. This method suffers from the motor-cogging speed perturbations previously discussed. Also, the antenna position may be subject to drift, because no position control is exerted. One means of eliminating the position drift would be to key the switching of the square wave to the antenna position indicated by the shaft encoder.

With the position loop closed, a sector scan is produced by injecting a triangular waveform into the outer loop. Scan speed is now determined by the slope of the waveform. Since this signal is effectively superimposed on the normal loop, position control is available in the usual fashion from either the control panel switches or the computer command. The point of injection of this waveform is immediately preceding amplifier A₁ (Fig. 76). An input terminal for this purpose is available at the rear of the control chassis. A square wave injected at this point will also result in a sector scan with the speed determined by the velocity limit.

In place of these analog signals, the equivalent digital signals may be inserted at the normal input. Again, these signals may be either triangular with the desired slope or square wave utilizing the velocity limit for scan speed. For triangular drive there is a position lag error given by $\theta_e = \theta/K_v$. If this is undesirable, an integrator may be added to the outer loop or the tachometer feedback may be AC coupled. This latter change (or, at least, a different apportioning of loop gains) will also be required if the present velocity limit of 0.25 rad/s is to be removed during use of the position loop.

4. Power Amplifier: The power amplifier (Bulova Model DCA 1000-3 (Appendix A)) is capable of delivering 15.5 A at 65 VDC and requires a 75 VDC supply. To better match the 2.8- Ω motor winding to the amplifier, a 1- Ω , 225 W resistor was connected in series with the motor. Some additional cable resistance brought the total load to about 4 Ω . The amplifier was connected in the preferred current mode where output current is proportional to input voltage. Hence motor torque is proportional to input voltage (neglecting saturation effects). The full torque of 300 lb-ft is developed at the maximum current output of the amplifier.

The power amplifier specifications include a dissipation rating of 1000 W as well as an ability to sustain indefinitely a short circuit at full drive (which gives $65 \text{ V} \times 15 \text{ A} \approx 1 \text{ kW}$). However, the power amplifier output circuit is a bridge, only half of which is active at any one time. To successfully sustain 1 kW, all portions of the bridge must share the dissipation. This would require an input square wave, a condition normally not encountered in a servo system. In reality the internal dissipation capability was 500 W per side.

Support Structure for Radome and Gimbal

The primary requirement for the support structure was to support the gimbal pillow blocks and the radome. The design was severely driven by outside dimensional limitations on transportable width and bridge clearance height. The radome imposed a flatness requirement of 0.060 in. on the mounting flange, a requirement that was maintained while using a 4-point leveling system. Potential loss of radome transparency at 95 GHz (because of inside water condensation) was minimized by using a ventilating blower system having a recirculation mixing capability and an exhaust louver system. Entrance and egress with Arctic clothing dictated the door design.

Figure 77 shows the radome and gimbal mounting surface as integral to economize on machining requirements. The mounting surface was heavily gusseted from below, and was tied to the four hydraulic jack leveling points by triangular bracing. The triangular bracing can be seen in Fig. 78, which shows the $250 \text{ ft}^3/\text{min}$ ventilating system in place. Above the ventilating system is a cable entrance port designed for Arctic service. The port is framed in wood with a hinged door covering the lower half. The opening is large enough for bulky connector ends to pass through. The door can then be clamped down tightly on the cable to exclude wind-driven snow and dirt.

The door was of low-cost construction with a latch designed to function in freezing weather and provided projections for sledgehammer-opening technique. The full perimeter weather seal on the door consisted of a cast-in-place fillet of room-temperature vulcanizing silicone rubber between the door and the door jamb.

The basic construction technique used welded 0.090-in. aluminum walls and portions of the floor over a channel grid connecting the jacking points. The finished weight was 1305 lb, including the blower.

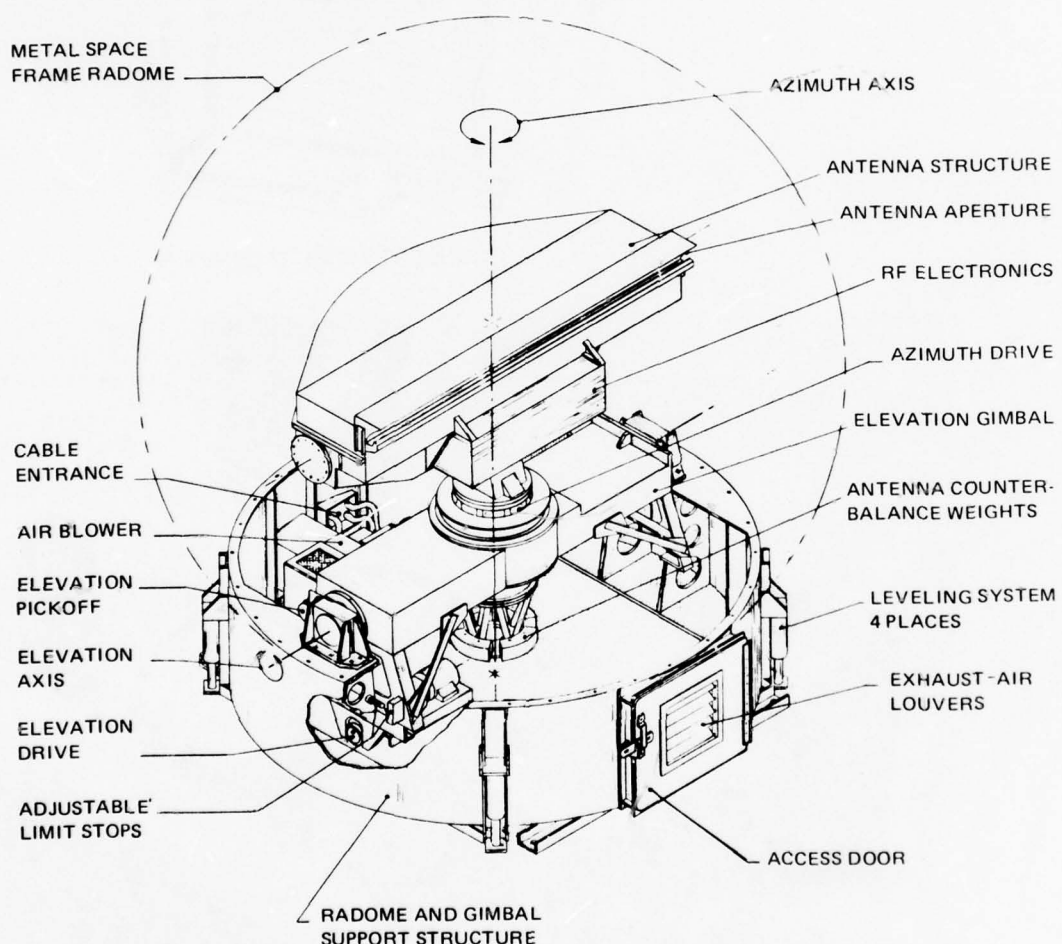
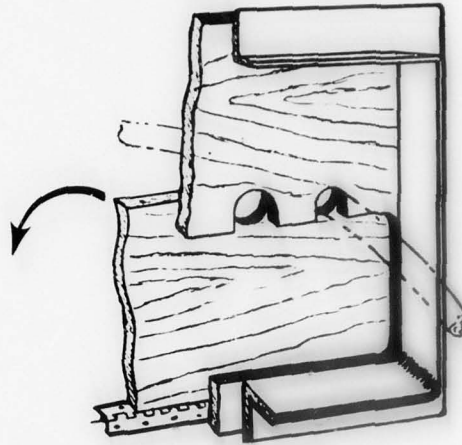


FIG. 77 RADOME AND GIMBAL SUPPORT STRUCTURE WITH PHASE I GIMBAL AND ANTENNA

THE JOHNS HOPKINS UNIVERSITY
APPLIED PHYSICS LABORATORY
LAUREL, MARYLAND



CABLE ENTRANCE TECHNIQUE

INTERNAL BRACING OF
RADOME AND GIMBAL
SUPPORT STRUCTURE →

CABLE ENTRANCE
PORT

HINGE LINE

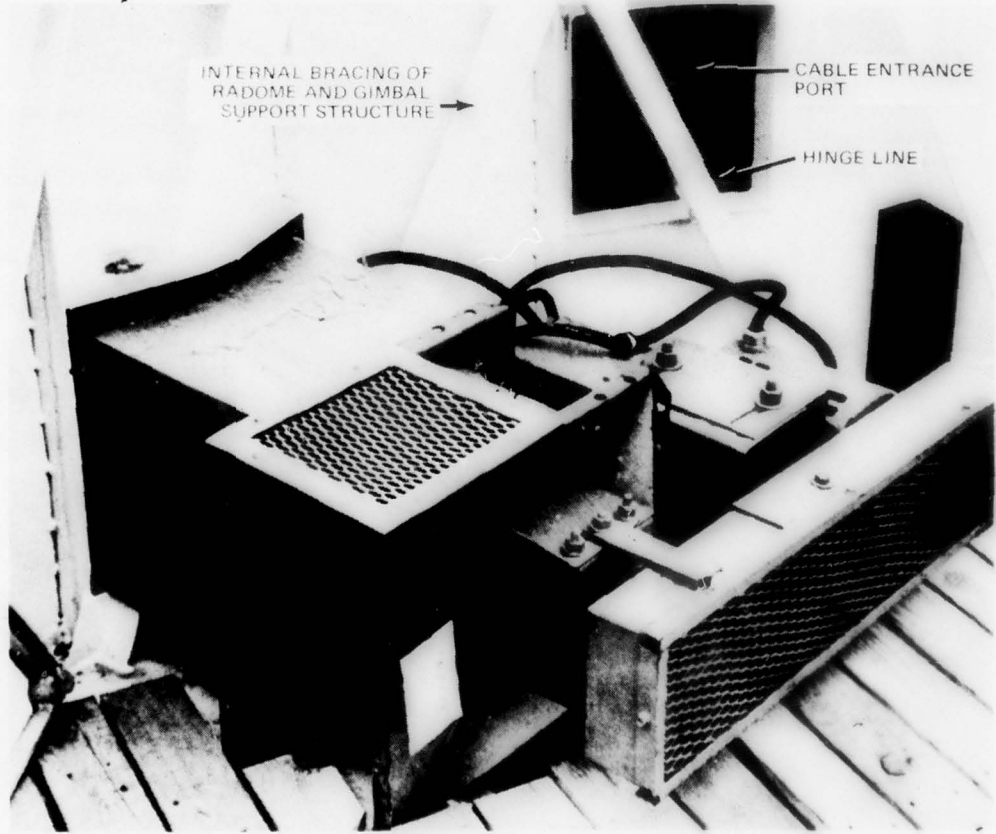


FIG. 78 RADOME-VENTILATION BLOWER FOR CONDENSATION CONTROL

Stabilized Gimbal

The stabilized gimbal for the Phase II program was designed, but the outer (or pitch) gimbal ring was not manufactured. A drawing of the SEV antenna mounted on the three-axis stabilized platform is shown in Fig. 79.

Some of the driving functions and fundamental decisions regarding the Phase II design were as follows:

1. Gimbal stabilization error budget was the pacing factor.
2. Electric torque-motor drive would be employed to eliminate Arctic subzero temperature hydraulic servo development problems.
3. The outer gimbal ring (pitch) would carry identical sets of equipment for implementing roll and pitch; viz., motors, bearings, seals, pickoff, and brakes.
4. The gimbal would require near mass balance in each axis.
5. The gimbal order of the SEV stable-platform and the mounting orientation of the Inertial Navigation Unit must match the gimbal order azimuth/roll/pitch where the innermost axis is named first.
6. The SEV stable platform should be able to uncouple $\pm 20^\circ$ of angular base motion in both axes.
7. Caution lights on the control panel would warn of gimbal angles over 10° .
8. Emergency brakes (pneumatic over hydraulic) would be applied if the stable platform error ever exceeded 1° .
9. A 5% beam area interference between the gimbal structure and the antenna aperture would be tolerated at high gimbal angles to reduce the counterweight size.
10. Use of narrative reports from prior SEV operations and Arctic experience should be heavily considered from all design aspects.
11. Personnel safety is paramount.
12. Design to cope with differential thermal expansion.

THE JOHNS HOPKINS UNIVERSITY
APPLIED PHYSICS LABORATORY
LAUREL MARYLAND

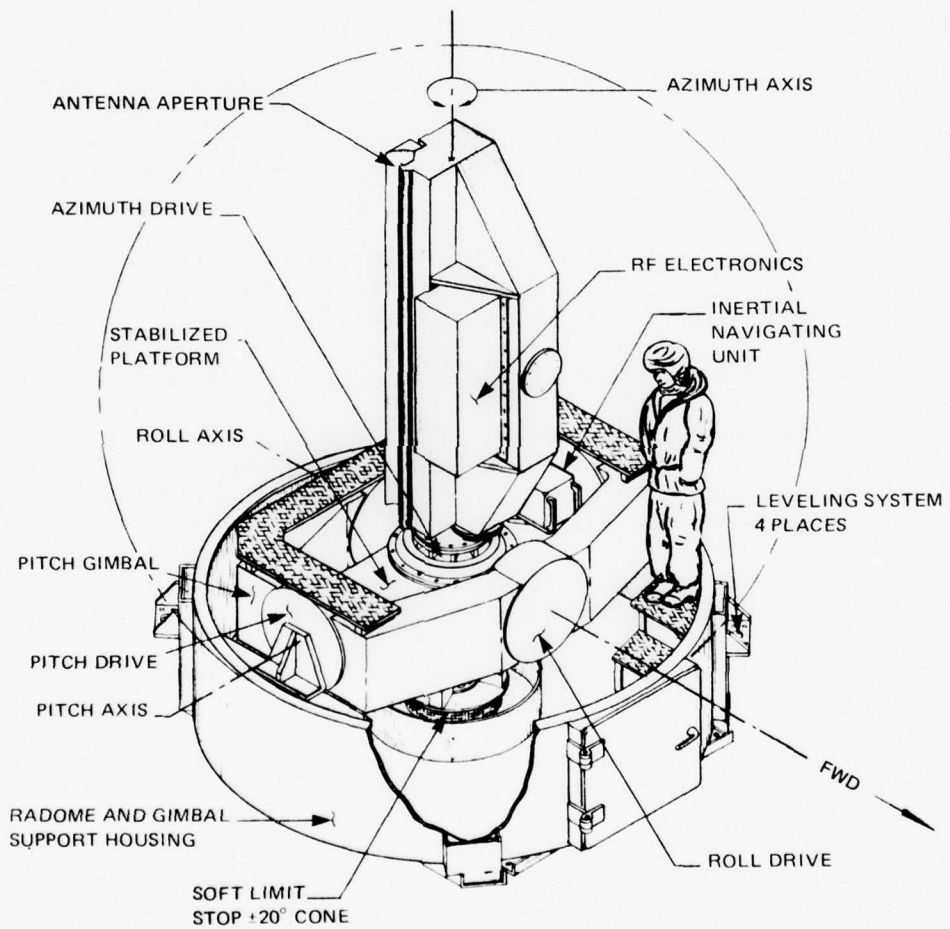


FIG. 79 SEV ANTENNA ON THREE-AXIS STABILIZED PLATFORM

13. Design for ease of fabrication, testability, assembly ease, and serviceability.

The conversion to a three-axis gimbal from a two-axis gimbal was to be implemented in the manner shown in Fig. 80. By this method the pitch gimbal pillow blocks would rest on the same support pads that the elevation pillow blocks had rested on, and the swept volume inside the radome would be correctly positioned.

The roll and pitch torque motor subassemblies used the same bearings as those used in the Phase I elevation axis; the bearings on the torque-motor end were locked in axial position whereas the bearings on the pickoff end were allowed to float axially to accommodate differential thermal expansion. The pickoff employed a 10:1 ant backlash gear pass and the braking system incorporated caliper disk brakes, the control of which was designed to avoid collision with the radome in the event the torque motor was unable to adequately follow the inertial commands. Both a torque motor and a pickoff subassembly are shown in juxtaposition as if mounted for the roll axis in Fig. 81. The mounting for the pitch axis would have both the motor assembly and pickoff assembly facing in opposite directions, that is, the central mounting flanges would be facing out instead of in. Figure 82 shows exploded views of the assembly order of both the roll and pitch subassemblies of the outer gimbal ring.

The torque motors weighed 165 lb and required special lifting provisions to assemble them to the bearings, which is done with a vertical axis. The torque motor and bearing subassembly are then lifted into the gimbal with a special tool for positioning the motor in a horizontal axis position.

The outer gimbal ring was designed to be as stiff and as light as possible. A model of the outer gimbal structure was constructed and tested, and remodeled for increased stiffness. The design employs deep-box thin-wall sections with added stiffening of the circular sections where the motor and pickoff subassemblies are secured. The success of a closed box as a highly stressed load-carrying member depends upon rigid edges and the integrity of the individual cells of the structure. Construction details are shown in the six construction steps outlined in Fig. 83, 84, 85, and 86.

The $\pm 20^\circ$ cone-angle bumper system was located in the central floor region of the gimbal support with the contact bumper attached below the counterweight. The entire bumper system was planned to hold shock loads on the antenna components to within the 1-g limit. The total size of the planned three-axis platform assembly and the bumper location are indicated in Fig. 79.

THE JOHNS HOPKINS UNIVERSITY
APPLIED PHYSICS LABORATORY
LAUREL MARYLAND

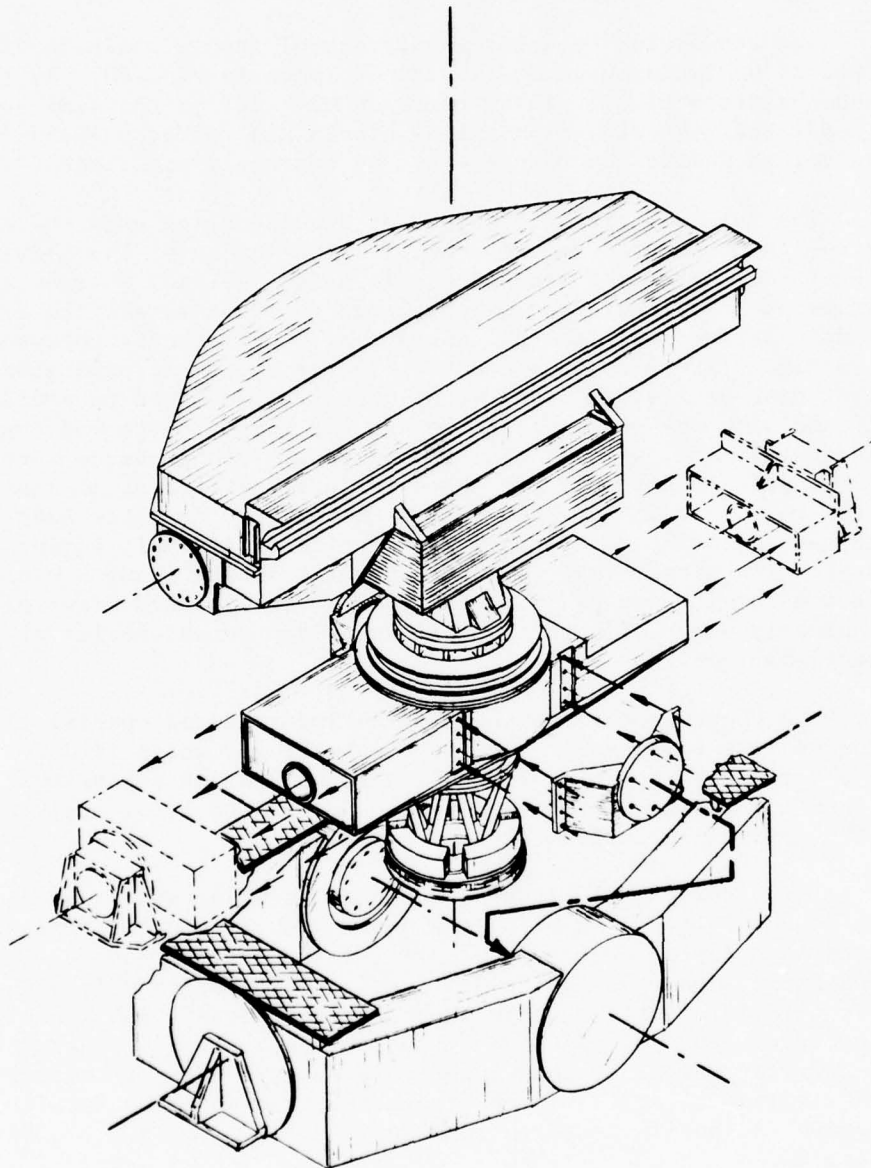


FIG. 80 CONVERSION FROM TWO-AXIS GIMBAL TO THREE-AXIS STABLE PLATFORM

THE JOHNS HOPKINS UNIVERSITY
APPLIED PHYSICS LABORATORY
LAUREL, MARYLAND

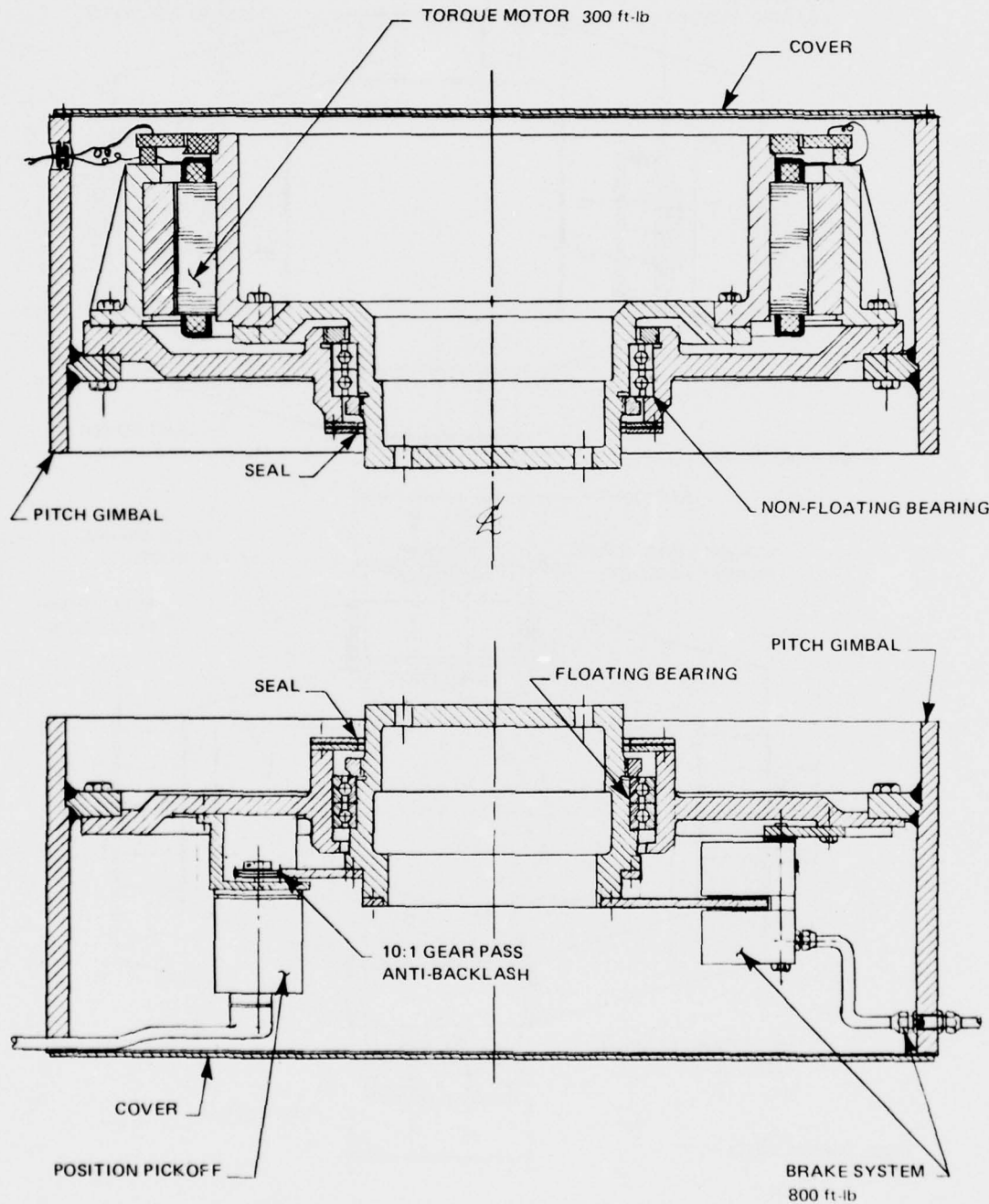


FIG. 81 DETAILS OF ROLL-AXIS BEARINGS, SEALS, MOTOR,
PICKOFF, AND BRAKES

THE JOHNS HOPKINS UNIVERSITY
APPLIED PHYSICS LABORATORY
LAUREL, MARYLAND

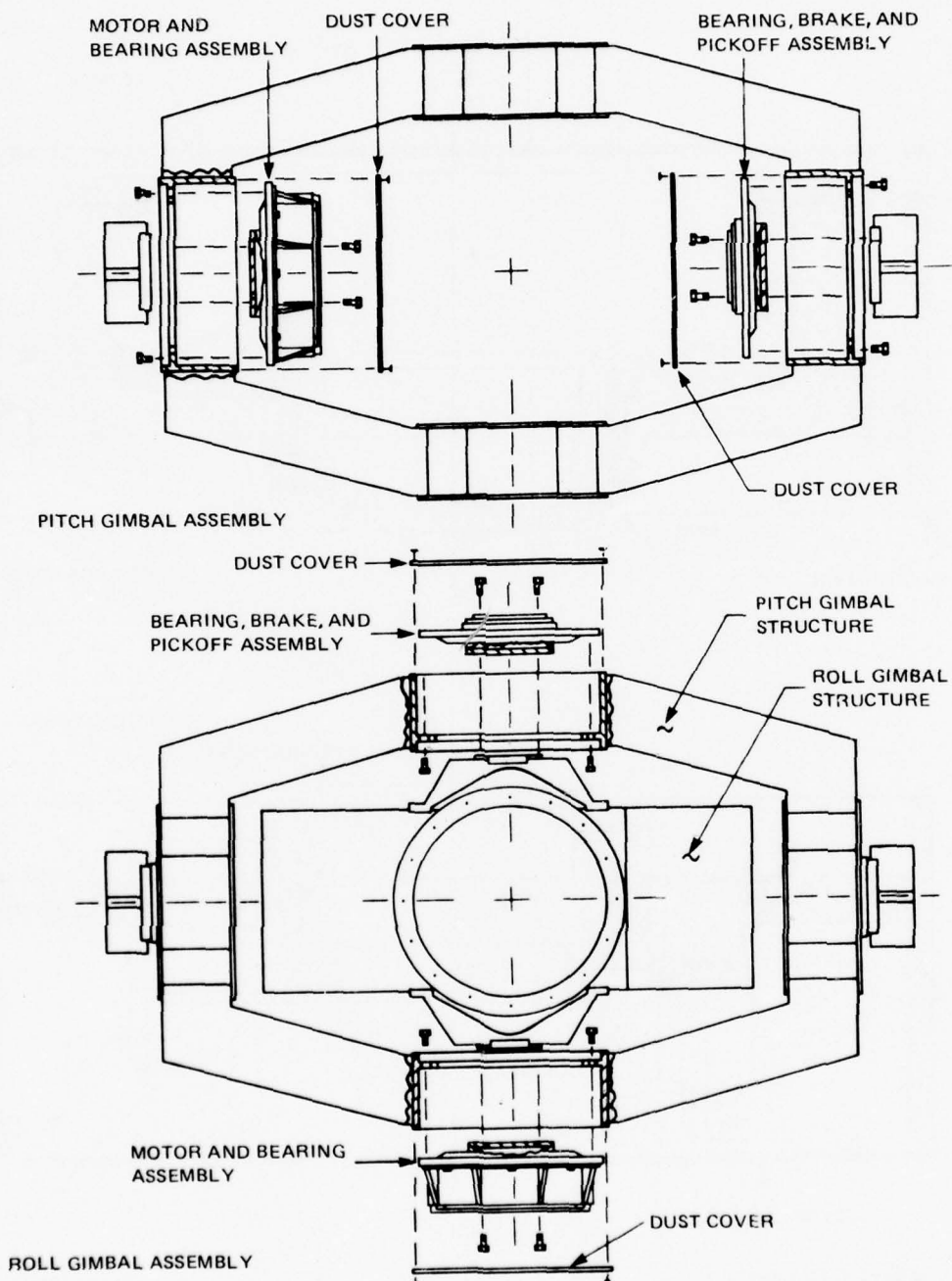


FIG. 82 STABLE PLATFORM ASSEMBLY PROCESS

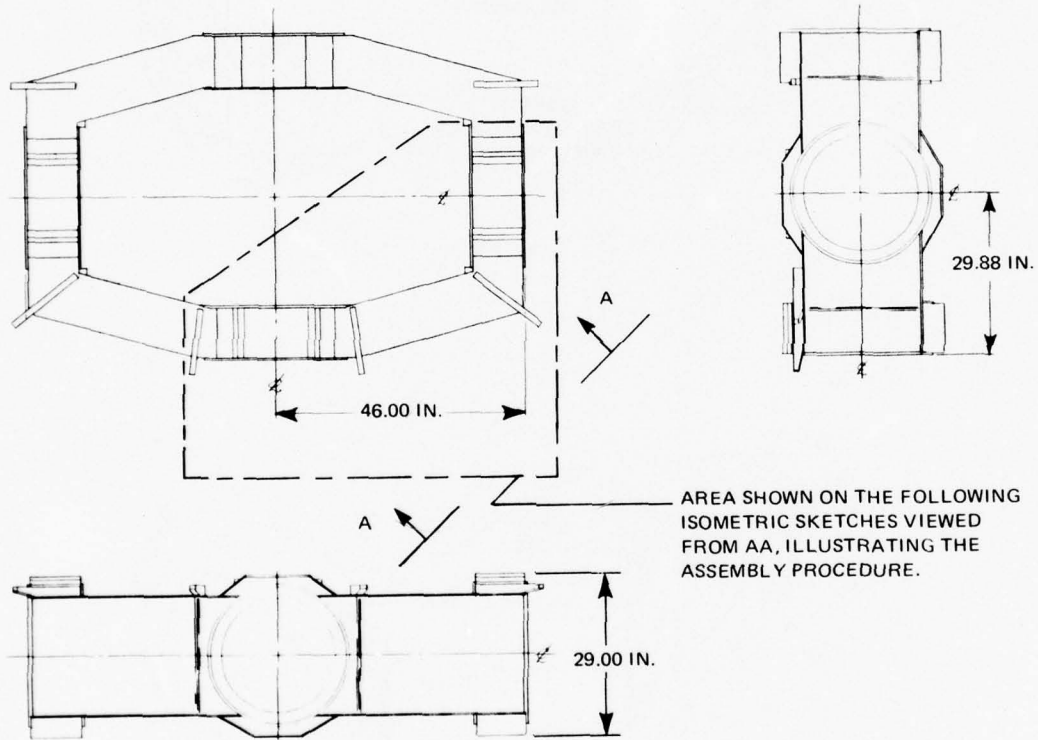
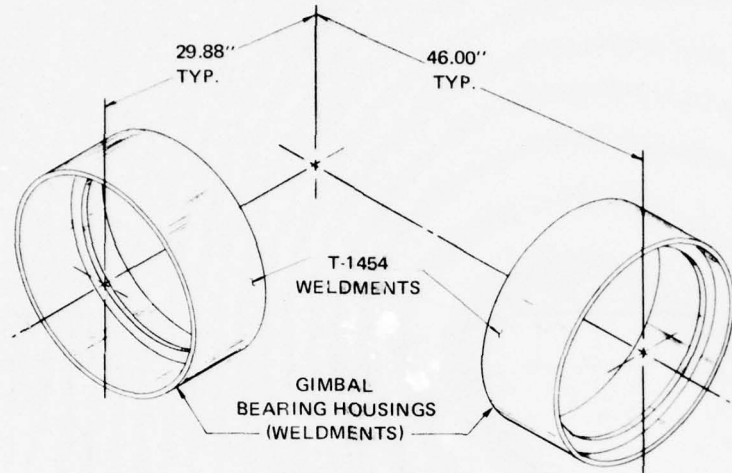
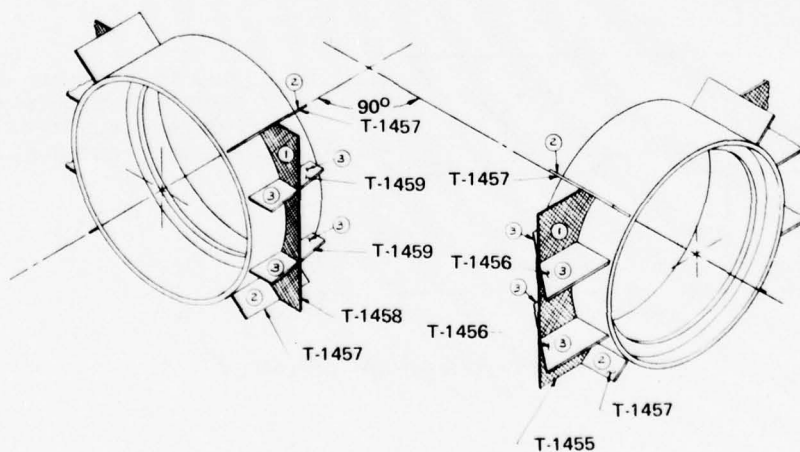


FIG. 83 OUTER GIMBAL ASSEMBLY

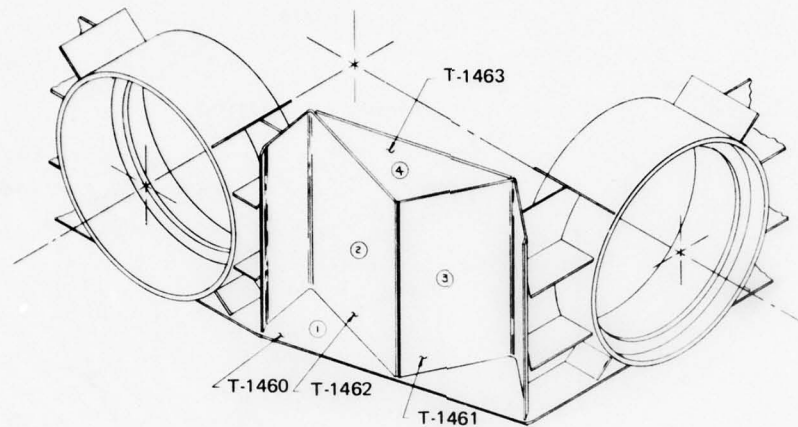


STEP 1

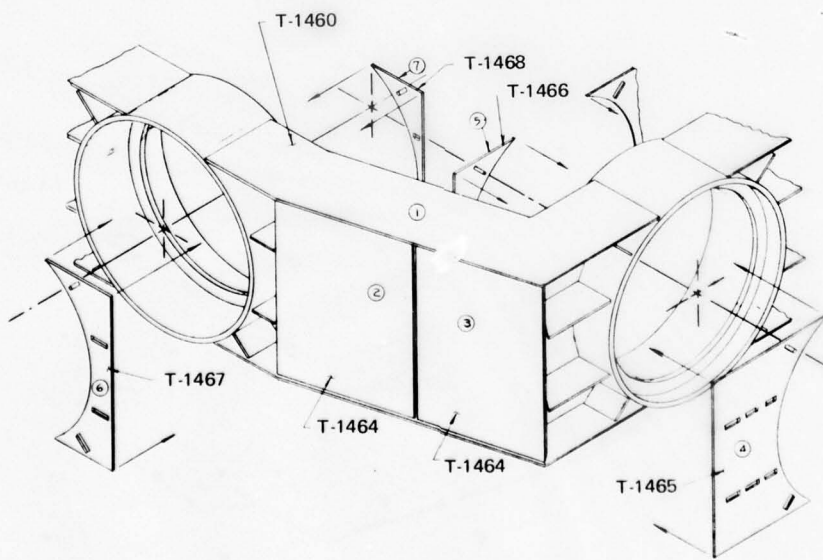


STEP 2

FIG. 84 OUTER GIMBAL ASSEMBLY STEPS 1 AND 2



STEP 3



STEP 4

FIG. 85 OUTER GIMBAL ASSEMBLY STEPS 3 AND 4

THE JOHNS HOPKINS UNIVERSITY
APPLIED PHYSICS LABORATORY
LAUREL, MARYLAND

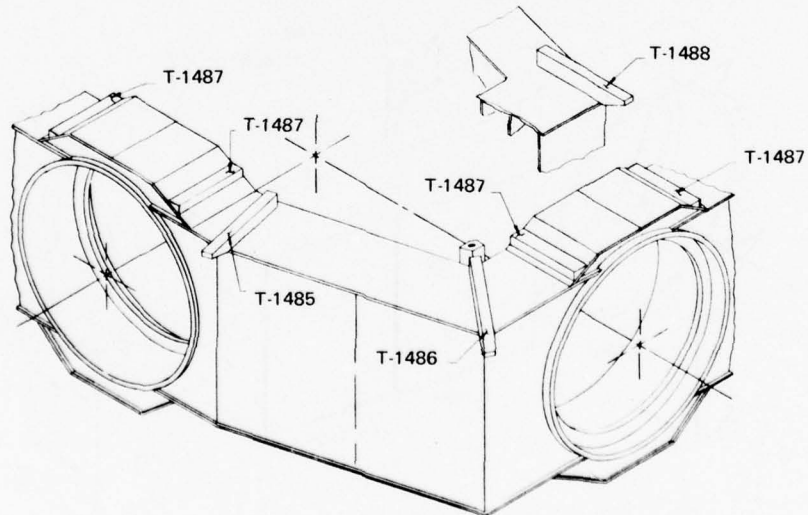
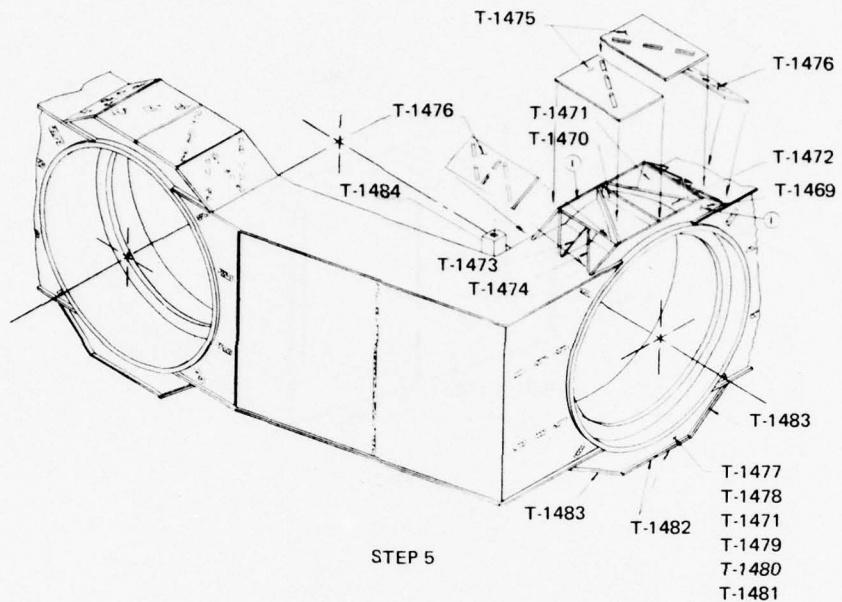


FIG. 86 OUTER GIMBAL ASSEMBLY STEPS 5 AND 6

PLATFORM CONTROLLER

The platform controller provides complete remote control of the antenna azimuth-drive pedestal. It includes three basic modes of operation. Using front-panel operator controls, the antenna can be either positioned to some desired fixed azimuth angle or scanned at a variable angular rate to a maximum velocity of about 2 rad/s. The third mode provides computer software control of the antenna position. Figure 87 is a photograph of the front-panel of the platform controller. It is noted that the unit also includes controls for the pitch and roll angles of the antenna platform. When the design was started, the overall SEV obstacle detection program included evaluation of the direct-measurement technique for height determination. This technique requires mounting the antenna on a horizontally stable platform. Design efforts on the pitch and roll controllers was stopped when the requirement was dropped from the program; therefore, further discussions will be restricted to the azimuth section only.

Power is applied to the unit through the panel ON/OFF switch at the bottom and the ON/OFF switch at the middle left-hand side of the center portion of the panel. A precision 16-bit shaft encoder is mounted directly on the antenna azimuth-drive shaft. A direct octal numeric display of these 16 bits is provided at the top of the front panel. Directly under the display are a series of octal thumbwheel switches, used to position the antenna to some desired angle manually. This mode is enabled by placing the HALT/RUN switch in the HALT position and the MANUAL/COMPUTER switch in the MANUAL position. As the operator keys in new position data through the switches, the azimuth-drive servo loop forces the shaft encoder reading to the same value. The servo loop associated with this mode has a bandwidth of 4 Hz with a maximum velocity limit of 0.25 rad/s.

The manual constant-scan-velocity mode is activated by placing the HALT/RUN switch in the RUN position. The velocity reference consists of a tachometer mounted on the azimuth drive shaft. Its output is continuously monitored on the velocity meter. In the manual constant-scan mode, the tachometer output is forced to follow the setting on the panel potentiometer, which is scaled in mrad/s so that the actual scan rate can be read directly from the dial. The CW/CCW switch provides direction control on the scan. The X1/X2 switch provides a factor-of-2 scale change on the potentiometer. The OUTPUT MONITOR jack provides for observation of the power amplifier output voltage.

The computer control mode is activated by placing the HALT/RUN switch in HALT position, and the MANUAL/COMPUTER switch in the

THE JOHNS HOPKINS UNIVERSITY
APPLIED PHYSICS LABORATORY
LAUREL, MARYLAND



FIG. 87 FRONT PANEL OF THE PLATFORM CONTROLLER

COMPUTER position. This mode uses the same servo loop as the MANUAL position mode, with the exception that the 16-bit reference data comes from the computer rather than the thumbwheel switches. An effective scan rate is accomplished by periodically updating the computer output at the desired rate. This was the primary operating mode used in the field tests of the experimental system. The shaft encoder output bits were also provided as an input to the computer.

Three warning lights are also provided on the front panel. The BRAKE light will be on whenever the manually operated brake (mounted on the platform) is engaged. The CURRENT light monitors the output current of the power amplifier that drives the torque motor. The CURRENT light is illuminated whenever the current exceeds some set threshold. A thermistor mounted inside the torque motor provides a temperature monitor on the motor. The TFMP light is illuminated when the motor temperature exceeds some specified value.

VIDEO PROCESSING AND TEST CONTROL

The video-processing and test-control functions are accomplished by the system computer with several specialized hardware units and appropriate software. As previously noted, processing concerned with target detection was accomplished after-the-fact. During test operations the primary software function was test control and data collection.

The video processing and test control subsystem is comprised of a high-speed analog-to-digital converter, a high-speed display unit, the system computer, and the processing and control software.

Analog/Digital Converter

The analog/digital converter transforms the logarithmic analog video of the radar return to 8-bit digital format and stores the data in an internal digital memory. The data are then transferred to the computer (at a lower rate) for further processing and recording. The converter is a Biomation, Inc. Model 8100 Transient Recorder. Figure 88 shows the front panel controls.

The unit is capable of sampling the radar returns at various time intervals down to 10 ns (equivalent to 5-ft range increments). Provisions are included to control the arm and trigger functions from external clock inputs. The actual conversion and storage process can be delayed further in time in whole steps of the sample-time interval. During operation of the experimental system, this delay feature was used to set the starting range for data recovery.

THE JOHNS HOPKINS UNIVERSITY
APPLIED PHYSICS LABORATORY
LAUREL, MARYLAND

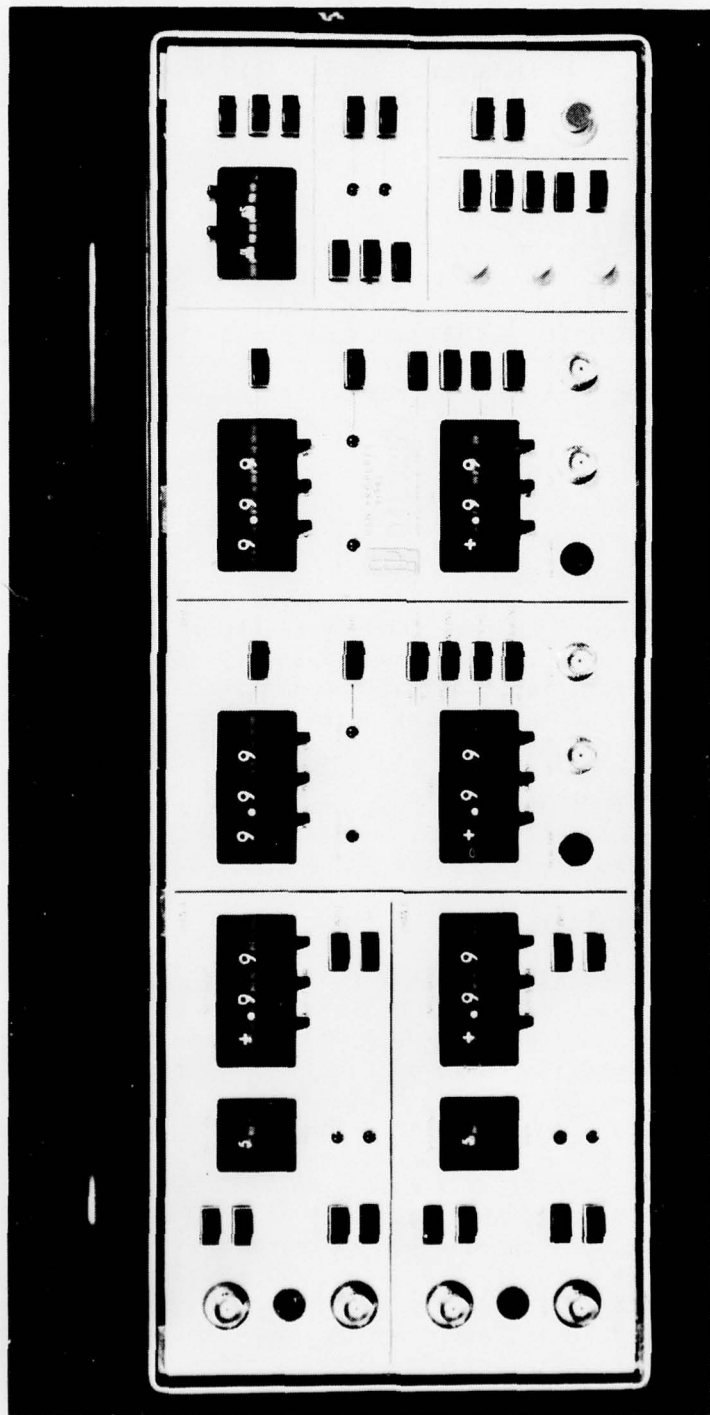


FIG. 88 FRONT PANEL OF THE TRANSIENT RECORDER

While the transient recorder (i.e., the 8100) has dual input channels, only one channel can be used at the low (0.01 μ s) sample interval. The input coupling can be either AC or DC, and the maximum range of the input voltage can be anywhere from ± 0.05 to ± 5.0 V. Typically, the unit was operated in the DC mode on the 5.0 V range. An input offset adjustment is provided to compensate for any biases on the input signal.

Interfacing logic (developed at APL) is provided between the transient recorder and the system computer. In addition to controlling the video data transfer from the transient recorder memory to the computer memory, the interface also provides computer software control over the arm and trigger functions. Whenever the software is ready for a new set of data, these functions are enabled and data are saved from the next radar trigger pulse. The radar itself operates continuously at the normal rate (1 kHz PRF), with data being saved from individual selected pulses.

High-Speed Color TV Display

A high-speed color display system has been developed that uses a studio quality TV monitor in conjunction with a digital memory. The memory provides full refresh capability for the three primary colors (red, blue, and green), covering 512 picture elements per line on a 480-line raster. In other words, data for the complete picture are stored in the memory and are read out and recycled in synchronism with the raster scan. The refresh results in a flickerless display, and is independent of the input-data frame time. The system is designed to display data in vector form in which there may be several color transitions along the vector. A new color-coded vector can be generated and loaded into the refresh memory over the time interval of three TV line scans (approximately 190 μ s). There is no limitation on the origin, length, or orientation of a vector, consistent with the number of resolution elements in the raster.

The primary display format for the SEV pilot is a limited-angle (60°) PPI with different colors to indicate terrain height. As each radar return is processed, a new color vector for the terrain is displayed at the proper angle. In a real-time environment, the display philosophy establishes a speed requirement that the display system be able to process color vectors at a rate equal to the pulse repetition rate (PRR) of the radar. For this particular radar, the PRR was 2 kHz (500 μ s period). The final design of the display system resulted in a processing cycle time equal to 190 μ s.

Several designs for the refresh memory organization and control were investigated with cost, complexity, and performance being

the primary tradeoff parameters. The least expensive design uses one long circulating shift register for each primary color, with sufficient storage for each picture element in the entire TV raster ($480 \times 512 = 245,760$ bits). However, this design provides access to each element for updating only once per frame period (33 ms), but preliminary storage of data is very complex. The simplest approach uses a much more expensive random access memory. The selected design consists of a combination of the two approaches. The data for one primary color on one TV line are contained in a single 512-bit MOS shift register. Each register is recirculated on every line scan. With proper rating in the feedback path, access is provided to every picture element once per line scan.

The vector data for the display are generated in the computer. In order to minimize the amount of data to be computed and transferred, the format for defining the color vector consists of the following: (a) X and Y coordinates of the vector origin (coordinate system origin in upper left-hand corner of the TV picture), (b) sine and cosine of the vector angle (measured positive clockwise from the vertical), and (c) a two-entry data table defining the range segments at which color transitions occur along the vector. Unique hardware logic in the display system then generates data for each element in the vector and loads it into the refresh memory at the appropriate location.

Since the refresh memory must be continuously clocked synchronously with the TV raster, it is not feasible to generate and load all of the vector into it in one operation. Two additional memories (buffer and control) are used to generate the complete vector. A simple block diagram of the complete display system is shown in Fig. 89. The buffer memory is physically the same size as the refresh memory. However, at any time, it contains data for only one color vector. The control memory is one-third this size, and its data define the picture elements associated with the vector presently in the buffer. The two memories are loaded in the following manner. Both memories are initialized with all bits in the 0 state. X and Y address counters are initialized with the vector origin coordinates and driven by a common clock multiplied by the sine and cosine of the vector angle, respectively. Consequently, at any point in time during the load process, these counters are addressing a picture element on the desired vector.

The range/color data table (R_t, C_t) is stored in a small vector memory that has capacity for 4⁴ entries. As the complete vector is generated, the vector memory supplies a range segment input to the range counter and three-bit color data to the buffer memory. The range counter is then counted down to zero with the same clock driving the addressing multipliers. When the range counter reaches

THE JOHNS HOPKINS UNIVERSITY
APPLIED PHYSICS LABORATORY
LAUREL, MARYLAND

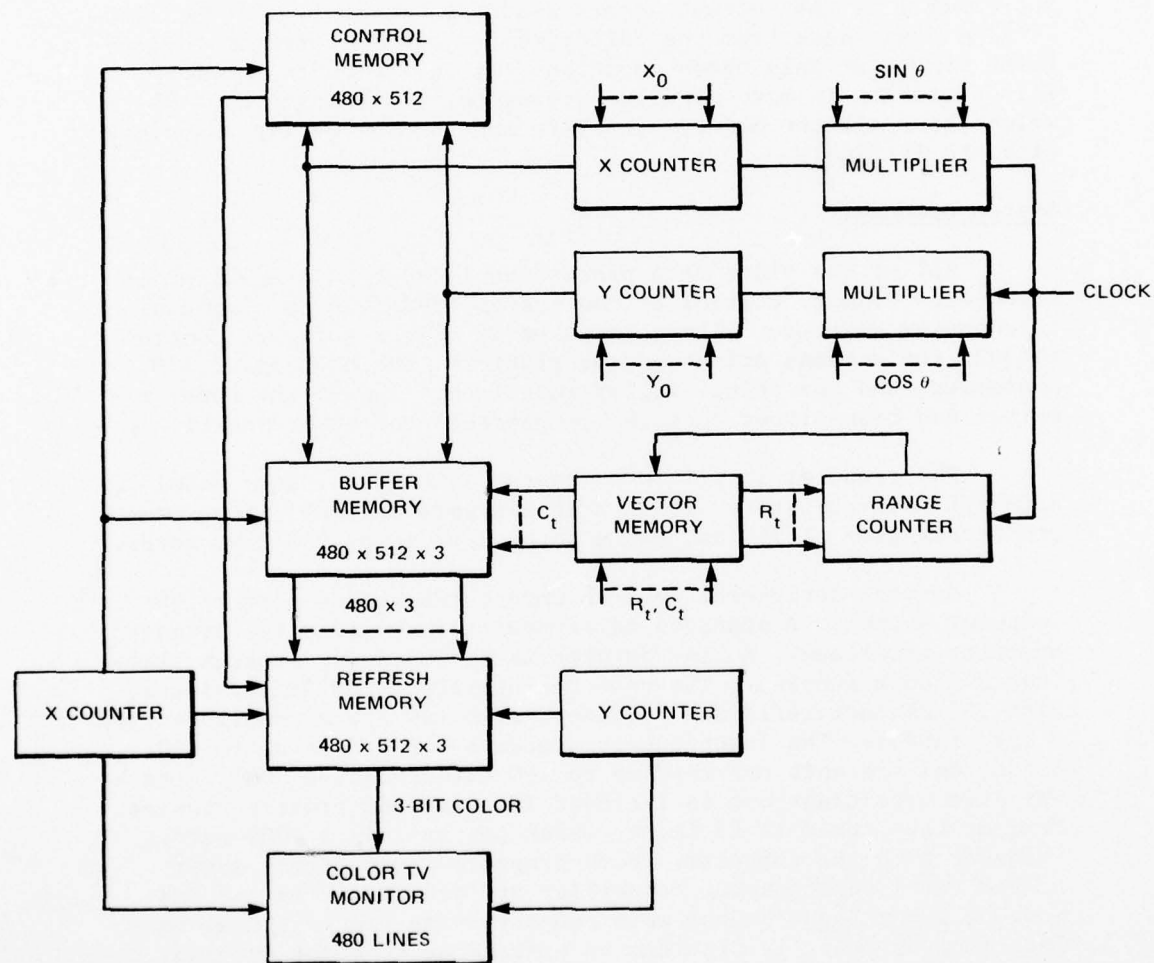


FIG. 89 COLOR DISPLAY SYSTEM BLOCK DIAGRAM

zero, new range and color data are read from the vector memory. This process continues until a special code in the range word defining the last segment is detected. When this operation is complete the buffer and control memories contain color and position data, respectively, only in those picture elements on the vector. This situation is shown pictorially in Fig. 90. The total time required for the operation under worst case conditions is approximately 120 μ s.

Clocking of the buffer and control memories is now under the control of the refresh-memory X-address counter. On the next TV line scan, data from the buffer memory are inserted in the refresh memory at only those locations set in the control memory. This operation is more clearly understood by examining Fig. 91, which shows all the memory registers and control gating associated with one TV line.

System Computer

All of the video data processing is done in a small mini-computer. Primary control of the system operation is also done in computer software. Those items under direct software control include the antenna azimuth-drive platform, the high-speed A/D converter, and the color-display interface. The 95-GHz radar receiver and transmitter operate independently of the computer.

The computer itself is a General Automation, Inc. Model SPC-16/65 minicomputer. It is a 16-bit/word machine with a memory access time of 960 ns, and a total core memory of 8192 words.

Several peripheral devices were purchased as part of the computer system. A standard teletypewriter provides the primary operator interface. A line printer is included for program listings and data dumping. The unit can operate at 60 lines/minute, with 132 characters/line. Program assemblies are accomplished via a card reader. The input/output stackers can handle up to 350 cards, and the unit can read up to 100 cards/minute. One 7-track magnetic tape transport is included for data and program storage. Maximum tape speed is 25 in./s, which can sustain a 4000-word/s transfer with the computer. Both programmed and direct memory access (DMA) input/output capability are provided. In the DMA mode, a 1-MHz input/output word transfer rate can be sustained. Interface hardware is provided to operate up to eight external devices on the single DMA channel available. Two of these eight subchannels are used by the card reader and magnetic tape interfaces within the computer system. Three of the remaining subchannels are used for the antenna platform control, A/D converter, and the color-display interface.

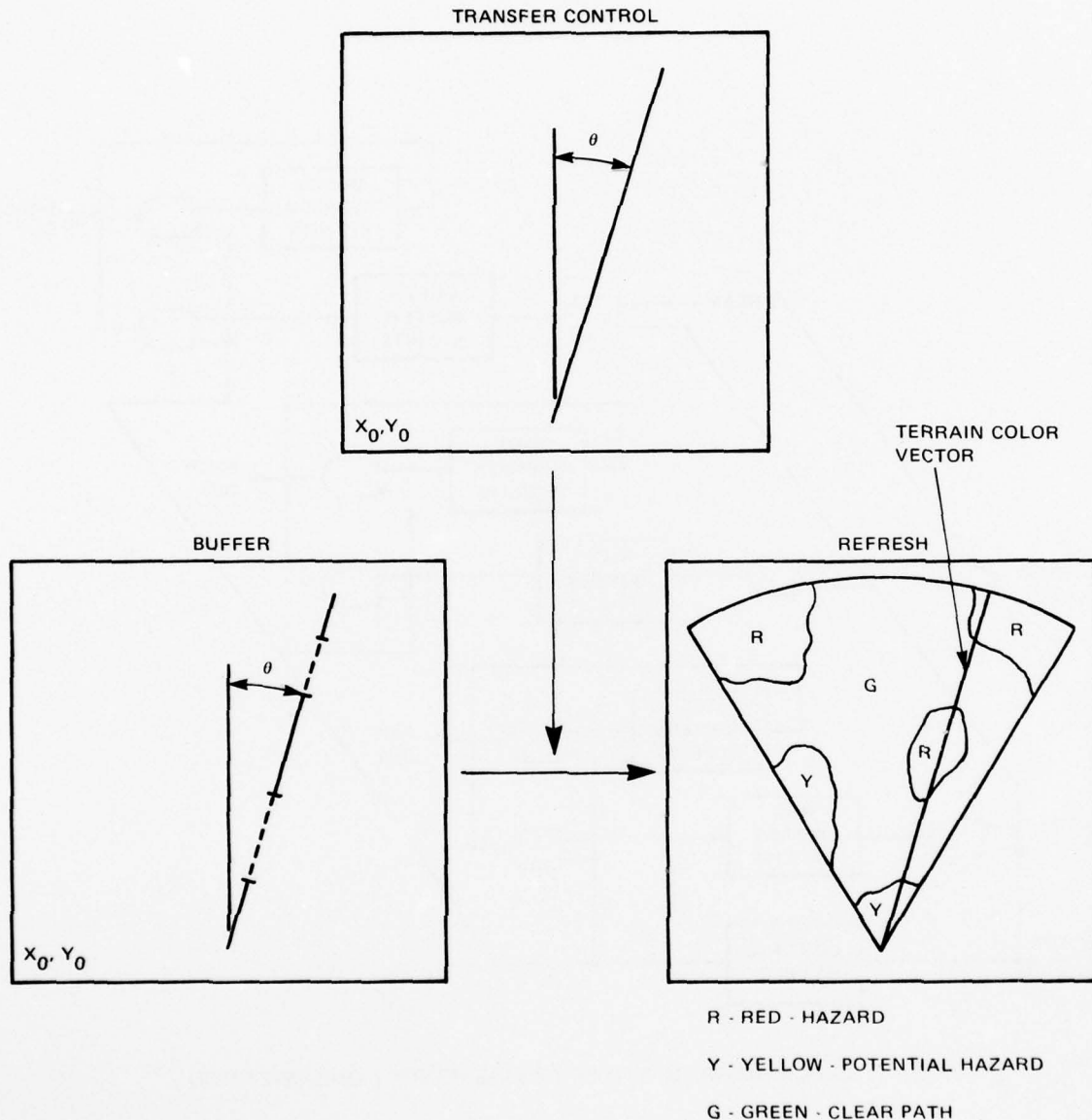


FIG. 90 DISPLAY MEMORY OPERATION, PICTORIAL SKETCH

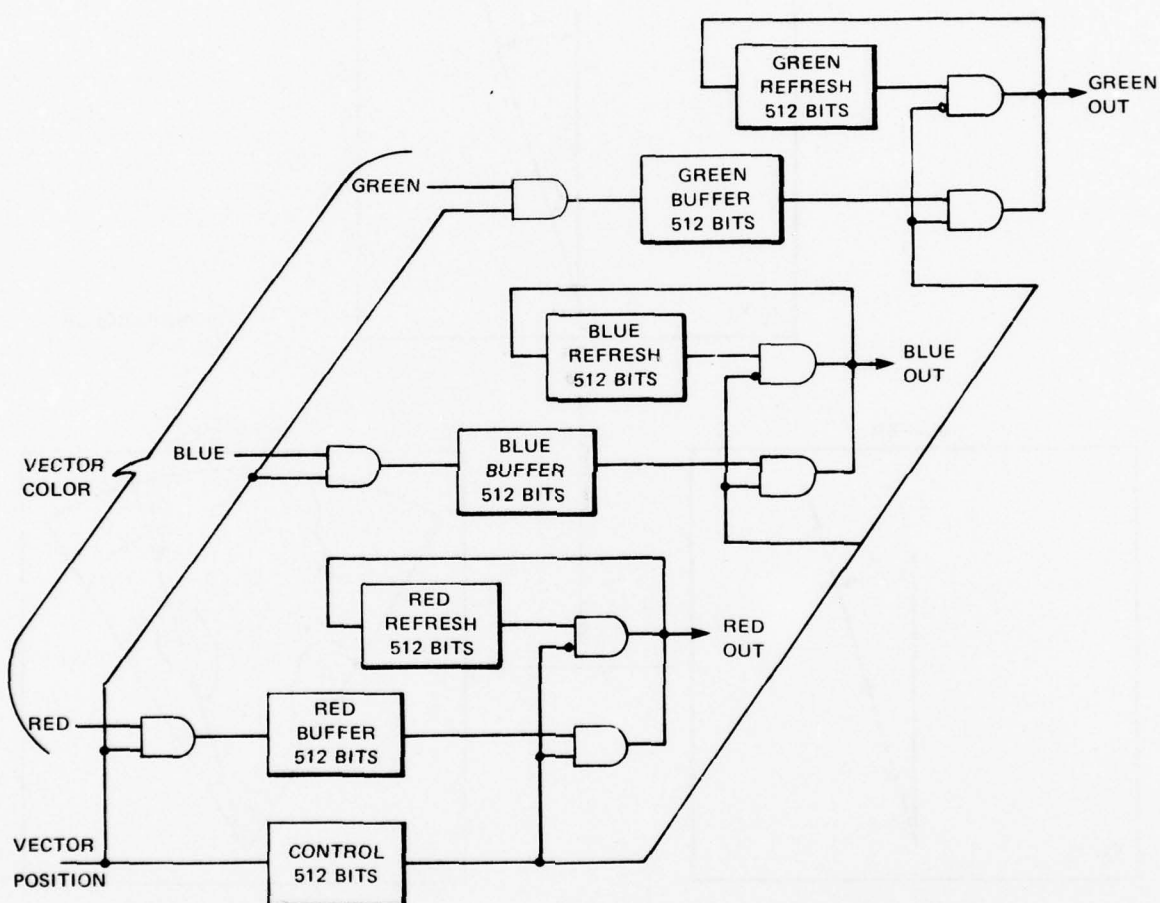


FIG. 91 BLOCK DIAGRAM, SINGLE TV LINE MEMORY ORGANIZATION

Data Processing Software

Versatility in the system and its operation is enhanced by implementing most of the control and all of the data processing functions in computer software. Two major computer programs were developed to support the experimental system tests. The first of these is a data recording and control program, and was used to record raw radar returns in digitized form from field tests. The second program is used for reading the raw-data tapes and contains all the video processing software associated with the shadowing technique.

Figure 92 is a simplified flow diagram of the data recording and control software. The program is initialized by manual entry (via the typewriter) of the desired test parameters. The program then controls the antenna scan, providing precision azimuth data to the platform controller, sets the sampling interval on the A/D converter and enables it; and transfers digitized video from the converter into computer memory. Once the data are in the computer, three options are available to either display, print, or record the raw data.

The primary test parameters are listed in Table 16. The most important parameter is the azimuth scan rate of the antenna. This is defined by the number of radar pulses to be processed as the antenna moves through an angle equal to the 3-dB beamwidth of the antenna pattern. Since the time required to digitize, process, and record the returns from a single pulse is dependent on the level of processing desired for a given data run, the computer software must provide precise control over antenna movement, which is accomplished in the following manner. A master hardware clock supplies an interrupt to the computer every millisecond. The software

Table 16
Experimental System Field Test Parameters

Antenna scan (hits/beamwidth)	3	5	7	10	15	20
Range bin sampling interval (ft)	5	10				
Obstacle size:						
Height (ft)	8	12	14			
Width (ft)	4	8	12	16		
Obstacle range (ft × 10 ³)	2	3	6	10		
Number of obstacles	1	2	3			
Obstacle shape		Rectangular		Triangular		

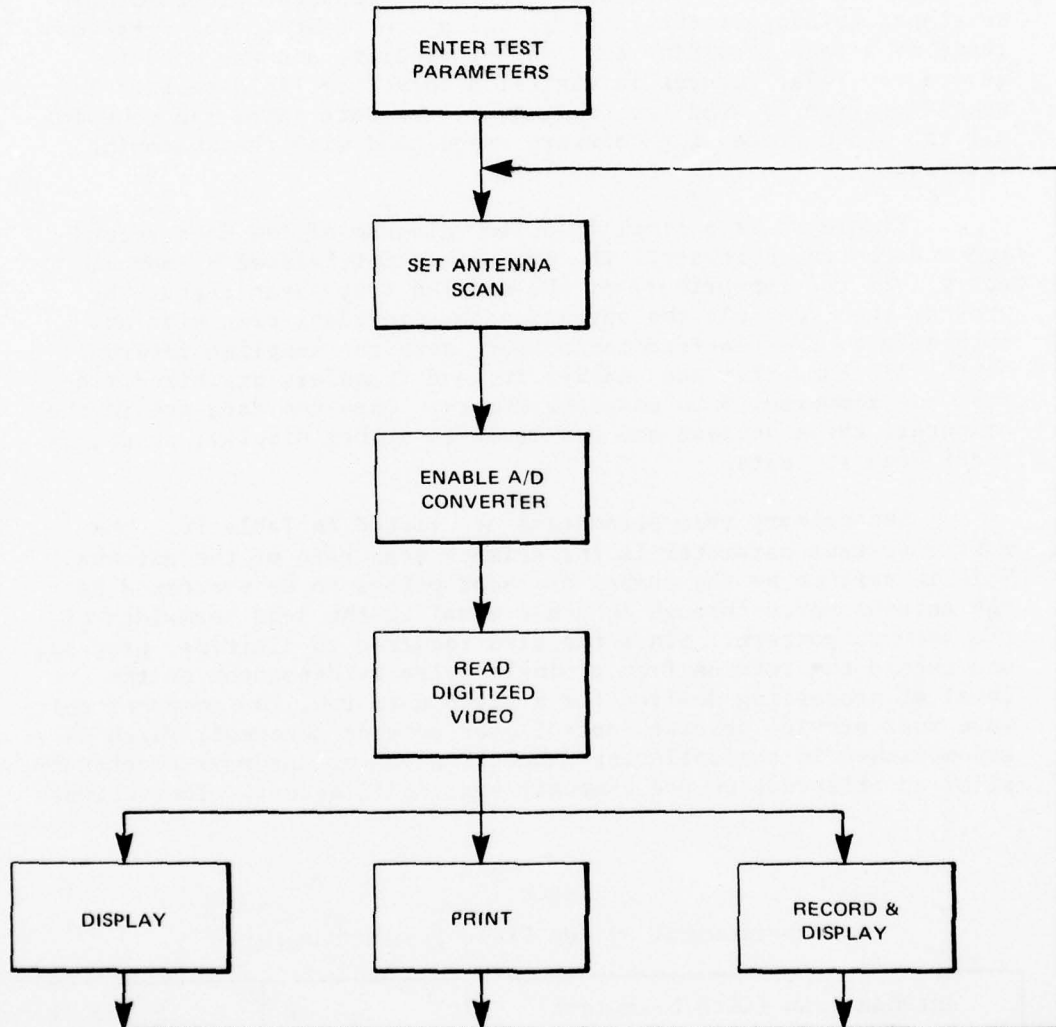


FIG. 92 EXPERIMENTAL SYSTEM RECORD AND CONTROL SOFTWARE

that responds to this interrupt counts the number of interrupts that occur during a complete processing cycle. It thus measures the actual time between processed pulses or the effective PRF of the radar. The same software commands the azimuth drive on the antenna to move one position on the precision shaft encoder (LSB ≈ 0.1 mrad or 1/20 beamwidth) at the proper time interval based on the number of hits/beamwidth desired. On each radar trigger pulse, the 16-bit shaft encoder is read and made available to the computer. These raw azimuth data are saved on each radar pulse that is processed and recorded. Figure 93 is a plot of actual shaft encoder outputs for a particular data run operating at 10 bits/beamwidth. It is seen that the deviation of the actual data from a straight line is about one resolution element on the shaft encoder.

Once the desired target is set up in the field, it must be located both in range and azimuth relative to the antenna. This is most easily accomplished by using the color display and displaying color-coded, thresholded video over an azimuth/range sector that is believed to contain the target. The total angle over which data are to be taken is set by the operator and entered into the computer prior to the start of the data run. The starting data range is adjusted by manually setting the delay time on the A/D converter. Successive scans allow proper setting of these limits. Once the target is properly located in the data sector, the data recording software is enabled on subsequent test scans. At the beginning of each new scan, one record that defines all the test parameters associated with that scan is put on tape.

The various options in the overall program are controlled by one memory location in the software and are therefore easily changed.

The second program is used for reading the raw-data tapes and includes all the radar-shadowing data-processing software. A functional flow diagram of the software is shown in Fig. 94. The program provides many options for printing and/or displaying data at all levels of processing. The processing functions include the following, in the order shown.

1. Search: a search routine used to select a data run containing specific test parameters. These test parameters are the size, shape, and number of targets used in the test, and the azimuth scan rate expressed as the number of radar hits per 3-dB beamwidth.
2. Range Processing: the raw radar returns on the data tapes, quantized in 5-ft (10 ns) range bins. In order

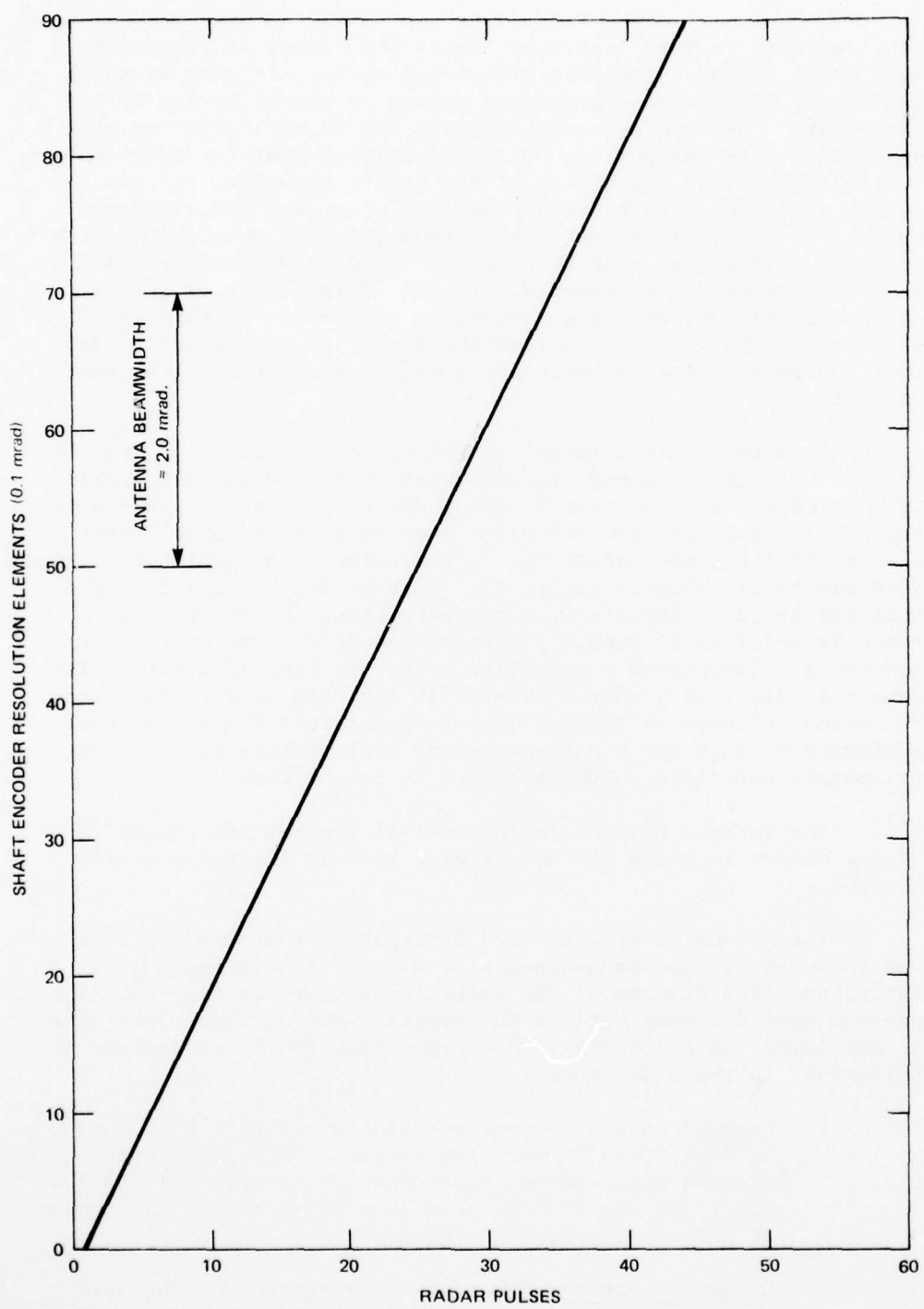


FIG. 93 SHAFT ENCODER AZIMUTH PLOT ANTENNA SCAN
AT 10 HITS/BEAMWIDTH

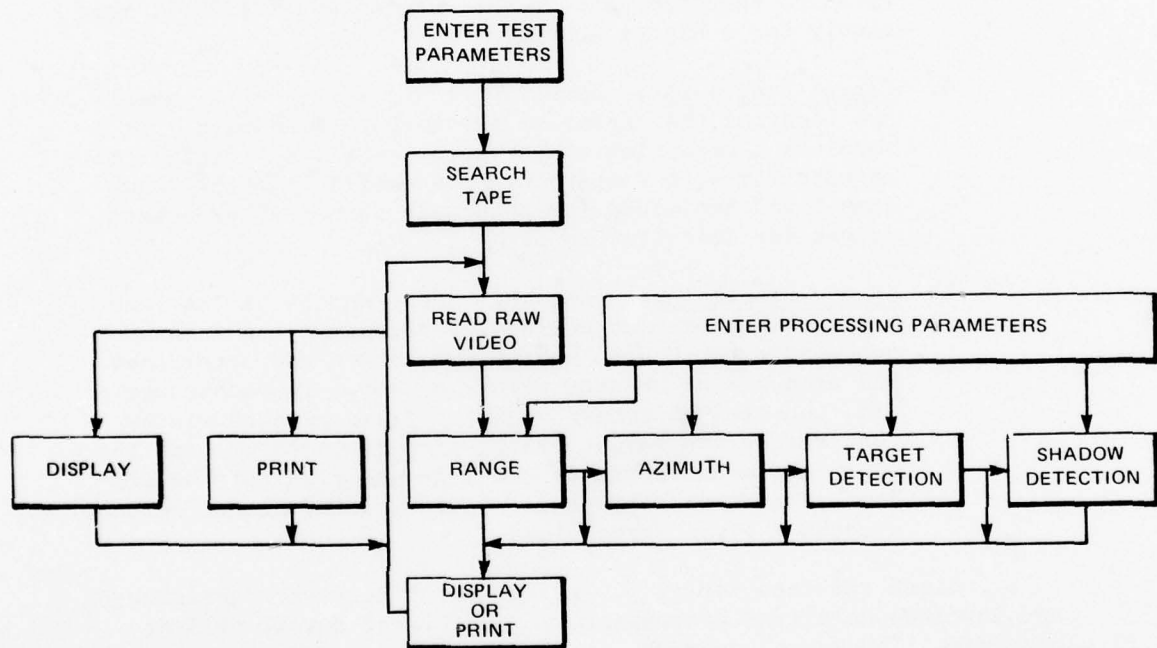


FIG. 94 EXPERIMENTAL SYSTEM-PLAYBACK SOFTWARE

to minimize processing times and to process in range bins more consistently with the radar pulse width (0.1 μ s), the raw data are averaged to provide a single return in a 50- to 100-ft range bin. The output can be either the average or the peak value, depending on the variance of the 5-ft data.

3. Azimuth Processing: The 50- to 100-ft range data processed in azimuth, using weighted azimuth averaging. The weighting function is simply the two-way antenna pattern normalized to unity at the center of the pattern. The average return in each range bin is recalculated using the weighted data from adjacent azimuth cells at the same range. The weighting function is related to the scan rate of the antenna and falls off more slowly for a higher number of hits.
4. Target Processing: detecting the presence of a target and locating the center of the target in azimuth. It involves examination of the return amplitude profile in azimuth for each range bin. The profile must be above some fixed amplitude for a certain number of processed pulses for detection to occur.
5. Shadow Processing: enabling of the shadow process once a target has been detected. It processes the data in successive range bins behind the target and determines the presence or absence of the shadow. In each range bin, the minimum return within a fixed azimuth window centered on the target center line is compared with the average ground return to the left and right of the window. Shadow conditions are satisfied if this difference exceeds a given threshold.

Since the tape search process is relatively straightforward and involves no actual processing, no additional detail will be provided. The range, azimuth, target, and shadow processes operate on the actual radar returns. Each process is now covered in detail with definition of the inputs and outputs including associated processing parameters, which are considered to be variable and subject to evaluation. A software flow diagram is also included for each process.

Range Processing

The raw analog logarithmic video is sampled at an extremely high rate (5- or 10-ft ranges) to ensure no loss of raw data. The A/D converter takes only a 10-ns sample of the input voltage

THE JOHNS HOPKINS UNIVERSITY
APPLIED PHYSICS LABORATORY
LAUREL, MARYLAND

regardless of the time between samples. No analog integration is performed between samples within the converter.

Integration of the raw video to longer range bins (50 to 100 ft) that are more compatible with the radar pulse width (0.1 μ s) is accomplished in software. This is accomplished by simply averaging the raw digitized video over the length of the desired processed range bin. If a high-amplitude return occurs within a processed range bin, the computer integrated or averaged return can be subject to error for two reasons: First because of the aperture time of the A/D converter, the digital samples on the leading or trailing edge of the pulse (i.e., where dv/dt is very high) are subject to considerable error, and second, a computed average would be biased low relative to the peak return amplitude. At the top of the pulse, the A/D error is very small (dv/dt is very small). Under these conditions, it is more desirable from a target detection standpoint to retain the peak amplitude in the processed range bin, as opposed to the average return. Therefore, over each processed bin, both the peak value and average value are computed. In addition, the variance in the raw data is computed and compared against a fixed variance threshold. If the measured variance exceeds the threshold, the peak video is retained for further processing. If not, the averaged video is used.

The variance threshold is considered to be a variable processing parameter. Its value is typically set such that the peak value is used when the standard deviation of the raw data exceeds 3 dB (variance greater than 9 on a dB scale).

Table 17 lists all these inputs, variable parameters, and output for the range processor. The number (RRCNT) and length (RRBIN) of the raw data range bins and the video data (RRVID) are read from the test parameter record associated with each data scan. The processed range bin length (RPBIN) and variance threshold (RVTHRS) are selected by the operator and manually entered via the teletypewriter. The number of processed range bins (RPCNT) and the number of raw data bins per processed bin (DRCNT) are computed via the following equations:

$$DRCNT = \frac{RPBIN}{RRBIN} \quad (14)$$

$$RPCNT = \frac{RRCNT}{DRCNT} \quad (15)$$

Then for each set of DRCNT raw video samples, the average and peak value, and the variance are computed as follows:

THE JOHNS HOPKINS UNIVERSITY
 APPLIED PHYSICS LABORATORY
 LAUREL, MARYLAND

Table 17
 Range Processing

Definition	Symbol
Inputs	
Raw-video samples	RRVID(L)
Total number of raw-data range bins	RRCNT
Raw-video range-bin length	RRBIN
Number of raw bins per processed bin	DRCNT
Total number of processed bins	RPCNT
Variable Parameters	
Processed range-bin length	RPBIN
Variance threshold on raw data	RVTHRS
Outputs	
Range processed video	RPVID(J)
Variance of raw data	RPVAR
Average value of raw data	RPAVE
Peak value of raw data	RPEAK

$$RPAVE(J) = \frac{\sum_{K=1}^{DRCNT} [RRVID(K)]}{DRCNT} \quad (16)$$

$$RPEAK(J) = \text{Maximum value of RRVID}(K) \text{ for } K = 1, 2, 3, \dots, DRCNT \quad (17)$$

$$RPVAR(J) = \frac{\sum_{K=1}^{DRCNT} [RRVID(K)]^2 - (DRCNT)(RPAVE)}{DRCNT} \quad (18)$$

The range processed video (RPVID) is then set subject to the determined variance:

$$\begin{aligned} \text{RPVID}(J) &= \text{RPAVE} \text{ if } \text{RPVAR} < \text{RVTHRS} \\ &= \text{RPEAK} \text{ if } \text{RPVAR} \geq \text{RVTHRS} \end{aligned} \quad (19)$$

The software flow diagram showing the sequence of operations is shown in Fig. 95. Figure 96 is a range amplitude profile plot from an actual radar return recorded in the field. This figure shows the relationship between the various inputs and outputs. The high-amplitude returns in the middle processed range bin are from one of the test targets.

Azimuth Processing

The range processing provides some filtering of the raw radar data. However, close examination of many sets of range-processed data revealed that there was still considerable noise in successive (azimuth) radar hits. This was true for both target and normal ground returns. Since subsequent target and shadow detection processing involve azimuth profiles of the return amplitude, it was necessary to do some additional filtering in the azimuth direction.

The simplest form of azimuth filtering is a sliding averager; i.e., an averager in which a running average of the returns in some range bin in azimuth is taken over a fixed number of hits to determine the return on the center hit. The approach given would tend to change the shape of the azimuth profile when there are large changes in the return amplitude; also it would reduce the peak return on very narrow targets (i.e., targets less than the averager width). In order to alleviate this problem, a weighted averaging process is used. The weighting function used in the processing of these test data is the two-way linear gain of the transmit/receive antenna. The center point in this weighting function is normalized to unity, and increasing distance from the center point results in a decreasing fractional weighting. The expression used to model the two-way antenna pattern is the following:

$$G(\theta_i) = 10^{-4} (1 - \cos \theta_i) ,$$

where $\theta_i = i \cdot (\pi/2) / (\text{antenna scan rate in hits/3 dB beamwidth})$

and $i = 0, 1, 2, 3, \dots$ up to the number of hits/beamwidth.

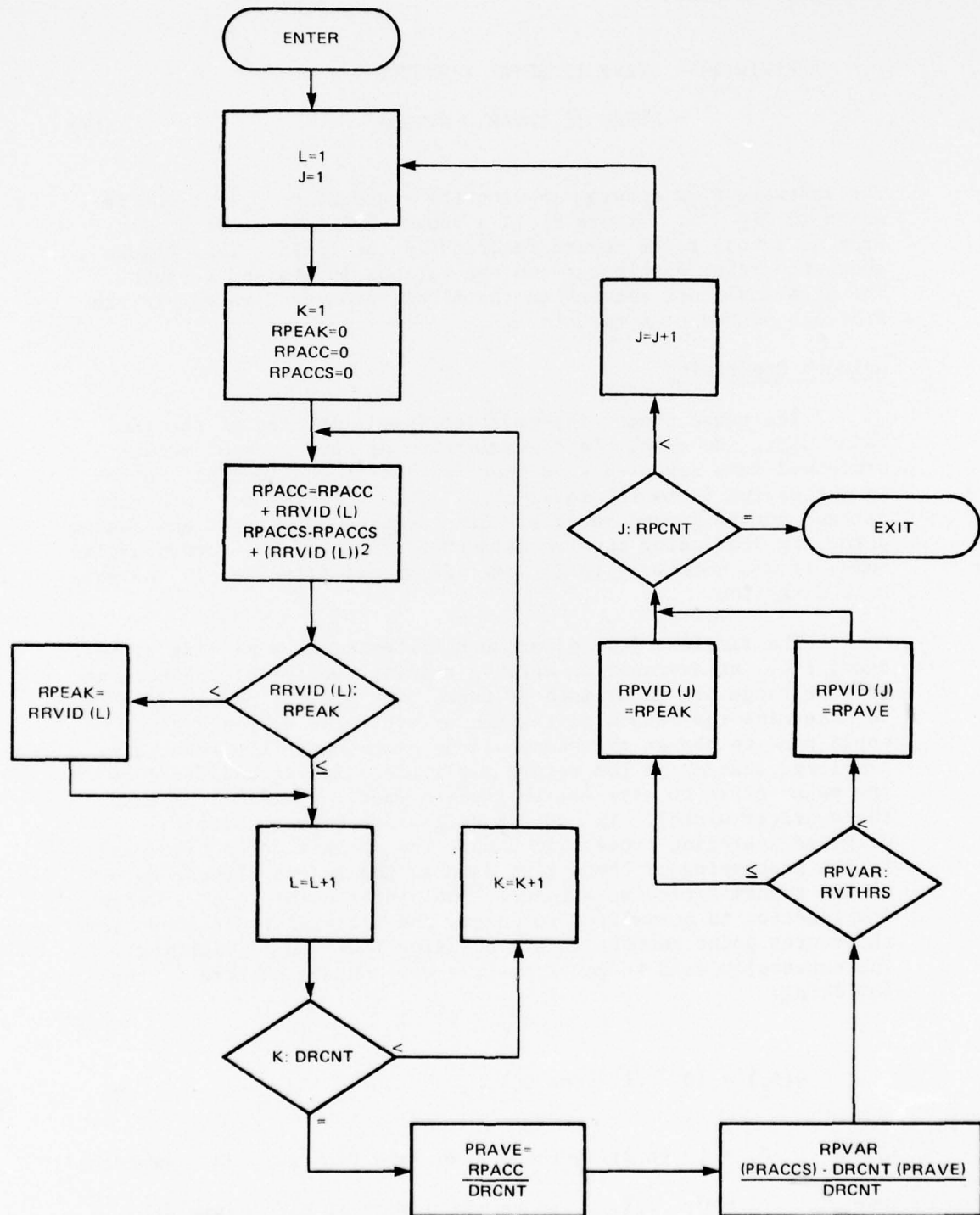


FIG. 95 FLOW DIAGRAM, RANGE PROCESSING

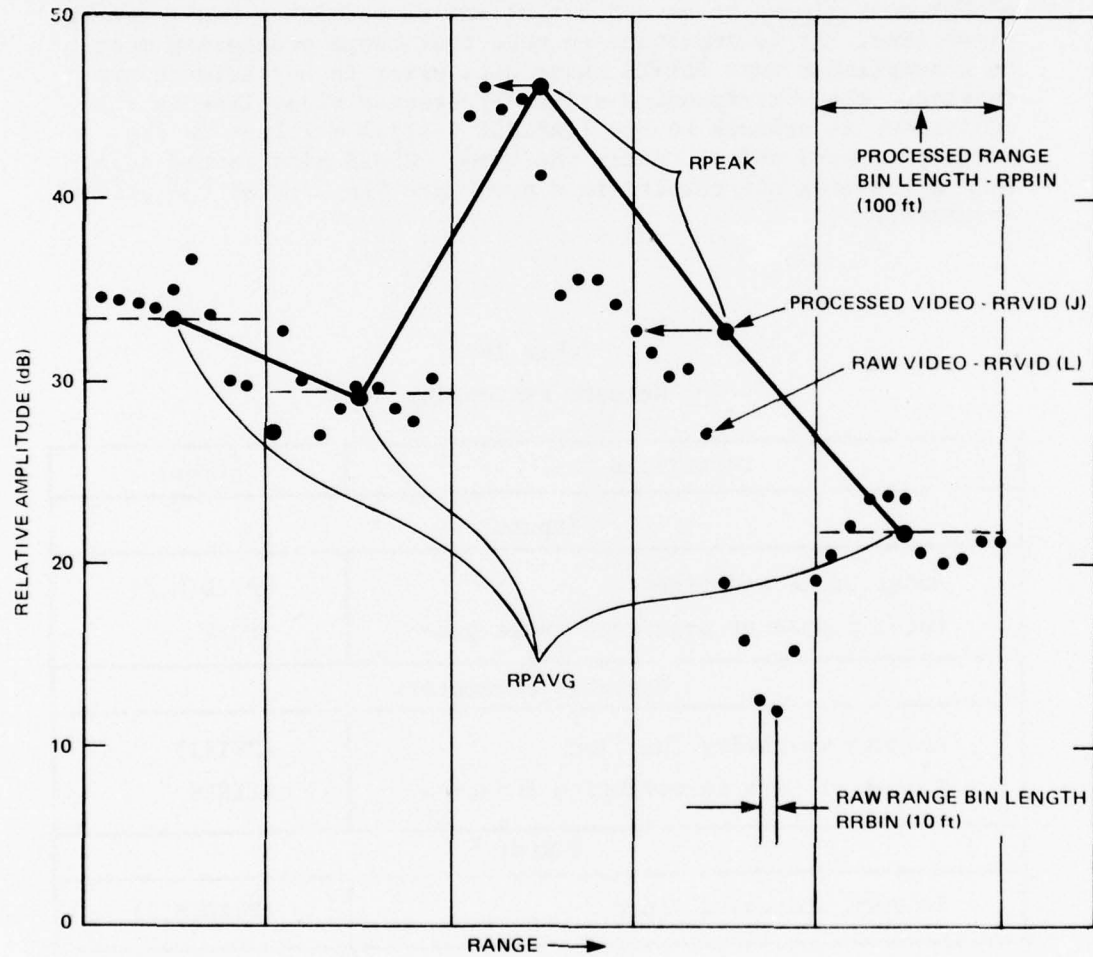


FIG. 96 RANGE PROCESSING

This weighting function worked very well in retaining the original shape of the azimuth profiles and still removing most of the noise.

Table 18 lists the inputs, output, and variable parameters for the azimuth video processor. The variable parameters include the width of the weighting function (AZLNES) in terms of the number of radar pulses and the shape of the function (AZWT(I)). AZLNES must always be an odd number and therefore it has a center video line. It is important to note that range processing must be accomplished over AZLNES radar hits prior to any azimuth processing. The corresponding azimuth-processed video line is then equivalent in azimuth to the $[(AZLNES - 1)/2] + 1$ line in the range processed video. After the first AZLNES hits in the scan, each succeeding hit results in a new video line out of the azimuth processor.

Table 18
Azimuth Processing

Definition	Symbol
Inputs	
Range processed video	RPVID(M,J)
Total number of processed range bins	RPCNT
Variable Parameters	
Azimuth weighting function	AZWT(I)
Number of hits in weighting function	AZLNES
Output	
Azimuth processed video	APVID(M,J)

The basic equation implemented in the azimuth processor is the following:

$$APVID(M, J) = \frac{\sum_{I=-(\frac{AZLNES-1}{2})}^{+(\frac{AZLNES-1}{2})} [AZWT(I) * RPVID(M+I, J)]}{\sum_{I=-(\frac{AZLNES-1}{2})}^{(\frac{AZLNES-1}{2})} AZWT(I)} \quad (20)$$

The expression in the denominator is simply the area under the weighting function and normalizes the APVID output to the RPVID input video level. It is noted that a simple averager is implemented by setting AZWT equal to unity at each point.

Figure 97 is a software flow diagram of the azimuth processor showing the sequence of operations. A graphical illustration of the process is shown in Fig. 98. This is a plot of video amplitude (in dB) versus azimuth (measured in radar hits) in a single range bin. The azimuth weighting coefficient is plotted on a linear amplitude scale and is shown for AZLINES equal to 9. The range and azimuth processed video are derived from actual raw data taken at a scan rate of 10 hits/beamwidth. As can be seen, there is considerable smoothing of the data in azimuth. Figure 99 is a profile similar to Fig. 98, but taken through a range bin containing one of the test targets. Here it is seen that the noise in ground return to the left and right of the target is reduced considerably while the basic profile of the target return is not distorted to any great extent.

Target Detection

The main purpose of the target detection logic is to determine the existence of an obstacle or target. Two items of data concerning the target are required, the azimuth line at the center of the target and some estimate of the width of the target. Target center line data are required to properly position the shadow processing in azimuth. In other words, radar shadow conditions should be the best along a line directly behind the center of the target. Target width data could be used to set the width on the shadow processing.

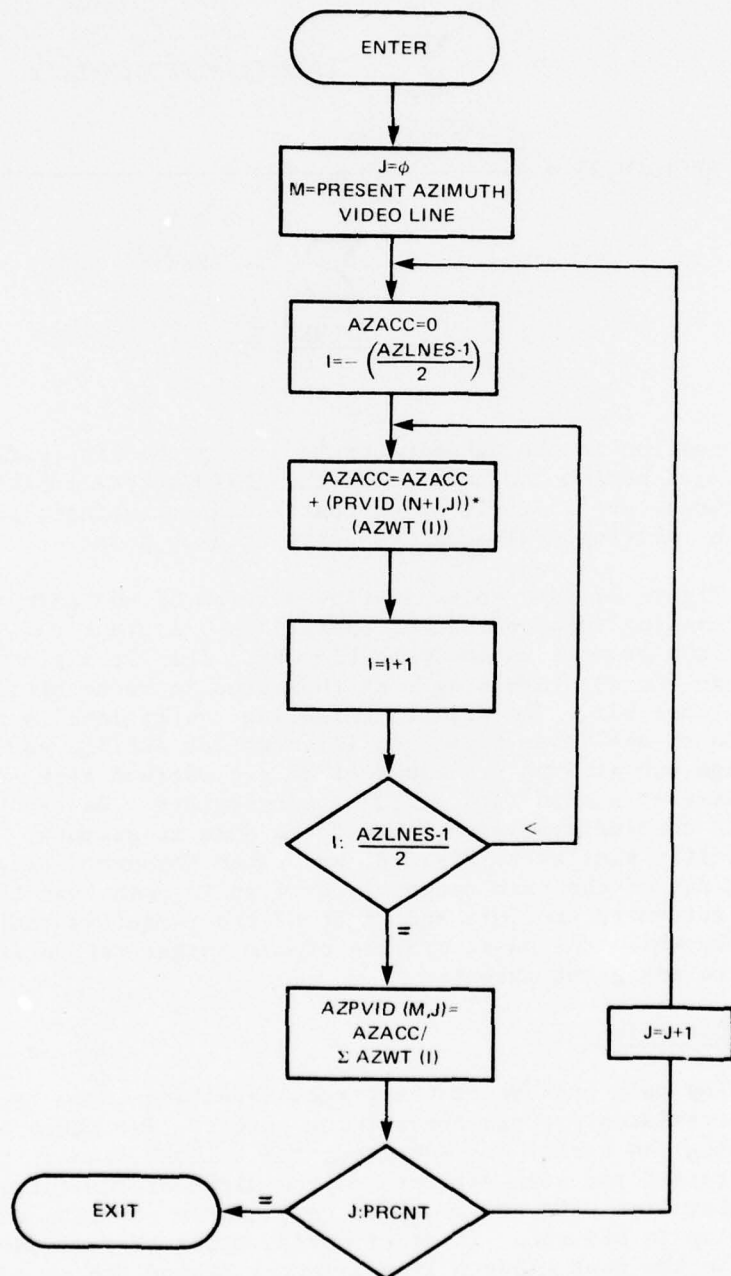


FIG. 97 FLOW DIAGRAM, AZIMUTH PROCESSING

THE JOHNS HOPKINS UNIVERSITY
APPLIED PHYSICS LABORATORY
LAUREL, MARYLAND

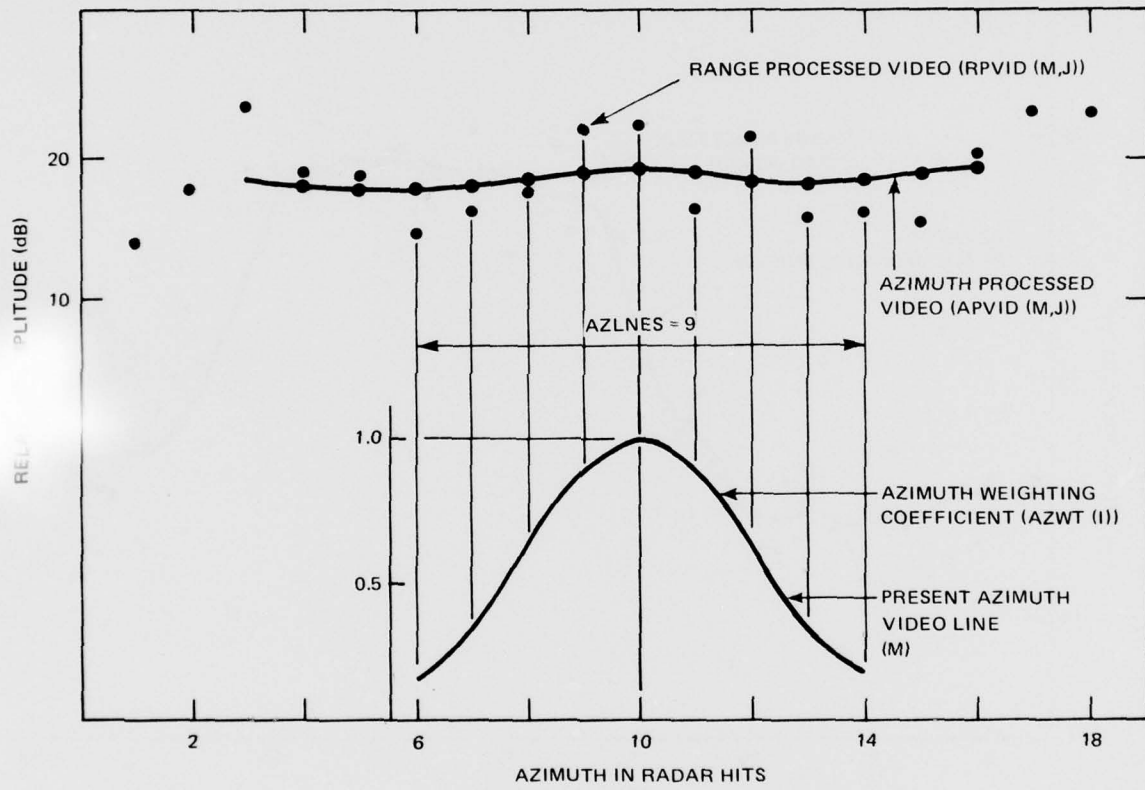


FIG. 98 AZIMUTH PROCESSING

THE JOHNS HOPKINS UNIVERSITY
APPLIED PHYSICS LABORATORY
LAUREL MARYLAND

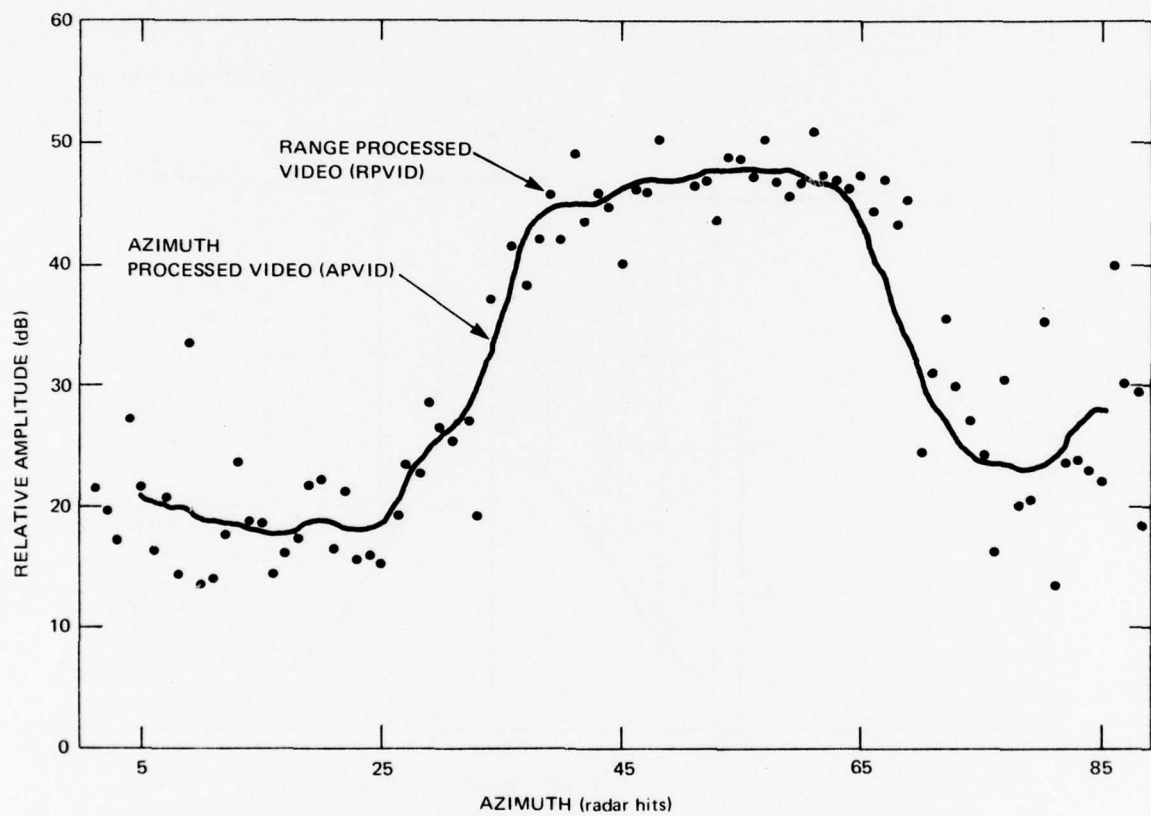


FIG. 99 TYPICAL TEST TARGET, AZIMUTH PROFILE

Basic Philosophy

It is assumed that any obstacle of significant physical size will provide a radar return that is considerably above the ground-radar return level in the adjacent area. This assumption was verified in the preliminary field tests conducted at Pt. Barrow.

Although target detection is an important aspect of the overall obstacle height-determining problem, the primary concern here is shadow detection. Therefore, a relatively simple target detection logic has been implemented, and its parameters have been somewhat tailored to the recorded field-test data.

The logic involves examination of the azimuth-return amplitude profiles in successive range bins using azimuth-processed video for the input. The requirement for target detection is that the return exceed some fixed amplitude threshold over a minimum number (also fixed) of radar hits. In other words, there are minimum requirements on the height and width of the azimuth amplitude profile. The azimuth is in terms of radar pulses and is therefore related to the antenna azimuth-scan rate.

In the actual target detection software, a wide processing window (about four beamwidths) is used. In addition to the height and width requirements described previously, a third condition for target detection is that the center of the azimuth profile be within one radar pulse of the center of the processing window. This provides maximum ground-return data on both sides of the shadow region. If the amplitude threshold is exceeded for the entire width of the processing window, target detection requirements are also considered to be met.

Table 19 lists the inputs, variable parameters, and output for the target processor. The variable parameters include a target detection amplitude threshold (TTHRS), and the total target processor width (TPLNES) and minimum target detection width (TDLNES) both expressed in number of radar hits. TPLNES must always be an odd number and therefore has a center video line. (Note that azimuth processing must be accomplished over TPLNES radar hits prior to any target processing.) The relationship between AZLNES and TPLNES is shown in Fig. 100. The first center line of TPLNES occurs ($\frac{AZLNES + TPLNES}{2} + 1$) radar hits after the beginning of the data scan. From that point on, each new video line read from the tape moves the entire process as seen in Fig. 100 one radar pulse to the right.

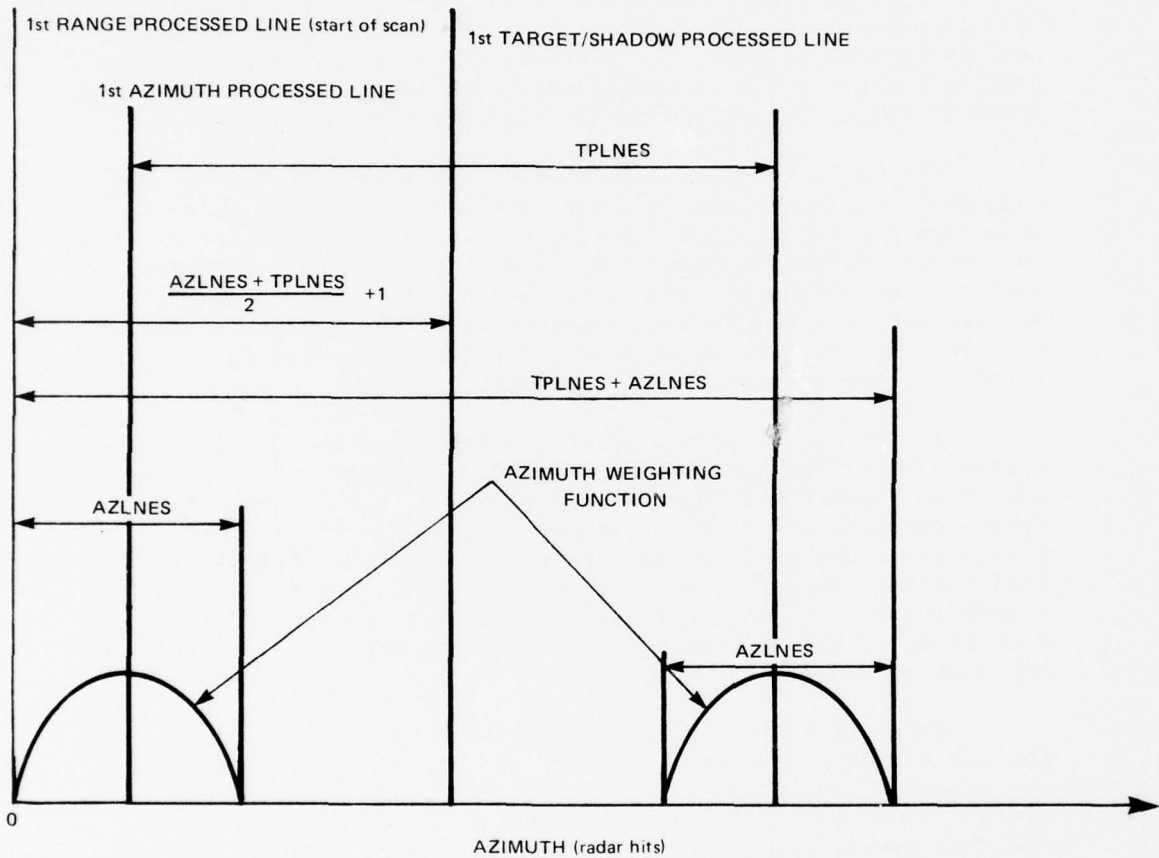


FIG. 100 AZIMUTH RELATIONSHIP BETWEEN AZIMUTH AND TARGET PROCESSES

Table 19
Target Processing

Definition	Symbol
Inputs	
Azimuth processed video	APVID(M,J)
Total number of processed range bins	RPCNT
Variable Parameters	
Target detection amplitude threshold	TTHRS
Target processor width (radar hits)	TPLNES
Target detection width (radar hits)	TDLNES
Output	
Target range-bin number	TRNGE

Figure 101 is a software flow diagram showing the sequence of operations performed. This process covers a single range bin only and the target range bin number (RNGE) is set equal to the present range bin if target conditions are satisfied. If no target is present, TRNGE = 0.

Figure 102 illustrates the target processing operation against actual field-test data. It is a plot of radar return amplitude as seen at the output of the azimuth processor versus antenna azimuth as measured in number of radar hits. The antenna scan rate is 10 bits per beamwidth. With the target detection threshold (TTHRS) set to approximately 32 dB, the measured target width is 16 radar hits. Target detection conditions are satisfied for a minimum detection width (TDLNES) of 10 hits. The target centerline is also at the midpoint of the target processing width (TPLNES).

Shadow Processing

Shadow-processing software was initially developed on the assumption that the radar-shadow trough (region of low-level return or receiver noise only) would follow in a straight line behind the target. It was also assumed that the average level of the return along this line would increase appreciably at ranges beyond

THE JOHNS HOPKINS UNIVERSITY
APPLIED PHYSICS LABORATORY
LAUREL, MARYLAND

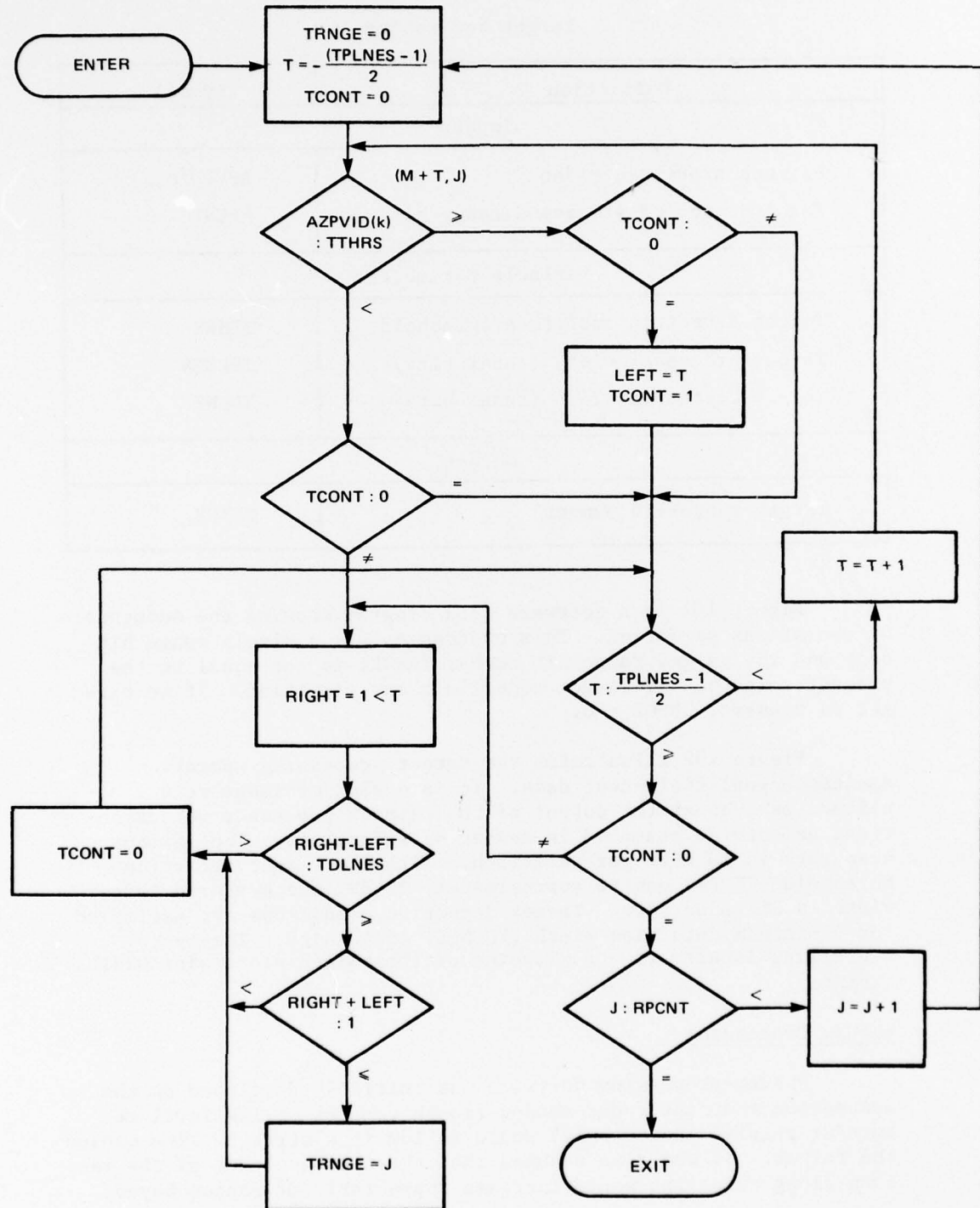


FIG. 101 FLOW DIAGRAM, TARGET PROCESSING

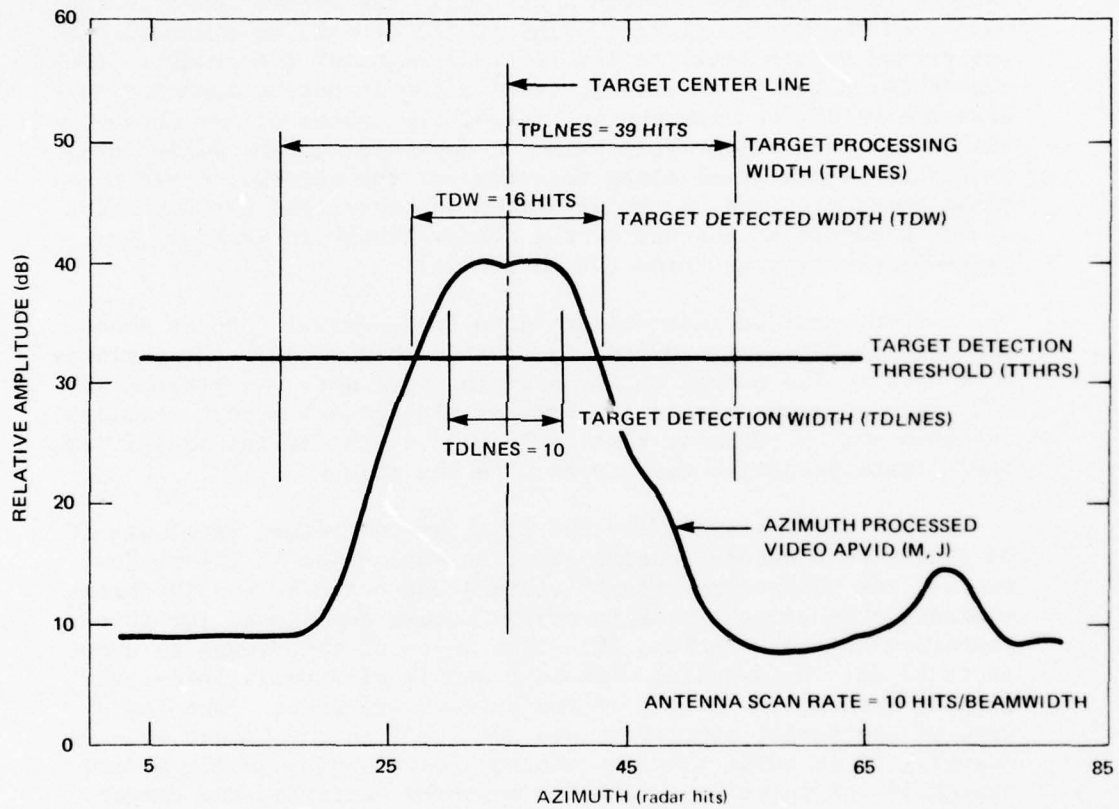


FIG. 102 TARGET PROCESSING

the end of the shadow; therefore, a simple shadow processor was implemented that determined the average return level over some range (e.g., 400 ft) and some number of radar hits centered on the target centerline. A reasonable increase in this average return level is successive 400-ft range bins then defined the end of the shadow.

This process was found to be unreliable for the following reasons. First, since the target detection logic did not always find the exact azimuth center of the target, the shadow processor would be positioned on the wrong azimuth line. Second, for narrow targets (3-dB antenna beamwidth or less), the return level in the center of the shadow (lowest point in the trough) is a function of the ground return level to the left and right of the shadow. Consequently, a change in average level alone is not necessarily indicative of shadow termination. Also, the center of the shadow trough can vary slightly in azimuth, depending on the difference in ground return level along the sides of the shadow. Based on these considerations, a new algorithm was developed for detection of the presence or absence of the shadow trough in each of the range-processor range bins (50 to 100 ft).

The recorded radar-return data from several antenna scans and test setups were examined in considerable detail. Comparisons were made at the output of the azimuth processor. An attempt was made to find some correlation between the azimuth return profiles in known shadow regions, that could lead to the definition of some basic characteristics associated with the shadow.

For those areas where the radar ground-return level was 10 to 15 dB above receiver noise level on both sides of the shadow region, the shadow was clearly visible and could be easily characterized. The azimuth profile of the return amplitudes for this situation is shown in Fig. 103. The depth of the trough is about 12 to 13 dB. Here again, this is a sample of actual field-test data as seen at the output of the azimuth processor. The position of the target centerline was derived from the Target Processor. It is noted that the minimum return point in the shadow trough is not coincident with the measured center of the target.

In many instances, the adjacent ground return level was high on only one side of the shadow region. This situation is illustrated in Fig. 104, which is again the azimuth return profile from a known shadow region taken from the field-test data. In this case, the shadow is even less discernible and could be interpreted as simply a change in the ground return level with no shadow actually being present. It is interesting to note the shift of the minimum detection point relative to the target centerline toward the side with the low ground return.

THE JOHNS HOPKINS UNIVERSITY
APPLIED PHYSICS LABORATORY
LAUREL, MARYLAND

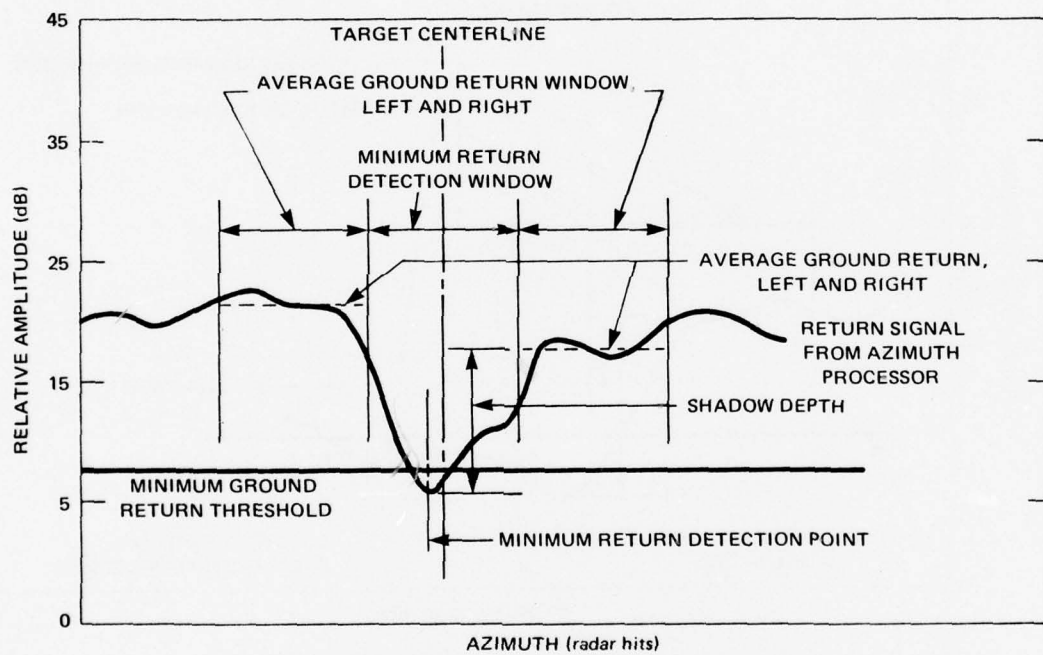


FIG. 103 SHADOW PROCESSING USED FOR HIGH GROUND RETURN, BOTH SIDES OF SHADOW

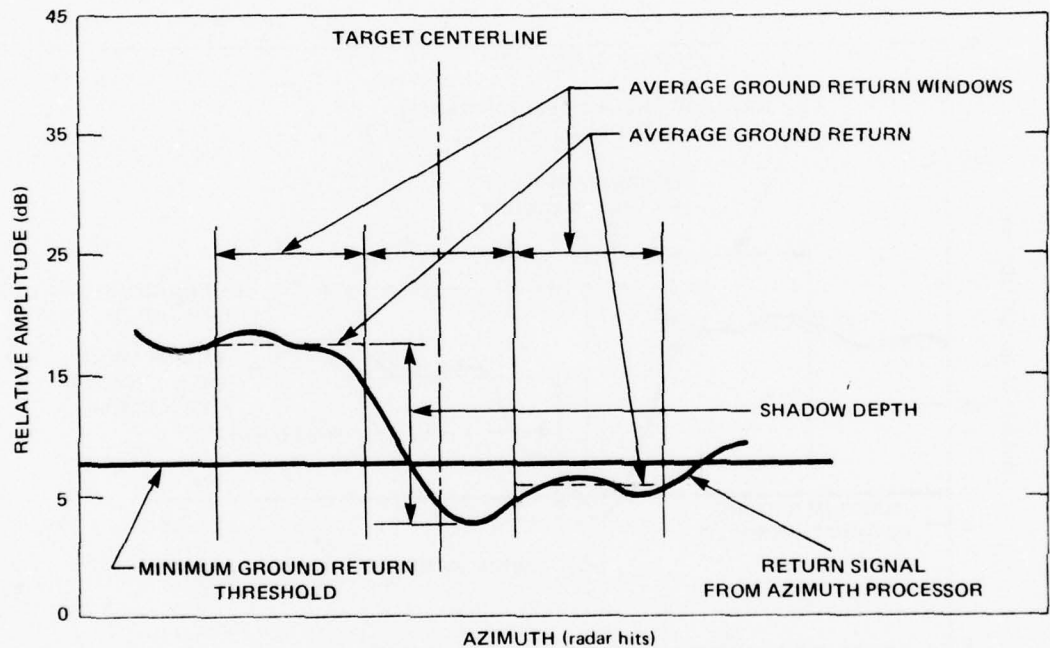


FIG. 104 SHADOW PROCESSING USED FOR HIGH GROUND RETURN,
ONE SIDE OF SHADOW

A third situation, also appearing with some consistency, was a low average return in and on both sides of the shadow region. In this case, the trough disappears completely (Fig. 105). The situation noted existed many times at ranges that were preceded and followed by the conditions shown in Fig. 103 where the adjacent ground return was high. This would seem to indicate the presence of a small (low height, but wider than the test target) obstacle in the natural terrain. Its shadow is short in range, but overlaps the target shadow in azimuth.

Based on these findings, the following shadow detection logic and associated parameters were defined. The process starts from the target centerline. Target detection requires that the return be above the target detection threshold (TDTHRS) over a fixed number of radar hits (TDLNES) in a given range bin. The center of the target is then defined as the azimuth line (a radar hit) that is halfway between the threshold crossing points. Three azimuth windows (number of radar hits) are positioned symmetrically around the target centerlines as shown in Figs. 101, 102, and 103. The two outside windows are defined as ground-return windows while the center one is called the shadow window. The widths of these windows (GRWDTH and SHWDTH) are considered to be variable parameters and are a function of antenna scan rate (hits per beamwidth). The width of the shadow window could also be a function of the target width being processed. (Table 20 lists the inputs, variable parameters, and output.)

The second operation computes the average ground-return level in each of the ground-return windows. The average levels are compared against a fixed minimum ground return threshold (GRTHRS) level. This level is also shown in Figs. 103, 104, and 105. GRTHRS is one of the variable parameters and could be made adaptable to the range from the radar. If both averages are below the threshold, the situation is indeterminate. It is assumed that the target shadow continues, and the process immediately moves to the next range bin. If both averages (left and right) are above the threshold, the lower one is retained for further processing. If only one is above the threshold, it alone is retained.

The next operation determines the minimum-return level within the shadow window, and subtracts it from the measured average ground-return level. This, then, is a measure of the depth (in amplitude) of the shadow trough, as illustrated in Figs. 103 and 104. The measured shadow depth is then compared against the minimum shadow depth threshold (SDTHRS). If the measured depth exceeds SDTHRS, shadow existence conditions are satisfied. This threshold is obviously one of the more important variable parameters.

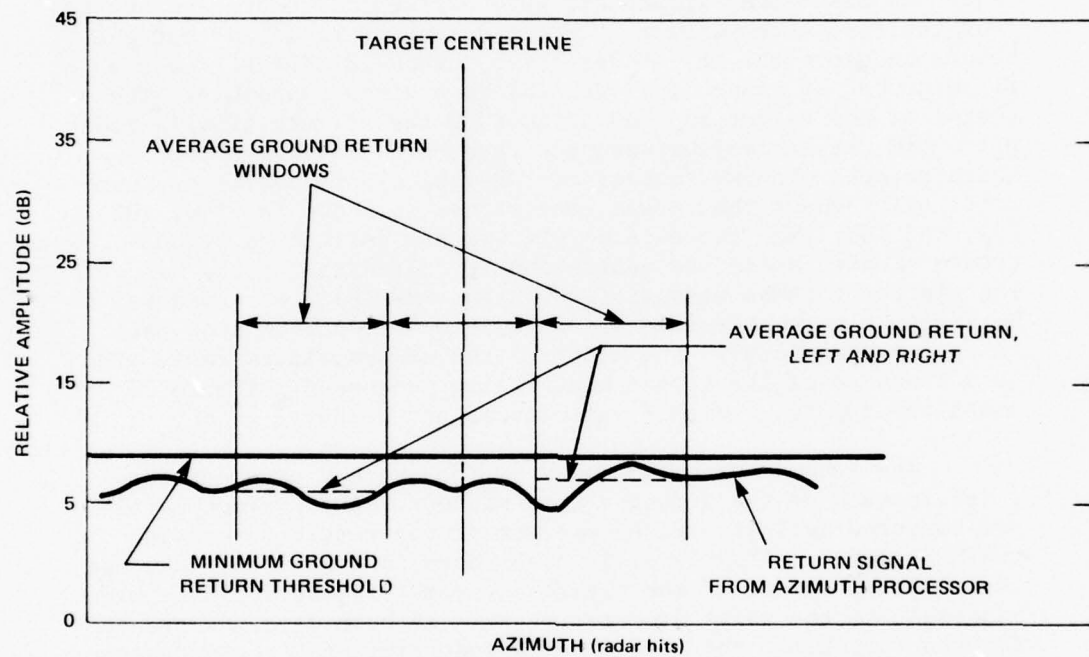


FIG. 105 SHADOW PROCESSING USED FOR LOW GROUND RETURN,
BOTH SIDES OF SHADOW

Table 20
 Shadow Processing

Definition	Symbol
Inputs	
Azimuth processed video	APVID(M,J)
Total number of processed range bins	RPCNT
Variable Parameters	
Minimum ground return threshold	GRTHRS
Minimum shadow depth threshold	SDTHRS
Width of ground return window (radar hits)	GRWDTH
Width of shadow window (radar hits)	SHWDTH
Dimensions of $M \times N$ detector	SHADM, SHADN
$M \times N$ detector length (range bins)	SHADL
Output	
Shadow length (number of processed range bins)	SRNGE

The determined shadow length is very sensitive to this threshold. With a high threshold, shadow lengths will tend to terminate prematurely, thereby indicating a low height for the obstacle. On the other hand, if the threshold is too low, normal ground return variations could satisfy the conditions for shadow detection, resulting in longer shadow lengths, and a high false-alarm rate on hazardous obstacles.

The shadow-termination logic, based on single range bin processing, was evaluated against a few field-test target situations. Invariably, the measured shadow length was shorter than the predicted length. Several different values for GRTHRS and SDTHRS were tried without success.

Additional filtering of the processed shadow data in range was implemented by a sliding $M \times N$ detector. The length of the detector (SHADL) was arbitrarily set at five range bins. M (SHADM) is the number of times the minimum ground return threshold (either to the left or right of the shadow region) is exceeded. N (SHADN)

is the corresponding number of times that the shadow depth threshold is exceeded. If the ground return threshold is not exceeded on either side, the shadow trough detection is neglected. The values of SHADM and SHADN that satisfy shadow conditions are listed in Table 21. The first detection of SHADN that does not meet these requirements terminates the shadow on the center range bin of the five-bin detector.

Table 21
Shadow-Existence Condition,
Five-Bin Sliding $M \times N$ Detector

SHADM	SHADN
5	3
4	2 of 4
3	2 of 3
2	2 of 2
1	1

SHADM = Number of average ground return detections

SHADN = Number of shadow depth detections

Figure 106 illustrates the operation of the $M \times N$ detector. The data are from two different field-test setups. The value "1" in the AR or AL lines indicates that the ground-return threshold was exceeded in that range bin in the right or left ground-return window. These lines may be interpreted as range-amplitude profiles along the center of the respective azimuth windows. A "1" in the trough line indicates either that the shadow depth threshold was exceeded, or that the ground-return level was too low on both sides, again in each range bin. The two T's in each line show the position of the test target. The vertical lines indicate the positions of the sliding $M \times N$ detectors at the shadow termination point. In the first test, $M = 3$, while $N = 1$. In the second test, $M = 5$ and $N = 2$. If the ground return threshold is not exceeded on either side, the indicated trough detection is neglected.

This data format is very useful for evaluating ground-return conditions. The ground return in the first set of data is somewhat sparse, and the actual end of the shadow is questionable. In the second set, the ground return is good over nearly all of the data range, and the shadow termination is much clearer.

THE JOHNS HOPKINS UNIVERSITY
APPLIED PHYSICS LABORATORY
LAUREL, MARYLAND

FIG. 106 SLIDING M x N DETECTOR WITH FIVE RANGE BINS

Figures 107 through 110 are software flow diagrams of the sequence operation performed. The first diagram covers the average ground return and minimum return data processing. The second diagram thresholds the ground return data, determines the shadow depth and checks it against the minimum depth threshold. The ground return and shadow troughs indicator for the $M \times N$ detector are set accordingly. The third diagram determines the values of SHADM and SHADN within the five range bin sliding window, and the last one checks these values for shadow termination conditions.

Test and Evaluation

The primary purpose of the experimental system is to provide a test bed for evaluating the radar shadowing technique as a method for measuring the height of obstacles. Considerable flexibility has been designed into the system in terms of being able to control its various parameters and determine their effect upon the height determination. Most of the data processing is accomplished in computer software and is therefore easily changed. The primary system parameters, and the ranges over which they were varied are shown in Table 16.

The azimuth scan rate of the antenna is defined by the number of radar pulses transmitted as the antenna moves through an angle equal to the 3-dB beamwidth of the antenna pattern. This is a critical parameter in detecting the presence of an obstacle and in measuring the length of its shadow. Obviously, the more hits per beamwidth that are processed, the greater the probability of correct shadow length and the consequent height determination. However, increasing the scan rate in these terms has an adverse effect on the PRF of the radar and the angular scan rate (rad/s) of the antenna. For a given PRF, the angular scan rate decreases as the hits/beamwidth increases. The proposed scan for an SEV obstacle detection system is a 60° sector scan centered on the vehicle's projected path of travel. A decreased angular scan rate has the effect of increasing the time between successive updates of the terrain data.

The range bin sampling interval is not a critical parameter for these tests. The 5- and 10-ft intervals were selected primarily to ensure no loss or distortion of the raw data, and to control the volume of recorded data.

The obstacles used for these tests consisted of simple two-dimensional plywood structures that were easily assembled to the desired size and shape in the field. The size of the obstacles varied between 8 to 14 ft in height and 4 to 16 ft in width. The shape of the top of the target could be either rectangular or

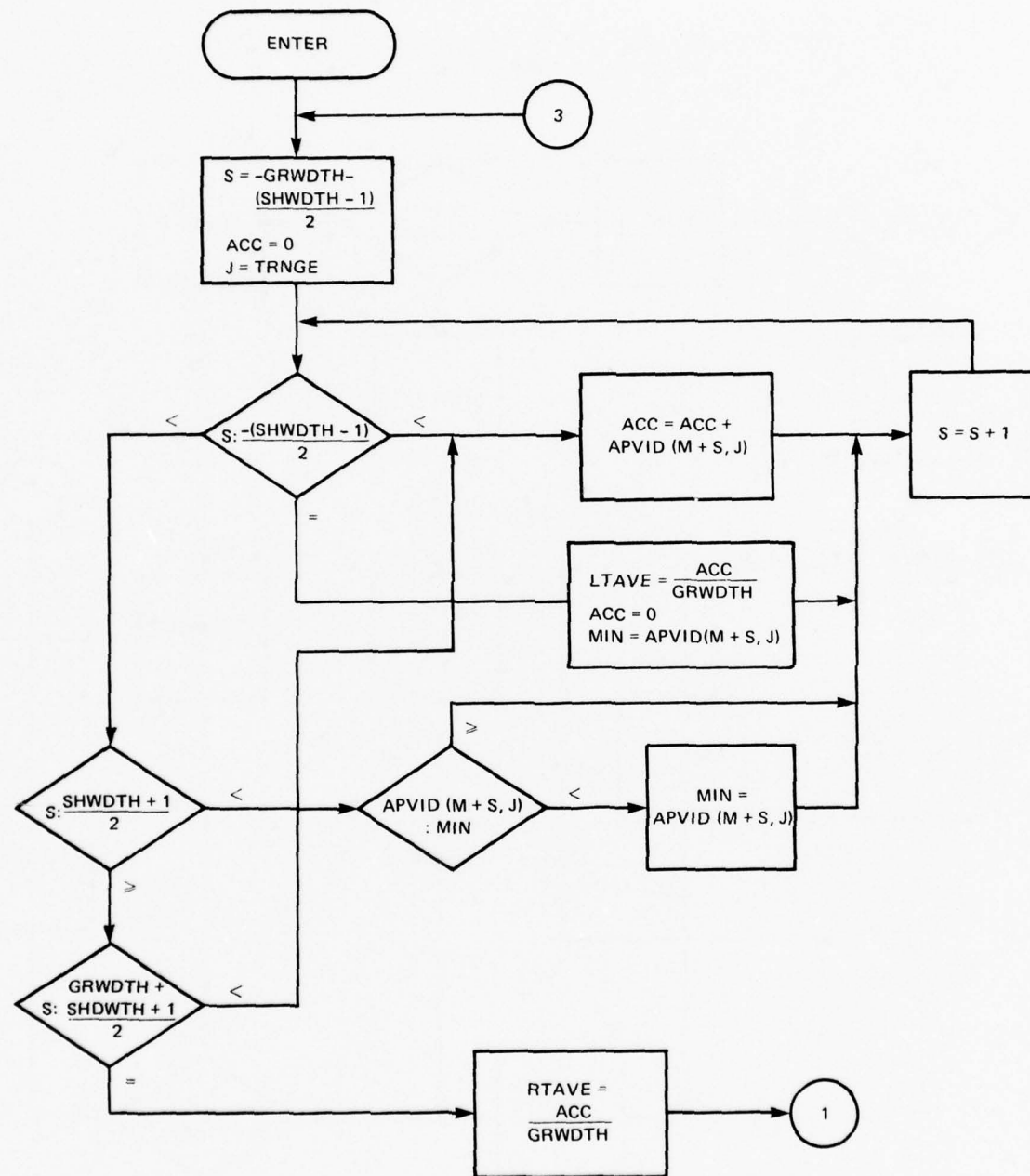


FIG. 107 SHADOW PROCESSOR FLOW DIAGRAM: DETERMINE AVERAGE GROUND RETURN AND MINIMUM SHADOW RETURN

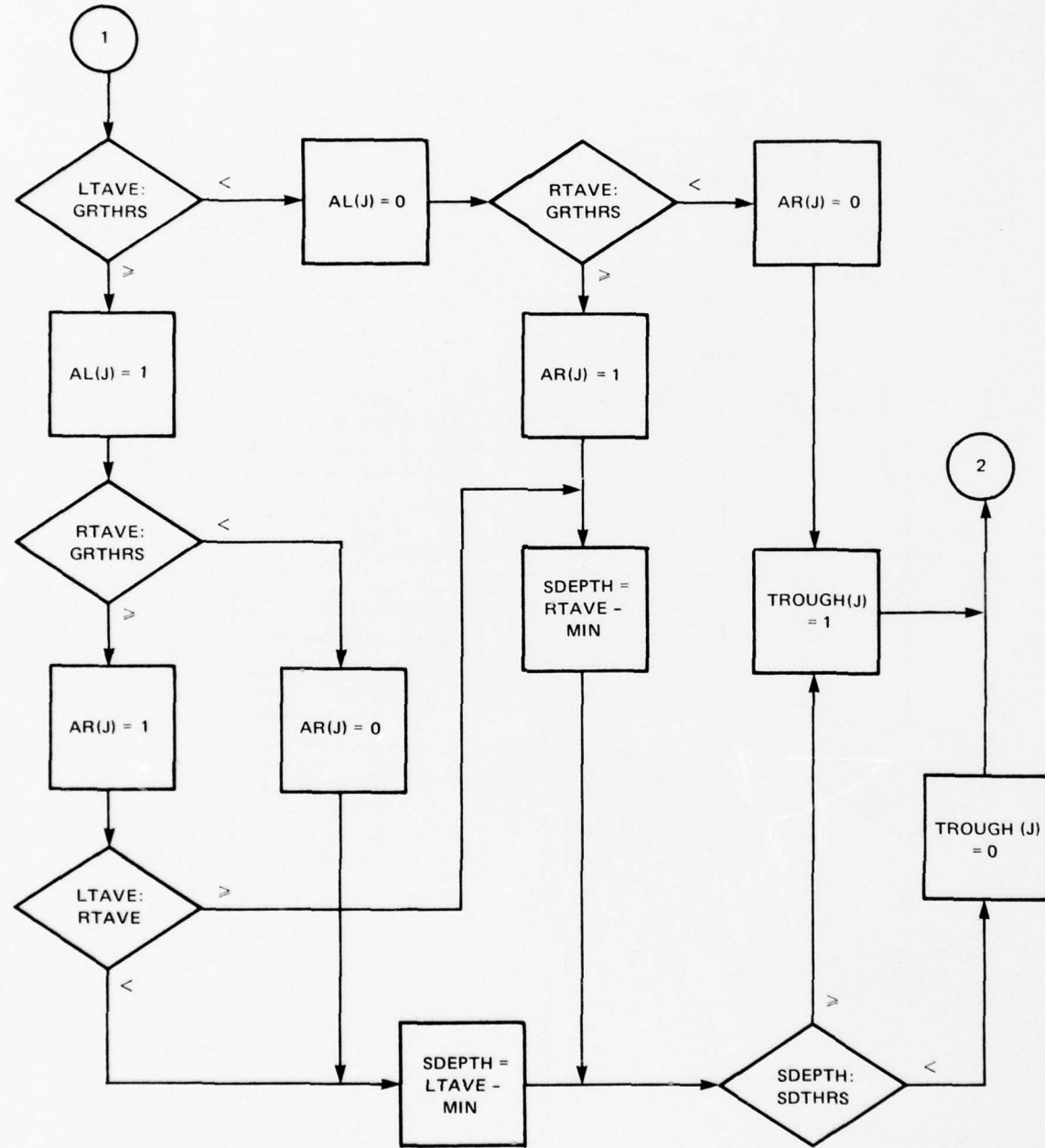


FIG. 108 SHADOW PROCESSOR FLOW DIAGRAM: THRESHOLD GROUND RETURN AND SHADOW DEPTH

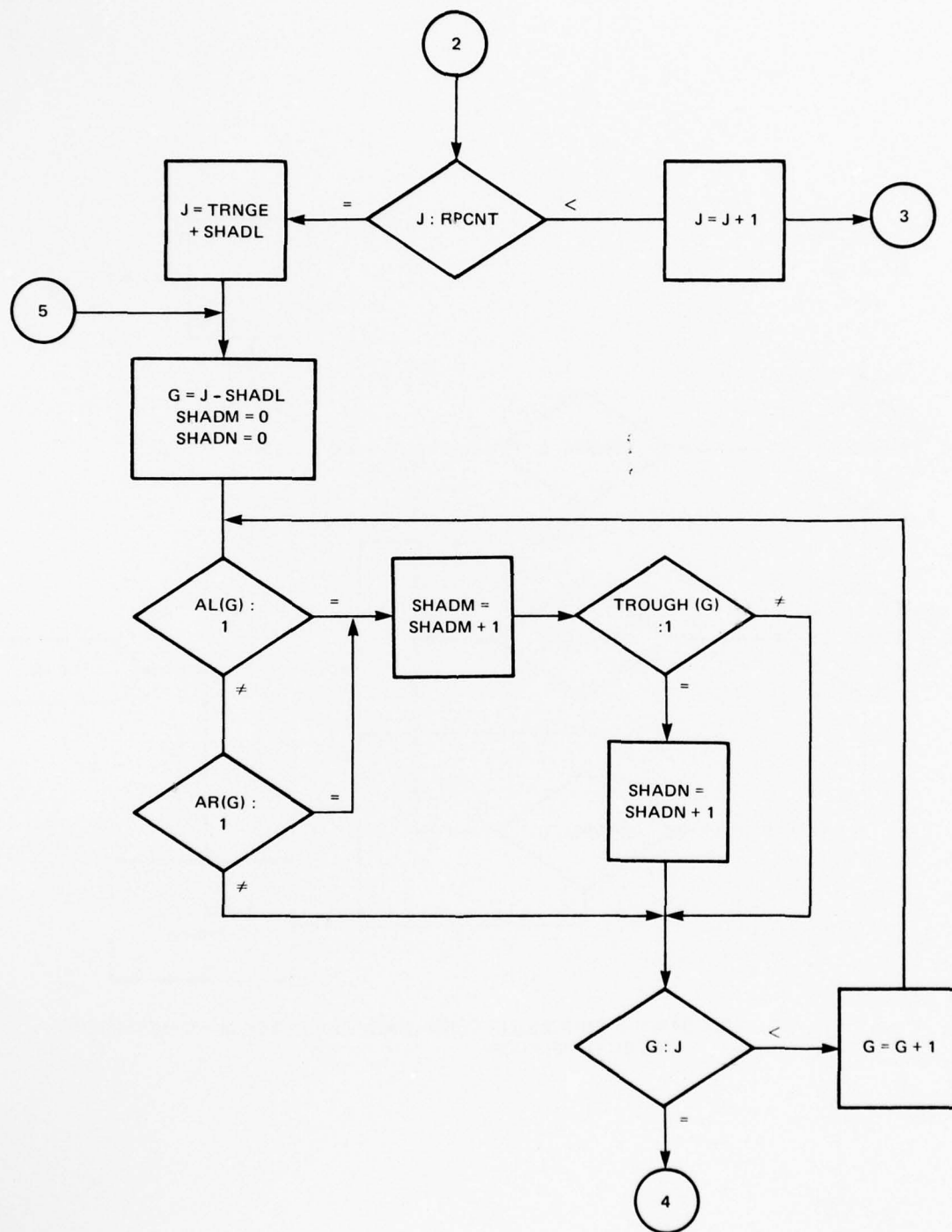


FIG. 109 SHADOW PROCESSOR FLOW DIAGRAM: DETERMINE M x N DETECTOR OUTPUT

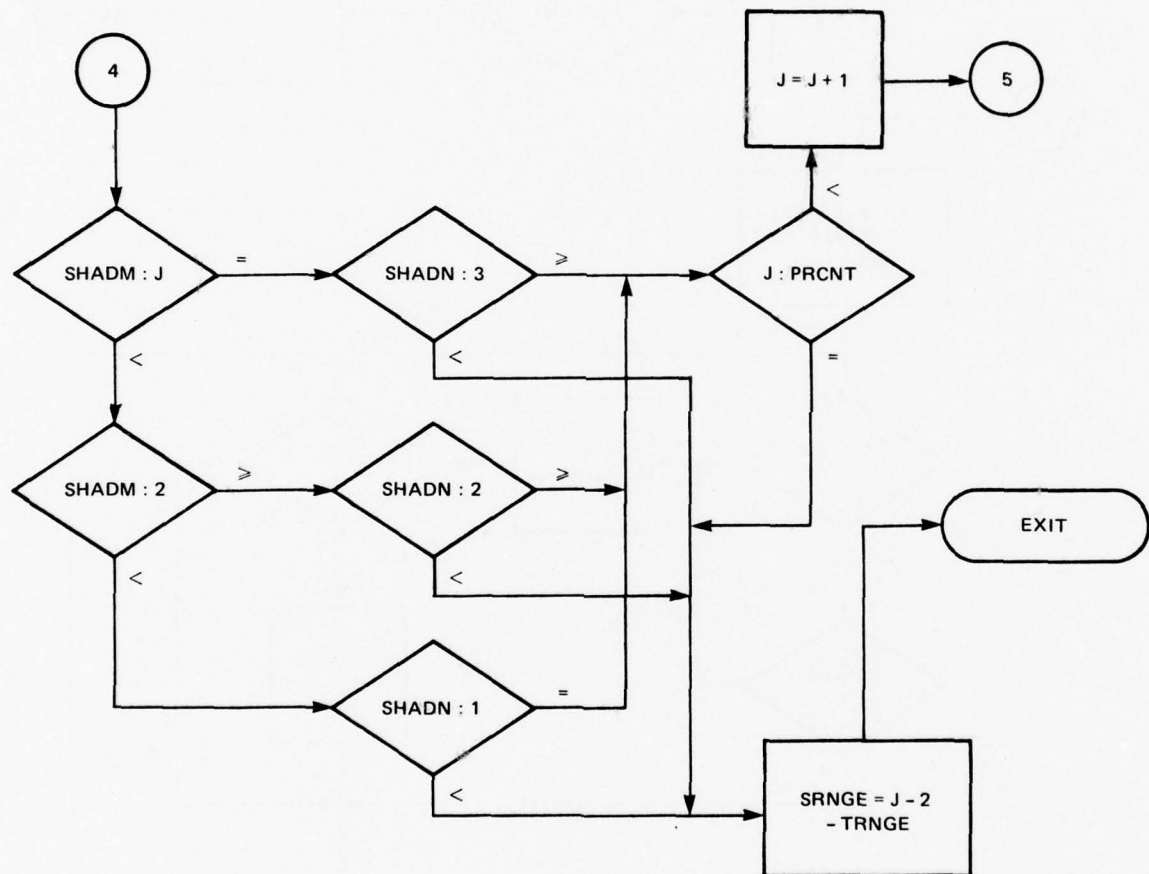


FIG. 110 SHADOW PROCESSOR FLOW DIAGRAM: CHECK $M \times N$ DETECTOR
FOR END OF SHADOW

THE JOHNS HOPKINS UNIVERSITY
APPLIED PHYSICS LABORATORY
LAUREL, MARYLAND

triangular. The range from the radar to the obstacle was varied between 1700 and 6200 ft. Multiple, up to three, obstacle situations were also set up to look at overlapping shadow conditions.

FIELD-TEST SYSTEM CONFIGURATION

For field-test operations and ease of movement, the experimental system was configured on two semitrailers. Figure 111 is a photograph of the initial test setup on the ground at APL. The antenna-support housing and protective radome were mounted on a lowboy semitrailer (left). The antenna azimuth drive, 95-GHz radar components, and the antenna itself were mounted inside this enclosure. For ease of movement on highways, a low-profile plywood cover was constructed to replace the protective radome on the support housing. The radome was then mounted directly on the trailer bed.

The conventional semitrailer (right) contains all the support and control electronics for the system. This equipment is mounted in five standard relay racks. Figure 112 shows three of the racks. The rack on the far left includes (from top to bottom) a master clock generator; a general-purpose oscilloscope, used primarily as a radar A-scope display; the high-speed A/D converter; klystron power; the radar control chassis; and a spare high-voltage power supply for the 95-GHz magnetron. The rack on the far right contains the color TV display and test signal generator; the platform control chassis; and the power amplifier and power supply for azimuth drive torque motor. The center rack houses a long persistence CRT and a special purpose PPI control panel. These units were initially designed into the system for use as a raw video PPI display. However, work was stopped on this unit once the color display system became operational. Figure 113 shows the two remaining racks. The right one contains the interface electronics and memory required for the color display system. The left rack houses the computer tape recorder and the General Automation computer with its interface chassis. The two large power supplies at the bottom are used by the color display system.

Field-Test Site

The basic requirement on the field-test sight was that it be relatively flat in order to simulate the conditions on the Arctic ice pack. The required clear-view range was set at 3 mi. This allowed for obstacle ranges of up to 2 mi, depending on the height of the obstacle. Since simulated obstacles were to be used, and then only up to three of them for any one test, the width requirement was set at a few hundred yards. Detailed requirements for

THE JOHNS HOPKINS UNIVERSITY
APPLIED PHYSICS LABORATORY
LAUREL MARYLAND



FIG. 111 TRAILER-MOUNTED TEST SETUP FOR INITIAL SEV FIELD TESTS

THE JOHNS HOPKINS UNIVERSITY
APPLIED PHYSICS LABORATORY
LAUREL, MARYLAND

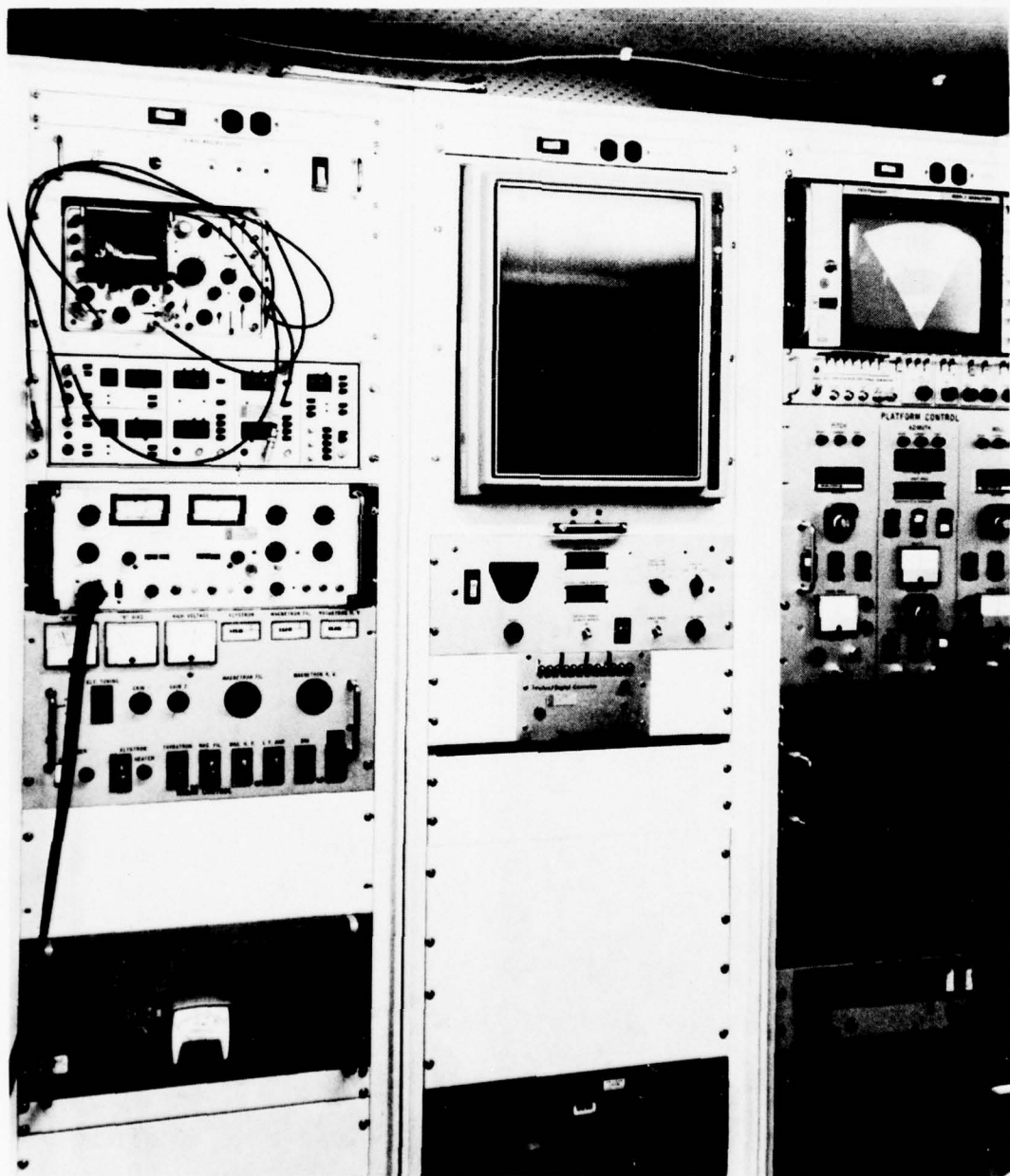


FIG. 112 SUPPORT AND CONTROL ELECTRONICS FOR SEV SYSTEM

THE JOHNS HOPKINS UNIVERSITY
APPLIED PHYSICS LABORATORY
LAUREL, MARYLAND

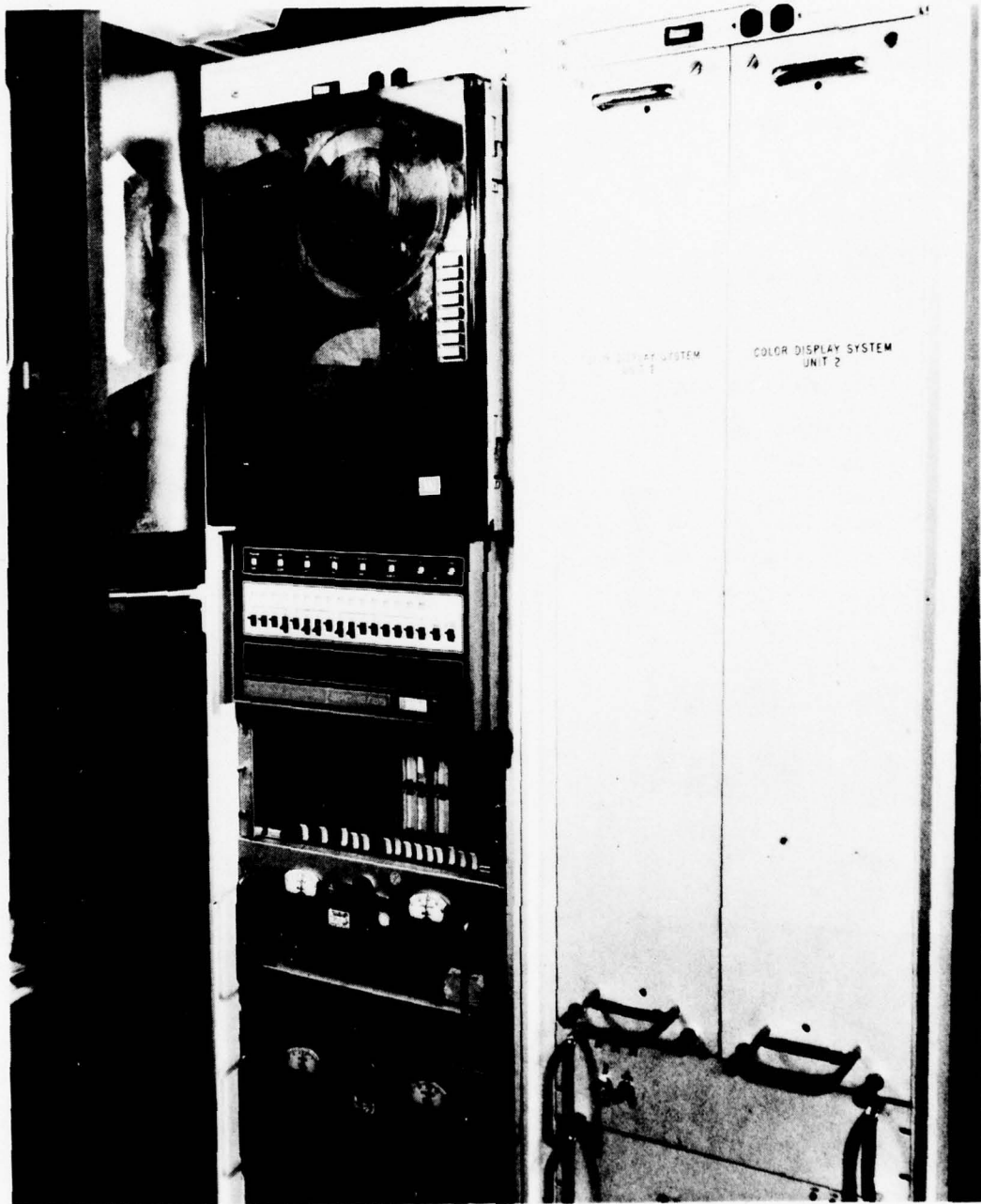


FIG. 113 INTERFACE ELECTRONICS AND MEMORY (RIGHT) AND THE COMPUTER RECORDER, GENERAL AUTOMATION COMPUTER, AND ITS INTERFACE (LEFT)

the overall test plan are covered in Ref. 32. An artillery range on the Army's Aberdeen Proving Ground (APG), Aberdeen, MD was selected as an acceptable site. It provided a relatively clear range about 6000 m long. A visit was made to APG to discuss details of support from Aberdeen personnel and of available facilities. It was pointed out that complete access to all areas of the test site was not possible without a tracked vehicle. A close inspection of the test site terrain indicated that most of the test objectives could be met with the placement of targets on existing roads on the range.

Field-Test Operations

During the first week, the system was again integrated. Exchange of the temporary plywood antenna cover and the protective radome was completed. The computer, its associated interfaces and peripherals, including the platform and radar consoles, and color display subsystem were checked out for proper operation.

With the lowboy semitrailer on the ground, the effective height of the antenna above ground was about 12 ft. The radar was positioned to view an area about 4000 yd in length and 200 yd wide. Figure 114 shows the area looking down range from immediately in front of the radome. The white artillery spotting towers are at 500-yd intervals down range. As can be seen, the area was covered with dead grass approximately 2 to 3 ft high. With the radar operating, it was found that this vegetation provided little or no ground return, even at ranges under 2000 ft. However, the telephone posts and artillery reference markers (stop-sign size) in the area provided strong radar returns. 95 GHz corner reflectors were mounted on poles at ranges of 1700 and 3000 ft. Radar returns from these reflectors indicated that the radar was operating as expected. In an attempt to improve the ground-clutter return level, a patch of grass 3000 ft long by 50 ft wide was mowed. This swath is shown in Fig. 115. No significant improvement in the ground return was seen. The ground and grass were very damp at the time because of heavy rains during the previous week. Because of the nature of the test objectives, no attempt was made to determine the cause of the lack of ground return.

Other test sites at APG were investigated and it was decided to locate the radar where the vegetation was very sparse and where more plowed ground was visible. Subsequent tests showed some improvement in the ground-return levels, but not at a range significant enough to conduct shadow tests. The decision was then made

Ref. 32. "SEV Field Test Plan (Track Tests - Fall 1973),"
APL/JHU S3R-74-154, 18 September 1973.

THE JOHNS HOPKINS UNIVERSITY
APPLIED PHYSICS LABORATORY
LAUREL, MARYLAND



FIG. 114 VIEW DOWN RANGE IMMEDIATELY IN FRONT OF RADOME



FIG. 115 SAME VIEW AS FIG. 114 EXCEPT THAT GRASS HAS BEEN
MOWED IN AN ATTEMPT TO REDUCE GROUND CLUTTER

THE JOHNS HOPKINS UNIVERSITY
APPLIED PHYSICS LABORATORY
LAUREL MARYLAND

to increase the height of the antenna by lifting the lowboy onto a 15-ft-high steel frame structure. Figure 116 shows the radome trailer on top of the steel frame, with the electronics van parked underneath. This increased the antenna height above ground to 24 ft. While this move was taking place, the RF box containing the 95-GHz radar components was removed from the antenna and returned to APL for laboratory testing. These tests verified that the radar was operating at expected values for transmitter power and receiver sensitivity.

The radar was again installed in the elevated antenna, and considerable improvement in the ground return was noted. An 8 × 8 ft plywood target was set up at a range of 1700 ft and tests were conducted to observe the shadow cast by displaying thresholded raw video on the color display system. While the target was clearly visible, there was no indication of the presence of a shadow. Figure 117 is the view down range from immediately in front of the radome. Note the grassy area with the mowed swath to the right. This is the test area previously described. The test target used can be seen vaguely in the middle of the road.

An attempt was made by placing corner reflectors on the ground behind the target at various ranges to determine the length of the radar shadow. Radar measurements taken on the corner reflectors, with the first target in position and the removed, showed that the target was somewhat transparent at 95-GHz. Measured two-way loss through the target varied considerably, with a minimum observed value of 6 dB.

To combat this situation, aluminum foil was taped to the front surface of the target as shown in Fig. 117. The above experiment was repeated, and the corner reflectors were no longer detectable with the target in place. However, thresholding of the raw video on the color display still did not show any strong shadowing. The length of the target's radar shadow was measured by moving the corner reflector to a point behind the target where the radar could see it. The measured 800-ft length agreed closely with the predicted value based on the height of the target, its range to the radar, and the radar antenna height.

Based on these measurements, it was felt that a problem existed somewhere in the receiver portion of the radar. The receiver was removed and returned to APL, where tests on the IF and video amplifiers revealed a recovery time of about 2 μ s from a high-energy radar return. This results in masking of shadows that are less than 1000 ft in length. Modifications were made in the impedance matching networks between the IF amplifier and the video detector and at the input to the log video amplifier. The final

THE JOHNS HOPKINS UNIVERSITY
APPLIED PHYSICS LABORATORY
LAUREL, MARYLAND

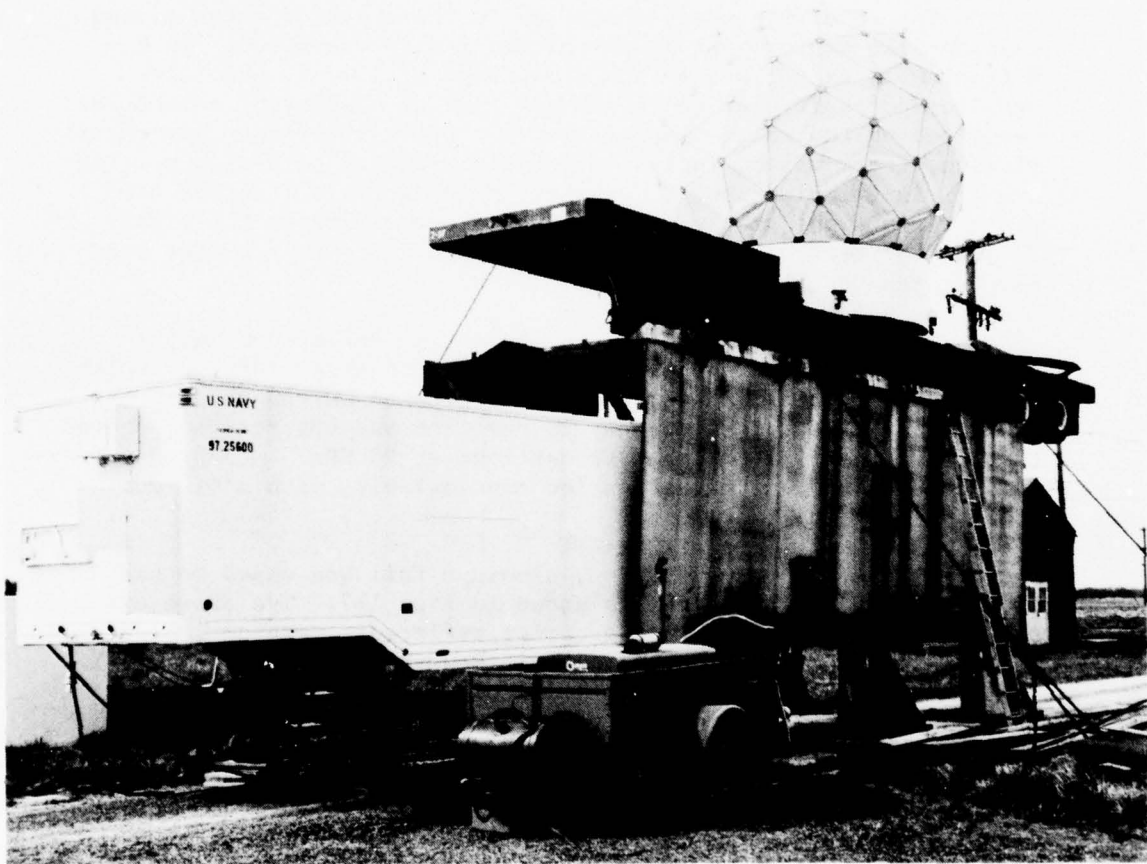


FIG. 116 EMPLACEMENT OF THE RADOME TRAILER MOUNTED ON
TOP OF A STEEL FRAME, WITH THE ELECTRONICS VAN
PARKED BENEATH

THE JOHNS HOPKINS UNIVERSITY
APPLIED PHYSICS LABORATORY
LAUREL, MARYLAND

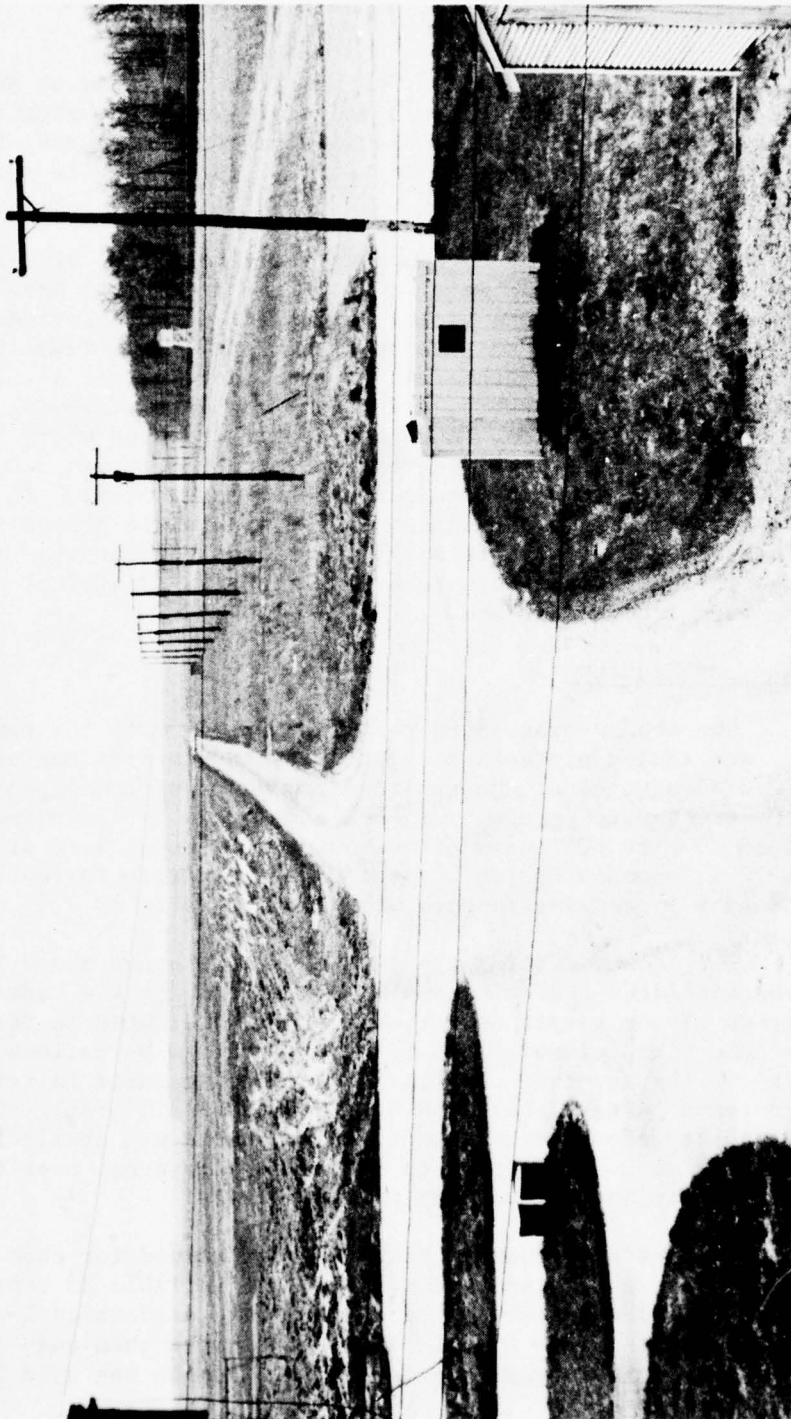


FIG. 117 VIEW DOWN RANGE, IN FRONT OF THE RADOME

result was a maximum recovery time of 0.6 μ s (300 ft in range) at return S/N ratios above 40 dB.

The receiver was again installed in the radar at APG. An 8 x 8 ft target was put up at a range of 1700 ft. Using the color display system to display thresholded raw video returns, the radar shadow cast by the target could be seen. Several data recording scans were immediately taken.

Prior to setting up other target situations, wide-angle scans of the test range were made to find areas that provided the best ground return. One sector was selected that provided continuous ground return out to a range of 6000 ft. Individual targets of various sizes and shapes and some multiple target situations were set up in this sector, and a complete data recording run was made for each condition. A second sector was used where a small rise in the terrain provided reasonable ground return between 8000 and 10 000 ft. Targets were set up at a range of 6200 ft so that the resulting shadow terminated in the area where ground return was present. Table 22 lists all the target combinations and ranges for which data were recorded. In all, 17 digital data tapes were recorded at APG.

Field-Test Results

The shadow-processing technique, along with the range, azimuth, and target processing logic described in previous sections, was exercised against the recorded raw returns from seven of the field-test target setups. In each case, data for an azimuth scan rate of 10 hits per beamwidth were used. Returns were processed from 10 independent azimuth scans past the target for each setup. The shadow processing results are given in Table 23.

The column listing the test-obstacle setups shows the sizes of the simulated obstacles and their ranges from the radar. Performance of the target detection logic is indicated in the Centerline Detection column. These data are the 1- σ variations (over 10 scans) in the detected obstacle centerline measured in terms of the antenna pattern beamwidth (3 dB points = 2.0 mrad). Since no independent reference azimuth to the obstacle was available, the variations are with respect to the measured average over the 10 scans, and do not include any unknown biases.

The obstacle shadow length was determined for each target detection on each antenna scan. The data in Table 23 represent the average measured shadow lengths and the associated 1- σ variations. When the same target was detected more than once in a single scan, the longest measured shadow length was used in the averaging process.

Table 22
Field-Test Target Configurations

Range (ft)	Height (ft)	Width (ft)	Shape*	No. of Targets
1700	8	8	R	1
1700	8	16	R	1
1700	8	4	R	1
1700	12	4	R	1
1700	12	4	T	1
3200	12	4	T	1
3200	8	8	R	1
3600	8	8	R	1
1700	12	4	R	3
1700	12	4	R	2
1700	12	4	T	3
2700	8	8	T	3
2700	8	8	T	1
2700 [†]	8	8	T	1
6200	8	8	R	1
6200	10	8	R	1
6200	10	8	T	1
6200	12	4	T	1
6200	10	4	R	1
6200	10	12	R	1
6200	10	12	R	3
1700	14	12	T	2
3200	8	8	R	1
1700	14	12	T	1

*R = rectangular, T = triangular

[†]Light rain falling

Table 23
 Shadow-Processing Results
 Obstacle Height Determination

Test Obstacle Setup			Centerline Detection Variation (beamwidths)		Shadow Length Determination			General Ground Return		
Range (ft)	Height (ft)	Width (ft)	Average Length (ft)	Variation (ft)	Average Height (ft)	Variation (ft)	Offset (ft)			
1700	8	8	0.08	740	7.3	1.0	-0.7	Moderate		
1700	8	4	0.14	1489	120	0.5	+3.2	Excellent		
1700	12	4	0.09	2400	334.7	14.0	0.8	+2.0	Excellent	
1700	12	12	0.09	2783	107	14.9	0.2	+2.9	Good	
3200	8	8	0.11	1229	167	6.7	0.6	-1.3	Moderate	
2800	8	8	0.13	1438	111	8.1	0.4	+0.1	Excellent	
6200	10	12	0.04	1850	92	5.5	0.2	-4.5	Very poor	

THE JOHNS HOPKINS UNIVERSITY
APPLIED PHYSICS LABORATORY
LAUREL, MARYLAND

The average obstacle height (h_o) is calculated from the known antenna height ($h_a = 24$ ft), the measured obstacle range (R_o), and the average shadow length (R_s) by the following equation:

$$h_o = \frac{R_s h_a}{R_s + R_o}$$

The height variation is based on the shadow-length sensitivity of the situation. It is determined by differentiating h_o with respect to R_s :

$$\frac{dh_o}{dR_s} = \frac{R_s h_a}{(R_s + R_o)^2} \cdot dR_s$$

The offset in height determination represents the error in the total process and is simply the difference between the average measured height and the actual height of the obstacle. General ground return conditions are indicated for each test setup.

The following conclusions are drawn from these data:

1. Repeatability in determining the azimuth centerline of the obstacle was very good.
2. The variation in the measured height was also good, averaging about 0.5 ft.
3. The offset, or measured error, shows considerable variation but is reasonably well correlated with the general ground-return conditions.
4. The measured height is always high under good conditions and low when the ground return is poor.
5. A constant value for the shadow-depth threshold parameter is probably the major contributor to this condition.

No attempts were made to optimize this threshold or any other of the data-processing parameters.

5. NAVIGATION SYSTEM

Design of a navigation system is a complex mission-dependent task. There are many navigation techniques available and quite often a multiplicity of techniques are required. The primary objective of the navigation system is to determine vehicle position (i.e., where the vehicle is) and velocity (i.e., where the vehicle is going). The precision, dimensionality (number of position and velocity coordinates), and data-rate requirements are mission dependent. Additional factors, such as a requirement for precision attitude data, can also influence the design.

NAVIGATION SYSTEMS

One of the most widely used navigation systems is an Inertial Navigation System (INS). Basically the INS senses acceleration, and given a set of initial conditions (position, velocity, and alignment of the accelerometers relative to the navigation reference coordinates) the system integrates once to determine velocity and twice to determine position. The INS has the distinct advantage of independent operation after the initial conditions are established, and it also provides craft-attitude data as a by-product of the navigation. However, since the desired outputs are determined through integration, any bias errors in measurement do accumulate. The cumulative bias error, coupled with a drift of the measurement axes relative to the reference axes, leads to loss of precision that increases with time. Inertial systems with very gradual precision degradation have been developed, but they are usually very expensive. Unless very short mission durations are planned, most precision systems using an INS include a method for resetting (reinitializing) the inertial reference.

Doppler systems (either radar or sonar) can be used to sense vehicle velocity relative to the earth. These data can be integrated from a set of initial-condition data to provide position information. Here again, precision degrades with time. Such systems are typically less accurate than an INS. Air-flow and water-flow measurements are also used for velocity measurement, but these do not directly measure velocity relative to the earth's surface and are therefore less accurate.

Celestial navigation uses angular measurement of the positions of known stars coupled with a knowledge of time (earth

THE JOHNS HOPKINS UNIVERSITY
APPLIED PHYSICS LABORATORY
LAUREL MARYLAND

rotation) to determine position. These systems are seriously limited by visibility constraints.

There are a number of radio navigation systems that can provide position and velocity information. The primary systems to be considered are Loran, Omega, and satellite-based systems. The land-based systems (Loran and Omega) are primarily two-dimensional, providing latitude and longitude information and in some implementations velocity in these two coordinates. Where required, barometric or radar altimeters are used for the third coordinate. Satellite systems can be used to provide a three-dimensional capability. The currently available Navy Navigation Satellite System (NNSS) is primarily used as a two-dimensional position update system. The planned Global Positioning System (GPS) is intended to provide a three-dimensional position and velocity determination capability.

Loran-C, at 100 kHz, is accurate to about 0.1 nmi in an uncalibrated grid. Currently, Loran is not available in the Arctic basin and no new stations are planned for the Canadian Arctic or Alaska in the near future (Ref. 33). If a group of Loran stations were installed from Alaska across Canada, in Greenland, and in Northern Scandinavia, they would be capable of providing usable signals over approximately half the Arctic basin.

The 10 kHz Omega system is planned to be a world-wide navigation aid by the late 1970's, with an accuracy of 2 to 4 nmi. The VLF signals from Omega suffer from diurnal and atmospheric effects and recent tests indicate that the signals experience extremely high attenuation over ice and permafrost, which may render the system useless in the polar regions (Ref. 34).

Satellite navigation systems offer considerably more promise for navigation in the Arctic than that of Loran or Omega type systems. Currently the satellite system available is the NNSS, although within the next few years the feasibility demonstration of the system of the GPS will be available.

The NNSS has been providing highly accurate position information to both military and civilian users for over seven years. The satellites, originally developed as a navigation aid for the

Ref. 33. F. C. Paddison, "Status of APL Work on Navigation, Communication and Obstacle Avoidance," APL/JHU CQO-913, April 1972.

Ref. 34. J. E. Sater et al., "Arctic Environment and Resources," Arctic Institute of North America, Washington, DC, 1971.

Polaris Fleet, are in view intermittently from any point in the world. In the Arctic regions, satellites are in view approximately every 20 minutes.

PROPOSED NAVIGATION SYSTEM

The need to provide attitude data to the obstacle detection system and the need to provide a high-data-rate navigation capability (and not impose maneuverability constraints) leads to the selection of an INS as the basic navigation system. Since the SEV problem is primarily two-dimensional (i.e., it is a surface craft), and since the NNSS is currently available with frequent Arctic passes, the NNSS will be used to update the INS.

Unlike mid-latitude systems, the azimuth reference for the INS can vary rapidly in the polar region. Therefore the NNSS system will also be used to provide azimuth updates. A system for this purpose, Aztran (AZimuth from TRANSit), was conceived and tested in the mid 1960's, but the application planned at that time was not pursued. Aztran is based on simultaneous reception of satellite signals through two antennas separated by a short distance on the craft. The antennas form an interferometer and the direction of the line between the antennas can be determined relative to the known satellite path.

Figure 118 is a block diagram of the proposed SEV navigation system. Signals received by one (or possibly both) receiver(s) are processed along with the continuous INS data in a Kalman filter to estimate vehicle position and velocity. Similarly the phase-difference data from the two receivers is processed to update the estimate of azimuth. The navigation data are continually provided to the pilot's display along with mode and status data. Basically the INS provides the continuous navigation capability while the satellite system provides an external reference for periodically updating the inertial system.

The interferometer concept, used by Aztran, is illustrated in Fig. 119. When the satellite is at position A, the signal has to travel further to reach the left antenna than the right antenna. This path-length difference causes a phase difference in the received signal. As the satellite proceeds to point B, this path-length difference, and consequently the phase difference, changes. It is this change in phase difference that is measured and used to compute the azimuth angle of the antenna baseline.

The performance characteristics of the NNSS as a position update system are well known and should meet the most demanding

THE JOHNS HOPKINS UNIVERSITY
APPLIED PHYSICS LABORATORY
LAUREL, MARYLAND

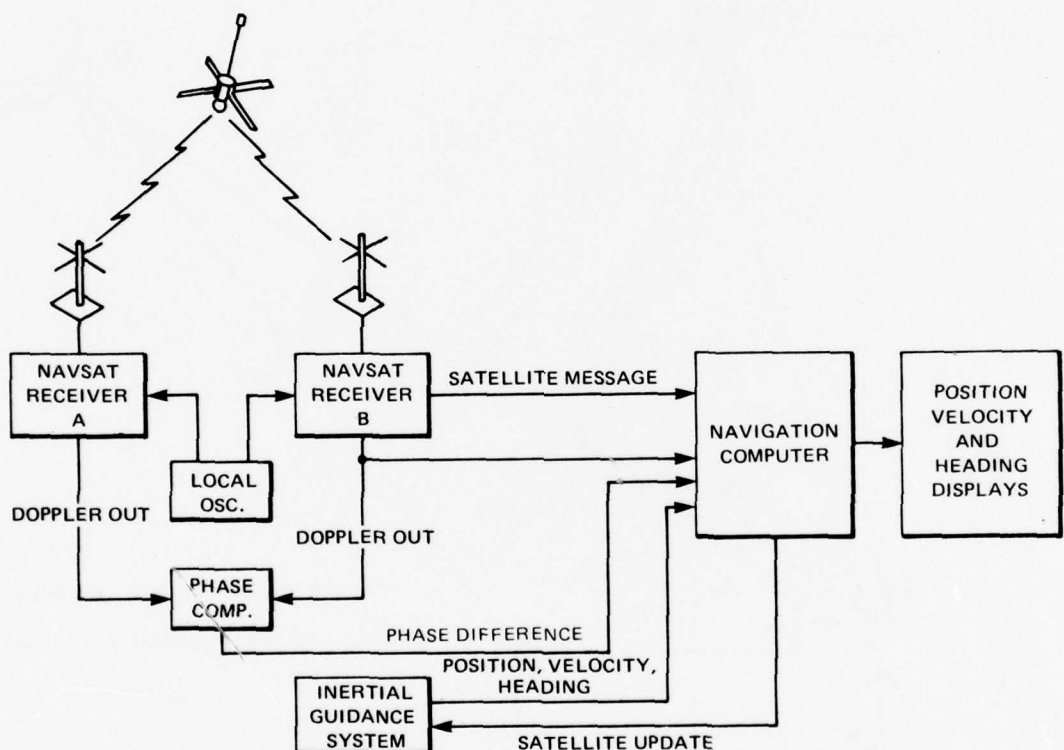


FIG. 118 SEV NAVIGATION SYSTEM

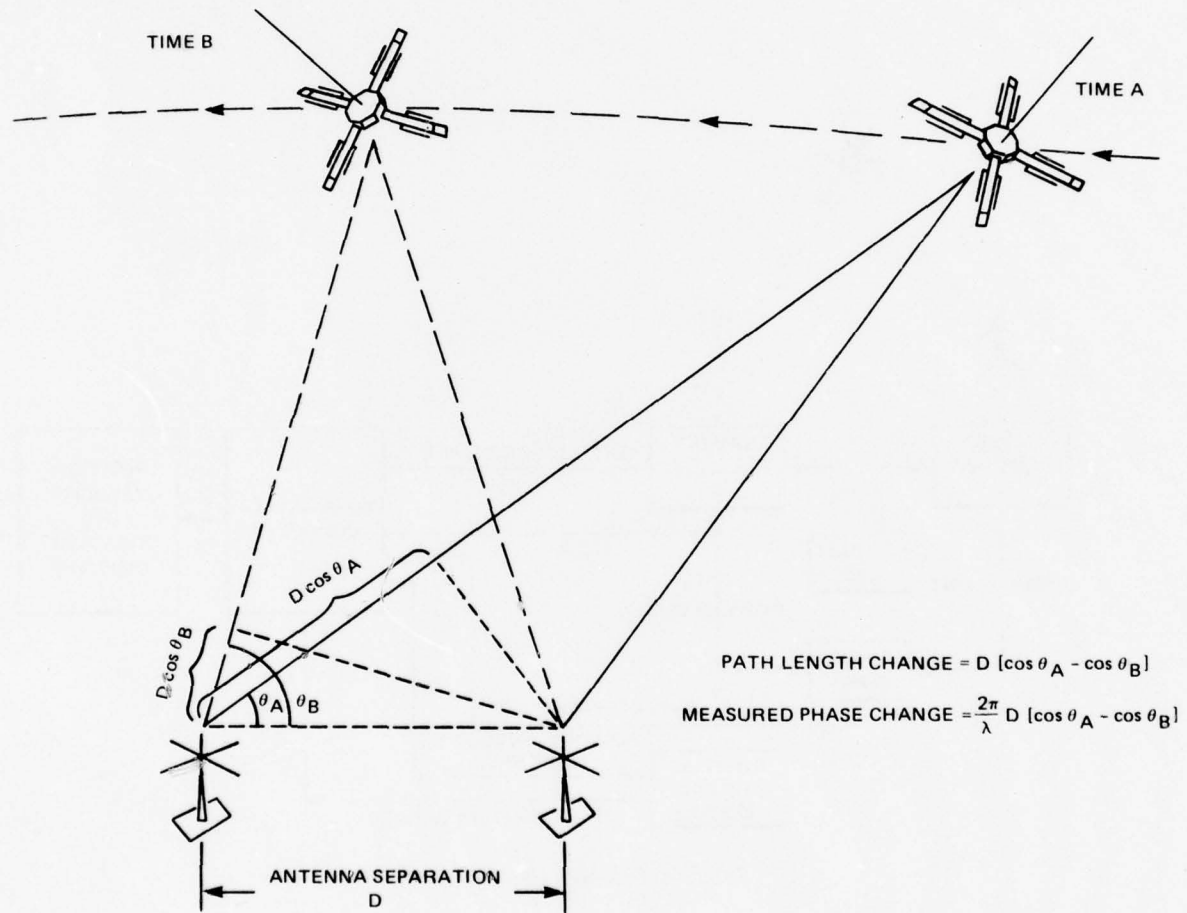


FIG. 119 AZTRAN CONCEPT

requirements of an Arctic SEV. However, the Aztran system has not been as extensively analyzed or tested. Therefore, within this program, emphasis has been placed on determining the performance characteristics of Aztran.

AZTRAN ERROR ANALYSIS

A mathematical error model of the Aztran system was developed to study the limiting accuracies of the system. Reasonable measurement uncertainties were selected, and used as inputs to the model. Based on these uncertainties, it was determined that a 50-m baseline system should be able to achieve an accuracy of about 50 to 60 arc-seconds rms and a 100-m baseline system should approach 25 arc-seconds rms in the mid latitudes. The values vary somewhat with the azimuth angle of the antenna and the pass geometry.

A group of satellite passes were simulated for the north polar regions (72° N, 160° W) near Pt. Barrow. At this latitude, all passes are visible as they cross the pole and the lowest observed elevation at closest approach for any pass is about 20° . The angular accuracy for the polar passes was somewhat better than the mid-latitude passes. The 50-m baseline system showed an rms accuracy of about 25 to 30 arc-seconds while the 100-m system had an error of just under 15 arc-seconds.

Uncertainties of 15 m rms in latitude and longitude and 1 m in height were used for the navigator's position. This degree of accuracy is obtainable by averaging a small group of refraction-corrected passes. The error in the navigator's position contributes almost nothing to the total system error and could be 10 to 100 times greater before it approached the value of some of the other errors.

An rms value of 8 m in positional uncertainty was assumed for the satellite in each of the three Cartesian coordinates at any one fiducial mark. No error correlation was assumed from measurement to measurement. The position errors contribute little to the system error and could be greater by a factor of 10 before they would begin to become significant.

Two pairs of uncertainties were used for estimates of the antenna separation and height difference. For the first pair 3 cm and 1 cm in separation and height difference, respectively, were used. At this measurement accuracy, these uncertainties tended to be the dominant error source for a 100-m baseline system. The second set of uncertainties were 1 cm in separation and 0.5 cm in

height difference. These values require more precise measurement techniques, but are still feasible. In this case the antenna measurement errors were significant for a 50-m baseline system, however in a 100-m baseline system the dominant error source was the phase measurement error.

In the current Aztran system, phase is sampled 100 times per second by the computer in a second-order digital filter. The maximum phase frequency followed is about 1 Hz. Sources of phase error are jitter in the receiver phase-locked loops, multipath reflections, and sampling error. A value of 0.01 cycle of phase error was selected as the rms measurement error. This is not to imply an error of 0.01 cycle per phase sample, but that the smoothed output from the digital filter (which is stored every 15 seconds) will have this rms error. Because of the high sampling rate (1500 samples between stored value) the error from stored value to stored value was assumed to be uncorrelated.

AZTRAN PERFORMANCE

The error equations used to analyze the Aztran performance are derived in Appendixes B and C. Results of the analysis are discussed in the following paragraphs.

Figures 120 through 124 show a summary of the results over APL for various elevation passes as a function of the antenna baseline azimuth. In these graphs the solid line represents a 100-m baseline system with antenna measurement accuracy of 3 cm in separation and 1 cm in height difference. The dashed line is also a 100-m system but with 1 cm and 0.5 cm errors in antenna measurements. The third line (alternate dots and dashes) represents a 50-m baseline system.

In general it can be seen from these graphs that accurate antenna measurement is quite critical for the success of the system. For moderate-to-high elevation passes, it is definitely advantageous to have the antennas oriented in an east-west direction. Figure 125 illustrates this point even more graphically. This graph shows a group of passes from the northeast to the south over APL for antenna baselines of 0°, 40°, and 90°. From these curves it can be seen that the optimal configuration consists of antennas in an east-west direction, using moderate to high elevation passes. This configuration also tends to minimize multipath problems and refractive effects.

The results indicate the Aztran performance to be expected at mid latitudes and also provides a basis of comparison to test

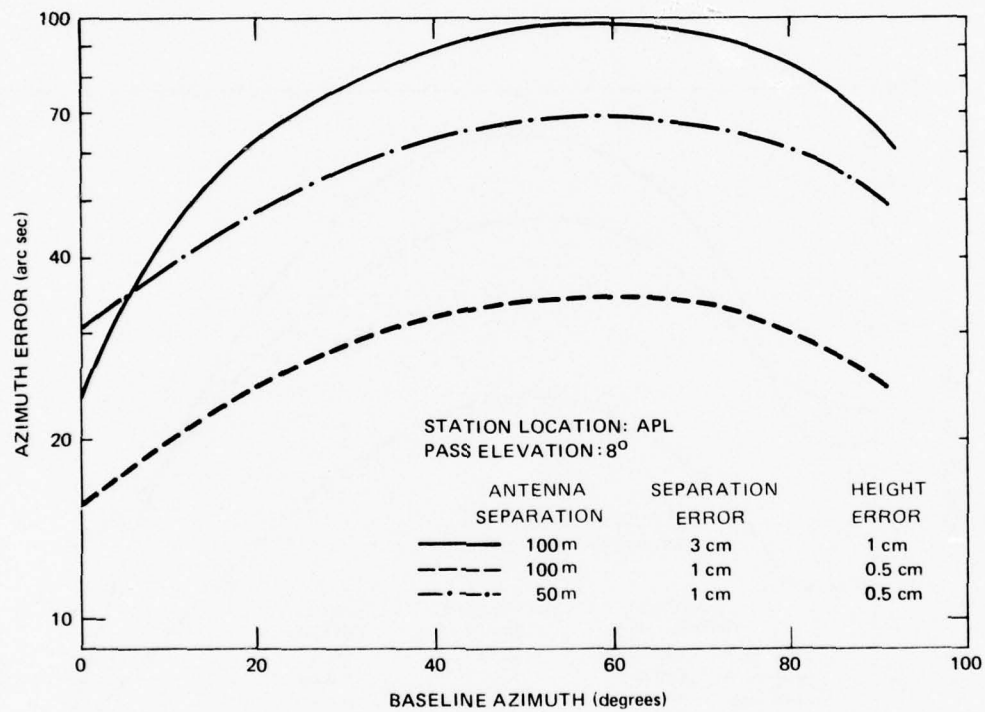


FIG. 120 AZTRAN ERRORS: CASE 1

THE JOHNS HOPKINS UNIVERSITY
APPLIED PHYSICS LABORATORY
LAUREL, MARYLAND

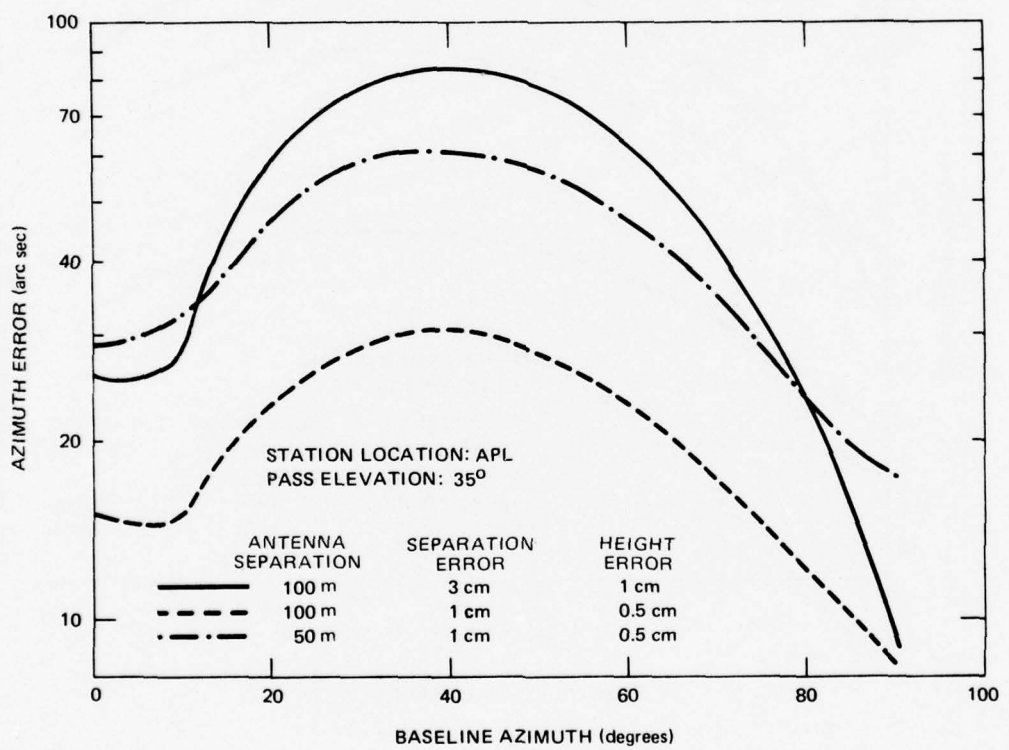


FIG. 121 AZTRAN ERRORS: CASE 2

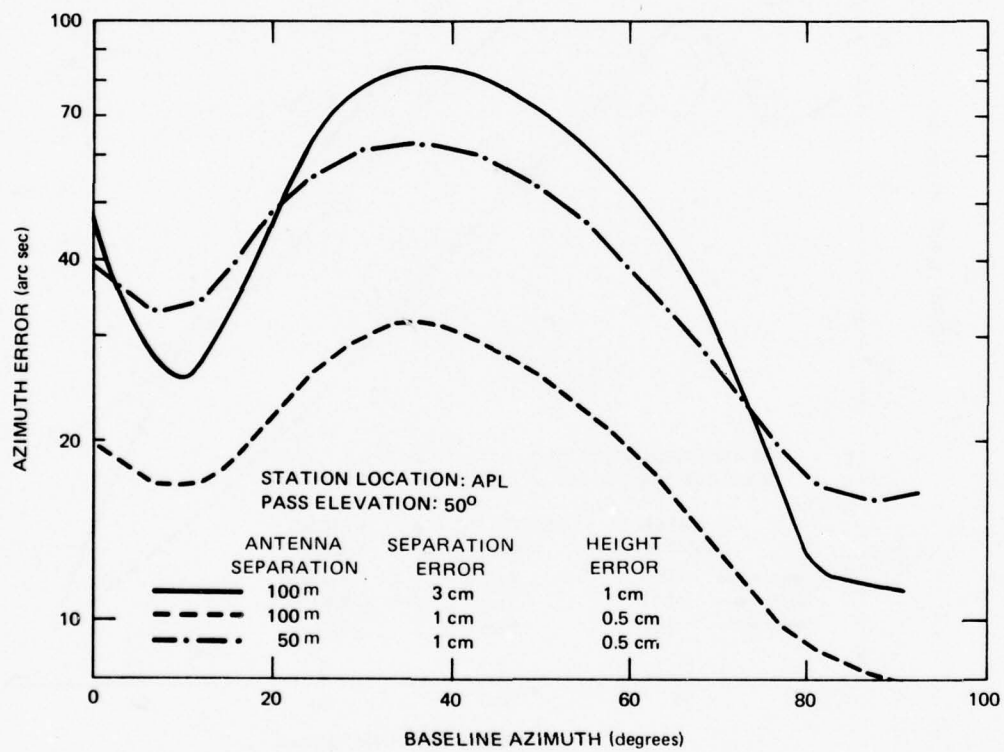


FIG. 122 AZTRAN ERRORS: CASE 3

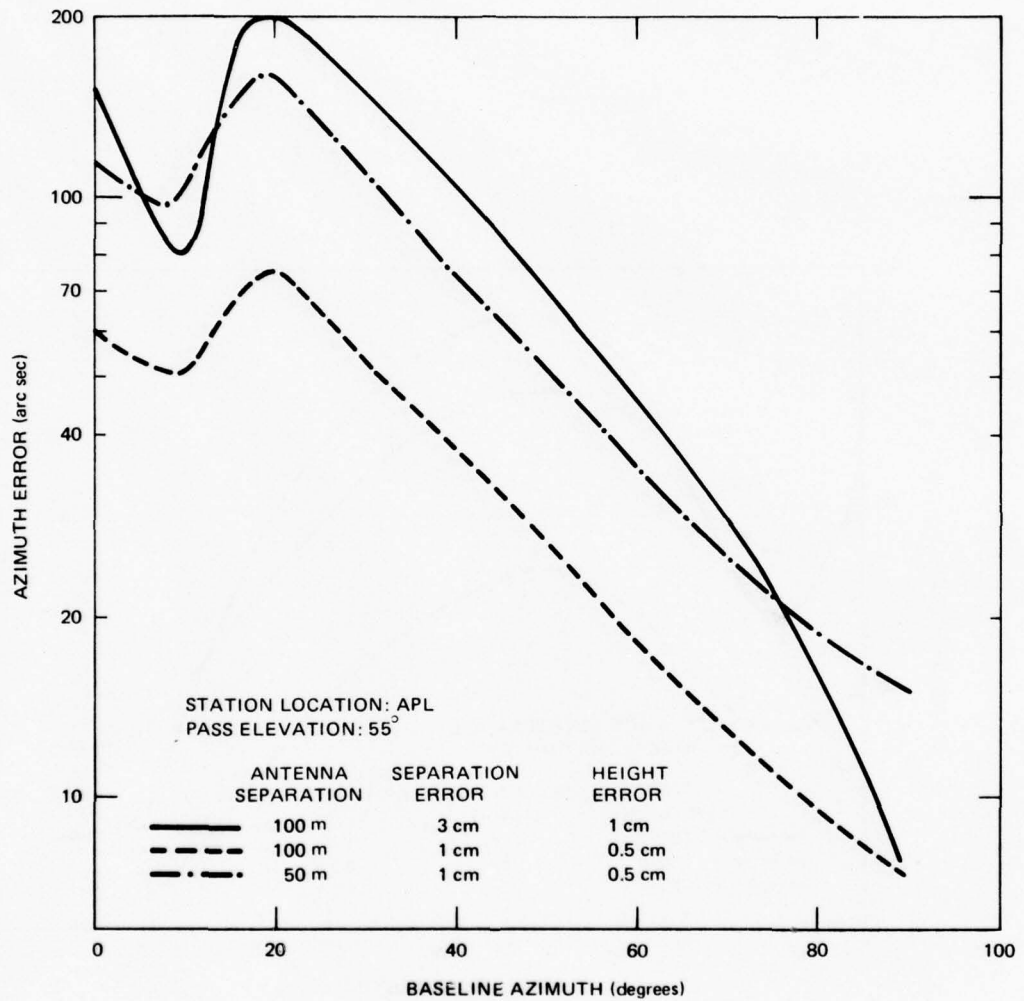


FIG. 123 AZTRAN ERRORS: CASE 4

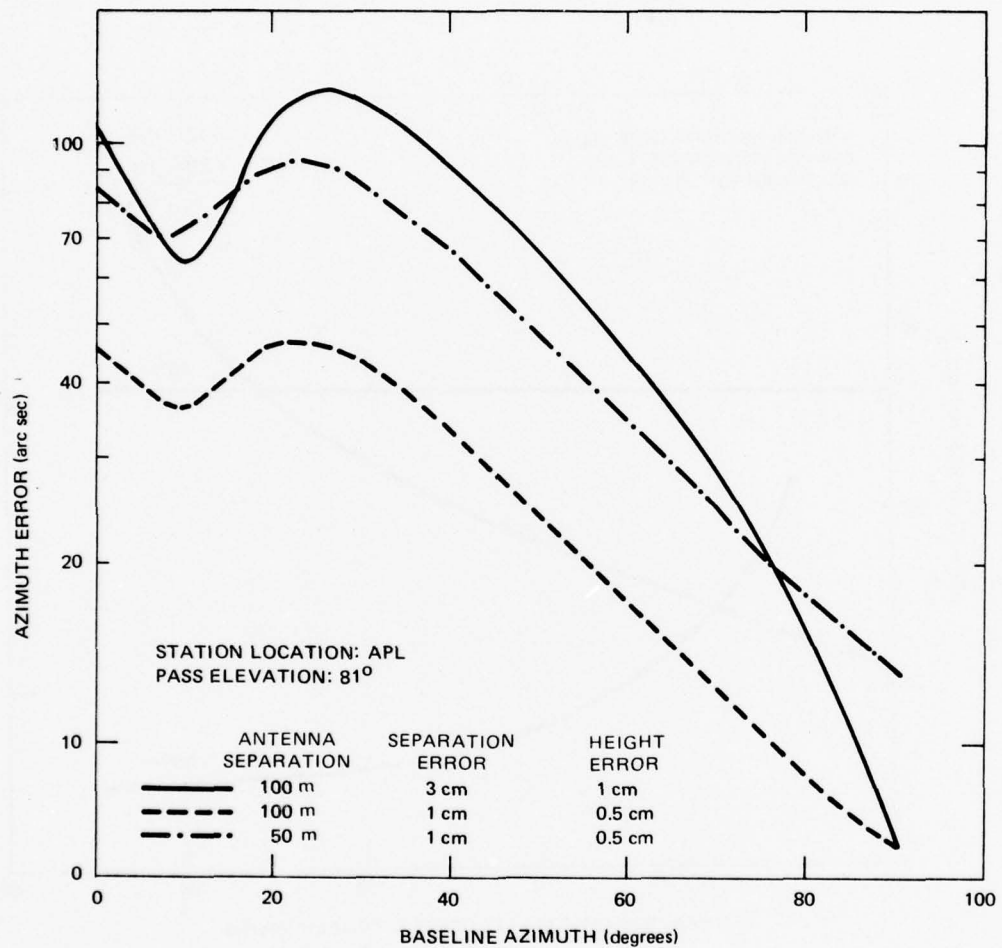


FIG. 124 AZTRAN ERRORS: CASE 5

THE JOHNS HOPKINS UNIVERSITY
APPLIED PHYSICS LABORATORY
LAUREL, MARYLAND

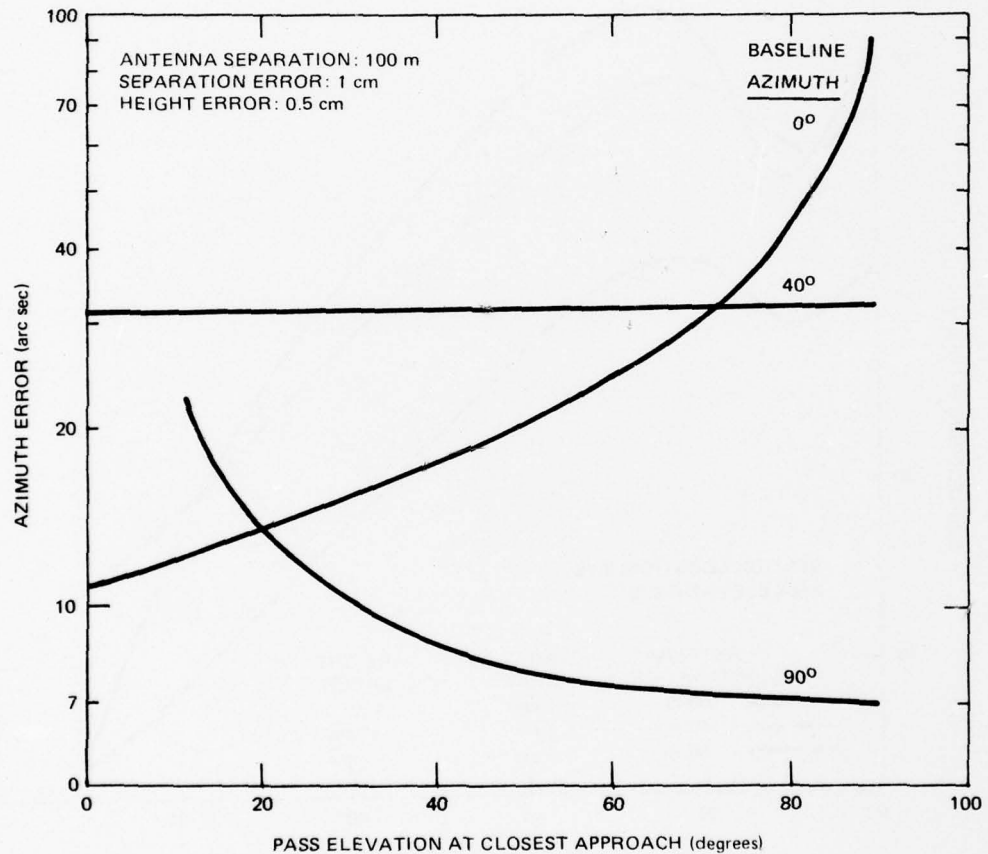


FIG. 125 AZTRAN ERRORS VS. PASS ELEVATION FOR SEVERAL BASELINE AZIMUTHS AT APL

THE JOHNS HOPKINS UNIVERSITY
APPLIED PHYSICS LABORATORY
LAUREL MARYLAND

the data collected at APL. A series of tests were conducted at APL with a 50-m antenna separation and an antenna baseline azimuth of 70°. From the varying elevation angle of 17 closest-approach passes of the satellite, the rms error was about 50 arc-seconds (Ref. 35).

An average of the predicted errors from Figs. 120 to 124 (averaged over elevation) taken at the 73° baseline azimuth is approximately 30 arc-seconds. The measured data appear to be degraded primarily by multipath errors. The error source is not included in the current error model.

Since the primary interest of this study was Aztran performance in the polar region, the error analysis was repeated for a high-latitude location (Pt. Barrow). Figures 126 through 128 show the results for this location. It will be noted that these results are somewhat better than those indicated at the APL location. On the assumption that the effect of neglected errors will be no worse in the polar region than the effect of those observed in APL tests, the values indicated in Figs. 126 through 128 should not degrade by more than 50%.

The effect of antenna baseline dynamics could not be studied within the scope of this program; however to study this effect would be the next step toward development. To properly include these effects, a combined Aztran/navigation-error analysis based on use of a Kalman-filter on the data from two navigation receivers and the INS is required. However, it is anticipated that results indicated by this analysis will not change substantially in the final system configuration.

Ref. 35. J. R. Albertine, "An Azimuth Determination System Utilizing the Navy Navigation Satellites," Navigation: Journal of the Institute of Navigation, Vol. 21, No. 1, Spring 1974, pp. 54-60.

THE JOHNS HOPKINS UNIVERSITY
APPLIED PHYSICS LABORATORY
LAUREL, MARYLAND

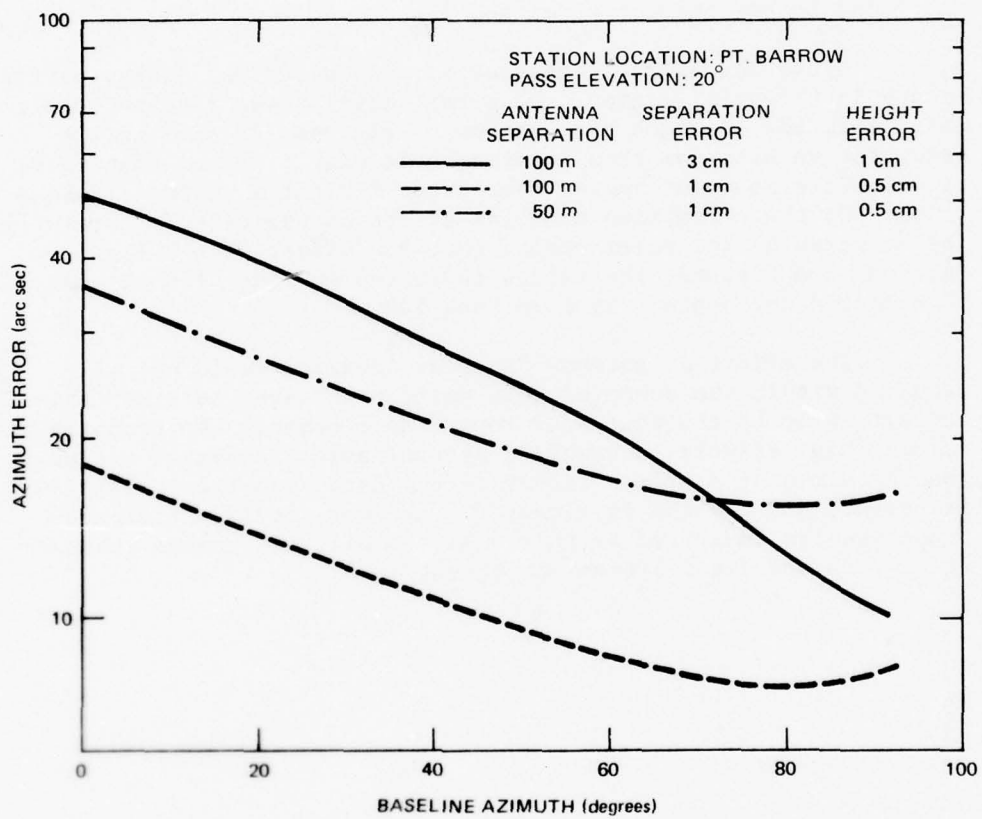


FIG. 126 AZTRAN ERRORS: CASE 6

THE JOHNS HOPKINS UNIVERSITY
APPLIED PHYSICS LABORATORY
LAUREL, MARYLAND

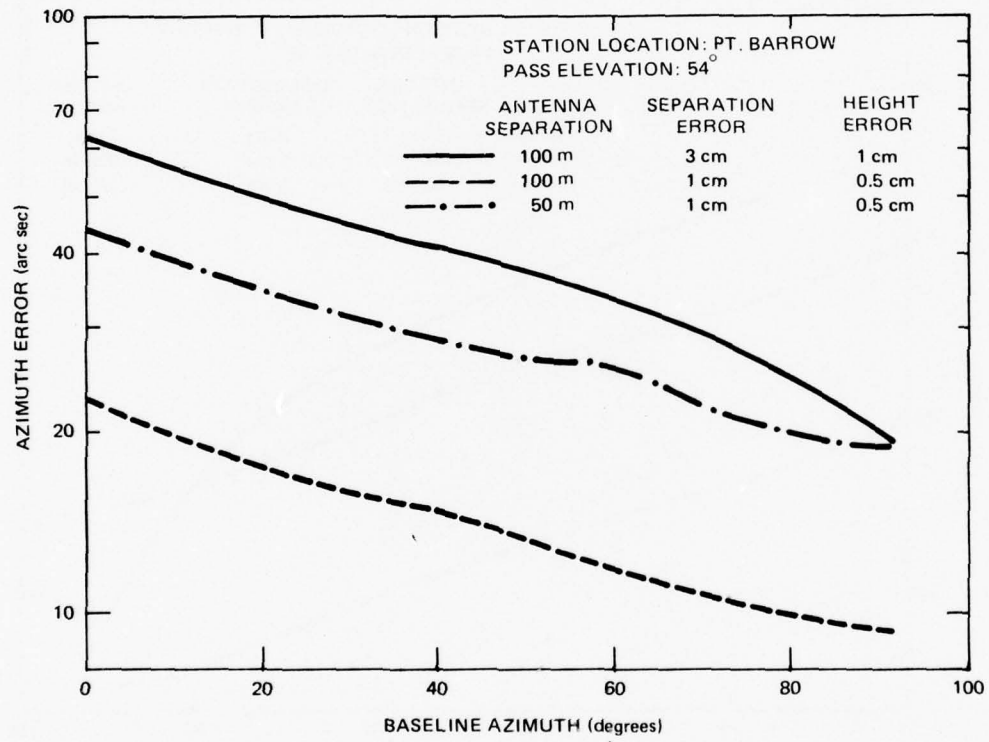


FIG. 127 AZTRAN ERRORS: CASE 7

THE JOHNS HOPKINS UNIVERSITY
APPLIED PHYSICS LABORATORY
LAUREL, MARYLAND

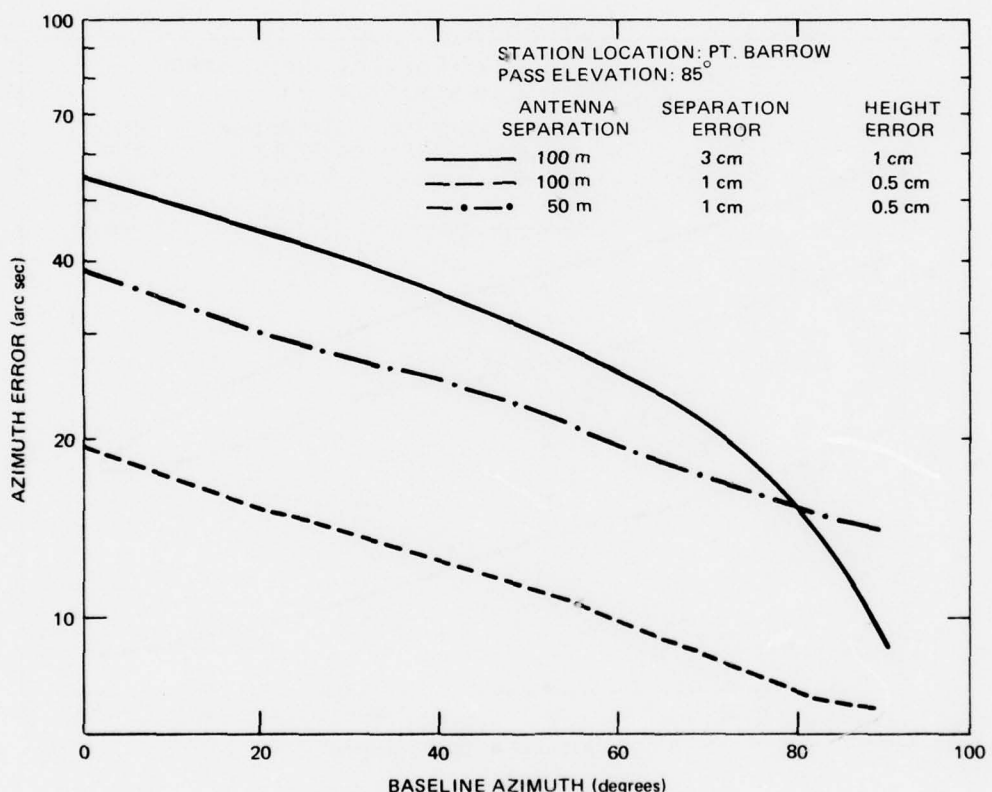


FIG. 128 AZTRAN ERRORS: CASE 8

6. COMMUNICATION SYSTEM

INTRODUCTION

Military command, control, and communications in the Arctic, as in any forward operational area, present several problems. Communications must be provided between the various elements operating within the Arctic and also between the Arctic and the continental United States. Conditions in the Arctic preclude the use of land lines, not only over the ocean areas but also over extensive land areas.

As with the navigation system, satellites appear to allow the maximum capability for communications. Two synchronous tactical communications satellites are now in orbit, DSCS (Defense Support Communication System), and Phase II DCA (Defense Communication Agency). Fleet SATCOM (Satellite Communications) has a system of four satellites in development for launch within the next few years. When these satellites become available, they should provide coverage in the lower portion of the Arctic basin, but will not cover the entire polar regions. An Air Force Polar Data Satellite system is also under development that will provide additional coverage.

Pt. Barrow is currently equipped with a high-power Navy communications center capable of wide frequency diversity. This center, operated by the Coast Guard, is capable of providing MF, HF, and VHF coverage of the Arctic basin.

An extensive study of the tactical communications problem in the Arctic is addressed in an ARPA (Advanced Research Projects Agency) Forward Based System Study-Command and Control Task.

PROPOSED SYSTEM

Because of the uncertainty of satellite communications in the Arctic the proposed system is based on conventional radio communications systems. To provide for long-range communication the vehicle should be equipped with AN/ARC-142 equipment or equivalent. This unit provides a transmission power of 1 kW, capable of

THE JOHNS HOPKINS UNIVERSITY
APPLIED PHYSICS LABORATORY
LAUREL MARYLAND

operating over the range of 2 to 30 MHz in the AM, SSB, or CW modes. A dual system should be provided for increased reliability (Ref. 36).

Provisions must be made for short-range communication between the SEV and supporting vehicles such as aircraft or snowmobiles. To provide the ability to communicate with any of these vehicles, the SEV can be equipped with VHF and UHF transceiver equipment. The equipment would provide the capability of both AM or FM transmissions and be capable of being tuned to any frequency within their band rapidly with a minimum of 40 W output (Ref. 37).

In operations of the type in which the SEV may be involved, it is often necessary to communicate with crews on the ground in the immediate vicinity. For this purpose, a system consisting of up to six hand-held walkie-talkie type radios are needed plus a compatible unit aboard the vehicle. An intercom system would also be a necessity for communications between crew stations. Its complexity would be determined by the craft size and crew.

It is essential that a vehicle operating in the Arctic environment be provided with portable emergency communication units that can operate independently of the vehicle in case of a disaster. These devices should be extremely rugged and located in such a manner that they can be reached from the outside of the vehicle in an emergency where the crew has made a rapid exit. Two types of units should be provided. First, HF units capable of long-range communication and operating on the standard shipboard emergency frequency of 2182 kHz and second, hand-held pilot emergency locator units operating on the 243 MHz aircraft emergency frequency.

Ref. 36. L. L. Warnke, "General Characteristics of the Obstacle Avoidance, Navigation and Communications Systems for an Arctic SEV," APL/JHU S3R-72-105, 26 May 1972.

Ref. 37. Reference Data for Radio Engineers (5th Edition), Howard W. Sams & Company, New York, 1968.

7. CONCLUSIONS AND RECOMMENDATIONS

OBSTACLE DETECTION AND AVOIDANCE

The proposed all-weather obstacle detection and avoidance system is a combination of a 95-GHz radar/display, a 10-GHz radar/display, and a laser radar. A multicolor operator display for obstacles with heading/speed, range markers, vehicle maneuvering limits, and vehicle stopping position were included.

A computer for processing the radar and laser data is provided in the basic system.

The shadow-detection process has been shown to be a feasible technique in which sufficiently narrow fan-beam antennas are practical. The geometric limitations of the shadow-detection process should present no serious problems for travel on the Arctic Ocean.

It is recommended that an advanced model of the obstacle detection system with radar shadowing technique and microprocessor/display for the SEV configuration be developed. Emphasis on space and weight savings would be a goal.

NAVIGATION

The proposed navigation system utilizes the LTN-51 Inertial Navigation System (having a drift rate of less than 1 nmi/hr), operated in a Kalman-filter software mode, and updated by the Navy Navigation Satellite's (TRANSIT) receiver and processor, which are accurate to within 0.02 nmi (static). The satellite receivers will be operated in a dual mode to provide azimuth (50 to 60 arc-seconds) and to update the INS data. A microprocessor will be contained within the system to process the data for display. The backup system will be a gyrocompass, i.e., Mk 27 and Loran/Omega receivers.

It is recommended that an advanced model of the system using "off-the-shelf" subsystems be designed and fabricated to minimize space and weight requirements within the SEV. The software will also be coded and checked out for the proposed system.

COMMUNICATIONS

A communication system was proposed using the AN/ARC-142 for long range, UHF/VHF for short range, and a battery-operated HF system for emergency with normal shipboard and aircraft emergency frequencies.

THE JOHNS HOPKINS UNIVERSITY
APPLIED PHYSICS LABORATORY
LAUREL MARYLAND

It is recommended that a study be made of the new Marisat or Fleet satellite communications (GHz range) equipment (e.g., the WSC-3 equipped with either a blade antenna or small dish antenna). An advanced model of the system should be packaged for SEV configurations.

THE JOHNS HOPKINS UNIVERSITY
APPLIED PHYSICS LABORATORY
LAUREL MARYLAND

ACKNOWLEDGMENT

The contributions of the following government and industrial organizations for support in the areas noted are gratefully acknowledged:

ARPA - Program Definition and Funding

Arctic Tests, Pt. Barrow 1971

NSRDC - Direction and coordination of the SK-5 testing program

CRREL - Support for ground-truth measurements and fog particle distribution measurements, and reduction of stereo photographs

NARL - Facilities support

USCG - Operation and maintenance of the vehicle and communications support

NAVOCEANO - Reduction of stereo photography

Amperex - Photography for ground-truth data (mapping)

RCA - Support of laser experiment

Newell - Wideband video recording

The following Applied Physics Laboratory personnel are commended for their contributions in the preparation of this report.

J. R. Albertine
C. C. Kilgus
R. H. Lapp
C. S. Morris
L. G. Smith

REFERENCES

1. "Contract N00017-62-C-0604; Technical Plan and Cost Estimate for the U.S. Naval Ship Research and Development Center," APL Ltr. AD-4788-39a, 27 July 1970.
2. L. L. Warnke, "Program Plan for Development of an Obstacle Detection System - Arctic SEV," APL/JHU S3R-71-349, 13 October 1971.
3. T. Thompson and A. C. Schultheis, "NSRDC Arctic SEV Program Plan," APL/JHU S3R-71-368, 4 November 1971.
4. APL Arctic SEV Program Plan, QM-72-040, APL/JHU SEV-002 (revision of APL Arctic Program Plan, QM-71-033, APL/JHU SEV-001), April 1971.
5. L. L. Warnke, "APL Arctic SEV Program - Revised Plan and Schedule for FY 1974 and FY 1975," APL/JHU S3R-73-093, 15 May 1973.
6. Arctic Surface Effect Vehicle Program Technology Summary and Design Development, NSRDC Report 4595, Naval Ship Research and Development Center, August 1975.
7. "SEV Arctic Environment Data Package," USACRREL Report 16, U.S. Army Cold Region Research and Engineering Laboratory, 1970.
8. P. V. Sellman et al., "Terrain and Coastal Conditions on the Arctic Alaska Coastal Plan," Supplement 1 to "SEV Arctic Environmental Data Package," USACRREL Special Report 165, U.S. Army Cold Region Research and Engineering Laboratory, 1972.
9. W. D. Hibler, III, "Characterization of Cold Regions Terrain Using Airborne Laser Profilometry," Symposium on Remote Sensing in Glaciology, Cambridge, England, 1974.
10. W. D. Hibler, III, "Statistical Variations in Arctic Sea Ice Ridging and Deformation Rates," SNAME Symposium on Ice Breaking and Related Technology, Montreal, Canada, 1975.
11. W. D. Hibler, III, et al., "Statistical Aspects of Sea Ice Ridge Distributions," AIDJEX Bulletin, Vol. 12, Division of Marine Resources, University of Washington, Seattle, WA, 1972, pp. 117-162.

THE JOHNS HOPKINS UNIVERSITY
APPLIED PHYSICS LABORATORY
LAUREL, MARYLAND

12. W. D. Hibler, III and S. F. Ackley, "Height Variation Along Sea Ice Pressure Ridges and the Probability of Finding Holes for Vehicle Crossings," USACRREL Special Report 197, U.S. Army Cold Regions Research and Engineering Laboratory, 1973.
13. W. D. Hibler, III and S. F. Ackley, "A Sea Ice Terrain Model and its Application to Surface Vehicle Trafficability," USACRREL Research Report 314, U.S. Army Cold Regions Research and Engineering Laboratory, 1973.
14. D. E. Kerr (Ed.), Propagation of Short Radio Waves, McGraw-Hill, New York, 1951 (Sections by J. H. Van Vleck and H. Goldstein).
15. J. V. Evans and T. Hagfors (Eds.), Radar Astronomy, McGraw-Hill, New York, 1968 (Section by T. F. Rogers).
16. H. C. van de Hulst, Light Scattering by Small Particles, John Wiley and Sons, New York, 1975.
17. R. Kingslake (Ed.), Applied Optics and Optical Engineering, Vol. I, Academic Press, New York, 1965 (Section by H. S. Stewart and R. F. Hopfield).
18. H. Barhydt, D. P. Brown, and W. B. Dorr, Comparison of Spectral Regions for Thermal Imaging Infrared Sensors, Hughes Aircraft Co., Fullerton, CA.
19. R. K. Crane, "Propagation Phenomena Affecting Satellite Communications Systems Operating in the Centimeter and Millimeter Wavelength Bands," Proc. IEEE, Vol. 59, No. 2, February 1971, pp. 173-188.
20. O. Ya. Usikov, V. L. German, and I. Kh. Vakser, "Investigation of Absorption and Scattering of Millimeter Waves under Conditions of Precipitation," Ukr. Phys. J., Vol. 6, No. 5, trans. by Aztec School of Languages, 1961, pp. 618-641.
21. G. E. Weibel and H. O. Dressel, "Propagation Studies in Millimeter-Wave Link Systems," Proc. IEEE, Vol. 55, No. 4, April 1967, pp. 497-513.
22. B. J. Mason, The Physics of Clouds, Clarendon Press, Oxford, 1971.

THE JOHNS HOPKINS UNIVERSITY
APPLIED PHYSICS LABORATORY
LAUREL, MARYLAND

23. P. Hoekstra and D. Spanogle, "Radar Cross Section Measurements of Snow and Ice for Design of SEV Pilotage System," CRREL Report under ARPA Order 1615, U.S. Army Cold Regions Research Laboratory, June 1971.
24. "SEV Feasibility Study, RAT SCAT Radar Backscatter and Cross Section Measurements of Snow and Ice," report AFSWC-TR-71-19 prepared for RAT SCAT (Radar Target Scatter Division), Air Force Special Weapons Center (Holloman Air Force Base, NM) by General Dynamics, Convair Aerospace Division (Fort Worth, TX), May 1971.
25. "SEV Feasibility Study - RAT SCAT Radar Backscatter and Cross Section Measurements of Snow and Ice," AFSWC-TR-71-19, Radar Target Scatter Division (RAT SCAT)/Air Force Special Weapons Center, May 1971.
26. P. Hoekstra and D. Spanogle, "Radar Cross Section Measurements of Snow and Ice for Design of SEV Pilotage System," CRREL Report under ARPA order 1615, U.S. Army Cold Regions Research and Engineering Laboratory, June 1971.
27. J. Perry, "Summary of Measurements on Millimeter Wave Propagation through Ice Fog," U.S. Army Cold Regions Research and Engineering Laboratory, June 1973.
28. J. W. Perry and A. W. Straiton, "Dielectric Constant of Ice at 35.3 and 94.5 GHz," J. Appl. Phys., Vol. 43, No. 2, February 1972, pp. 731-733.
29. J. W. Perry, Ph.D. Thesis (University of Texas, 1971).
30. T. Ohtake, "Unusual Crystal in Ice Fog," J. Atmos. Sci., Vol. 27, No. 3, 1970, pp. 509-511.
31. ARPA Arctic SEV Program Radar Field Tests Point Barrow, Alaska, APL/JHU SEV 003 (QM-75-083), September 1972.
32. "SEV Field Test Plan (Track Tests - Fall 1973)," APL/JHU S3R-74-154, 18 September 1973.
33. F. C. Paddison, "Status of APL Work on Navigation, Communication and Obstacle Avoidance," APL/JHU CQO-913, April 1972.
34. J. E. Sater et al., "Arctic Environment and Resources," Arctic Institute of North America, Washington, DC, 1971.

THE JOHNS HOPKINS UNIVERSITY
APPLIED PHYSICS LABORATORY
LAUREL, MARYLAND

35. J. R. Albertine, "An Azimuth Determination System Utilizing the Navy Navigation Satellites," Navigation: Journal of the Institute of Navigation, Vol. 21, No. 1, Spring 1974, pp. 54-60.
36. L. L. Warnke, "General Characteristics of the Obstacle Avoidance, Navigation and Communications Systems for an Arctic SEV," APL/JHU S3R-72-105, 26 May 1972.
37. Reference Data for Radio Engineers (5th Edition), Howard W. Sams & Company, New York, 1968.
38. J. R. Albertine, "AZTRAN: A Method of Azimuth Determination Using Artificial Satellites," APL/JHU S3R-71-156, 26 May 1971.

THE JOHNS HOPKINS UNIVERSITY
APPLIED PHYSICS LABORATORY
LAUREL MARYLAND

BIBLIOGRAPHY

This bibliography was prepared by the Space Development Department at APL to provide a comprehensive listing of all material published at APL on the SEV Development Program. Internal memoranda as well as reports published primarily for external distribution are included. The arrangement is chronological by APL group (S3E, S1A, and S2C), and by functional area (SEV, Aztran, and Nap-of-the-Earth Radar Project).

THE JOHNS HOPKINS UNIVERSITY
APPLIED PHYSICS LABORATORY
LAUREL MARYLAND

SEV REPORTS AND MEMORANDA
(Space Development Department)

No.	Title	Author	Date
S3R-70-134	Preliminary SEV Schedule and Budgetary Estimate for FY 70, 71, 72, and 73	A.C.Schulteis	24 Apr 70
S3R-70-207	SEV Program Tasks	A.C.Schulteis	18 Jun 70
S3R-70-292	Progress on SEV and TRIAD-I Programs During Period August 10-21, 1970	C.S.Morris	21 Aug 70
S3R-70-337	CRREL Meeting, 9/24/70; RCA Meeting, 9/23/70	T.T.Thompson	18 Sep 70
S3R-70-342	IR Laser System Design Equations for SEV	J.R.Albertine	21 Sep 70
S3R-70-352	Meeting with Grumman, 9/30/70	T.T.Thompson	25 Sep 70
S3R-70-358	CRREL Meeting at APL, 9/24/70	C.S.Morris	1 Oct 70
S3R-70-369	Minutes of SEV (SK-5) Instrumentation Meeting with DSRDC and Aerospace Personnel	L.L.Warneke	15 Oct 70
S3R-70-380	Tape Recorder for SEV Instrumentation	C.S.Morris	29 Oct 70
S3R-70-381	SK-5 SEV Instrumentation Program Plan	C.S.Morris/ L.L.Warneke	29 Oct 70
S3R-70-395	SEV Laser Radar	L.G.Smith	10 Nov 70
S3R-70-423	Loan of Sony Recorder for Use in the Surface Effects Vehicle Program	A.C.Schulteis	2 Dec 70
S3R-70-432	SEV Progress Report	C.S.Morris	7 Dec 70
S3R-70-435	Anticipated Component Costs for 94 GHz Radar Unit in SEV Program	J.D.Schneider	7 Dec 70
S3R-70-446	SK-5 Terrain Surveillance Test Plan	T.T.Thompson	23 Dec 70
S3R-71-001	The Relative Absorptivity of 40 kHz Ultrasonic Signals Measured by the Ultrasonic Height Detection System	J.Trennepohl	5 Jan 71

THE JOHNS HOPKINS UNIVERSITY
 APPLIED PHYSICS LABORATORY
 LAUREL MARYLAND

SEV REPORTS AND MEMORANDA
 (Space Development Department)

No.	Title	Author	Date
S3R-71-021	Measurement of the Effects of Ultrasonic Height Detector	J.Trennepohl	18 Jan 71
S3R-71-025	Test Plan for Terrain Surveillance Experiment with the SK-5 Vehicle	L.L.Warnke	21 Jan 71
S3R-71-034	Preliminary Testing of the X-Band Radar for the SEV Program	J.D.Schneider	29 Jan 71
S3R-71-052	Progress Report on SEV for January 1971	C.S.Morris	10 Feb 71
S3R-71-059	Moving Vehicle Tests - Terrain Surveillance Experiments on the SK-5	L.L.Warnke	19 Feb 71
S3R-71-060	Support Requirements for Terrain Surveillance Tests	L.L.Warnke	19 Feb 71
S3R-71-066	Required Manpower for Proposed Work Task on SEV for FY 72 and 73	L.L.Warnke	24 Feb 71
S3R-71-082	Crews for Arctic SK-5 Tests April-June 1971	T.T.Thompson	10 Mar 71
S3R-71-113	SEV Progress Report for March 1971	C.S.Morris	6 Apr 71
S3R-71-118	TV Camera Requirements for SEV (SK-5) Tests	L.G.Smith	7 Apr 71
S3R-71-142	Stabilization of the SEV Obstacle Detection System	A.Finkel	10 May 71
S3R-71-184	SK-5 Terrain Sensing Tests 5/71	T.T.Thompson	17 Jun 71
S3R-71-202	94 GHz Calculations, Part I	R.Eberhart	
S3R-71-211	94 GHz Calculations, Part II	R.Eberhart	9 Jul 71
S3R-71-217	Outfitting of Mobile Van for 95 GHz Radar	J.D.Schneider	14 Jul 71
S3R-71-220	94 GHz Calculations, Part III	R.Eberhart	16 Jul 71
S3R-71-221	94 GHz Scintillation	R.Eberhart	16 Jul 71
S3R-71-222	94 GHz Biological Effect, Part I	R.Eberhart	16 Jul 71
S3R-71-225	Layout and Performance of the 95 GHz Radar	J.D.Schneider	19 Jul 71

THE JOHNS HOPKINS UNIVERSITY
 APPLIED PHYSICS LABORATORY
 LAUREL MARYLAND

SEV REPORTS AND MEMORANDA
 (Space Development Department)

No.	Title	Author	Date
S3R-71-232	94 GHz Bio Effects Meeting	R.Eberhart	22 Jul 71
S3R-71-268	94 GHz Biological Effects, Part II	R.Eberhart	19 Aug 71
S3R-71-271	Terrain Sensing Test - June 1971	T.T.Thompson	26 Aug 71
S3R-71-281	EPA/APL 94 GHz Bio Effects Meeting	R.Eberhart	25 Aug 71
S3R-71-282	Preliminary Requirements for SEV Obstacle Avoidance, Sensing, and Navigation Systems	L.L.Warnke	25 Aug 71
S3R-71-283	Communications for an Arctic SEV	E.E.Westerfield	25 Aug 71
S3R-71-295	Trip Report - Point Barrow, Alaska	W.A.Craig	3 Sep 71
S3R-71-304	SEV 94 GHz Radar and Laser Instrumentation Effects on Environment	C.S.Morris	14 Sep 71
S3R-71-318	Specification Update 95 GHz Radar	J.D.Schneider	21 Sep 71
S3R-71-349	Program Plan for Development of Obstacle Detection System - Arctic SEV	L.L.Warnke	13 Oct 71
S3R-71-352	Exposure Level Testing for 95 GHz Radiation	J.D.Schneider	15 Oct 71
S3R-71-368	NSRDC Arctic SEV Program Plan	T.T.Thompson / A.C.Schulteis	4 Nov 71
S3R-71-372	Issuance of Clothing for Personnel Working in Radar Van	J.D.Schneider	9 Nov 71
S3R-71-415	Procurement Plans for a Scanning Antenna System for 95 GHz Radar Test System	J.D.Schneider	28 Dec 71
S3R-71-417	Evaluation Concepts in Predicting Performance of Scanning 95 GHz Radar	J.D.Schneider	30 Dec 71
S3R-72-017	Return of Loaned Tape Recorder for SEV Instrumentation	C.S.Morris	18 Jan 72
S3R-72-040	Technique for Estimating Detection Probabilities of Ice Objects with the APL 95 GHz Radar	J.D.Schneider	11 Feb 72

SEV REPORTS AND MEMORANDA
 (Space Development Department)

No.

S3R-72-068	Ice Object Detection Probabilities for the 95 GHz Radar Under Adverse Weather Conditions	J.D.Schneider	22 Mar 72
S3R-72-072	Point Barrow Terrain Sensing Tests - 1971	T.T.Thompson	31 Mar 72
S3R-72-075	SEV Instrumentation Equipment, Status of	W.A.Craig	4 Apr 72
S3R-72-080	SEV Arctic Instrumentation Equipment, Return of	W.A.Craig	11 Apr 72
S3R-72-100	Servo Loop for the SEV Stable Platform	A.Finkel	24 May 72
S3R-72-105	General Characteristics of the Obstacle Avoidance, Navigation, and Communication Systems for an Arctic SEV	L.L.Warnke	26 May 72
S3R-72-119	Procurement Specification for a Computer System SEV Experimental Obstacle Detection and Avoidance System	L.L.Warnke	3 Jul 72
S3R-72-137	Effect of SEV Vehicle Performance Parameters on Obstacle Detection System Characteristics	L.L.Warnke	8 Aug 72
S3R-72-140	Specification for 95 GHz Radar Slip Ring Assembly	J.D.Schneider	15 Aug 72
S3R-72-170	SEV Obstacle Avoidance - Effects of Obstacle Shape on Height Determination	L.L.Warnke	26 Sep 72
S3R-72-179	Lease of Inertial Navigation System	A.Finkel	11 Oct 72
S3R-72-181	ARPA Atmospheric Measurements Program	F.W.Schenkel	17 Oct 72
S3R-72-184	Laser Radar Design Support Instrumentation	F.W.Schenkel	23 Oct 72
S3R-72-186	SEV Laser Radar Program Schedule	F.W.Schenkel	26 Oct 72
S3R-72-188	Weight, Size, Power, and Cost Estimate for a 95 GHz Radar Obstacle Detection System	L.L.Warnke	30 Oct 72
S3R-72-189	Suggested Decision Points and APL - SEV Program Plan	L.L.Warnke	30 Oct 72
S3R-72-190	SEV Laser Radar Program Schedule	F.W.Schenkel	26 Oct 72
S3R-72-194	Suggested Decision Points and APL - SEV Program Plan	L.L.Warnke	7 Nov 72

THE JOHNS HOPKINS UNIVERSITY
 APPLIED PHYSICS LABORATORY
 LAUREL MARYLAND

SEV REPORTS AND MEMORANDA
 (Space Development Department)

No.	Title	Author	Date
S3R-72-205	Computer System Selection and Recommendations for SEV Obstacle Detection and Avoidance	L.L.Warnke/ O.Gooding	14 Nov 72
S3R-72-213	Justification of Computer for SEV Experimental Avoidance System	O.Gooding	30 Nov 72
S3R-72-222	Design and Fabrication of the Stable Platform and Pedestal Structures - ARPA Arctic SEV Program - Experimental Obstacle Detection System	L.L.Warnke	11 Dec 72
S3R-72-228	Revision to Cost Estimate for Hybrid Simulator	L.L.Warnke	22 Dec 72
S3R-72-229	Requirement for Hybrid Simulator - SEV Obstacle Detection and Avoidance	L.L.Warnke	26 Dec 72
S3R-72-230	SEV Related Laser Radar Program	F.W.Schenkel	29 Dec 72
S3R-72-231	Moments of Inertia for SEV Radar Antenna and Platform	A.Finkel	29 Dec 72
S3R-73-002	Correlation of SEV 94 GHz Radar Data with Truth Data	R.E.Hametz	4 Jan 73
S3R-73-007	SEV Laser Radar Presentation Given to Dr. Zirkland and Col. Dereska of ARPA on 1/15/73	F.W.Schenkel	17 Jan 73
S3R-73-012	Effects of Antenna Resonance of Platform Servos	A.Finkel	26 Jan 73
S3R-73-013	Raytheon Unsolicited Proposal Log No. S-4460	F.W.Schenkel	26 Jan 73
S3R-73-022	Alternate Uses of a CO ₂ Heterodyne Laser Radar	F.W.Schenkel	12 Feb 73
S3R-73-024	Response to USRDC Request for Data on Composite System Design	L.L.Warnke	12 Feb 73
S3R-73-026	Justification for Letter of Intent to Procure SEV Computer	O.Gooding	15 Feb 73
S3R-73-031	SEV Laser Radar Program Schedule	F.W.Schenkel	22 Feb 73
S3R-73-038	Allocation of Space for Stable Platform and Antenna Assembly and Testing	A.Finkel	28 Mar 73

THE JOHNS HOPKINS UNIVERSITY
 APPLIED PHYSICS LABORATORY
 LAUREL MARYLAND

SEV REPORTS AND MEMORANDA
 (Space Development Department)

No.	Title	Author	Date
S3R-73-055	SEV 94 GHz Radar Field Test Site Requirements	L.L.Warnke	20 Mar 73
S3R-73-056	Raytheon Contract on "Atmospheric Measurements" Using a Heterodyne Laser Radar, APL Subcontract 372268, 30 January 1973	F.W.Schenkel	21 Mar 73
S3R-73-057	SEV Experimental 95 GHz Radar Data Processing	O.E.Gooding / J.M.Whisnant	23 Mar 73
S3R-73-058	ARPA Quarterly Report	F.W.Schenkel	28 Mar 73
S3R-73-069	Arctic SEV Program — Revised Schedule for FY 1974 and FY 1975	L.L.Warnke	6 Apr 73
S3R-73-093	APL Arctic SEV Program Revised Plan and Schedule for FY 1974 and FY 1975	L.L.Warnke	10 May 73
S3R-73-099	Response to NSRDC Request for Data on Composite System	L.L.Warnke	23 May 73
S3R-73-108	Preliminary Outline of APL Arctic SEV Summary Documentation	L.L.Warnke	6 May 73
S3R-73-116	Radar Cross Section Measurements of Wire at 95 GHz	J.Albertine	29 Jun 73
S3R-73-128	Minutes of Symposium	J.D.Schneider	20 Jul 73
S3R-73-154	SEV Field Test Plan	L.L.Warnke	18 Sep 73
S3R-73-144	Vehicle Arrangements for SEV Field Test	C.S.Morris	16 Sep 73
S3R-73-187	SEV Antenna Drive Characteristics	A.Finkel	19 Dec 73

THE JOHNS HOPKINS UNIVERSITY
 APPLIED PHYSICS LABORATORY
 LAUREL MARYLAND

SEV REPORTS AND MEMORANDA
 (Space Development Department)

No.	Title	Author	Date
SIA-211-72	SLA Work Tasks for the Arctic SEV Simulation, Q2HO	J.M.Whisnant	2 Feb 72
SIA-224-72	Selection of Radar Frequencies for Hazard Avoidance in the Arctic Environment	H.Hopfield	15 Mar 72
SIA-261-72	Processing of Information on the CRREL DATA Tape	J.M.Whisnant/ S.T.Haywood	11 Jul 72
SIA-278-72	Arctic SEV Display Concepts	J.M.Whisnant	13 Sep 72
SIA-292-72	The Relationship of the APL Hybrid Simulation to the Boeing Simulator: A reply to part of ARPA Question No. 4	J.M.Whisnant	26 Oct 72
SIA-301-72	A Discussion of a Special Set of Linear Equations Associated with an SEV Radar Problem	S.T.Haywood	21 Nov 72
SIA-302-72	On Obtaining a Resolution of Less Than One Beamwidth by Processing Radar Return Data	S.T.Haywood/ J.M.Whisnant	28 Nov 72
SIA-307-72	Arctic Terrain Model I	J.M.Whisnant/ S.T.Haywood	14 Dec 72
SIA-310-72	Comments on the Maneuvering and Control Task Section of Boeing's October Monthly Progress Report	J.M.Whisnant	21 Dec 72
SIA-317-73	Comments on the Conclusions of the Arctic SEV Program Technical Interchange Meeting at Boeing in November 1972	J.M.Whisnant	15 Jan 73
SIA-319-73	SEV Analysis and Software	J.M.Whisnant/ L.L.Warnke	17 Jan 73
SIA-320-73	An Obstacle Height Determination Program for the SEV Computer	J.M.Whisnant	3 Apr 73
SIA-323-73	Sensitivity Analysis for the SEV Radar Shadowing Technique	J.M.Whisnant	6 Feb 73
SIA-326-73	Additional Information on Arctic Terrain Model I	S.T.Haywood/ J.M.Whisnant	12 Feb 73
SIA-417-73	The SEV Display Program	H.K.Utterback	Nov 73

THE JOHNS HOPKINS UNIVERSITY
 APPLIED PHYSICS LABORATORY
 LAUREL MARYLAND

SEV REPORTS AND MEMORANDA
 (Space Development Department)

No.	Title	Author	Date
S2C-0-266	SEV Meeting with NSRDC	P.E.P.White	21 Dec 70
S2C-0-267	SEV Instrumentation Schedule	P.E.P.White	28 Dec 70
S2C-0-276	Spare Parts Lists for SK-5 Instrumentation	P.E.P.White	26 Mar 71
S2C-0-277	"Daily Operation Procedure" and "Sensor Document"	P.E.P.White	31 Mar 71
S2C-0-278	Documentation for SK-5	P.E.P.White	2 Apr 71
S2C-0-284	Documentation for SK-5	P.E.P.White	15 Jul 71
S2C-2-306	Installation of Sensors on the SK-5 Surface Effect Vehicle	C.A.Dunnell	24 Mar 71
S2C-2-319	Report on the SK-5 Instrumentation Operations	G.B.Seymour	30 Aug 71
S2C-2-322	Communications for an Arctic SEV	G.B.Seymour	14 Sep 71
S2C-3-177	SK-5 Instrumentation Check-Out Status on February 1	H.H.Elliott	2 Feb 71
S2C-3-179	Height Radar Test Set (SK-5 Craft)	J.F.Jaworski	7 Apr 71
S2C-3-181	SK-5 Hovercraft Electronic Instrumentation Technical Manual	H.H.Elliott	28 Jun 71

THE JOHNS HOPKINS UNIVERSITY
APPLIED PHYSICS LABORATORY
LAUREL, MARYLAND

AZTRAN REPORTS AND MEMORANDA
(Space Development Department)

No.	Title	Author	Date
Jansky and Baily (Div. of Atlantic Research Corp), Washington, DC	The Loran-C System of Navigation	E.E.Westerfield	Feb 62
S3R-69-384	AZTRAN Development	E.E.Westerfield	
S3R-70-143	Budgetary Estimates for AZTRAN	E.E.Westerfield	30 Apr 70
S3R-70-153	Development of AZTRAN Calculation	J.R.Albertine	6 May 70
S3R-70-209	AZTRAN Results	J.R.Albertine	23 Jun 70
S3R-71-032	Summary of AZTRAN Results Using a 50 Meter Baseline	J.R.Albertine	27 Jan 71
S3R-71-156	(Thesis) AZTRAN: A Method of Azimuth Determination Using Artificial Satellites	J.R.Albertine	26 May 71
<u>Navigation,</u> <u>Vol. 18,</u> <u>No. 2</u>	Omega	E.R.Swonson	(Summer) 71
S3R-71-375	AZTRAN Error Model Results	J.R.Albertine	15 Nov 71
S3R-72-121	Position and Azimuth Ambiguities in the Navigation Satellite System	J.R.Albertine	7 Jul 72
S3R-73-051	Request for Naval Approval of AZTRAN Abstract	J.R.Albertine	16 Mar 73

THE JOHNS HOPKINS UNIVERSITY
APPLIED PHYSICS LABORATORY
LAUREL MARYLAND

AZTRAN REPORTS AND MEMORANDA
(Space Development Department)

No.	Title	Author	Date
S3R-73-155	Request for Naval Approval of AZTRAN Paper	J.R.Albertine	21 Sep 73
<u>Proceedings</u> <u>of Radio</u> <u>Navigational</u> <u>Symposium,</u> <u>Institute</u> <u>of Navi-</u> <u>gation,</u> <u>Washington,</u> DC	A Review and Application of VLF and LF Transmissions for Navigation and Tracking	J.M.Beukers	13-15 Nov 73
	<u>Navigation,</u> Vol. 21, No. 1	J.R.Albertine (Spring) 74 An Azimuth Determination System Utilizing the Navy Navigation Satellites	

THE JOHNS HOPKINS UNIVERSITY
 APPLIED PHYSICS LABORATORY
 LAUREL MARYLAND

NAP-OF-THE-EARTH RADAR PROJECT
 (Space Development Department)

No.	Title	Author	Date
S3R-73-037	Helicopter Terrain Scanning (Laser Radar Q2HO)	F.W.Schenkel	28 Mar 73
S3R-73-044	Helicopter Terrain Scanner Meeting at ARPA	F.W.Schenkel	8 Mar 73
S3R-73-059	Helicopter Terrain Scanner Study Program	F.W.Schenkel	28 Mar 73
S3R-73-063	Helicopter Nap of Earth Terrain Scanner Study	F.W.Schenkel	3 Apr 73
S3R-73-076	FY 74 Budget for Helicopter Nap of Earth Terrain Scanner	F.W.Schenkel	13 Apr 73
S3R-73-117	ARPA Quarterly - Apr-Jun 1973 Helicopter Terrain Scanner and Wire Detection Study	F.W.Schenkel	2 Jun 73
S3R-73-129	95 GHz Radar for Helicopter Wire Detection	F.W.Schenkel	26 Jul 73
S3R-73-133	Nap-of-the-Earth Terrain Scanner and Wire Detection Systems Feasibility Study (Transmittal of S3R-016)	F.W.Schenkel	8 Aug 73
S3R-73-156	ARPA Quarterly Report Covering Helicopter Nap-of-the-Earth	F.W.Schenkel	24 Sep 73
S3R-73-169	Proposal for Helicopter Wire Detection System	F.W.Schenkel	26 Oct 73
S3R-73-174	Helicopter Wire Detection System Proposal	F.W.Schenkel	9 Nov 73
BEP-73-17	Notes on ARPA Problem	J.Gebhard	6 Apr 73
BEP-73-24	Meeting at Pentagon Re. Nap-of-Earth Flying in Helos at Night	R.Hanes	27 Apr 73
TG 1225	Helicopter Nap-of-the-Earth Terrain Scanner and Wire Detection Systems Feasibility Study	F.W.Schenkel / J.R.Albertine	Oct 73
,			
TG 1235	An Azimuth Determination System Using the Navy Navigation Satellites	J.R.Albertine	-

THE JOHNS HOPKINS UNIVERSITY
APPLIED PHYSICS LABORATORY
LAUREL MARYLAND

SEV REPORTS AND MEMORANDA

No.	Title	Author	Date
SEV 001 (QM-71-033)	APL Arctic SEV Program Plan		Apr 71
MMS-3-043	Performance of the Kaar Radar over a Flat, Snow-Covered Surface	E.Shotland	6 Apr 71
CQ0-821	Final Documentation, SK-5 Instrumentation System	F.C.Paddison	20 Sep 71
TG 1190	Transportation in the Arctic	F.C.Paddison A.M.Stone	Apr 72
SEV 002 (QM-72-040) (Revision to SEV 001)	APL Arctic SEV Program Plan		Apr 72
CQ0-913	APL Presentation Material to ARPA SEV Contractors	F.C.Paddison A.M.Stone	10 Apr 72
SEV 003 (QM-72-083)	ARPA Arctic SEV Program, Radar Field Tests, Point Barrow, Alaska		Sep 72

THE JOHNS HOPKINS UNIVERSITY
APPLIED PHYSICS LABORATORY
LAUREL MARYLAND

SEV REPORTS AND MEMORANDA

No.	Title	Author	Date
CQO-1028	Review of APL Arctic SEV Program	F.C.Paddison A.M.Stone	22 Nov 72
EES/GIT Project A-1430	Engineering Experiment Station, Georgia Institute of Technology Final Technical Report on Phases I and II, 94-GHz Fixed Fan-Beam Antenna	D.G.Dobnar R.A.Moore J.W.Coffer, Jr. R.M.Goodman, Jr. L.A.Stapleton	Jun 73
MED-SR/647	A 95 GHz Phase Interferometer as a Terrain Avoidance Sensor for the Arctic SEV	R.C.Mallalieu	14 Feb 73

THE JOHNS HOPKINS UNIVERSITY
APPLIED PHYSICS LABORATORY
LAUREL, MARYLAND

Appendix A

VENDOR SPECIFICATIONS

TORQUE MOTOR
TACHOMETER
SHAFT ENCODER
THERMISTOR
POWER AMPLIFIER

Torque Motor Specifications*

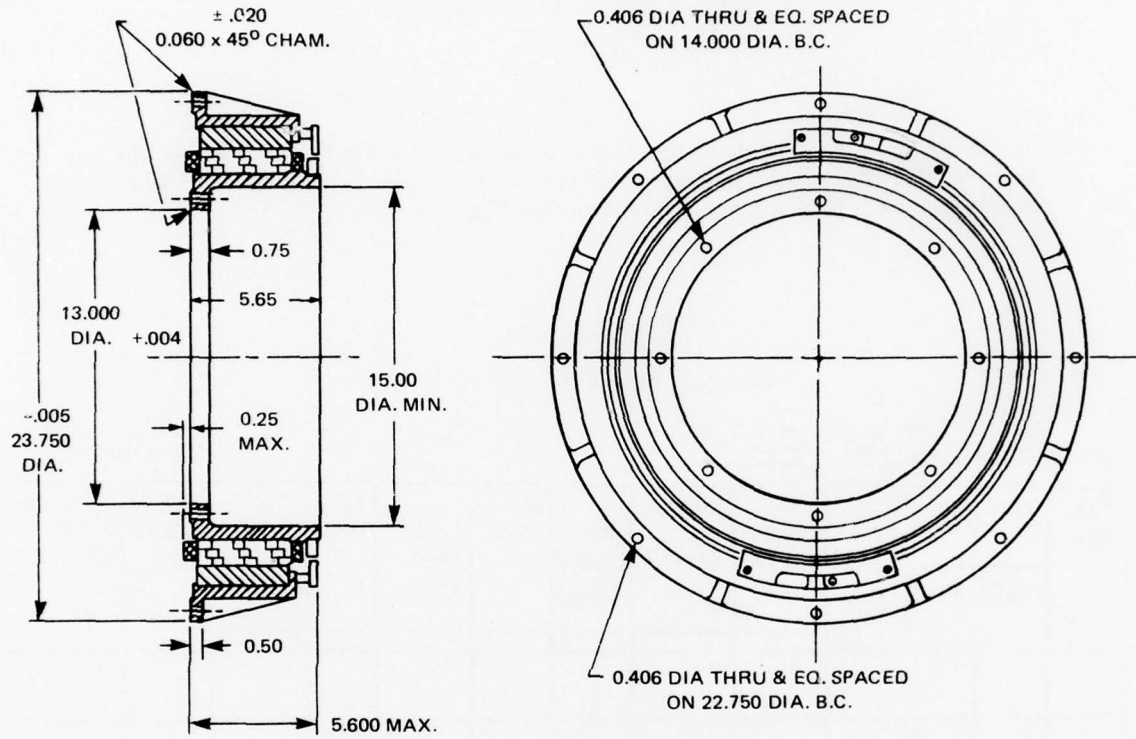
Table A-1 is a reproduction of a data sheet supplied for motor type 232-05A, serial numbers 0003, 0004, and 0005. Detailed general specifications are given in Fig. A-1.

Table A-1
Torque Motor Specifications

SER. NO.	NO-LOAD		DIR. OF ROTA.	NO- LOAD R.P.M.	TORQUE	Kt	TORQ. AMPS.	BREAK- AWAY AMPS.	RES. OHMS	HIPOT VOLTS	TRAV. NO. DATE INSP. BY
	VOLTS	AMPS									
			CW	CCW							
0003	50	.40	CW	18.0	270	19.3	14	.38	2.8	—	OK 2-2-73
0004	50	.40	CW	17.5	272	19.4	14	.35	2.8	OK	{(m) 1) RK
0005	50	.50	CW	17.5	272	19.4	14	.40	2.8	OK	
5			CCW		308	19.3	16				2-2-73

*Data supplied by Magnadyne, Inc., Carlsbad, CA.

THE JOHNS HOPKINS UNIVERSITY
APPLIED PHYSICS LABORATORY
LAUREL, MARYLAND



WINDING CONSTANT	UNITS	SYM	VALUE
PEAK TORQUE	lb-ft	T _P	300
MOTOR CONSTANT	lb-ft/ $\sqrt{\text{watt}}$	K _M	10.4
ELECT TIME CONSTANT	ms	T _E	15.2
MECH TIME CONSTANT	ms	T _M	6.3
POWER @ PK TORQUE (25°C)	W	P _P	835
DAMPING (ZERO Z)	lb-ft/(rad/s)	F _O	147
FRICITION TORQUE	lb-ft	T _F	26
RIPPLE TORQUE (AVG TO PK)	%	T _R	1
RIPPLE CYCLES/REV	CYCLES/REV	—	133
ULTIMATE TEMP RISE/WATT	°C	TPR	0.2
MAX WINDING TEMP	°C	—	155
ROTOR INERTIA	lb-ft·s ²	J _M	93
MAX POWER RATE	lb-ft·s ²	P	96500
THEORETICAL ACCEL	rad/s ²	α _M	3220
NO LOAD SPEED	rad/s	ω _{NL}	—
WEIGHT	lb	—	165
DC RESISTANCE	OHMS	Ω	2.8
VOLTS @ PEAK TORQUE	VOLTS	V _P	0.43
AMPS @ PEAK TORQUE	AMPS	I _P	15.4
TORQUE SENSITIVITY	lb-ft/A	K _T	194
BACK EMF	V/rad/s)	K _B	26.1
INDUCTANCE	mH	L	>42
NUMBER OF POLES	—	—	24

FIG. A-1 TORQUE MOTOR SPECIFICATION (source of information: Magnadyne Inc.
Carlsbad, California DWG No. 232-05 dated 5-10-72)

Tachometer Specifications*

The Inland Motor Corporation of Virginia describes their Model TG 5723 tachometer generator as

"a frameless DC-permanent-magnet precision tachometer generator...the smallest known tachometer available with a ripple voltage, average-to-peak, of 0.1%..., it has a temperature coefficient of $0.01\%/\text{ }^{\circ}\text{C}$. Attached directly to the drive shaft, it functions as a rate reference in rate-servo systems and as a velocity damping device in position-servo systems.

"It is shipped as three unmounted components: rotor, brush ring assembly, and permanent magnet field with keeper. The keeper must not be removed until the rotor is fully in place. When installed, it is required that the structure with which the circumferentially oriented field is in direct contact be nonmagnetic. Rotor-to-field eccentricity should not exceed 0.002 in. The commutator is gold plated and brushes are of precious metal alloy. Brush life will normally exceed 3×10^6 revolutions. Rotor hubs and field adapters are supplied to customer specification."

Additional data on the TG 5723 tachometer generator are listed in Table A-2.

*Data supplied by Inland Motor Corporation of Virginia, Radford, VA.

Table A-2

Tachometer Data

Inside diameter, in.	3.94
Outide diameter, in.	7.38
Tach generator friction torque, lb-ft	0.14
Ripple voltage (average-to-peak), %	0.1
Ripple cycles per revolution	139
Rotor moment of inertia, lb-ft-s ²	0.0075
Tach generator weight, lb	10.1
Max. permissible winding temp., °C	135
Max. terminal voltage, V	200
Temperature coefficient, %/°C	0.01
Nominal winding constants*	
DC resistance, Ω @ 25°C	5130
Voltage sensitivity, V/(rad/s)	11.6
Inductance, h	6.9
Min. load resistance, kΩ	513
Max. operating speed, rad/s	17.3
Volts @ max. operating speed, V	200

*Special winding

THE JOHNS HOPKINS UNIVERSITY
APPLIED PHYSICS LABORATORY
LAUREL, MARYLAND

Shaft Encoder Specifications*

The Measurement Systems Division of Itek describes their DIGISEC RA16/55(S) encoder as one of a series of

"encoders available in resolutions up to 19 bits (524,288 parts per turn) of natural binary data. These encoders are housed in a rugged package. The 3/4-in. thru-hole permits passage of a light beam or coax cable through the axis of rotation. External precision couplings are available to compensate for misalignments that occur in the installation."

The separate electronics (S) configuration permits field maintenance of the system, since the electronics are packaged on plug-in printed circuit cards. A 10-foot interconnecting cable between the optical unit and the electronics package is supplied with the system. Also, a binary lamp display and serial readout are available as options.

The electrical and mechanical specification of the RA16/55(S) encoder are listed in Table A-3.

*Data supplied by Measurement Systems Division of Itek Corporation, Newton, MA.

Table A-3
 RA16 Encoder Specifications

<u>Electrical</u>			
Resolution			
Quanta/revolution	65 536		
Angular resolution (arc-sec)	19.78		
Logic (output)			
Format	Parallel whole-word and optional serial readout		
Level	Voltage	Current	Impedance
"ONE"	+4.0 to +6.0 VDC	Source: 3 mA max.	300 Ω, max.
"ZERO"	0.0 to +0.5 VDC	Sink: 20 mA max.	10 Ω, max.
Hold pulse (input)*			
ON	+3.5 to +10.0 VDC		
OFF	±0.5 VDC		
Impedance	500 Ω, min.		
Settling time	3 μs		
Power requirements[†]			
+6 VDC (2% regulation)	1 800		
-6 VDC	200		
+12 VDC (1% max., p-p ripple)	--		
<u>Mechanical</u>			
Outline dimensions			
Rotation (for increasing count)	Drawing C2000-207 (S)		
Operating speed (max.)			
Speeds (rpm)	45		
Slew speed (nonoperating)	500 rpm, max.		
Operating temperature range	-40 to 71°C		
Torque			
Breakaway	2.0 oz-in., max. at 25°C		
Running	1.5 oz-in., max. at 25°C		
Moment of inertia	6.0 oz-in. ² , max.		
Shaft loading			
Axial	10 lb, max.		
Radial	7 lb, max. (at mtg face)		
Weight	7.5 lb		
<u>Other</u>			
Product specification	A2000-604		
Humidity	MIL-STD-202, Method 103, Condition B (0 to 95%)		
MTBF	20 000 to 50 000 h calculated per MIL-HDBK 217A depending on encoder type and application		
Rated life, bearings	10 ⁹ revolutions, min.		
Rated life, lamps	10 000 hours, min.		

*Hold pulse input temporarily freezes the states of all parallel bits.

[†]All values in milliamperes. Does not include current required for options RA3 and RA4.

THE JOHNS HOPKINS UNIVERSITY
APPLIED PHYSICS LABORATORY
LAUREL, MARYLAND

Thermistor Specifications *

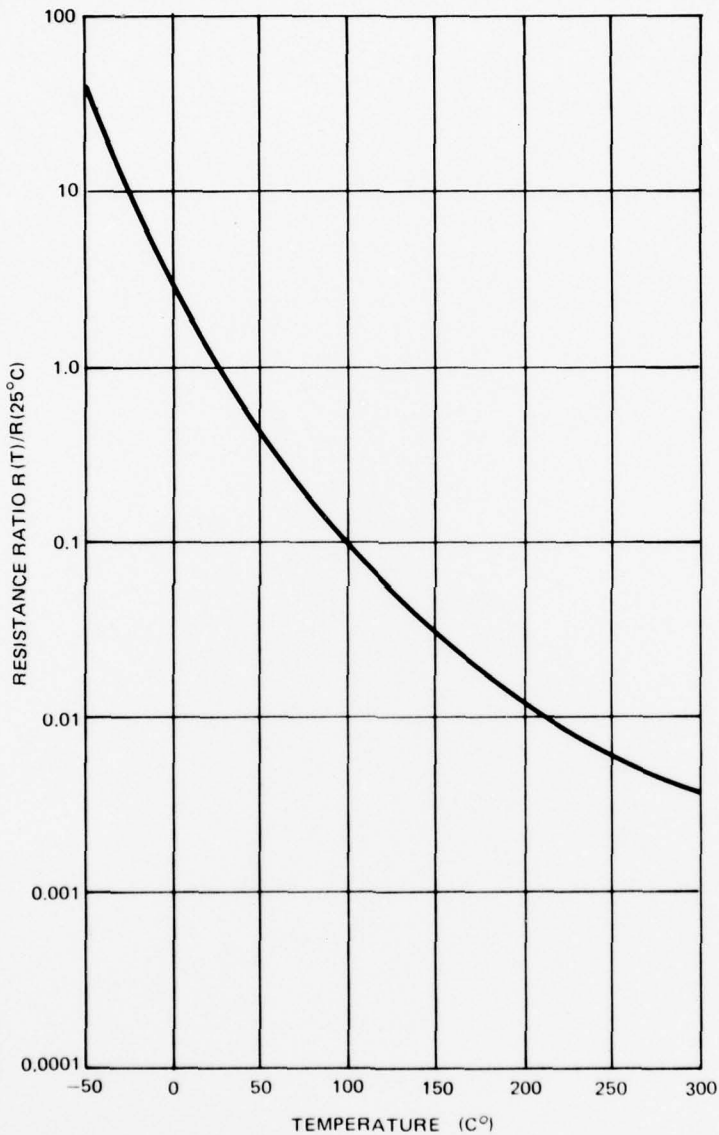


FIG. A-2 THERMISTOR RESISTANCE-TEMPERATURE CHARACTERISTIC

*Data supplied by Victory Engineering Corporation, Springfield, NJ.

DCA1000-3 Power Amplifier Specifications*

The Bulova Watch Company describes their Model DCA1000 DC servo amplifier as

"a linear DC power amplifier designed for servo applications requiring a DC motor drive of up to 1,000 watts. Amplifier will output ± 65 VDC @ 15 amperes peak current. Unit has self-contained cooling fan and is capable of 1,000 watts continuous dissipation @ 25° ambient temperature with no external heat sinking. Output current limiting is continuously adjustable in the range of 10% to 100% of rated load. Unit will withstand a sustained short circuit on output under full drive condition.

"User has option for -1, -2, or -3 unit, requiring plus and minus supply power, plus supply power and -15 VDC bias, and only plus supply power, respectively.

"The DCA1000 consists of a preamplifier stage (μ A741) whose gain and frequency response can be shaped by the proper combination of passive components, that can be placed on terminals available on the printed circuit board. Two inverting and one noninverting input signal terminals are provided for optional parallel or differential signal summing. Output circuit consists of a power amplifier that can be operated in either voltage or current feedback mode, with a voltage gain of 10 or voltage to current transfer ratio of 2.5 A/V. Provision is also made for an input terminal to the power amplifier stage where tachometer feedback can be parallel summed with the preamp output signal. The -3 unit also includes a low-power level...+75 VDC to -15 VDC, DC-DC converter."

The electrical specifications of the DCS1000-3 are listed in Table A-4.

*Data supplied by Bulova Watch Co., Inc., Electronic Division, Woodside, NY.

Table A-4
Electrical Specifications (@ 25°C)

<u>Preamplifier (frequency compensated)</u>	
Open loop gain	94 dB minimum
Unity gain crossover	1 MHz
Input offset voltage*	5 mV maximum
Input offset current	5 nA maximum
Input offset voltage drift	10 μ V/°C maximum (average)
Input offset current drift	0.1 nA/°C maximum (average)
Input resistance	2 MΩ minimum
Common mode rejection ratio	80 dB minimum
Power dissipation ($V_o=0$)	85 mW maximum
<u>Power Amplifier</u>	
Voltage gain (VOLTAGE FDBK MODE)	10 V/V
Current gain (CURRENT FDBK MODE)	2.5 A/V
Input resistance (also tach input term)	10 kΩ
Power input	+75 VDC ±5 VDC @ 15 A
Power output	±65 VDC @ 15 A
Current limit	Adjustable 10% to 100% of full rating
Full power frequency response	1 kHz typical
Small signal frequency response	5 kHz typical
Output null offset	100 mV maximum
Output null offset drift	1 mV/°C maximum
Internal power dissipation	1000 W max @ 25°C ambient Derate 10 watts/°C to + 70°C
Operating ambient temp range	-20°C to +70°C
Fan power	115 Vrms, 60 Hz

*Adjustable to zero through potentiometer located on component board.

THE JOHNS HOPKINS UNIVERSITY
APPLIED PHYSICS LABORATORY
LAUREL, MARYLAND

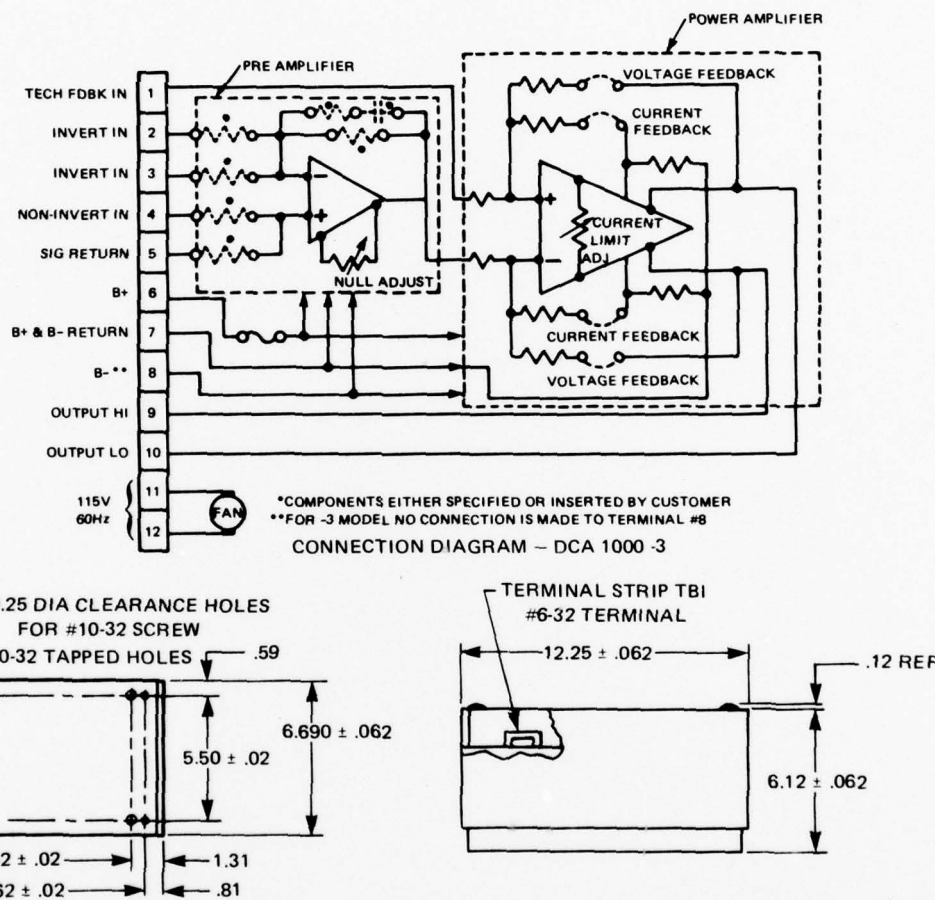


FIG. A-3 BULOVA SERVO PRODUCTS DC SERVO AMPLIFIERS MODEL DCA1000

THE JOHNS HOPKINS UNIVERSITY
APPLIED PHYSICS LABORATORY
LAUREL MARYLAND

Appendix B

AZTRAN ERROR MODEL EQUATIONS

Appendix B

AZTRAN ERROR MODEL EQUATIONS

In the Aztran system, a difference in signal path length exists between the two antennas. This difference is determined by measuring the phase difference of the two received signals.

$$\Delta SR = \lambda_f \cdot [N + \frac{F}{360}] , \quad (B-1)$$

where

ΔSR = the slant range difference,

λ_f = wavelength of received frequency,

N = the whole number (unmeasurable) of wavelengths,
and

F = the number of degrees (measurable) in the fractional wavelengths.

By making repetitive measurements and taking their difference, the unmeasurable constant N drops out of the equation.

From Eq. 30 in Ref. 38, ΔSR can also be expressed

$$\Delta SR = -[X \cdot \Delta X + Y \cdot \Delta Y + Z \cdot \Delta Z] / SR , \quad (B-2)$$

where, in Cartesian coordinates,

$$X = X_{sat} - X_{nav}$$

$$Y = Y_{sat} - Y_{nav}$$

$$Z = Z_{sat} - Z_{nav}$$

From Eq. 28 in Ref. 40,

$$D = [\Delta X^2 + \Delta Y^2 + \Delta Z^2]^{1/2} \quad (B-3)$$

where D is the antenna separation.

Ref. 38. J. R. Albertine, "AZTRAN: A Method of Azimuth Determination Using Artificial Satellites," APL/JHU S3R-71-156, 26 May 1971.

THE JOHNS HOPKINS UNIVERSITY
 APPLIED PHYSICS LABORATORY
 LAUREL, MARYLAND

Again from Ref. 38,

$$\begin{aligned}\Delta X = & - D[\sin \phi \cos \lambda \cos \theta + \sin \lambda \sin \theta] \\ & + \Delta H \cos \phi \cos \lambda\end{aligned}\quad (B-4)$$

$$\begin{aligned}\Delta Y = & - D[\sin \phi \sin \lambda \cos \theta - \cos \lambda \sin \theta] \\ & + \Delta H \cos \phi \sin \lambda\end{aligned}\quad (B-5)$$

$$\Delta Z = D \cos \phi \cos \theta + \Delta H \sin \phi \quad (B-6)$$

where

ϕ = navigator's latitude

λ = navigator's longitude

θ = baseline azimuth angle

ΔH = antenna height difference.

From Eqs. (B-1) through (B-6), ΔSR can be defined as

$$\Delta SR = f(\phi, \lambda, HT, X_s, Y_s, Z_s, D, \Delta H, \theta). \quad (B-7)$$

The true ΔSR can be expressed in terms of a Taylor expansion about the nominal value:

$$\begin{aligned}\Delta SR_t &= \Delta SR_n + \frac{\partial f}{\partial \phi} (\phi_t - \phi_n) + \frac{\partial f}{\partial \lambda} (\lambda_t - \lambda_n) + \dots \\ &= \Delta SR_n + \frac{\partial f}{\partial \phi} \delta \phi + \frac{\partial f}{\partial \lambda} \delta \lambda + \frac{\partial f}{\partial HT} \delta HT + \dots\end{aligned}$$

The measured ΔSR can be expressed in terms of the true value

$$\Delta SR_m = \Delta SR_t + \frac{\lambda}{360} \delta \Delta SR_m.$$

By subtracting the nominal value from the measured value, the true value drops out.

$$\Delta SR_m - \Delta SR_n = \frac{\lambda}{360} \delta \Delta SR_m - \frac{\partial f}{\partial \theta} \delta \theta - \left[\frac{\partial f}{\partial \phi} \frac{\partial f}{\partial \lambda} \dots \frac{\partial f}{\partial \Delta H} \right] \begin{bmatrix} \delta \phi \\ \delta \lambda \\ \vdots \\ \delta \Delta H \end{bmatrix} \quad (B-8)$$

During a satellite pass, many measurements are made. An estimated azimuth angle is then improved in an iterative least-squares sense to drive the nominal ΔSR to the same value as the measured ΔSR . Equation (B-8) now becomes

$$\frac{\partial f}{\partial \theta} \delta \theta = \frac{\lambda}{360} \delta \Delta SR_m - \left[\frac{\partial f}{\partial \phi} \frac{\partial f}{\partial \lambda} \dots \frac{\partial f}{\partial \Delta H} \right] \begin{bmatrix} \delta \phi \\ \delta \lambda \\ \vdots \\ \delta \Delta H \end{bmatrix} \quad (B-9)$$

In a similar manner, the antenna separation error sensitivity can be determined.

$$\frac{\partial f}{\partial D} \delta D = \frac{\lambda}{360} \delta \Delta R_m - \left[\frac{\partial f}{\partial \phi} \frac{\partial f}{\partial \lambda} \dots \frac{\partial f}{\partial \Delta H} \frac{\partial f}{\partial \theta} \right] \begin{bmatrix} \delta \phi \\ \delta \lambda \\ \vdots \\ \delta \Delta H \\ \delta \theta \end{bmatrix} \quad (B-10)$$

THE JOHNS HOPKINS UNIVERSITY
APPLIED PHYSICS LABORATORY
LAUREL MARYLAND

Assume that during the satellite pass, N separate measurements are made, each representing a two-minute interval. Equation (B-9) now takes the form

$$\begin{bmatrix} \frac{\partial f_1}{\partial \theta} \\ \frac{\partial f_2}{\partial \theta} \\ \vdots \\ \vdots \\ \frac{\partial f_n}{\partial \theta} \end{bmatrix} \delta \theta = \frac{\lambda}{360} \begin{bmatrix} \delta \Delta S R_{m1} \\ \delta \Delta S R_{m2} \\ \vdots \\ \vdots \\ \delta \Delta S R_{mn} \end{bmatrix} - \begin{bmatrix} \frac{\partial f_1}{\partial \phi} & \frac{\partial f_1}{\partial \lambda} & \cdots & \frac{\partial f_1}{\partial \Delta H} \\ \frac{\partial f_2}{\partial \phi} & \frac{\partial f_2}{\partial \lambda} & \cdots & \frac{\partial f_2}{\partial \Delta H} \\ \vdots & \vdots & \ddots & \vdots \\ \vdots & \vdots & \vdots & \vdots \\ \frac{\partial f_n}{\partial \phi} & \frac{\partial f_n}{\partial \lambda} & \cdots & \frac{\partial f_n}{\partial \Delta H} \end{bmatrix} \begin{bmatrix} \delta \phi \\ \delta \lambda \\ \vdots \\ \vdots \\ \delta \Delta H \end{bmatrix} \quad (B-11)$$

Let Eq. (B-11) be represented in matrix notation as

$$\underline{R} \cdot \delta \theta = \frac{\lambda}{360} \cdot \underline{M} - \underline{K} \cdot \underline{ER} . \quad (B-12)$$

Using Eq. (B-12) and estimates of the various errors (ϕ , λ , ΔH , $\Delta S R_m$) an error in $\delta \theta$ can be determined to be

$$\delta \theta = \underline{R}^+ \cdot \left\{ \frac{\lambda}{360} \cdot \underline{M} - \underline{K} \cdot \underline{ER} \right\} \cdot \left\{ \frac{1}{\underline{R}^+ \underline{R}} \right\} . \quad (B-13)$$

However, the desired result is not the error from a single pass for a given set of biases but the statistical variance for a pass given an estimated variance in the error sources.

This becomes

$$[\delta \theta]^2 = \underline{R}^+ \cdot \left\{ \left(\frac{\lambda}{360} \right)^2 [\underline{M} \cdot \underline{M}^+] + \underline{K} \cdot [\underline{ER} \cdot \underline{ER}^+] \cdot \underline{K}^+ \right\} \cdot \underline{R} \cdot \left\{ \frac{1}{\underline{R}^+ \underline{R}} \right\}^2 . \quad (B-14)$$

In Eq. (B-14), $[M \cdot M^+]$ is the measurement-error-variance matrix which is diagonalized, implying no correlation from measurement to measurement. Similarly $[ER \cdot ER^+]$ is the diagonalized error-variance measurement, again assuming no correlation from error source to error source.

From Eq. (B-14) the system sensitivities to each variable can be derived and a total error budget can be determined. The only remaining problem is to determine the partial derivatives of f .

$$\Delta SR = \frac{-1}{SR} \cdot [X \cdot \Delta X + Y \cdot \Delta Y + Z \cdot \Delta Z]$$

Therefore the partial derivative of ΔSR can be written

$$\begin{aligned} \frac{\partial \Delta SR}{\partial i} &= -\frac{\partial(1/SR)}{\partial i} [X \cdot \Delta X + Y \cdot \Delta Y + Z \cdot \Delta Z] \\ &\quad - \frac{1}{SR} \cdot \left\{ \frac{\partial X}{\partial i} \Delta X + X \frac{\partial \Delta X}{\partial i} + \frac{\partial Y}{\partial i} \Delta Y + Y \frac{\partial \Delta Y}{\partial i} + \frac{\partial Z}{\partial i} \Delta Z + Z \frac{\partial \Delta Z}{\partial i} \right\}, \end{aligned} \quad (B-15)$$

where i is one of the variables $\phi, \lambda, X_s, Y_s, Z_s, D, \Delta H, \theta$.

$$1/SR = [X^2 + Y^2 + Z^2]^{-\frac{1}{2}},$$

$$\frac{\partial(1/SR)}{\partial i} = \frac{-1}{SR^3} \cdot \left\{ X \cdot \frac{\partial X}{\partial i} + Y \cdot \frac{\partial Y}{\partial i} + Z \cdot \frac{\partial Z}{\partial i} \right\}, \quad (B-16)$$

and

$$X = X_s - X_n,$$

or

$$X = X_s - (R + H_T) \cos \phi \cos \lambda, \quad (B-17)$$

where

$$R = R_e \cdot [\cos^2 \phi + (1 - f)^2 \sin^2 \phi]^{-\frac{1}{2}}$$

R_e = equatorial earth radius

ϕ = navigator's latitude

λ = navigator's longitude

H_T = navigator's height above the reference ellipsoid.

THE JOHNS HOPKINS UNIVERSITY
 APPLIED PHYSICS LABORATORY
 LAUREL MARYLAND

From Eq. (B-17) it can be seen that

$$\frac{\partial X}{\partial X_s} = 1 ,$$

$$\frac{\partial X_s}{\partial H_T} = - \cos \phi \cos \lambda ,$$

$$\frac{\partial X_s}{\partial \phi} = (R + H_T) \sin \phi \cos \lambda + \frac{R^3}{Re^2} \cdot f \cdot (f - 2) \cdot \cos^2 \phi \sin \phi \cos \lambda ,$$

$$\frac{\partial X_s}{\partial \lambda} = (R + H_T) \cos \phi \sin \lambda .$$

$$Y = Y_s - Y_n ,$$

$$Y = Y_s - (R + H_T) \cos \phi \sin \lambda . \quad (B-18)$$

Therefore

$$\frac{\partial Y}{\partial Y_s} = 1 ,$$

$$\frac{\partial Y}{\partial H_T} = - \cos \phi \sin \lambda ,$$

$$\frac{\partial Y}{\partial \phi} = (R + H_T) \sin \phi \sin \lambda + \frac{R^3}{Re^2} \cdot f \cdot (f - 2) \cdot \cos^2 \phi \sin \phi \sin \lambda ,$$

$$\frac{\partial Y}{\partial \lambda} = - (R + H_T) \cos \phi \cos \lambda .$$

$$Z = Z_s - Z_n ,$$

$$Z = Z_s - [R(1 - f)^2 + H_T] \sin \phi , \quad (B-19)$$

THE JOHNS HOPKINS UNIVERSITY
 APPLIED PHYSICS LABORATORY
 LAUREL MARYLAND

$$\frac{\partial Z}{\partial Z_s} = 1 ,$$

$$\frac{\partial Z}{\partial H_T} = - \sin \phi ,$$

$$\frac{\partial Z}{\partial \phi} = - [R(1-f)^2 + H_T] \cos \phi + \frac{R^3}{Re^2} \cdot (1-f)^2 \cdot f \cdot (f-2) \sin^2 \phi \cos \phi$$

$$\Delta X = -D[\sin \phi \cos \lambda \cos \theta + \sin \lambda \sin \theta] + \Delta H \cos \phi \cos \lambda \quad (B-20)$$

$$\frac{\partial \Delta X}{\partial D} = - \sin \phi \cos \lambda \cos \theta - \sin \lambda \sin \theta$$

$$\frac{\partial \Delta X}{\partial \theta} = D[\sin \phi \cos \lambda \sin \theta - \sin \lambda \cos \theta]$$

$$\frac{\partial \Delta X}{\partial \Delta H} = \cos \phi \cos \lambda$$

$$\frac{\partial \Delta X}{\partial \phi} = - D \cos \phi \cos \lambda \cos \theta - \Delta H \sin \phi \cos \lambda$$

$$\frac{\partial \Delta X}{\partial \lambda} = D[\sin \phi \sin \lambda \cos \theta - \cos \lambda \sin \theta] - \Delta H \cos \phi \sin \lambda$$

$$\Delta Y = -D[\sin \phi \sin \lambda \cos \theta - \cos \lambda \sin \theta] + \Delta H \cos \phi \sin \lambda \quad (B-21)$$

$$\frac{\partial \Delta Y}{\partial D} = - \sin \phi \sin \lambda \cos \theta + \cos \lambda \sin \theta$$

$$\frac{\partial \Delta Y}{\partial \theta} = D[\sin \phi \sin \lambda \sin \theta + \cos \lambda \cos \theta]$$

$$\frac{\partial \Delta Y}{\partial \Delta H} = \cos \phi \sin \lambda$$

$$\frac{\partial \Delta Y}{\partial \phi} = -D \cos \phi \sin \lambda \cos \theta - \Delta H \sin \phi \sin \lambda$$

$$\frac{\partial \Delta Y}{\partial \lambda} = -D[\sin \phi \cos \lambda \cos \theta + \sin \lambda \sin \theta] + \Delta H \cos \phi \cos \lambda$$

THE JOHNS HOPKINS UNIVERSITY
APPLIED PHYSICS LABORATORY
LAUREL, MARYLAND

$$\Delta Z = D \cos \phi \cos \theta + \Delta H \sin \phi$$

(B-22)

$$\frac{\partial \Delta Z}{\partial D} = \cos \phi \cos \theta$$

$$\frac{\partial \Delta Z}{\partial \theta} = -D \cos \phi \sin \theta$$

$$\frac{\partial \Delta Z}{\partial \Delta H} = \sin \phi$$

$$\frac{\partial \Delta Z}{\partial \phi} = -D \sin \phi \cos \theta + \Delta H \cos \phi$$

THE JOHNS HOPKINS UNIVERSITY
APPLIED PHYSICS LABORATORY
LAUREL MARYLAND

Appendix C

AZTRAN THEORY AND ERROR ANALYSIS

- 303 -

PRECEDING PAGE BLANK-NOT FILMED

Appendix C

AZTRAN THEORY AND ERROR ANALYSIS

INTRODUCTION

The goal of precision navigation can be simply stated as successfully traveling from an arbitrary location to a desired location in an optimal manner. To solve this problem, two pieces of information are required. First, the navigator must know his current location and second, he must know a reference direction. By using these two pieces of information and knowing his destination, the direction of travel can be determined.

A solution to the second problem, the determination of reference direction or azimuth, will be discussed here. There are in existence many techniques for determining azimuth such as magnetic compasses, gyro compasses, star sighting, and radio beacons.

Each of the above-mentioned techniques has drawbacks, such as accuracy limitations or geographic or weather limitations. Star sighting, for example, is weather dependent while magnetic and gyro compasses will not function in the polar latitudes. A gyro compass aligned to an external reference will hold the alignment, however, it will not self-align in the polar latitudes.

The proposed azimuth determination technique has no weather limitations and is available worldwide, offering a new tool for high latitude navigation. This method uses two nondirectional antennas in an interferometer configuration receiving signals from the Navy Navigation Satellites. These satellites are in polar orbit and give worldwide coverage.

Aztran, an abbreviation for Azimuth from Transit, is a system that determines north reference from a single pass of a navigation satellite. The system utilizes two antennas separated by a baseline distance of between 50 and 100 m. Due to the separation of the antennas, there is a path-length difference from the antennas to the satellite. From Fig. C-1 it can be seen that the path difference $\Delta P = D \cdot \cos(E_1) (Az_{sat} - Az_{ant})$. When the signals from the two antennas are compared, there is a phase difference due to this path-length difference. The phase difference equals $(2\pi D/\lambda) \cdot \cos(E_1) \cdot \cos(Az_{sat} - Az_{ant})$, where λ is the wavelength of the received signal, E_1 is the satellite elevation and Az_{sat} is the satellite azimuth angle.

THE JOHNS HOPKINS UNIVERSITY
APPLIED PHYSICS LABORATORY
LAUREL, MARYLAND

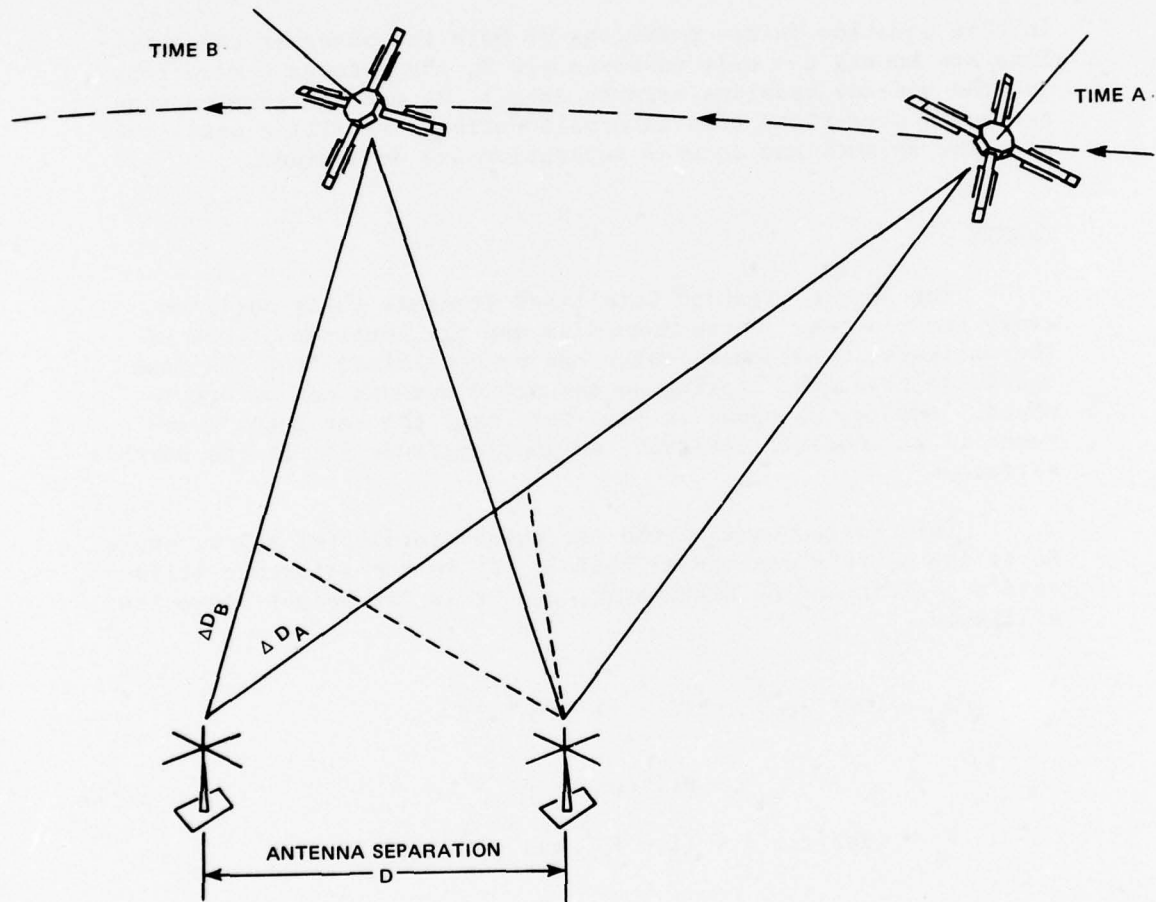


FIG. C-1 AZTRAN CONCEPT

As the satellite moves across the sky, the path-length difference and corresponding phase angle change. This phase change is measured between time A and time B and is equal to:

$$\{2\pi D/\lambda\} \{ [\cos(EI) \cos(Az_{sat} - Az_{ant})]_B - [\cos(EI) \cos(Az_{sat} - Az_{ant})]_A \} .$$

In this equation (since positions of both the observer and satellite are known) the only unknowns are D, the antenna separation, and the antenna baseline azimuth Az_{ant} . By making repeated measurements over fixed time intervals during a satellite pass, the baseline azimuth and antenna separation are determined.

THEORY

Military Navigation Satellites transmit their position every 10 minutes. Given these data and the location of one of the satellites' antennas, which can be determined from the same satellite pass, the bearing to the other antenna can be determined. Assume, as shown in Fig. C-2, that the navigator's antenna is at geodetic latitude ϕ and longitude λ' on the earth's surface.

This corresponds to the Cartesian coordinates below, where R_e is the earth's equatorial radius, f is the reference ellipsoid's coefficient of flattening, and H_t is the height above the ellipsoid.

$$x_n = \{R_e / [\cos^2 \phi + (1 - f)^2 \sin^2 \phi]\}^{1/2} + H_t \cos \phi \cos \lambda' , \quad (C-1)$$

$$y_n = \{R_e / [\cos^2 \phi + (1 - f)^2 \sin^2 \phi]\}^{1/2} + H_t \cos \phi \sin \lambda' , \quad (C-2)$$

and

$$z_n = \{R_e(1 - f)^2 / [\cos^2 \phi + (1 - f)^2 \sin^2 \phi]\}^{1/2} + H_t \sin \phi . \quad (C-3)$$

The second antenna is a distance D away from the first at coordinates $x_n + \Delta X$, $y_n + \Delta Y$, and $z_n + \Delta Z$, and at an azimuth angle θ from North.

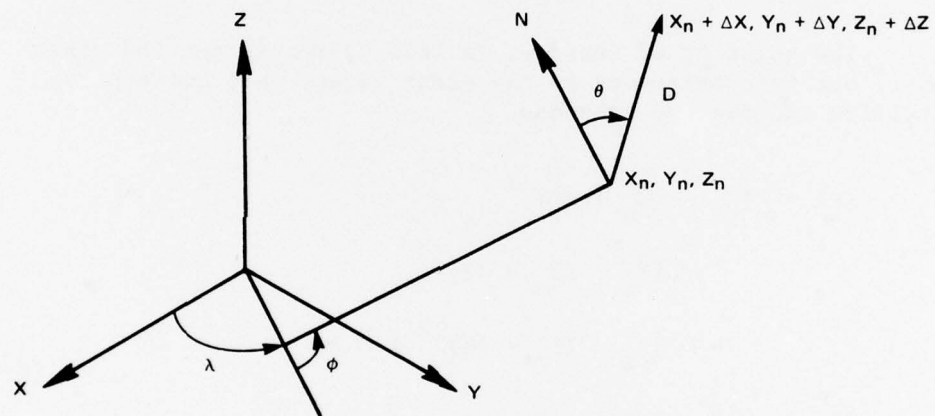


FIG. C-2 COORDINATES USED IN DERIVING EQUATIONS

If the position of the satellite is X_s , Y_s , Z_s in earth fixed coordinates, then the slant range to the satellite is

$$SR = [(X_s - X_n)^2 + (Y_s - Y_n)^2 + (Z_s - Z_n)^2]^{\frac{1}{2}}$$

$$SR = [X_{\text{net}}^2 + Y_{\text{net}}^2 + Z_{\text{net}}^2]^{\frac{1}{2}}, \quad (C-4)$$

where $X_{\text{net}} = X_s - X_n$, etc.

From Fig. C-2, it can also be seen that the antenna separation D is

$$D = [(\Delta X)^2 + (\Delta Y)^2 + (\Delta Z)^2]^{\frac{1}{2}}. \quad (C-5)$$

The quantity of interest in this system is not the slant range, but the difference in the slant range, ΔSR , between the satellite and the two antennas.

$$\begin{aligned} \Delta SR &= \{[X_s - (X_n + \Delta X)]^2 \\ &\quad + [Y_s - (Y_n + \Delta Y)]^2 \\ &\quad + [Z_s - (Z_n + \Delta Z)]^2\}^{\frac{1}{2}} - SR \\ \Delta SR &= [SR^2 - 2(X_{\text{net}} \cdot \Delta X \\ &\quad + Y_{\text{net}} \cdot \Delta Y + Z_{\text{net}} \cdot \Delta Z) \\ &\quad + D^2]^{\frac{1}{2}} - SR \end{aligned} \quad (C-6)$$

If D^2 is neglected and the bracketed term is expanded, then:

$$\begin{aligned} \Delta SR &= [SR - (1/SR)(X_{\text{net}} \cdot \Delta X \\ &\quad + Y_{\text{net}} \cdot \Delta Y + Z_{\text{net}} \cdot \Delta Z)] - SR \\ \Delta SR &= - (1/SR)(X_{\text{net}} \cdot \Delta X \\ &\quad + Y_{\text{net}} \cdot \Delta Y + Z_{\text{net}} \cdot \Delta Z) \end{aligned} \quad (C-7)$$

The only remaining problem is to determine ΔX , ΔY , and ΔZ in terms of the antenna separation D and azimuth angle θ . Define a new variable ΔH , which is the height difference between the antennas. Then

$$D = [D_{\text{plane}}^2 + (\Delta H)^2]^{1/2},$$

where D_{plane} is the in-plane separation of the antennas.

From Fig. C-2 and the preceding definitions, it can be shown that

$$\begin{aligned} \Delta X = & - D_{\text{plane}} [\sin \phi \cos \lambda' \cos \theta + \sin \lambda' \sin \theta] \\ & + \Delta H \cos \phi \cos \lambda', \end{aligned} \quad (C-8)$$

$$\begin{aligned} \Delta Y = & - D_{\text{plane}} [\sin \phi \sin \lambda' \cos \theta - \cos \lambda' \sin \theta] \\ & + \Delta H \cos \phi \sin \lambda', \end{aligned} \quad (C-9)$$

and

$$\Delta Z = D_{\text{plane}} \cos \phi \cos \theta + \Delta H \sin \phi. \quad (C-10)$$

Finally, Eq. (C-8), (C-9), and (C-10) are inserted into Eq. (C-7) to yield a usable result.

$$\begin{aligned} \Delta SR = & \{D_{\text{plane}} / SR\} \{ [(X_{\text{net}} \cos \lambda' \\ & + Y_{\text{net}} \sin \lambda') \sin \phi \\ & - Z_{\text{net}} \cos \phi] \cos \theta + [X_{\text{net}} \sin \lambda' \\ & - Y_{\text{net}} \cos \lambda'] \sin \theta \\ & - [\Delta H / SR] [(X_{\text{net}} \cos \lambda' \\ & + Y_{\text{net}} \sin \lambda') \cos \theta + Z_{\text{net}} \sin \phi] \} \end{aligned} \quad (C-11)$$

The path-length difference between the satellite and the two antennas, ΔSR , can be expressed in wavelengths as $N \cdot \lambda$, where λ is the wavelength of the frequency being received and N is the number of cycles. If another measurement were taken at a later time, $\Delta SR_2 = N_2 \lambda$.

It is not possible to measure the actual value of N . Therefore, the change in phase with time is determined by counting cycles of phase change between time₁ and time₂. This gives $\Delta SR_2 - \Delta SR_1 = (N_2 - N_1) \cdot \lambda$. The process is repeated for as many time intervals as possible during a satellite pass in a manner similar to the standard satellite navigation technique. Using this method it never becomes necessary to know the original N_1 , only the difference counts.

An example of the solution technique will be shown where it will be assumed that ΔH is known, while θ and D are the variables of solution. An iterative least-squares solution is employed using an initial estimate of θ and D . This estimate is improved by each iteration until the improvements are sufficiently small.

Assume that M data intervals were collected during a satellite pass. N_k is the measured phase change during the k th interval and ΔSR_k is Eq. (C-11) for the k th interval. The mean-square error can be defined as follows:

$$E(\theta, D_{\text{plane}}) = \sum_{k=1}^M [N_k \cdot \lambda - (\Delta SR_k - \Delta SR_{k-1})]^2 . \quad (\text{C-12})$$

In order to obtain a least-squares fit, one requires that

$$\partial E / \partial \theta = \partial E / \partial D_{\text{plane}} = 0 .$$

To obtain this least-squares solution we define an $(M \times 3)$ matrix, which for the k th interval is:

THE JOHNS HOPKINS UNIVERSITY
APPLIED PHYSICS LABORATORY
LAUREL, MARYLAND

$$C(k, 1) = N_k \cdot \lambda - (\Delta SR_k - \Delta SR_{k-1})$$

$$C(k, 2) = \partial(\Delta SR)_k / \partial(D_{\text{plane}})$$

$$- \partial(\Delta SR)_{k-1} / \partial(D_{\text{plane}}) \quad (C-13)$$

$$C(k, 3) = \partial(\Delta SR)_k / \partial(\theta)$$

$$- \partial(\Delta SR)_{k-1} / \partial(\theta),$$

where

$$\begin{aligned} \partial \Delta SR / \partial D_{\text{plane}} = & \{1/SR\} \{ [(X_{\text{net}} \cos \lambda' \\ & + Y_{\text{net}} \sin \lambda') \sin \phi \\ & - Z_{\text{net}} \cos \phi] \cos \theta \\ & + [X_{\text{net}} \sin \lambda' \\ & - Y_{\text{net}} \cos \lambda'] \sin \theta \} \end{aligned} \quad (C-14)$$

$$\begin{aligned} \partial \Delta SR / \partial \theta = & \{D_{\text{plane}} / SR\} \{ [X_{\text{net}} \sin \lambda' \\ & - Y_{\text{net}} \cos \lambda'] \cos \theta \\ & + [(X_{\text{net}} \cos \lambda' \\ & + Y_{\text{net}} \sin \lambda') \sin \phi \\ & - Z_{\text{net}} \cos \phi] \sin \theta \} \end{aligned} \quad (C-15)$$

In this C matrix, the values of θ and D_{plane} are the current estimated values. From the C matrix, an A matrix is defined, where

$$A_{ij} = \sum_{k=1}^M C_{ki} \cdot C_{kj} \quad i = 2, 3$$

$$j = 1, 2, 3 \quad (C-16)$$

Given this A matrix, the corrections to θ and D can be obtained:

$$d(D_{\text{plane}}) = [A_{31}A_{23} - A_{21}A_{33}] / [A_{22}A_{33} - A_{32}A_{23}] \quad (\text{C-17})$$

$$d(\theta) = [A_{21}A_{32} - A_{31}A_{22}] / [A_{22}A_{33} - A_{32}A_{23}] \quad (\text{C-18})$$

These values are added to the old estimates of θ and D and the iteration is repeated until the corrections become insignificant.

The above technique permits the determination of both azimuth and antenna separation. If it were possible to know the antenna separation by some other means, such as a survey, then the antenna azimuth would be the only variable of solution. In addition to simplifying the equations, the accuracy of the azimuth solution is increased.

INITIAL TESTS

The initial Aztran tests employed two APL translocation backpacks as satellite receivers. These units, as shown in Fig. C-3, received the 400-MHz satellite signals on antennas separated by about 50 m. Both receivers were driven by the same 5-MHz local oscillator to provide phase coherence between the 32-kHz intermediate frequency outputs.

The phase difference between the two 32-kHz outputs was measured by the phase comparator. A flip-flop was turned on by the negative-going zero crossing of one 32-kHz IF and turned off by the negative-going zero crossing of the other. The flip-flop's output was then integrated over many cycles producing an analog voltage proportional to the phase shift between the IF signals and fed to a strip-chart recorder.

A number of satellite passes were taken using this configuration. The phase was recorded on a strip chart and the two-minute time marks were superimposed over the phase. To determine the number of phase counts during a two-minute interval, the charted

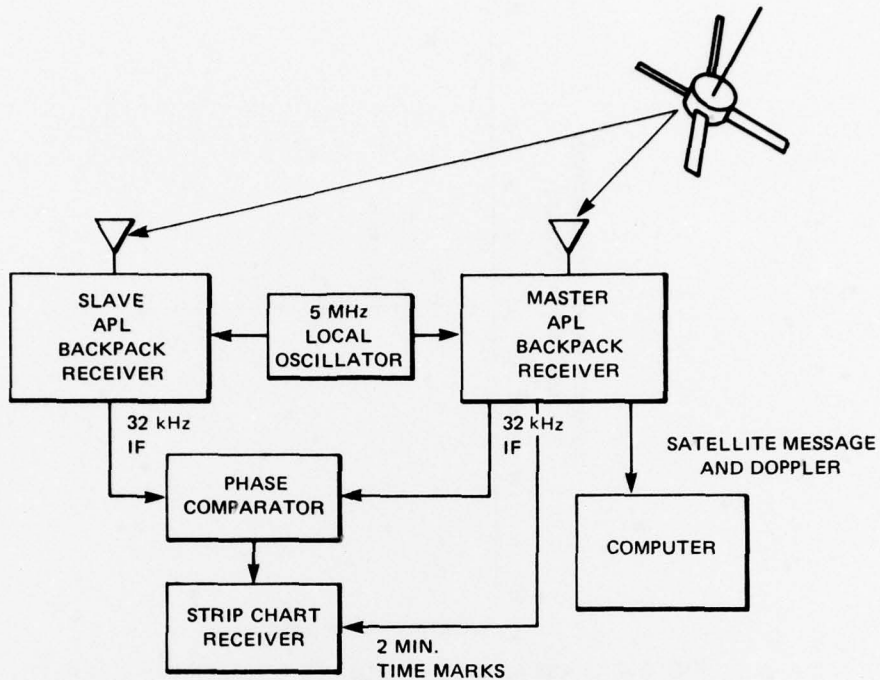


FIG. C-3 AZTRAN BLOCK DIAGRAM

sawtooth waveforms were counted between the time markers and recorded.

From a survey, the azimuth of the antenna baseline was determined and compared to the computed results. The errors in various passes are plotted in Fig. C-4 against the number of usable two-minute data intervals received. As can be seen, the errors were strongly dependent on the number of intervals, indicating a great deal of noise in the data.

Many intervals had to be discarded because one or the other of the receivers would occasionally lose the satellite's signal. If this happened for even a second then the data from the entire two-minute interval had to be discarded. This initial test configuration demonstrated the system concept; however, it became apparent that if more accuracy were desired, better use would have to be made of the available data.

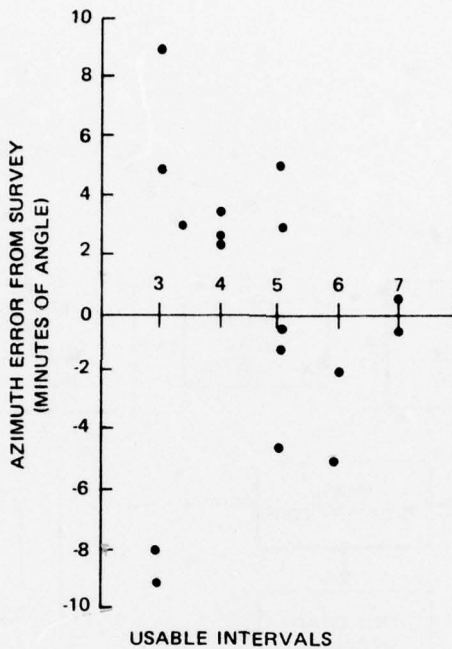


FIG. C-4 PASS AZIMUTH ERRORS VS. NUMBER OF USABLE 2-MINUTE INTERVALS

IMPROVED TEST CONFIGURATION

There were two basic problem areas in the initial test configuration. The first problem was the large amount of usable data that was being discarded due to the receivers occasionally losing the signal. This problem was minimized by changing the measurement intervals from two minutes to 15 seconds. Thus only 15 seconds of data would be lost if a receiver were to lose the signal momentarily. Shortening the measurement interval required a knowledge of the satellite position every 15 seconds instead of every two minutes. These coordinates were obtained by a fourth-order Lagrangian interpolation of the two-minute interval XYZ coordinates.

The second problem involved the data reduction. In the original system, it was necessary to read manually the strip-chart recording and estimate the true phase from the noisy phase recording. It became desirable to automate the entire process, which would allow data collection on a 24-hour basis. To solve this problem, an available Honeywell H-21 computer was used. This is an 8-K, 18-bit word computer that was already interfaced to the APL backpack receiver to do the navigation calculations.

A different phase comparator was built that gave a digital measure of the phase difference in the signal. On command from the computer, one counter would count the number of 10-MHz clock pulses occurring in one complete cycle of one of the 32-kHz IF outputs. Another counter would simultaneously count the number of 10-MHz clock pulses occurring between negative-going zero crossings of the two IF outputs. These two counts were transferred to the computer and a ratio of them taken giving the percentage phase delay to an accuracy of about 2° .

The computer sampled the phase up to 100 times per second and then fed these samples through a second-order digital filter. The filter predicted the next phase measurement and the error in the prediction was used to generate a correlation value. When a significant difference between the measured and predicted phase appeared, it was assumed that one or both of the receivers had lost the signal and the particular data interval was disregarded.

The value of the output of the filter was stored every 15 seconds and used in the Aztran calculations. Figure C-5 is a flow chart of the steps involved in generating the filtered phase output.

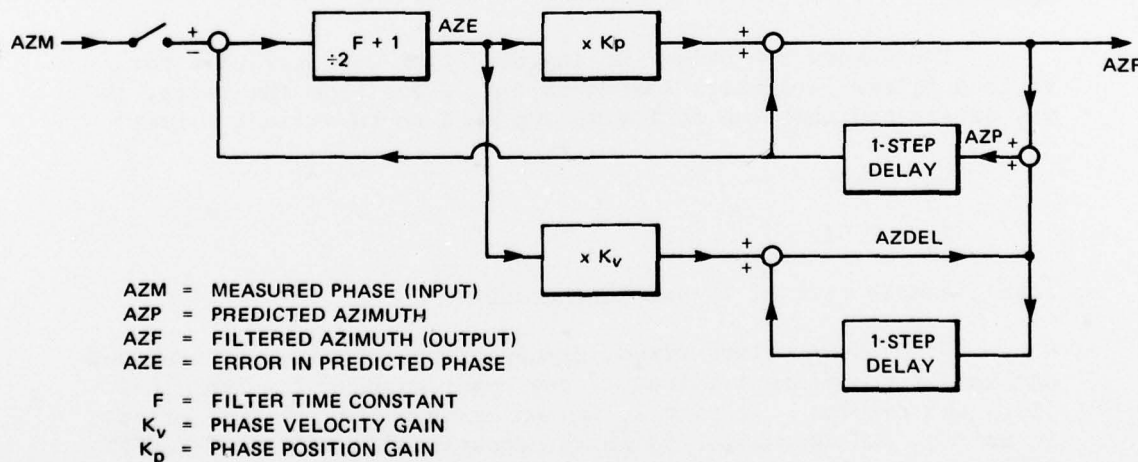


FIG. C-5 AZTRAN SECOND-ORDER DIGITAL FILTER

During a satellite pass the computer stores the satellite message and the doppler counts used for navigation. Simultaneously the computer digitally filters the measured phase and stores the output of the filter every 15 seconds. At the conclusion of the satellite pass, the computer executes the navigation calculations and prints the results. The stored values from the digital filter for every 15 seconds during the pass and the satellite's XYZ coordinates are then punched on paper tape for later processing. When a roll of paper tape is accumulated, usually in about three days, it is transferred to magnetic tape and used as an input to the Aztran calculations program. This PL-1 program computes the azimuth and separation or just the azimuth, if the antenna separation is known.

Figure C-6 shows Aztran equipment installed in a van. On the left is the Teletype that prints the results from the computer, which is to its right. In the equipment rack are, top to bottom, the phase measuring interface, paper-tape reader and punch, and one of the two satellite receivers. On the table to the right are a strip-chart recorder and the second receiver.

Figure C-7 is a photo of one of the two Aztran antennas. It is a 10-ft-tall quad, helix wound for 400 MHz. This antenna was designed to have uniform coverage in the upper hemisphere and attenuate sharply any reflections from below the horizon in order to reduce phase errors.

RESULTS

Tests were run using the improved test configuration for various filter parameters listed in Fig. C-5. From the tests, it was determined that the following appeared to be optimum values:

$$K_v = 0.8$$

$$K_p = 0.03$$

with a sample rate of 12 samples/second.

With these values fixed, groups of passes were received and analyzed for different values of the constant FSHIFT. Table C-1 lists the results. In part A, it can be seen that the rms error in azimuth and separation is fairly constant for values of FSHIFT less than 9. In this calculation, azimuth and separation were both variables of the solution. In part B, one of the groups of passes was analyzed, solving only for azimuth. The separation was determined by a survey. The rms error in this instance was about half

THE JOHNS HOPKINS UNIVERSITY
APPLIED PHYSICS LABORATORY
LAUREL, MARYLAND

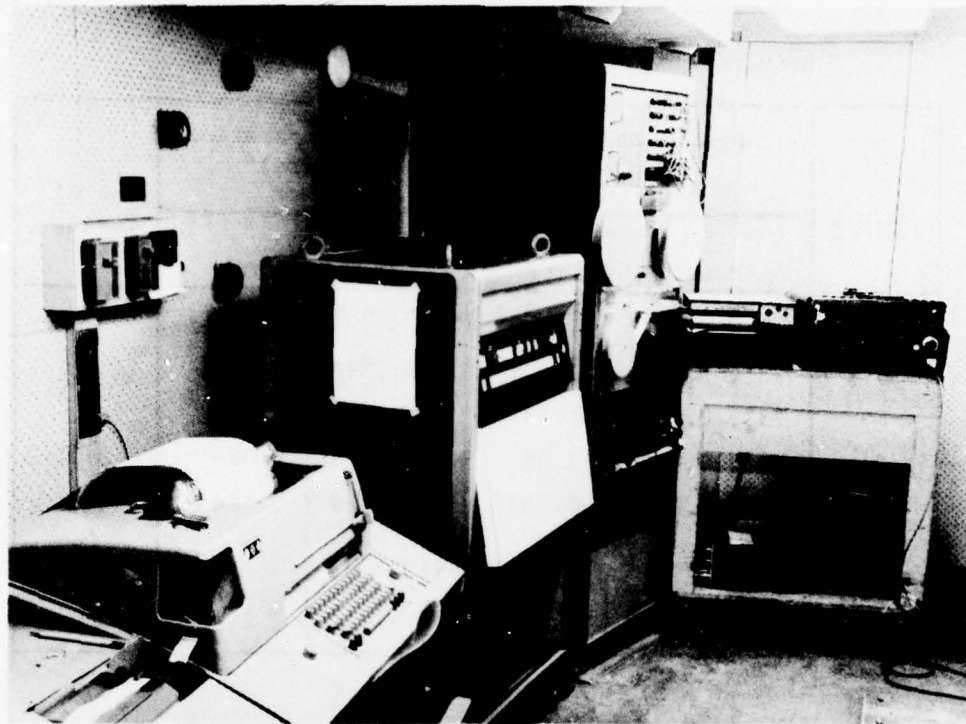


FIG. C-6 AZTRAN EQUIPMENT



FIG. C-7 ONE OF TWO AZTRAN ANTENNAS

Table C-1
 Results of Computer Filtered Aztran Passes

FSHIFT	Antenna Azimuth		Antenna Separation (meters)		No. of Passes
	Mean	rms	Mean	rms	
A. Azimuth and Separation Solution					
6	73°, 0.316'	1.63'	51.899	0.072	6
7	73°, 0.094'	1.64'	51.846	0.115	9
8	73°, 0.463'	1.69'	51.868	0.099	16
9	73°, 1.907'	6.834'	51.829	0.214	13
B. Azimuth Solution					
8	73°, 0.705'	0.88'			17

that of obtained in part A. This again indicates that there is a great deal of noise in the data since most of these passes had six or seven good two-minute intervals.

CONCLUSIONS

The tests run to date have given very encouraging initial results. The theory and system concept have been proven to be practical. If the system errors can be further reduced to about twenty seconds of arc, a factor of three improvement, then the system can compete with north-seeking gyro compasses in the equatorial and mid-latitude regions. Aztran shows promise as a unique tool for navigation in the polar regions.

Certain questions remain to be answered. The system's error sources, such as multipath reflections, which may be causing phase distortion, need more careful study.

INITIAL DISTRIBUTION EXTERNAL TO THE APPLIED PHYSICS LABORATORY*

The work reported in SEV 005 (QM-76-110) was done under Navy Contract N00017-72-C-4401, and is related to Task Q2HO, which is supported by DARPA.

ORGANIZATION	LOCATION	ATTENTION	No. of Copies
DEPARTMENT OF DEFENSE			
Asst. Sec'y. of Defense	Washington, DC	Install & Logistics	1
Dir. Defense Prog. Anal. and Eval.	Washington, DC		1
Dir., Defense Research/Engineering	Washington, DC		1
Deputy Dir. Defense Research/Engineering	Washington, DC	Res. & Ad. Tech. Mr. R. W. Ziem	1
Prin. Deputy Dir. Defense Research/ Engineering	Washington, DC		1
Asst. Dir. Defense Research/Engineering	Washington, DC	Land Warfare Eng. Development	1
Special Asst. Dir. Defense Research/ Engineering	Washington, DC		1
IDA	Washington, DC	Net. Ech. Assess.	1
DIA	Washington, DC	Wpn. Sys. Eval. Grp.	1
DARPA	Washington, DC	Director	1
		Div. for Sci. & Tech. Intel.	1
		Director	1
		Deputy Dir.	1
		Dir. MISD	1
		Dir. IPT	1
		Dir. TTO: R. Moore	1
DDC	Alexandria, VA-	J. A. Tegnelia	1
		L. B. James	1
			12
<u>Department of the Navy</u>			
<u>Department Offices</u>			
CNO	Washington, DC	OP-03	1
		OP-030	1
		OP-090D	1
		OP-096D	1
		OP-37	1
		OP-371	1
		OP-05W	1
		OP-0982	1
		OP-0987	1
NAVPRO	Laurel, MD		1
Asst. Sec'y. of Navy	Washington, DC	R&D	1
Chief of Naval Research	Washington, DC	R. Cooper (Mech. Br.)	1
Chief of Naval Material	Washington, DC	R. McGregor	1
NAVEASYSYSCOM	Washington, DC	NMAT-03L (Dir. Nav Labs)	1
		NMAT-033	1
		SEA-00	1
		SEA-01	1
		SEA-02	1
		SEA-03	1
		SEA-031	1
		SEA-032	1
		SEA-034	1
		SEA-035	1
		SEA-037	1
		PMS 405-22	1
		PMS 304-42	1
NAVAIRSYSCOM	Washington, DC	Capt. R. VonGerichten	1
NAVELEXSYSCOM	Washington, DC	Code 05L	1
		Mr. Charman	1
		Code 0520A	
		Attn: Mr. Nordberg	1
NAVOCEANO	Bay St. Louis, MS	Cdr. K. Goodman	1
Office of Naval Research	FPO New York, NY	Cdr. H. Jordan	1
NAVSUP Headquarters	Washington, DC	Commander	1

Requests for copies of this report from DoD activities and contractors should be directed to DDC,
Cameron Station, Alexandria, Virginia 22314 using DDC Form 1 and, if necessary, DDC Form 55.

*Initial distribution of this document within the Applied Physics Laboratory has been made in accordance with a list on file in the APL Technical Publications Group.

INITIAL DISTRIBUTION EXTERNAL TO THE APPLIED PHYSICS LABORATORY*

SEV 005

-2-

ORGANIZATION	LOCATION	ATTENTION	No. of Copies
<u>Department of the Navy (cont'd)</u>			
<u>Laboratories</u>			
NRL	Washington, DC	Director	1
NCSL	Panama City, FL	Tech. Dir.	1
NARI	Pt. Barrow, AK	Dir.	1
<u>Centers</u>			
NELC	San Diego, CA	Dave Washburn	1
NUC	New London, CT	Dr. Tom Lang	1
NWC	China Lake, CA	Code 12	1
NSWC	White Oak, MD	Commander	1
NSWC	Dahlgren, VA	Commander	1
NUSC	Newport, RI	Commanding Officer	1
NAVSEC	Washington, DC	SEC-6000	1
		SEC-6100	1
		SEC-6100B1	1
		SEC-6100-01 R. Leopold	1
		SEC-6110-02 R. Lacey	1
		SEC-6112	1
		SEC-6114 R. Johnson	1
		Commander	1
CBC	Gulfport, MS		
<u>Task Forces</u>			
COMOPTEVFOR	Norfolk, VA		1
<u>Ship Yards</u>			
NAVSHIPYD CHASN	Charleston, SC	Commander	1
NAVSHIPYD MARE	Mare Island, CA	Commander	1
NAVSHIPYD BREM	Bremerton, WA	Commander	1
NAVSHIPYD PEARL	Pearl Harbor, HI	Commander	1
NAVSHIPYD PTSMH	Portsmouth, VA	Commander	1
NAVSHIPYD PHILLA	Philadelphia, PA	Commander	1
NAVSHIPYD NORVA	Norfolk, VA	Commander	1
<u>Schools</u>			
U.S. Naval Academy	Annapolis, MD	Div. Eng. & Wpn.	1
NAVPGSCOL	Monterey, CA	Hd. Dept. Naval Sci.	1
NROTC, MIT	Cambridge, MA	Superintendent	1
NADC	Warminster, PA	Commanding Officer	1
NAWWARCOL	Newport, RI	Commander	1
		President	1
<u>Facilities</u>			
NAVFAC	Alexandria, VA	PAC 031	1
<u>Marine Corps</u>			
Marine Corps Headquarters	Washington, DC	Lt. Col. J. Gonzales (372M)	1
Marine Corp. Dev. & Ed. Command	Quantico, VA	J. Sellwood	1
Commandant, Marine Corps	Washington, DC	A. L. Slafkosky, MCRD-1	1
		Commanding Officer	1
		R&D	1
<u>Department of the Air Force</u>			
<u>Department Offices</u>			
Air Force Systems Command	Washington, DC	SCSME	1
Air Force Chief of Staff	Washington, DC	AFRDQRF	1
<u>Laboratories</u>			
Wright-Patterson AFB	Dayton, OH	AFIT-CE	1

*Initial distribution of this document within the Applied Physics Laboratory has been made in accordance with a list on file in the APL Technical Publications Group.

INITIAL DISTRIBUTION EXTERNAL TO THE APPLIED PHYSICS LABORATORY*

SEV 005

-3-

ORGANIZATION	LOCATION	ATTENTION	No. of Copies
<u>Department of the Air Force (cont'd)</u>			
<u>Schools</u>			
Air University	Maxwell AFB, AL	Commandant	1
<u>Department of the Army</u>			
Headquarters, U.S. Army	Washington, DC		1
Asst. Sec'y. of the Army	Washington, DC		1
Army Office of the Chief of Staff	Washington, DC		1
Army Asst. Chief of Staff	Washington, DC	SAAS-RD DACS-ZB Intel. DAMI-DO	1 1 1 1
<u>Laboratories</u>			
Army Air Mobility Equipment R&D Ctr.	Ft. Belvoir, VA	Attn: John Sargent	1
Army Cold Regions Res. & Eng. Lab.	Hanover, MA	CRREL Library	1
Army Natick Laboratory	Natick, MA	Dr. K. F. Sterrett	1
Army Night Vision Laboratory	Ft. Belvoir, VA	Commander	1
Army Foreign Sci. & Tech. Ctr.	Charlottesville, VA	Attn: Mr. J. Martino	1
Army Waterways Experimental Station	Vicksburg, MS	S. Dibbern D. R. Freitag	1 1
<u>Commands</u>			
Army Combat Development Command	Ft. Eustis, VA	Commanding Officer	1
Army Materiel Dev. & Readiness Command	Washington, DC	Commander	1
Army Tank Auto Command	Ann Arbor, MI	Commander	1
<u>Schools</u>			
U.S. Military Academy	West Point, NY	Prof. of Ordnance	1
U.S. Army Intelligence School	Fort Huachuca, AR	Commander	1
National War College	Washington, DC	Commandant	1
<u>U. S. GOVERNMENT AGENCIES</u>			
Dept. of Transportation, Office of the Sec'y. of Trans.	Washington, DC	R&D	1
Maritime Admin.	Washington, DC	R&D (C.G.)	1
Central Intelligence Agency	Washington, DC	J. A. Higgins M. Pitkin Ch. Phy. Sci. & Tech. Div.	1 1 1
<u>STATE GOVERNMENT</u>			
Governor, State of Alaska	Juneau, AK		1
<u>COLLEGES AND UNIVERSITIES</u>			
California Institute of Technology	Pasadena, CA	Dr. A. J. Acosta	1
Cornell University	Ithaca, NY	S. F. Shen	1
Massachusetts Institute of Technology	Cambridge, MA	Dean A. Keil	1
Princeton University	Princeton, NJ	Prof. D. Hazen	1
Stevens Institute of Technology	Hoboken, NJ	Library	1
University of Alaska	College, AK	Library	1
University of Maryland	College Park, MD	Dr. J. Weske	1
University of Michigan	Ann Arbor, MI	Dr. T. F. Ogilvie	1
University of Toronto	Toronto, Ontario, Canada	Dr. P. A. Sullivan	1
<u>CONTRACTORS</u>			
Aerojet-General Corp.	Takoma, WA	F. Herman	1
Aerospace Corp.	Los Angeles, CA	R. Scott	1
Arctic Institute of N. America	Montreal, Quebec, Canada	R. Taylor	1
Bell Aerospace Corp.	Washington, DC	W. G. Johnson	1
Bell Aerospace Corp.	New Orleans, LA	J. Chaplin	1
Boeing Co.	Seattle, WA	R. Miller	1
		W. A. Eul	1

*Initial distribution of this document within the Applied Physics Laboratory has been made in accordance with a list on file in the APL Technical Publications Group.

INITIAL DISTRIBUTION EXTERNAL TO THE APPLIED PHYSICS LABORATORY*

SEV 005
-4-

ORGANIZATION	LOCATION	ATTENTION	No. of Copies
CONTRACTORS (cont'd)			
Delphi Corp.	McLean, VA	Dr. L. D. Strom	1
Goodyear Tire and Rubber Co.	Akron, OH	H. Boyd	1
Grumman Aerospace Corp.	Bethpage, NY	W. Wohleking	1
Hydronautics, Inc.	Laurel, MD	Mr. V. Johnson	1
National Academy of Sci.	Washington, DC	National Res. Council	1
Rohr Industries, Inc.	San Diego, CA	W. Eggington	1
Science Application, Inc.	Arlington, VA	N. Ray	1
Science Application, Inc.	Redbank, CA	W. S. Vance	1
Southwest Research Institute	San Antonio, TX	Dr. H. B. Abramson	1
FOREIGN			
Canadian Dept. of Transportation	Ottawa, Ontario, Canada	Mr. John Doherty	1
Dept. of Industry, Trade, & Commerce	Ottawa, Ontario, Canada	Mr. J. E. Seal	1
Dir. Canadian Coast Guard	Ottawa, Ontario, Canada	Mr. J. L. Harrison	1
Northern Transportation, Ltd.	Ottawa, Ontario, Canada	Capt. W. J. H. Stuart	1
Admiralty Surface Weapons Establishment (West)	Hampshire, England	Mr. B. W. Mead	1
British Embassy	Washington, DC	P. Grantham	1
British Hovercraft	Yeovil, England	R&D	1
EMI Electronics, Ltd.	London, England	Library	1
Royal Signal Radar Establishment	London, England	S. G. Woolcock	1
Vosper Hovercraft	Paul's Grove, Hampshire, England	Donald McDonald	1
		Library	1

*Initial distribution of this document within the Applied Physics Laboratory has been made in accordance with a list on file in the APL Technical Publications Group.